TECHNISCHE UNIVERSITÄT MÜNCHEN

MAX-PLANCK-INSTITUT FÜR EXTRATERRESTRISCHE PHYSIK

An X-ray investigation of the Small Magellanic Cloud with XMM-Newton

Richard K. N. Sturm

Vollständiger Abdruck der von der Fakultät für Physik der Technischen Universität München zur Erlangung des akademischen Grades eines

Doktors der Naturwissenschaften

genehmigten Dissertation.

Vorsitzender: Univ.-Prof. Dr. Michael Ratz
Prüfer der Dissertation:
1. Priv.-Doz. Dr. Jochen Greiner
2. Univ.-Prof. Dr. Lothar Oberauer

Die Dissertation wurde am 27.9.2012 bei der Technischen Universität München eingereicht und durch die Fakultät für Physik am 22.11.2012 angenommen.

An X-ray investigation of the Small Magellanic Cloud with XMM-Newton

Abstract

Observations of Local Group galaxies allow detailed studies of their stellar and interstellar content. With a distance of only 60 kpc, the Small Magellanic Cloud (SMC) is the second nearest star-forming galaxy. The XMM-*Newton* survey of the SMC provides for the first time a complete coverage of the SMC main body with imaging X-ray optics in the (0.2−12.0) keV band down to a luminosity of $\sim 10^{34}$ erg s^{-1}. The observations reveal the large population of high-mass X-ray binaries (HMXBs), supernova remnants (SNRs), super-soft X-ray sources (SSSs), and the hot interstellar medium (ISM) in the SMC, as well as active galactic nuclei (AGN) behind the SMC. Based on the XMM-*Newton* data, this thesis is focusing on the point-source population in the SMC field, individual X-ray sources, and the diffuse X-ray emission in the SMC.

To investigate the X-ray point-source population, I searched for sources in the EPIC images using maximum-likelihood techniques. This yielded 3053 unique X-ray point-sources with a median position uncertainty of 1.3″ in a field of 6.32 deg^2. In total 49 SMC HMXBs, 4 SSSs, 34 foreground stars, and 72 AGN behind the SMC could be identified. I classified other X-ray sources using hardness ratios, X-ray variability, and their multi-wavelength properties. This resulted in candidates for 45 SMC HMXBs and 8 faint SSSs, as well as 2092 AGN and 13 galaxy clusters. I discuss statistical properties, like spatial distribution, X-ray colour diagrams, luminosity functions, and time variability of the population. The bright-end power-law slope for the differential luminosity function of HMXBs in the SMC is significantly steeper ($\alpha = 3.30^{+2.17}_{-1.38}$) than found for HMXB populations of other nearby galaxies above a luminosity of 10^{38} erg s^{-1}. This indicates a different behaviour of Be/X-ray binaries and supergiant HMXB.

Three X-ray sources were analysed and discussed in detail: The symbiotic binary SMC 3, an accreting white dwarf (WD) with thermonuclear surface burning, was found at its highest X-ray luminosity as observed until now. I found, that the X-ray variability can be explained by variations either in normalisation (by a factor of ∼50) or in temperature ($kT = 24 - 34$ eV) but not by photoelectric absorption around an eclipse. XMMU J010147.5-715550 was found as a new faint SSS in the point-source catalogue and correlates with AzV 281, an early Be star. The X-ray spectrum is well represented by black-body and WD atmosphere models with highly model-dependent temperature (20 – 100 eV). I discuss the source as the first candidate for a Be/WD binary system in the SMC. To investigate the observational boundary conditions for Be/WD systems and to constrain stellar-evolution models, it is of high importance to find more such systems. Four previously unknown transient sources were found during the survey, of which XMMU J004814.0-732204 is discussed as an example. Coherent X-ray pulsations with a period of 11.86642(17) s and the hard power-law-like ($\Gamma = 0.66 \pm 0.03$) X-ray spectrum reveal the neutron-star nature of the compact object. The long-term X-ray variability and the Hα emission line of the optical counterpart identify the source as a HMXB of Be type.

To analyse the diffuse emission, I created a background-subtracted X-ray mosaic image of the SMC field and developed a method for the spectral analysis of diffuse emission with low surface brightness detected by the EPIC-pn camera. The morphology and derived spectral parameters confirm the hot ISM of the SMC as origin of the diffuse X-ray emission. The spectra are well described by collisionally ionised plasma emission with a temperature of $kT \sim 200$ eV. I obtain an absorbed and unabsorbed luminosity of the SMC plasma in the (0.2−2.0) keV band with statistical uncertainties of $7.08^{+0.06}_{-0.06} \times 10^{36}$ erg s^{-1} and $3.95^{+0.05}_{-0.07} \times 10^{37}$ erg s^{-1}, respectively. For the first time, I show that the X-ray luminosity of the ISM correlates with star formation in the SMC ∼40 Myr ago.

The results of the thesis yield deeper insights into the statistical and individual properties of X-ray emitting sources in the SMC, where fainter sources can be studied and discriminated from each other than in more distant star-forming galaxies. Also the connection to the star-formation history can be investigated in more details. The point-source catalogue is the most comprehensive list of X-ray sources in the SMC field. It will, together with the spectral parametrisation of the diffuse emission, contribute complementary information to subsequent research.

Eine Röntgenstudie der Kleinen Magellanschen Wolke mit XMM-Newton

Zusammenfassung

Beobachtungen von Galaxien der Lokalen Gruppe ermöglichen detaillierte Studien ihrer stellaren und interstellaren Bestandteile. Mit einer Distanz von nur 60 kpc ist die Kleine Magellansche Wolke (SMC) die zweitnaheste sternbildende Galaxie. Mit der Durchmusterung the SMC im Rahmen eines XMM-*Newton large-programme* wurde erstmalig eine komplette Abdeckung des SMC-Hauptkörpers mit abbildenden Röntgenoptiken im (0.2−12.0) keV Band erzielt, welche SMC Quellen mit Leuchkräften bis zu $\sim 10^{34}$ erg s^{-1} erfasst. Die Beobachtungen enthüllen die große Population an massereichen Röntgendoppelsternen (HMXBs), Supernovaüberresten (SNRs), superweichen Röntgenquellen (SSSs) und das heiße interstellare Medium in the SMC, so wie aktive Galaxienkerne hinter der SMC. Basierend auf den XMM-*Newton* Daten wurden in dieser Dissertation die Punktquellenpopulation, einzelne Röntgenquellen und die diffuse Röntgenemission untersucht.

Für die Untersuchung der Punktquellenpopulation wurden Quellen in EPIC Bildern mit einer Maximum-Likelihood-Methode gesucht. Dies resultierte in einen Katalog, der 3053 einzelnen Röntgenquellen mit einer mittleren Positionsungenauigkeit von 1.3″ in einem 6.32 deg^2 großem Feld umfasst. Insgesamt konnten 49 SMC HMXBs, 4 SSSs, 34 Vordergrundsterne, und 72 AGN hinter der SMC identifiziert werden. Mittels spektraler und zeitlicher Eigenschaften und der Emission in anderen Wellenlängen wurden die übrigen Quellen klassifiziert. Dies ergab Kandidaten für 45 SMC HMXBs und 8 lichtschwache SSSs, so wie 2092 AGN und 13 Galaxienhaufen. Statistische Eigenschaften, wie die räumliche Verteilung, Röntgenfarbdiagramme, Leuchtkraftfunktionen, und die Zeitvariabilität der einzelnen Populationen werden diskutiert. Die differentielle Leuchtkraftfunktion von HMXBs der SMC folgt bei helleren Leuchtkräften einem Potenzgesetz, welches signifikant steiler ist ($\alpha = 3.30^{+2.17}_{-1.38}$) als bei anderen nahen Galaxien oberhalb einer Leuchtkraft von 10^{38} erg s^{-1} beobachtet wird. Dies weißt auf unterschiedliche Eigenschaften von Be HMXBs und Überriesen HMXB hin.

Drei Röntgenquellen wurden näher untersucht: Das symbiotische Binärsystem SMC 3, ein akkretierender Weißer Zwerg (WD) mit thermonuklearem Oberflächenbrennen, wurde während der Durchmusterung mit bislang hellster Röntgenleuchtkraft beobachtet. Ich zeige, dass die Röntgenvariabilität durch Änderung der Normierung (um einen Faktor von ∼50) oder der Temperatur ($kT = 24-34$ eV) beschrieben werden kann, aber nicht durch photoelektrische Absorption um einen Bedeckungsumgang. XMMU J010147.5-715550 wurde als neue leuchtschwache SSS im Punktquellenkatalog gefunden und korreliert mit AzV 281, einem frühen Be Stern. Das Röntgenspektrum kann mit Schwarzkörperstrahlung und WD-Atmosphären-Modellen beschrieben werden, wobei sich stark modellabhänige Temperaturen ergeben (20 – 100 eV). Ich diskutiere die Quelle als ersten Kandidaten für ein Be/WD System in der SMC. Die Suche solcher System ist wichtig um die Beobachtungsbedingungen und Parameter für Sternentwicklungsmodelle festzulegen. Vier Röntgenausbrüche vorher unbekannte Quellen wurden innerhalb der Durchmusterung gefunden. Als Beispiel wird XMMU J004814.0-732204 diskutiert. Kohärente Röntgenpulsationen mit einer Periode von 11.86642(17) s und das harte, einem Potenzgesetz ($\Gamma = 0.66 \pm 0.03$) folgende Spektrum weisen einen Neutronenstern als kompaktes Objekt nach. Die langzeitige Röntgenvariabilität und die Hα Emission des Begleitsternes identifizieren die Quelle als HMXB vom Be Typ.

Um eine Analyse der diffusen Emission durchzuführen, erzeugte ich ein Röntgenmosaikbild der SMC und entwickelte eine Methode für die spektrale Analyse von diffuser Emission mit schwacher Oberflächenhelligkeit für die EPIC-pn Kamera. Die Untersuchungen bestätigen das heiße ISM der SMC als den Ursprung der diffusen Emission. Die Spektren können mit der Emission von stoßionisiertem Plasma mit einer Temperatur von $kT \sim 200$ eV beschrieben werden. Die absorbierte und unabsorbierte Leuchtkraft im (0.2−2.0) keV Band beträgt $7.08^{+0.06}_{-0.06} \times 10^{36}$ erg s^{-1} und $3.95^{+0.05}_{-0.07} \times 10^{37}$ erg s^{-1}. Erstmalig zeige ich, dass die Röntgenleuchtkraft des ISM mit der Sternbildungsrate vor 40 Millionen Jahren korreliert.

Die Ergebnisse dieser Dissertation führen zu einem tieferen Verständnis der statistischen und individuellen Eigenschaften der röntgenemittierenden Quellen in der SMC, wo im Vergleich zu weiter entfernten sternbildenden Galaxien, Quellen mit schwächerer Leuchtkraft beobachtet und einzelnen Quellen besser unterschieden werden können. Ebenso kann der Zusammenhang von Röntgenemission und Sternenstehung besser untersucht werden. Der Punktquellenkatalog ist der bislang umfangreichste Röntgenquellenkatalog im SMC Feld. Er wird, ebenso wie die spektralen Parametrisierung der diffusen Röntgenemission zu späteren Studien beitragen.

Contents

List of Figures

List of Tables

1. Introduction

Nearby galaxies in the Local Group enable detailed studies of the stellar and interstellar content of complete galaxies. The Small Magellanic Cloud (SMC, Westerlund 1997) is a gas-rich dwarf irregular galaxy that is orbiting the Milky Way. Gravitational interaction with the Large Magellanic Cloud (LMC) and the Galaxy are believed to have triggered recent bursts of star formation (Zaritsky & Harris 2004). The investigation of sources in the SMC has several advantages:

In contrast to the Milky Way, where most sources in the Galactic plane are obscured by large amounts of absorbing gas and dust, sources in the SMC are only moderately affected by Galactic foreground absorption of $N_H \approx 6 \times 10^{20}$ cm^{-2} (Dickey & Lockman 1990). For Galactic sources, the determination of distances can be complicated, leading to uncertain luminosities. Sources in the SMC can be assumed to be at the same and well known distance of ≈60 kpc (e. g. Hilditch et al. 2005). A size of the SMC on the sky of a few degrees enables the investigation of the complete galaxy with few observations, whereas for the Milky Way an all-sky survey would be necessary. The comparison between the SMC and the Milky Way is interesting, due to different metallicities ($Z_{smc} \approx 0.2 Z_\odot$, Russell & Dopita 1992), which influence e. g. the stellar evolution and stellar winds.

In contrast to more distant Local Group galaxies, we can study fainter sources in the Magellanic Clouds. As an example, the flux of a source would decreases by a factor of ∼170 when the source was observed at the distance of the SMC or the Andromeda galaxy (M 31), respectively. In even more distant galaxies, the angular separation of individual sources becomes problematic as well and at even larger distances only the integrated emission of a complete galaxy can be measured. For the SMC, an angular separation of 1″ corresponds to a distance of only 0.29 pc. This allows to separately analyse individual sources. Therefore, an understanding of nearby galaxies like the Magellanic Clouds is important to understand the emission of more distant galaxies.

Due to recent star formation, the SMC harbours a remarkably large population of high-mass X-rays binaries (HMXBs), in which a neutron star (NS) accrets matter from a massive companion star. Due to the short life time of massive stars, also several supernova remnants (SNRs) are observed. The subsequent explosion of SNRs will heat the interstellar medium (ISM) to temperatures of $\sim 10^6$ K. Both the accretion onto compact objects and hot plasma can cause X-ray emission. Soft X-rays, above ∼100 eV, can penetrate large amounts of neutral gas. The focusing of X-ray photons is possible up to several keV with today's X-ray telescopes. This enables X-ray imaging and spectroscopy and the research of the highly energetic astrophysical processes in the SMC.

The X-ray observatory XMM-*Newton* is operated by the European Space Agency (ESA) and has three X-ray telescopes with unprecedented effective area. The XMM-*Newton* large-programme survey of the SMC (PI: Frank Haberl) was performed between May 2009 and March 2010, to further study this galaxy in the (0.2−12.0) keV regime. Previously, the SMC was surveyed with the *Einstein* observatory between 1979 and 1980 (Seward & Mitchell 1981; Wang & Wu 1992) and ROSAT in the 1990s (Kahabka et al. 1999; Haberl et al. 2000; Sasaki et al. 2000). *Chandra* (Weisskopf et al. 2000) observations only cover some disconnected fields in the SMC. In combination with archival observations, the XMM-*Newton* survey provides the first complete coverage of the SMC main body after the ROSAT observations and the very first above 2 keV.

In this thesis, the XMM-*Newton* large-programme survey of the SMC and archival data was analysed homogeneously to achieve three main goals:

1. The study of individual sources in the SMC, e. g. new transient X-ray sources appearing during the survey, interesting sources found during the statistical analysis of the point-source catalogue, and extended sources found in the mosaic image.

2. The creation of an X-ray catalogue and classification of X-ray sources by their spectral, temporal, spatial, and multi-wavelength characteristics, to discriminate between sources in the SMC and in the fore- and background. The catalogue will serve as basis for further studies of HMXBs and super-soft X-ray sources (SSSs) in the SMC and also allow an efficient search for background objects behind the SMC.

3. The complete coverage of the SMC main body allows an investigation of the diffuse X-ray emission and will help to improve the understanding of the ISM of the SMC.

The thesis is organised as follows: In Chapter 2, the reader will find a brief description of the SMC and the XMM-*Newton* observatory, a basic introduction to the physical processes causing X-ray emission and absorption, and a summary of X-ray source classes in the SMC field. The survey and archival XMM-*Newton* observations of the SMC and the reduction of the data are presented in Chapter 3. The XMM-*Newton* SMC point-source catalogue and its characteristics are described in Chapter 4. This Chapter also includes the cross-correlation with other catalogues, the identification and classification of X-ray sources and the analysis of statistical properties of the data set. This study has been submitted to A&A (Sturm et al. 2012a). The results of the analysis of individual X-ray sources are presented in Chapter 5: As an example for a HMXB, the newly discovered Be/X-ray binary pulsar XMMU J004814.0-732204 is presented (Sturm et al. 2011a). I contributed similar X-ray analyses of other HMXBs to the papers by Coe et al. (2011), Coe et al. (2012), Haberl et al. (2012b), and Sturm et al. (2012c). Further I present the analysis of the symbiotic nova SMC 3 (Sturm et al. 2011b) and the first candidate for a Be/white dwarf system in the SMC (Sturm et al. 2012b). The combined mosaic image of the SMC revealed several new SNRs candidates (Haberl et al. 2012a). As an example, XMMU J0056.5-7208 is presented in the thesis. Chapter 6 contains a detailed characterisation of the EPIC-pn detector background, followed by the spectral analysis of fields without point and extended sources, and a discussion of the morphology and spectral properties of the diffuse emission in the SMC. I show that the diffuse X-ray emission correlates with star formation. Finally, the results of the thesis are summarised in Chapter 7 and future prospects are discussed in Chapter 8. Acronyms and terms that are common in high-energy astrophysics and in X-ray astronomy and used in this thesis are listed in Appendix A. The used XMM-*Newton* observations of the SMC and the results of the spectral analysis of the diffuse emission are tabulated in Appendix B. Appendix C contains EPIC images of the individual XMM-*Newton* observations with results of the source detection as well as the merged background-subtracted mosaic image.

2. Basics

2.1. The Small Magellanic Cloud

The Small Magellanic Cloud is a gas-rich irregular dwarf galaxy and the second nearest star-forming galaxy after the Large Magellanic Cloud. The recent star formation was triggered by gravitational interaction of both galaxies with each other and with the Milky Way. A summary of the basic properties of the SMC is given in Table 2.1. In the following, I summarise the research history, multi-wavelength observations, and the derived properties of the Small Magellanic Cloud. Due to the large amount of details that are observable in nearby galaxies, this section can only give a few aspects of Magellanic Cloud research.

Table 2.1. Properties of the Small Magellanic Cloud.

		Reference
Optical centre (J2000)	$00^h\ 48^m$ -73.2°	Westerlund (1990)
Kinematic centre (J2000)	$01^h\ 05^m$ -72.4°	Stanimirović et al. (2004)
Diameter on sky	7° ≙ 7.3 kpc	Westerlund (1990)
Total visual magnitude	+2.4 mag	Westerlund (1990)
Distance Modulus	(18.91 ± 0.11) mag	Hilditch et al. (2005)
Distance	∼60 kpc	Hilditch et al. (2005)
Line-of-sight depth	∼8 kpc	Kapakos et al. (2011)
Line-of-sight velocity (helio-centric)	160 (90−215) km s^{-1}	Stanimirović et al. (2004)
Total mass	$2.4 \times 10^9 M_\odot$	Stanimirović et al. (2004); Harris & Zaritsky (2006)
Mass of H I	$4.2 \times 10^8 M_\odot$	Stanimirović et al. (2004)
Mass of stars	$\sim 3 \times 10^8 M_\odot$	Leroy et al. (2007)
Mass of dark matter	$7.5 \times 10^7 M_\odot$ (?)	Bekki & Stanimirović (2009)
Mass of H_2	$3.2 \times 10^7 M_\odot$	Leroy et al. (2007)
Mass of dust	$3 \times 10^5 M_\odot$	Leroy et al. (2007)
Metallicity	$\sim 0.2 Z_\odot$	Russell & Dopita (1992)
Gas/Dust ratio	5-11 times galactic	Leroy et al. (2007)
Foreground N_H	$(3-8) \times 10^{20}$ cm^{-2}	Dickey & Lockman (1990)
Maximum line-of-sight N_H	1.43×10^{22} cm^{-2}	Stanimirović et al. (1999)
Star formation rate	$(0.05-0.4) M_\odot$ yr^{-1}	Shtykovskiy & Gilfanov (2005, and references therein)

2.1.1. History

Both Magellanic Clouds were known prehistorically, because they are visible by naked eye as nebulous structures on the southern sky. First traditions can be found by South-Sea natives, Australian Aborigines, by the Persian astronomer Al Sufi (10^{th} century), and by mariners of the Middle Ages (Westerlund 1997, and references therein). Today, both clouds are named after Fernão de Magalhães, who led the first circumnavigation of the globe 1519 – 1522. The report of this voyage by Antonio Pigafetta brought the Clouds into common knowledge.

The nearby galaxy nature of the Clouds was recognised in the 19^{th} century (e. g. Abbe 1867). The

location on the southern hemisphere, however, complicated the access for modern-age astronomers. The situation improved since the 1960s, when large radio and optical observatories were build on the southern hemisphere and observations in the infra-red and X-ray regime became possible due to the first satellites. As an example, the Magellanic Clouds were the first extragalactic objects, from which the 21 cm emission of H I was detected (Pawsey 1959).

With continuously improving instruments, stellar and interstellar emission from the Magellanic Clouds has been studied in great detail. Research is driven by three comprehensive main aspects:

(i) Because of the relatively short distance and low Galactic foreground extinction and absorption, individual rare objects can be studied that are not always accessible in the Milky Way, where sources can be covered by gas and dust of the Galactic plane. A famous example is SN 1987 A in the LMC, the nearest observed supernova since the Galactic supernova in 1604 reported by Kepler. Due to the short distance, 11 and 6 neutrinos could be detected with Kamiokande II and the Irvine-Michigan-Brookhaven experiment, which proved the core-collaps nature of the SN with an energy output of $8{\times}10^{52}$ erg s^{-1} (Hirata et al. 1987; Svoboda et al. 1987). Explosive nucleosynthesis was proven by the detection of the 847 keV line of ^{56}Co (Matz et al. 1988) and subsequent hard X-ray emission (Sunyaev et al. 1990; Englhauser 1996). Today, the rise of a new SNR is observed (McCray 2007).

(ii) Besides of interesting single objects, complete populations of sources can be studied, all at the same and nowadays well known distance. For Galactic sources, the determination of luminosities is often hampered by large uncertainties in the distances measurements. An example is the discovery of the period-luminosity relation of Cepheides in the SMC by Leavitt & Pickering (1912). After a calibration of this relation, Cepheides can be used as *standard candles* to measure extragalactic distances in the local Universe. An accurate knowledge of the distance of nearby galaxies is important for the *cosmic distance ladder*, which enables the distance measurement of more distant objects.

(iii) For extragalactic astronomy, an understanding of the Magellanic Clouds is important, as they are among the nearest galaxies that can be observed completely. In addition, the Clouds give observable examples of tidally triggered star formation and for the interaction and evolution of galaxies. Therefore, the Clouds can be used to test theories of the chemical evolution of stars and galaxies, the kinematic evolution during galaxy mergers and effects on their structure. The low metallicity of the ISM in the SMC might also help to understand the conditions in high-redshift galaxies (Witt & Gordon 2000). A good knowledge of the individual emission components of nearby galaxies is needed, to understand the emission of more distant galaxies, where individual sources cannot be resolved.

Therefore, both Magellanic Clouds are observed in all available wavelengths today. Some examples that are also used as complimentary data in this thesis are given in the following.

2.1.2. Multi-wavelength observations of the SMC

Radio continuum observations of the SMS are available from Australian telescopes. They reveal non-thermal emission of SNRs, and thermal emission from H II regions in the SMC, as well as background quasars and radio galaxies (Filipović et al. 1998). The radio catalogue of Payne et al. (2004) contains 717 sources detected between $\lambda = 73$ cm and 3 cm in a 20 deg^2 area. Most of these sources (86%) are classified as background objects. 3% are classified as SNRs and 10% as H II regions in the SMC. The relatively weak radio emission of planetary nebulae limits the number of radio detections in the SMC to four (Filipović et al. 2009). A 13 cm radio continuum image is presented in Figure 2.1g.

The 21 cm emission line from the hyperfine transition of neutral hydrogen allows to measure the distribution of cold gas in the SMC and the Magellanic System. An H I image of the SMC is presented in Figure 2.1c. By measuring the Doppler shift of this line, the velocity of the gas along the line-of-sight can be measured. For X-ray studies, H I maps are useful to constrain the photoelectric absorption.

Mid- and far-infrared surveys of the SMC with the *Spitzer Space Telescope* (Bolatto et al. 2007; Gordon et al. 2011) reveal the galaxy from $\lambda = 160$ μm to 3.6 μm. Photometric catalogues of mid-infrared point sources have limiting magnitudes between 18 mag and 14 mag and are suitable for studying the late-type stellar population, but also to discriminate between stars and background AGN (e. g. Kozłowski & Kochanek 2009). The 160 μm and 24 μm images are shown in Figure 2.1e and f, revealing diffuse emission from cold and hot dust.

Several photometric surveys have been performed with ground-based optical and near infrared (NIR) telescopes. E. g. the Magellanic Cloud Photometric Survey (MCPS) of Zaritsky et al. (2002) provides *U*, *B*, *V*, and *I* magnitudes for 5 156 057 objects – mainly stars in the SMC – in a field of 18 deg^2 size. It has a completeness of 50% up to magnitudes of $V = 21 - 22$ mag (Harris & Zaritsky 2004). An example for an NIR survey (*J*, *H*, and K_S band) is the InfraRed Survey Facility (IRSF) Magellanic Clouds Point Source Catalog (Kato et al. 2007) with 2 769 682 sources in an 11 deg^2 area of the SMC. Typical limiting magnitudes are 20 to 22 mag and thus probing the main sequence down to A stars as well as the horizontal and giant branch. The recently performed *Swift*/UVOT survey of the SMC will provide UV photometry. The Magellanic Clouds were covered with less sensitive all-sky surveys and catalogues like 2MASS (Skrutskie et al. 2006), Tycho-2 (Høg et al. 2000), or the guide star catalogue (Lasker et al. 2008). Further, long-term monitoring programmes frequently observe the SMC, e. g. the Optical Gravitational Lensing Experiment (OGLE, Udalski et al. 2008) in the *I*-band since 1992. Although the main motivation of these observations is the detection of gravitational micro-lensing events, variable sources like background AGN or Be stars in the SMC can be found.

Narrow-band emission-line observations enable to investigate the ionised ISM down to a one pc resolution and reveal H II regions, planetary nebulae, SNRs, and super-bubbles amongst others. E. g. the Magellanic Cloud Emission Line Survey (MCELS, Smith et al. 2000; Winkler et al. 2005) was performed in Hα, [S II], and [O III]. An Hα image of the SMC tracing ionised hydrogen is shown in Figure 2.1d. A catalogue of emission-line stars is available by Meyssonnier & Azzopardi (1993), containing planetary nebulae and Be stars.

X-ray emission from the SMC was detected first by Price et al. (1971) with a sounding rocket experiment. With the *UHURU* satellite, one time-variable X-ray source, SMC X-1, was seen (Leong et al. 1971). The two transient sources SMC X-2 and SMC X-3 were detected by Li et al. (1977) later on. Meanwhile, these sources are identified as HMXBs. Since the early days of X-ray astronomy, the galaxy was covered by imaging X-ray surveys conducted with the *Einstein* observatory and later with ASCA and ROSAT. The *Einstein* data revealed 70 X-ray sources (Seward & Mitchell 1981; Wang & Wu 1992) and the ASCA observations resulted in 106 sources (Yokogawa et al. 2003). This led to the discovery of further HMXBs and X-ray detections of SNRs. The increased sensitivity and large field of view (FoV) of ROSAT resulted in the detection of 563 individual X-ray sources (Kahabka et al. 1999; Haberl et al. 2000; Sasaki et al. 2000) in a $6^\circ \times 6^\circ$ field covering the SMC. In addition to the discrete X-ray sources, ROSAT detected diffuse X-ray emission from the hot ISM with temperatures between 10^6 and 10^7 K (Sasaki et al. 2002). An X-ray image from ROSAT is presented in Figure 2.1h. The non-imaging *Rossi X-ray Timing Explorer* (RXTE) mission monitored the SMC for about 14 years, which lead to the discovery of the bulk of the X-ray pulsar population of the SMC (e. g. Galache et al. 2008). RXTE could detect HMXBs only during bright outburst and for some systems, the coordinates are still uncertain, as the FoV of RXTE covered $\sim 1^\circ$.

Although a large number of targets were observed in the SMC with present-day observatories like XMM-*Newton* or *Chandra* since 1999, the smaller FoV of their X-ray telescopes compared to *Einstein* and ROSAT led to an inhomogeneous and incomplete coverage of the galaxy. The XMM-*Newton* large-programme survey combines these observations to a continuous field of the SMC main body

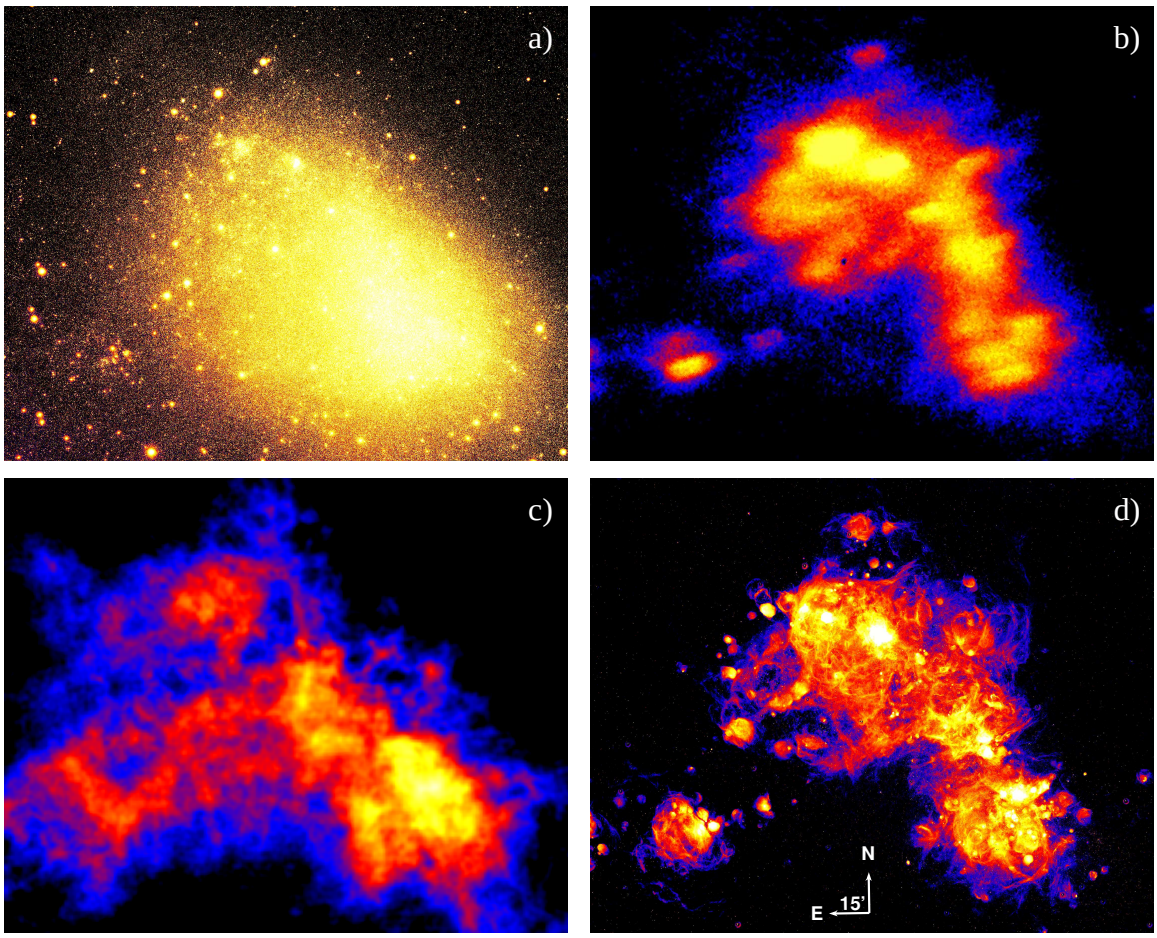

Figure 2.1. Logarithmically scaled false-colour images of the Small Magellanic Cloud at several wavelengths. Images are centred on 1^h-$72.^\circ6$ and have a size of $3.4^\circ \times 2.8^\circ$ covering the complete XMM-*Newton* main field. [(a)] *R*-band image from MCELS (Smith et al. 2000; Winkler et al. 2005). [(b)] UV image (135 nm) from FUVCAM-Shuttle/STS-39 (Gordon et al. 1994). [(c)] H I column density from Stanimirović et al. (1999). [(d)] Continuum-subtracted Hα image from MCELS. Continued on next page.

(see Sec. 3.1) and is the next step for the exploration of the SMC in X-rays.

γ-rays form the SMC were discovered within *Fermi*/LAT observations after 17 months exposure with a flux of $(1.9 \pm 0.2) \times 10^{-8}$ photons cm^{-2} s^{-1} in the (0.2−20) GeV band (Abdo et al. 2010b). The emission is not time variable and extended. A correlation with pulsars, cold gas, massive stars or SNRs is not observed, but the γ-ray emission might be associated with super-giant shells. In a similar study of the LMC (Abdo et al. 2010a), a correlation with ionised gas in star forming regions was found. The γ-rays can be caused by cosmic-ray interaction with the ISM of the SMC and a contribution of unresolved high-energy pulsars.

2.1.3. Properties of the SMC

The overall morphology of the SMC at several wavelengths is presented in Figure 2.1. The old stellar population dominates the red part of the optical spectrum (Figure 2.1a). In contrast to the LMC, the SMC has no stellar disc. The 3-dimensional distribution, as e. g. probed with red-clump and RR Lyrae stars by Subramanian & Subramaniam (2012), can be described by a spheroid with axes ratio of

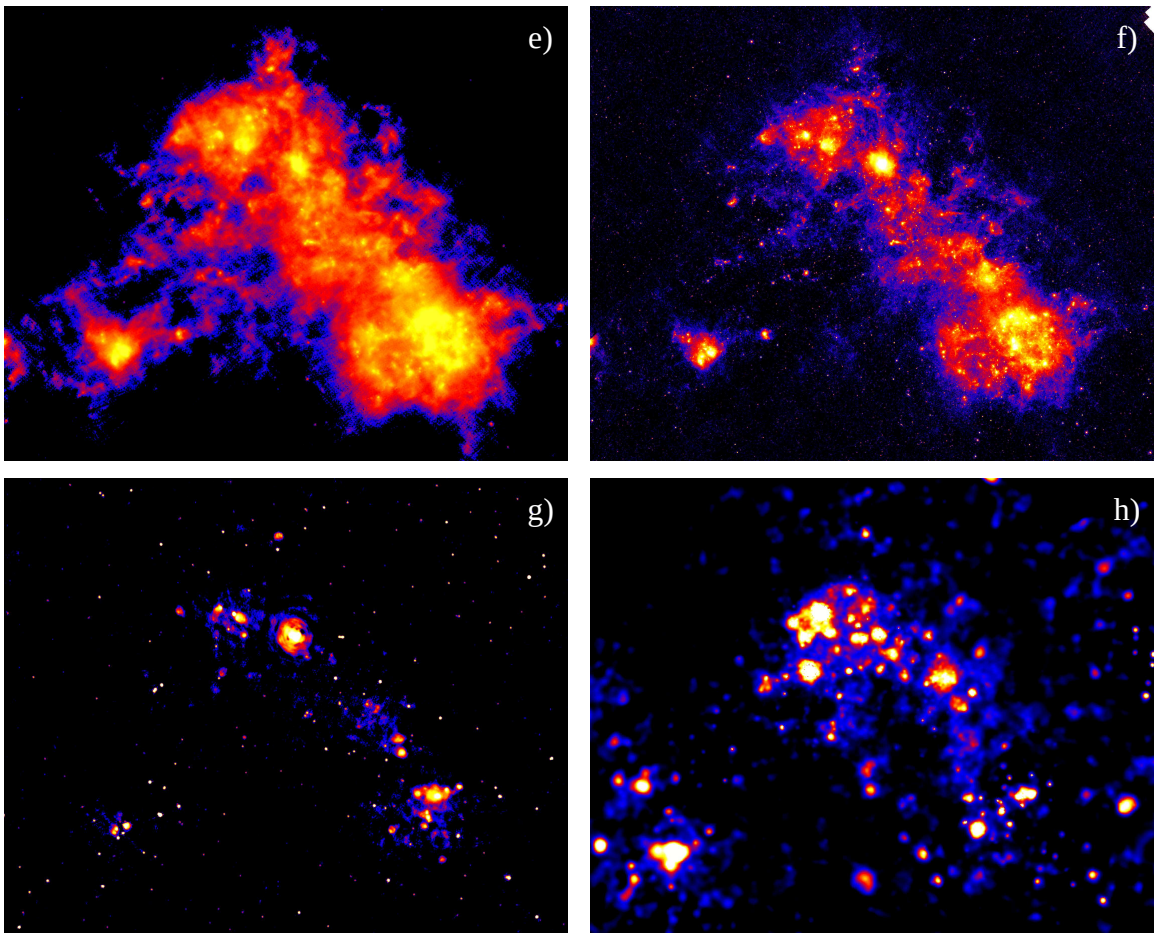

Figure 2.1. Contiued from previous page. [(e)] 160 μm image from the *Spitzer* SAGE-SMC survey (Gordon et al. 2011). [(f)] 24 μm image from the *Spitzer* SAGE-SMC survey. [(g)] 4.8 GHz radio-continuum image from Dickel et al. (2010). [(h)] ROSAT X-ray image in the (0.5−2.0) keV band (Haberl et al. 2000).

1/1.33/1.61, where the longest axis has an inclination with the line of sight of only 2.6°. There is an indication that the north-eastern part is slightly nearer, than the south-western part. The line-of-sight velocity of the neutral gas reveals a velocity gradient ranging from 91 km s^{-1} in the north east to 200 km s^{-1} in the south west that indicates a differential rotation for the gaseous main body of the SMC (Stanimirović et al. 2004).

Using eclipsing binaries from OGLE in combination with spectroscopic observations, Hilditch et al. (2005) derived a distance modulus of 18.91 ± 0.03 ± 0.1 mag corresponding to a distance of (60.6 ± 1.0 ± 2.8) kpc. The analysis of OGLE light curves of RR Lyrae variables yields a distance modulus of 18.90 ± 0.18 mag (Kapakos et al. 2011) and a 1σ line-of-sight distribution of 4.13 ± 0.27 kpc. The distance modulus, derived from Cepheids is in good agreement as well (18.93 ± 0.024 mag, Keller & Wood 2006). Throughout this thesis, we will assume a distance of 60 kpc.

Since massive stars have a short live-time, their distribution follows the region of high star formation. These hot stars contribute mainly to the blue and UV part of the spectrum (Figure 2.1b). Here we find a different morphology compared to that of the old stellar population and see most emission in the so-called bar of the SMC, reaching from the north-east to the south-west of the SMC. About one third of the UV emission is diffuse and originates from the interaction of the radiation field with dust (Pradhan et al. 2011). The bar is also the region, where most of the X-ray emitting HMXBs and

SNRs are located. Since early-type stars ionise the ambient medium via their UV radiation and at the end of their lives via supernova explosions, ionised hydrogen, as traced by Hα emission, indicates star formation as well (Figure 2.1d). Also hot dust, that is heated by the UV emission of young stars, is prominent in the bar (Figure 2.1f). Early-type stars are found in addition all over the so-called wing of the SMC, which is the region east of the bar.

Both structures, bar and wing, are also clearly present in the distribution of cold dust (Figure 2.1e) and neutral gas (Figure 2.1c). It is commonly believed, that bar and wing were formed by a recent collision of LMC and SMC, and the bar is rather a tidal structure than a real galaxy bar (Wayte 1990). This picture is also supported by the possible fragmentation of the SMC in depth and multiple velocity components seen along the line of sight in gas and stars.

Further evidence for a recent interaction of both Magellanic Clouds is provided by the structure of the Magellanic System. The H I distribution (e.g. Brüns et al. 2005) reveals that the whole Magellanic System includes – beside the LMC ($M_{\mathrm{H\,I}} \approx 4.41 \times 10^8 M_\odot$) and the SMC ($M_{\mathrm{H\,I}} \approx 4.02 \times 10^8 M_\odot$) – additional gas outside both galaxies ($M_{\mathrm{H\,I}} \approx 4.87 \times 10^8 M_\odot$). Most of it is in the Magellanic Bridge ($M_{\mathrm{H\,I}} \approx 1.84 \times 10^8 M_\odot$) that connects the SMC wing with the LMC. Further, both clouds are embedded in a common H I inter-cloud region ($M_{\mathrm{H\,I}} \approx 1.49 \times 10^8 M_\odot$). Other features are the Magellanic Stream that expands over $\sim 100^\circ$ on the sky, and other arms of H I that indicate ejection of material during the last collision of the Magellanic Clouds. Proper motion studies of the Magellanic Clouds revealed higher velocities ($\sim 1.2 \pm 0.2$ mas yr^{-1}, Kallivayalil et al. 2006) than expected, rising the question if the Magellanic Clouds are a bound system or if the Magellanic System is bound to the Milky Way.

By modelling the stellar content of multi-colour photometry with theoretical isochrones of stellar populations, Harris & Zaritsky (2004) found different epochs of enhanced star formation in the SMC: (i) Half of the stars in the SMC formed more than 8.4 Gyr ago. (ii) Relatively moderate star formation is found between 3 Gyr and 8.4 Gyr. No star clusters of this age are found in both Magellanic Clouds. (iii) Stronger star formation occurred in the last 3 Gyr with resolved bursts at 2.5 Gyr, 400 Myr, and 60 Myr. The recent star formation is estimated to 0.37 $M_\odot$ yr^{-1}. This also fits the number derived from SNRs. From other SFR indicators, lower values down to 0.05 $M_\odot$ yr^{-1} are derived (see discussion in Shtykovskiy & Gilfanov 2005).

As typical for dwarf galaxies, the chemical evolution of the Magellanic Clouds is slower than in the Milky Way. From spectroscopy of F-type supergiants and H II regions, Russell & Dopita (1992) derived an average metallicity of $Z \approx 0.004 \approx 0.2 Z_\odot$. With X-ray spectroscopy of older SNRs, where the emission is dominated by the ambient ISM, van der Heyden et al. (2004) found slightly higher but consistent values for the abundances of O, Ne, Mg, Si, and Fe. The dust component of the SMC is significant, but the gas to dust ratio is smaller by a factor of 5 to 11, compared to the Milky Way (Leroy et al. 2007). The low metallicity further causes a relatively high UV radiation field.

2.2. The XMM-Newton observatory

Since the atmosphere of the Earth is opaque for X-rays, observations of celestial X-ray-emitting sources have to be executed from high altitude balloons, sounding rockets, satellites, or space stations. This causes X-ray astronomy to be a young branch of observational astronomy. The Sun was detected in X-rays by Friedman et al. (1951) for the first time. The first extra-solar X-ray source – Scorpius X-1 – and a diffuse X-ray background were discovered by Giacconi et al. (1962).

The X-ray Multi-Mirror Mission (XMM, Jansen et al. 2001) is a cornerstone of the *Horizon 2000 science program* (Bonnet 1988) of ESA. The satellite was brought into space with an *Ariane V* launcher from the European space port Kourou, French Guiana, on 10$^{\mathrm{th}}$ December 1999. After the

successful launch, it was renamed to XMM-*Newton*. Since 2000, the observatory has been used for scientific guest-observer, guaranteed-time, and some calibration observations.

The satellite orbits Earth each 47.86 h in an ellipse with an eccentricity of $e = 0.68$, an apogee of 105 800 km, and a perigee of 15 300 km.[1] The long, high-altitude orbit provides the possibility for uninterrupted observations of up to 130 ks duration in a stable environment. During perigee passage, the satellite crosses the radiation belts, which affect the instruments and no useful data can be taken.

A schematic sketch of the 10 m long, 4 tonne weighting spacecraft XMM-*Newton* is presented in Figure 2.2. It holds three co-aligned X-ray telescopes that are described in Sec. 2.2.1. In the focal plane of each telescope, a European Photon Imaging Camera (EPIC) detects the X-rays. The cameras will be introduced in Sec. 2.2.2. The performance of the EPIC-telescope system is discussed in Sec. 2.2.3 and individual detector-background components in Sec. 2.2.4. XMM-*Newton* also carries two Reflection Grating Spectrometers (RGS, den Herder et al. 2001) for high-resolution spectroscopy of bright point sources observed on-axis. These obtain about half of the flux from two telescopes. The Optical Monitor (OM, Mason et al. 2001), a 30 cm Ritchey-Chrétien telescope allows simultaneous observations of sources in the ultraviolet (UV) or optical in the central FoV. Since data from the latter instruments are not used in this thesis, I will not go into details here. Further support instruments are the EPIC Radiation Monitor (ERM), that registers electrons above 50 keV and protons above 3.5 MeV up to 12 MeV, e. g. from the radiation belts and solar flares, and the Attitude & Orbit Control Subsystem (AOCS) that determines the spacecraft attitude with two star trackers and one sun sensor.

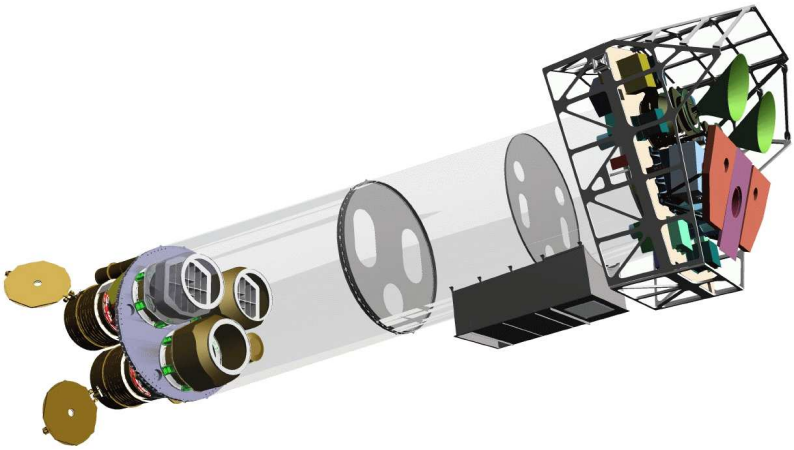

Figure 2.2. Schematic sketch of XMM-*Newton*. On the left, the mirror support platform carries the three X-ray telescopes. The upper two are equipped with reflection gratings. On the right, the focal plane platform contains the EPIC detectors with radiators shown in green (for EPIC-MOS) and magenta (EPIC-pn). Image courtesy of Dornier Satellitensysteme GmbH and ESA.

2.2.1. Technical description of the X-ray telescopes

A telescope gathers and focuses electromagnetic radiation. For the deflection of X-rays, conventional lenses or mirrors such as utilised in optical telescopes cannot be used, since an X-ray photon is either absorbed or transmitted, when it passes through matter. However, total external reflection under grazing incidence provides a possibility to "bend" X-rays. As shown by Wolter (1952), focusing with reflection at small angles can be achieved using a combination of paraboloidal and hyperboloidal surface. These so-called *Wolter type-I telescopes* are commonly used for today's X-ray observatories[2]. The precision of the reflector shape and the smoothness of its surface are important aspects for the focusing of X-rays.

[1] All parameters for May 2012. See XMM-*Newton* Users' Handbook, Issue 2.9, Table 28.

[2] Examples beside XMM-*Newton* are the currently active missions *Chandra* X-ray Observatory, *Swift*, and NuSTAR as well as past missions like *Einstein* and ROSAT and future missions like eROSITA.

The X-ray telescopes of XMM-*Newton* (see de Chambure et al. 1999a; Aschenbach 2002) were designed to achieve highest possible effective area in the (0.2−10.0) keV band to collect a high number of photons e. g. for spectral analysis with an acceptable spatial resolution. To obtain a large effective area several mirror shells with different radii but the same focal length are nested into each other. In the case of XMM-*Newton* for each of the three telescopes, 58 mirror shells have been nested with small radial separation. For this purpose and to reduce the weight, it was necessary to produce mirrors as thin as possible, which was achieved by replicating the mirrors from a polished negative-shaped mandrel, instead of forming and polishing the mirrors directly. The mandrels are coated with 0.2 μm of gold, which is supported by a nickel layer that was added in an electrolytic bath later on. The mirrors have a thickness of only (0.47−1.07) mm depending on the radius of the shell. After nesting the 58 individual mirror shells with a packing distance between 1 mm and 5 mm, one telescope has a radial diameter of 70 cm and an axial length of 60 cm. A picture of one mirror module is presented in Figure 2.3a. In front of the mirror shells, a spider-like structure of 16 spokes is visible that supports the individual shells. X-rays are reflected at the grazing angles between 17′ and 40′, resulting in an effective area of ∼1400 cm^2 at 1.5 keV. As the critical angle for total reflection decreases with increasing photon energy, the focal length has to be as high as possible. For XMM-*Newton* the focal length is 7.5 m to allow imaging of high energy photons.

In addition to the mirror module, each telescope carries an *X-ray baffle* (de Chambure et al. 1999b) in front. This baffle absorbs photons from off-axis angles between 20′ and 80′, which otherwise could reach the focal plane by only one reflection at the hyperbola. These photons are not focused accurately in one point but form arclike structures. The baffle consists of two plane-parallel plates with annular co-axial sieves, which act as a pre-collimator. The baffle reduces single reflections by a factor of ∼0.8. Further stray-light suppression for even higher off-axis angles is provided by an *entrance baffle*. This is a 90 cm long cylinder, in front of the X-ray baffle. Behind each mirror module, an *electron deflector* generates a toroidal magnetic field that diverts electrons with energies up to 100 keV, which are reflected by the X-ray mirrors towards the focal plane instruments.

Table 2.2. EPIC science modes.

Instrument	Mode	$T^{(a)}$ (ms)	$f_{oot}{}^{(b)}$ (%)	$R_{max}{}^{(c)}$ (cts s^{-1})	available imaging FoV
EPIC-pn	full frame (ff)	73.4	6.3	6	full coverage
	extended full frame (eff)	199.1	2.3	1	full coverage
	large window (lw)	47.7	0.16	6	inner half of each CCD (198×384 pix)
	small window (sw)	5.7	1.1	50	63×64 pix of CCD 4
	timing (ti)	0.03	–	800	no imaging data
	burst (bu)	0.007	–	60000	no imaging data
EPIC-MOS	full frame (ff)	2600	0.35	0.7	full coverage
	large window (lw)	900	0.5	1.8	300×300 pix of CCD 1 and full outer CCDs
	small window (sw)	300	0.5	5	100×100 pix of CCD 1 and full outer CCDs
	timing uncompressed (ti)	1.75	–	100	imaging data only from outer CCDs

Notes. Values according to XMM-*Newton* Users' Handbook, Issue 2.9, Tables 3 and 6. (a) Time resolution. (b) Fraction of out-of-time events. (c) Point-source count-rate limit for pile-up.

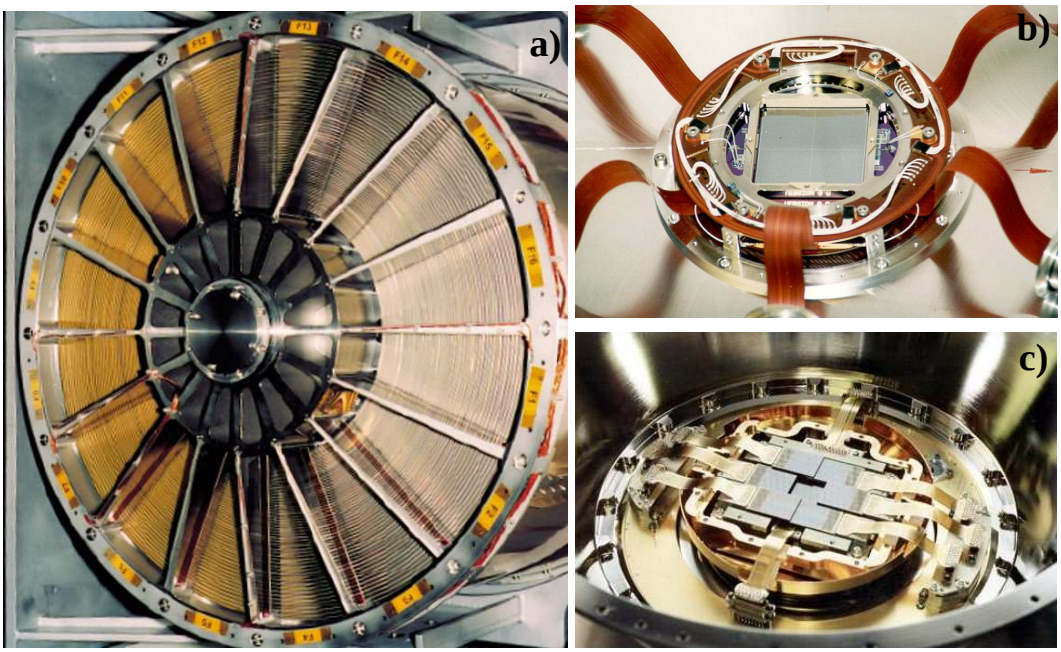

Figure 2.3. Pictures of XMM-*Newton* components: [(a)] X-ray mirror module, including 58 concentric X-ray mirrors, visible behind the 16 arms of the "spider". Image courtesy of Dornier Satellitensysteme GmbH, and ESA. [(b)] The monolithic EPIC-pn waver with 12 CCDs on it. Image courtesy of MPI-semiconductor laboratory, MPE, Astronomisches Institut Tübingen, Germany, and ESA. [(c)] EPIC-MOS array of 7 CCDs. Image courtesy of Leicester University, University of Birmingham, CEA Service d'Astrophysique Saclay, and ESA.

2.2.2. Technical description of the European Photon Imaging Camera

X-ray sensitive silicon charge-coupled devices (CCDs) are broadly used in today's X-ray missions[3]. In contrast to the measurement of optical radiation, where one photon creates one electron-hole pair, an X-ray photon is sufficiently energetic to liberate a large amount of electrons, e. g. one per ~3.7 eV in silicon on average. This enables single photon counting, with moderate spectral resolution, as the number of electrons scales with photon energy. After a certain exposure time of the CCD to X-rays, so-called *frame*, the liberated electrons are shifted from pixel to pixel to the rim of the CCD, where the integrated charge is amplified by the read-out electronics. For each *event*, i. e. a signal above threshold, the time of the frame, pulse intensity and two dimensional pixel coordinate is known. Thus one can obtain high-resolution images and medium-resolution spectra at a desired time resolution. Depending on the location of an incident X-ray, the liberated charge cloud can be distributed over one or more pixels. Therefore, several *patterns* are distinguished. E. g. in the case of EPIC-pn, most events are single-pixel events, followed by double-pixel events, where in two neighbouring pixels a signal is detected above threshold. Charge clouds, created by X-ray photons never extend to more than four EPIC-pn pixels. Depending on the count rate, frame time and pixel size, two photons can hit the same pixel during one frame, which is called *pile up*. These two photons cannot be separated and only one event at higher energy will be detected. Signature of this effect is an unexpected single- to double-event ratio.

[3]Examples beside XMM-*Newton* are the currently active missions *Chandra* X-ray Observatory, *Suzaku*, and *Swift*, as well as future missions like eROSITA.

The EPIC has two types of detectors. A pn-CCD wafer (EPIC-pn, Strüder et al. 2001) behind one telescope obtains an unobstructed beam, and two Metal Oxide Semi-conductor CCD arrays (EPIC-MOS, Turner et al. 2001), receiving about 44% of the photons from the other two telescopes. The rest is used for the gratings or lost due to structural obscuration. Each EPIC detector covers an area of ∼36 cm^2 in the focal plane. All cameras have fields in the corners of the FoV that are read out but shielded form celestial X-rays of the telescopes. In other directions than towards the X-ray telescopes, the detectors are shielded with at least 3 cm of aluminium. The detectors are in a radiative cooler and operated between −90 °C and −120 °C.

EPIC-pn consists of a 2×6 array of backside-illuminated CCDs, all on the same wafer (see Figure 2.3b) to have a homogeneous environment. The CCDs have an individual size of 3×1 cm^2 and are separated by insensitive gaps of 40 μm or 190 μm. Each of the twelve CCDs has 200×64 pixels with a pixel size of 150×150 μm^2. The CCDs provide a detector volume with a depth of 270 μm that is backside illuminated, to avoid absorption of X-rays in the read-out electronics. This improves the quantum efficiency in the sub-keV energy band and provides a higher resistance to radiation damage. The camera can be operated in several *science modes*, as listed in Table 2.2. E. g. in *full frame* mode all CCDs are used completely. To achieve a higher timing resolution or avoid pile up in observations of bright sources, the read-out time can be reduced by reading out a smaller part of the CCD. An *offset map* is used to correct the measured energy in each pixel. This map is measured at the beginning of each observation for EPIC-pn, which reduces the exposure time compared to EPIC-MOS, which use fixed offset maps.

The two EPIC-MOS instruments each consist of seven front-illuminated CCDs, arranged at different heights (see Figure 2.3c) to follow the shape of the focal plane and improve the point spread function (PSF) for off-axis sources. Here the size of the 600×600 pixels is 40×40 μm^2. Each EPIC-MOS CCD has a frame-store region, which is shielded from X-rays and where the charge clouds are shifted on before read out. Since 2005 March 9, one of the outer CCDs (MOS1 CCD 6) is not operational any longer, probably due to an impact of a micro-meteroid (Abbey et al. 2006). The science modes of EPIC-MOS are also listed in Table 2.2. Here, the science modes only affect the central CCD, the outer six CCDs are read out completely each 2.6 s in all modes.

Filters in front of the detectors are used to shield the CCD from lower energy photons in the UV, optical and Infrared (IR) band. Such photons would increase the detector noise and cause an offset in the energy-scale. Depending on the expected optical flux, three filter types can be used: *thin*, *medium*, and *thick*. The first two consist of a 16 μm poly-imide film covered with 4 μm and 8 μm of aluminium, respectively. The thick filter has a 33 μm thick polypropylene layer coated with 11 μm of aluminium and 4.5 μm of tin. In addition all detectors can be shielded completely with 1050 μm of aluminium in *closed* filter position. This is necessary to protect the detectors during intervals with strong radiation and to measure the detector background.

2.2.3. Performance

XMM-*Newton* is the observatory with the highest effective area in the (0.2−10.0) keV band of today's X-ray missions. The on-axis energy dependence of the total effective area is presented in Figure 2.4a. Solid, dashed, and dotted lines correspond to the thin, medium and thick filters of the EPIC-pn (black) and EPIC-MOS (blue). The lower effective area of EPIC-MOS is caused by the obscuration from the RGS in general and at lower energies by the lower quantum efficiency due to the front-side illumination. The decreasing effective area below 2 keV for both instruments is caused by lower quantum efficiency of the detectors and absorption of X-rays by the filters, which also causes the absorption edges of C, N, O, and Al. Further edges are caused by a drop in quantum efficiency of ∼5% at the

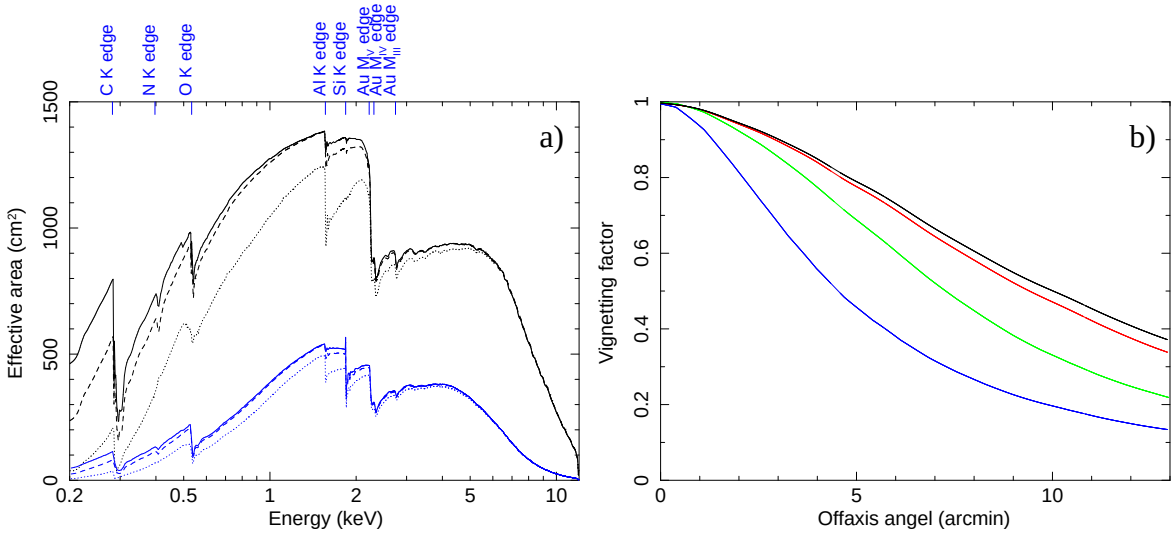

Figure 2.4. (a) Effective area as function of photon energy for EPIC-pn (black) and one EPIC-MOS (blue) telescope system. Solid, dashed, and dotted lines correspond to thin, medium, and thick filters. The energies of absorption edges from several elements are marked by blue lines. (b) Vignetting as function of off-axis angle for photons with an energy below 2.0 keV (black), 5 keV (red), 8 keV (green), and 12 keV (blue).

O and Si K edges. The drop for energies above ∼2.3 keV is caused by the gold coating of the X-ray mirrors. Since the reflectivity of X-ray photons depends on gracing angle and energy of the photon, more energetic photons are only reflected at small angles, i. e. by the inner-most shells. This causes the decrease of effective area towards higher energies. The effective area decreases with increasing off-axis angle, because of higher gracing angles and obscuration effects. This so-called *vignetting* is energy dependent and reduces the effective area to (40−20) % at the edge of the FoV (see Figure 2.4b).

All three EPIC instruments cover nearly the same area on the sky with a diameter of ∼30′. This is similar to the angular diameter of the Moon as seen from Earth. The EPIC-MOS cameras have a pixel scale of 1.1″ pix^{-1} and EPIC-pn of 4.1″ pix^{-1}, respectively. The in-flight angular resolution (FWHM) of the telescope/EPIC system at 1.5 keV are 6.0″ (MOS1) and 4.5″ (MOS2). The resolution for EPIC-pn is slightly worse with 6.6″ (Jansen et al. 2001). The resolution also depends on the off-axis angle of the source, as the PSF becomes wider and transforms to a butterfly-like shape in the outer parts of the FoV. This complicates the separation of nearby sources as well as the discrimination between point-like and extended sources. The absolute astrometry for X-ray sources as derived from the AOCS has a precision of $\lesssim 4''$. The relative astrometry is better than 1.5″.

The spectral resolution of the CCD detectors depends on an accurate calibration of the charge transfer inefficiency (CTI). In-orbit radiation damage, e. g. due to solar wind particles or cosmic rays, can create charge traps. These cause CTI, which affect the charge clouds during read out and thus degrades the spectral resolution. The energy resolution is monitored with an ^{55}Fe calibration source, emitting Mn K_α (5.893 keV) and Al K_α (1.487 keV). The degradation is around 1 eV yr^{-1} in the case of EPIC-pn (Briel et al. 2005) and was higher in the case of EPIC-MOS until the operation temperature was reduced. In general, the spectral resolution is better at the rim of the CCD close to the amplifiers where less shifting is necessary. The energy resolution after CTI correction depends on energy and is in the range of $E/\Delta E \approx 5{-}50$ (FWHM). It is better at higher energies and for single-pixel events. Examples are $E/\Delta E = 12.5$ at 1.5 keV or 37.5 at 6 keV for EPIC-pn. The analogous values for EPIC-MOS are $E/\Delta E = 16.6$ and 44.4. The energy redistribution function, which describes the

probability that a photon with given energy is detected in a certain channel, shows a shoulder below the main peak, which becomes dominant at lowest energies. A time-dependent increased redistribution of measured photon energies is known for EPIC-MOS around the EPIC-pn and RGS prime-pointing position, where most targets are placed (Read et al. 2006).

The time resolution simply depends on the science mode in which the CCD is operated during the observation (see Table 2.2).

2.2.4. Background components

The dominant background components are caused by read-out noise, energetic particles, as well as some effects of inaccurately measured X-rays, like single reflections on the mirrors or out-of-time events. These components will be described in the following:

Individual *hot pixels* have a higher probability to deliver a false signal above threshold by chance. Similarly, a defect location in a CCD can affect a whole CCD column. The signals from such known pixels and columns are already rejected on board. Some pixels brighten for a short time and vanish again. Here a screening needs to be done during the data processing. The variability of such pixels can show variations up to 10% within one observation (Carter & Read 2007) and more between individual observations. CAMEX read-out noise only contributes significantly to the softest energies ($E \lesssim 0.5$ keV) in EPIC-pn. It depends on read-out mode, and had been increasing since beginning of the mission, but does not show variation during observations. Enhanced contribution is seen close to the read-out edge of the CCD and towards the rims of the CCDs. For EPIC-MOS this noise is negligible, but individual outer CCDs are affected from time to time by increased low-energy background during individual observation. They enter a so-called *anomalous state.* However, since this background component only influences energies below 1 keV, the affected CCDs can be recognised (Kuntz & Snowden 2008).

Cosmic rays with an energy of some MeV penetrate the spacecraft and the detector from all directions and liberate ∼80 electrons per μm in silicon. In the case of EPIC-pn, these minimum ionising particles (MIPs) have a flux of ∼1.4 cts cm^{-2} s^{-1} and cause about 400 background events per second (Strüder et al. 2000). Tracks of these particles are recognised by the high deposited energy ($E > 15$ keV) and partly rejected on board. From an unrecognised remaining component and subsequent energetic electrons and γ-rays, a quiescent particle background (QPB) is observed with a continuous energy distribution (Strüder et al. 2000; Lumb et al. 2002). Strüder et al. (2000) suggest an origin of this component from Compton-scattered electrons from γ-rays, which causes $\sim 10^{-2}$ cts cm^{-2} s^{-1} in the (0.1−15) keV band for EPIC-pn. Additionally, X-ray fluorescent emission, caused by MIPs in the surrounding structure, will be detected by the CCDs and cannot be separated from focused celestial X-rays. These fluorescent lines show intensities with spatial dependence according to the distribution of the camera material around the detectors (Freyberg et al. 2004). A time variability of this component is known, showing an increase since revolution 100, but no short-term variability.

Low-energy charged particles, e. g. accelerated by the magnetosphere of Earth, show flares independent from a signal in the ERM. These particles cannot penetrate the detector shielding, but reach the CCDs via the X-ray telescopes, because the X-ray mirrors can scatter protons (Aschenbach 2007; De Luca & Molendi 2004; Strüder et al. 2000). These can additionally be focused by the electron deflectors. Therefore, this component is commonly referred to as soft proton flares (SPFs). During strong flares, the data is not useful, except for the brightest X-ray sources. Whereas for EPIC-MOS, these particles do not reach the shielded detector corners, it was found that this assumption is not valid for EPIC-pn (Sec. 6.1.1). The flares occur on a time scale of some 10^{1-4} s, where the intensity increases by several orders of magnitude, but can also have a weak quiescent contribution (Kuntz &

Snowden 2008). Flares are more frequent near perigee and may show a seasonal dependence. The SPF component shows a continuous energy distribution with a vignetting flatter than for photons. For EPIC-MOS some spatial dependence, possibly due to the grating structures, is observed.

Since the CCDs are exposed to X-rays from the telescopes during the read-out process, so-called out-of-time (OOT) events are created. These events are assigned a wrong position along the read-out direction. The statistically expected fraction f_{oot} depends on science mode and can be found in Table 2.2. Whereas for EPIC-MOS the OOT fraction is negligible due to the frame-storage of the CCDs, for EPIC-pn it holds for 6.3% of all events in full-frame mode. This effect increases the background along the read-out direction of bright sources. The spectral distribution and time variability follows the emission of the source. In addition, sky background contributes to the signal in the EPIC (Sec. 2.4).

2.3. Physical basics of X-ray astronomy

2.3.1. Processes causing X-ray emission

Several physical processes can lead to X-ray emission. The most important ones are summarised briefly in the following. For more details, see Longair (1999), Mewe (1999), and Liedahl (1999).

Synchrotron radiation is emitted from charged particles, which are accelerated in a magnetic field. Due to their small mass, the emission of electrons is dominant. This results in a continuous and polarised emission. The spectrum depends on the electron energy distribution. If this distribution follows a power law, also the synchrotron spectrum can be described by a power law.

Inverse Compton scattering can transfer energy from an energetic electron to a low-energy photon. The resulting spectrum depends on the electron and incident photon energy distributions.

Bremsstrahlung is emitted by charged particles that are accelerated in an electric field. The dominant case is the acceleration of electrons in the Coulomb field of protons. The emission from ion-ion interactions is negligible because of the higher mass of the ions compared to electrons. If the electron velocities follow a Boltzmann distribution, the thermal Bremsstrahlung spectrum is given by

$$I(E,T) = CG(E,T) n_{\mathrm{e}} n_i Z_i^2 T^{-\frac{1}{2}} e^{-\frac{E}{kT}} \tag{2.1}$$

where Z_{i} and n_{i} are the charge and number density of the target ion i, $G(E,T)$ is the Gaunt factor, k the Boltzmann constant, and C a constant.

Discrete line emission from electron transitions to K and L shells of several elements have energies in the soft X-ray regime. These lines are characteristic for each element. A discrete X-ray line emission with energy $h\nu = E_i - E_k$ must be preceded by an excitation or ionisation process of an electron in state k. E. g. this takes place in the case of (i) fluorescent emission, where an electron has been ionized by an energetic photon. A famous example is the fluorescent line of Fe at 6.4 keV. (ii) Collisional ionisation can be caused by the interaction of energetic electrons and ions. If the ion is in an excited state after the collision, subsequent X-ray emission causes prominent lines by transitions to the K shell of hydrogen- and helium-like ions of N, O, Ne, Mg, Si, S, and Fe as well as L shell transitions of Fe. The relative line fluxes depend on abundances, temperature and ionisation state. (iii) Another mechanism is charge exchange. During the interaction of ions and neutral molecules, an electron can be transferred to the ion followed by radiative decay (e. g. Dennerl 2010).

Black-body radiation is a useful approximation for many celestial objects in local thermodynamic equilibrium and can cause X-ray emission in the case of high temperatures. The emission can be

described by the Planck spectrum.

$$I(E,T) = \frac{2E^3}{h^2c^2}\frac{1}{e^{\frac{E}{kT}}-1} \tag{2.2}$$

The bolometric luminosity, radius (for spherical symmetric emission), and the temperature are related by the Stefan-Boltzmann law, where σ is the Stefan-Boltzmann constant.

$$L_{\mathrm{bol}} = 4\pi R^2 \sigma T^4 \tag{2.3}$$

An upper limit for the luminosity of a source is given by the Eddington luminosity. Assuming that the radiation pressure balances gravity in a spherically symmetric configuration, one obtains for the accretion of hydrogen-rich matter

$$L_{\mathrm{edd}} = \frac{4\pi G m_{\mathrm{p}} c}{\sigma_{\mathrm{T}}} M \approx 1.26 \times 10^{38} \frac{M}{M_\odot} \mathrm{erg\ s^{-1}} \tag{2.4}$$

with σ_{T} the Thomson-scattering cross-section and m_{p} the mass of the proton.

Two important astrophysical scenarios, that can provide the energy input for these processes, are the propagation of shock waves and the accretion onto compact objects, as described in the following.

2.3.2. Heating of plasma by shock waves

The terminal velocities of the winds of massive stars as well as the velocities of ejecta of supernova explosions will reach values above 10^3 km s^{-1}. This is supersonic in the surrounding medium, which causes the propagation of shock waves into the ambient ISM and the ejecta. Assuming the conservation of mass, momentum, and energy in a one-dimensional steady flow of a fluid, the physical condition before and after a strong ($\mathrm{v_{sh}}/c_{\mathrm{sound}} \gg 1$) shock wave follow from the Rankine-Hugoniot relations (e. g. Zel'Dovich & Raizer 1966).

$$\mathrm{v}_2 = \frac{2}{\gamma+1}\mathrm{v_{sh}} \overset{\gamma=5/3}{=} \frac{3}{4}\mathrm{v_{sh}} \tag{2.5}$$

$$\rho_2 = \frac{\gamma+1}{\gamma-1}\rho_1 \overset{\gamma=5/3}{=} 4\rho_1 \tag{2.6}$$

$$P_2 = \frac{2}{\gamma+1}\rho_1 \mathrm{v_{sh}^2} \overset{\gamma=5/3}{=} \frac{3}{4}\rho_1 \mathrm{v_{sh}^2} \tag{2.7}$$

where ρ is the densities and P the pressure before (subscript 1) and after (subscript 2) the shock wave. Velocities are given in the reference frame of the unshocked medium ($\mathrm{v}_1 = 0$). The adiabatic index γ is $5/3$ for a monatomic gas with three degrees of freedom. The shock wave converts kinetic energy into thermal energy. If one assumes an instantaneous equilibration of the electron and ion temperature, the temperature is connected to the velocity of the shock wave by

$$kT = \frac{3}{16}\mu m_{\mathrm{p}} \mathrm{v_{sh}^2} \tag{2.8}$$

where μm_{p} is the mean atomic weight.

Therefore, collisionless shock waves compress, heat, and accelerate the ISM, which can result in a highly ionised plasma with a temperature of 10^6 K and more. Such plasma will emit X-rays. The spectrum mainly constitutes from a thermal-bremsstrahlung continuum and emission lines, with

smaller contributions of recombination and two-photon decay continua. Beside of SNRs and the hot phase of the ISM, such plasma are also found in the coronae of late-type stars and ClG.

Collisional ionisation will produce ions, where the ratio of ionisation species depends on the temperature T, abundances and the ionisation time τ of the plasma, with

$$\tau(t) = \int_0^t n_\mathrm{e}(t')dt' \tag{2.9}$$

After a while ($\tau \gtrsim 10^{13}$ s cm^{-3}) the plasma will be in collisional ionisation equilibrium (CIE), where the ratio of ionisation species as well as the luminosities of emission lines are independent of τ. The luminosity of a plasma depends on temperature T, densities n_e and n_H and volume V, where the later two are expressed as emission measure EM

$$L_\mathrm{X} \propto f(T) \underbrace{\int n_\mathrm{e} n_\mathrm{H} dV}_{EM}. \tag{2.10}$$

The dependence on temperature is approximately $f(T) \approx \sqrt{T}$.

2.3.3. Accretion onto compact objects

Another way to power X-ray emission is the accretion onto compact objects, where the energy release is caused by the gravitational potential the matter is falling into. The accretion luminosity (e. g. Meszaros 1992) with the gravitational constant G and accretion rate $\dot{M}$ is

$$L = \frac{GM\dot{M}}{R} \approx L_\mathrm{edd} \left(\frac{R}{10\ \mathrm{km}}\right)^{-1} \left(\frac{M}{M_\odot}\right) \left(\frac{\dot{M}}{1.45 \times 10^{-8} M_\odot \mathrm{yr}^{-1}}\right). \tag{2.11}$$

A fraction of this luminosity can be emitted by X-rays that are produced by a large variety of processes. E. g. angular momentum conservation of the infalling matter can lead to the build up of an accretion disc. Dissipative forces in this disc heat the material with increasing temperature towards smaller radii. The innermost part of the disc can reach temperatures, sufficiently high for X-ray emission. Optical thick accretion discs can be modelled by an integration of black-body spectra (Mitsuda et al. 1984).

In the case of an Active Galactic Nucleus (AGN), the last stable orbit of the accretion disc is too large to cause thermal X-ray emission. Here, a hot corona of electrons is discussed to produce X-rays by inverse Compton scattering.

In the strong magnetic fields of young NSs, the material will follow the magnetic field lines and be accreted onto the magnetic poles (Meszaros 1992). The rapid deceleration of this matter at the NS surface will heat the accretion column and the polar caps of the NS. Comptonisation effects will create a power-law continuum in the highly ionised plasma, although the emission originates from thermal processes.

In the soft X-ray band, the spectra of NS and AGN can be described well by a power law with spectral index[4] α.

$$I(E) = NE^{-\alpha} \tag{2.12}$$

Under sufficiently high temperatures and densities, the accreted material will undergo nuclear burn-

[4]Not to be confused with the photon index $\Gamma = \alpha + 1$ of a photon spectrum.

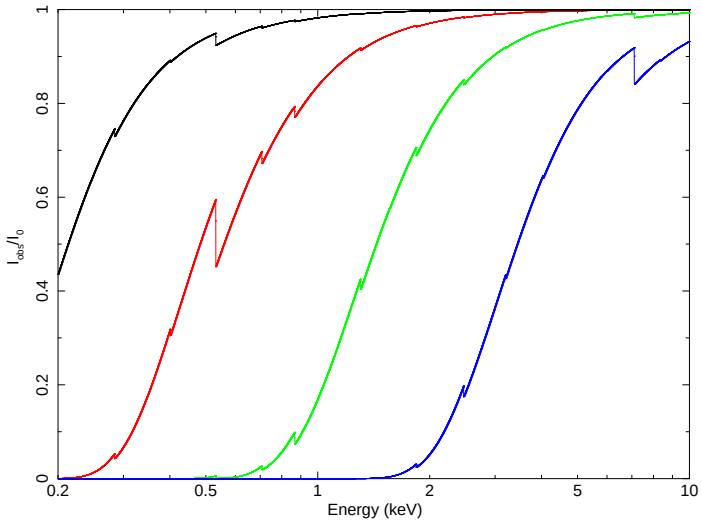

Figure 2.5. The fraction of observed X-ray emission dependent on energy is plotted in black, red, green, blue for $N_H = 10^{20}$, 10^{21}, 10^{22}, 10^{23} cm^{-2}, respectively. The ISM abundances were taken from Wilms et al. (2000).

ing. For hydrogen burning, this will cause an energy release of $L \approx 0.007\dot{M}c^2$. This can be neglected, compared to the gravitational energy release in accreting NSs and black holes (BHs) that is higher by a factor of ∼20. However, because of the larger radii of white dwarfs (WDs), the gravitational energy release is lower by a factor of 30 compared to the energy release of nuclear reactions that will power soft X-ray emission (Kahabka & van den Heuvel 1997).

2.3.4. Absorption of X-rays

X-rays are absorbed by matter in the line of sight between the source and the observer. This mainly takes place in the Galactic foreground ISM, the ISM of the SMC and eventually by material within the system of the X-ray source. In most cases, the dominant absorption mechanism is photoelectric absorption. Since the decrease of X-ray intensity depends on the passed equivalent hydrogen column density N_H along the line of sight ($dI \propto I_0 dN_H$), the observed intensity is given by:

$$I_{obs}(E) = I_0(E) \exp\left(-\sigma(E) N_H\right) \tag{2.13}$$

In general the cross-section σ depends on photon energy and atomic number according to $\sigma \propto Z^4 E^{-3.5}$. When the photon energy is sufficiently high, photoelectric interaction with K and L shell electrons of metals is possible, causing absorption edges, e. g. the oxygen K edge at 533 eV (cf. Figure 2.5). Therefore above ∼0.5 keV, the cross-section of metals becomes dominant and the absorption depends on metalicity (Wilms et al. 2000). K shell absorption is independent of chemical and physical condition, as long as the atoms are not highly ionised. Scattering of molecules and grains can be neglected as they are of the order of some per cent, compared to photoelectric absorption. The scattering appears mainly in forward direction at small incident angles, which can be observed in dust halos, for some sources with high foreground dust.

2.4. X-ray sources in the SMC field

Different kinds of celestial X-ray sources can be detected with the EPIC. These will be briefly discussed in the following. For each source class, the X-ray characteristics and if necessary for identification, also other wavelength properties will be mentioned. Due to the high number of source classes, which are known to emit X-rays, this section can only present the most important ones. Depending on the scientific objective, not all X-ray emitting sources are of interest but contribute to the celestial X-ray background.

2.4.1. Solar-wind charge exchange

In the case of solar-wind charge exchange (SWCX), ions of the solar wind pick up electrons from neutral atoms. This causes X-ray emission of e. g. comets and planets (Dennerl 2010). Charge-exchange processes also take place in the exosphere of Earth or the interplanetary medium. Below 1 keV, this can contribute to the X-ray background significantly, e. g. during solar flares on the time scale of some hours to days. This results in a pure emission-line X-ray spectrum, mainly from O IIV, O IIIV, Ne IX, and Mg XI (Snowden et al. 2004). This nearby component is evident in X-ray observations of the dark moon (Wargelin et al. 2004). The cumulative emission from SWCX within the heliosphere is discussed nowadays to be at least partly responsible for a diffuse homogeneous local X-ray component (Welsh & Shelton 2009). Variations on longer time scales (e. g. solar cycle) are not investigated so far. For the analysis of SMC sources, SWCX is not of interest, but contributes to the background.

2.4.2. Non-degenerate stars

X-ray emission has been detected from main-sequence late-type (F−M) stars and early-type OB stars, as well as some other stellar types, like accreting T Tau stars or binary systems of two interacting non-degenerate stars. The interaction in close binary stars, by magnetic fields and shocks can further increase the X-ray emission. For a review, I refer to Güdel & Nazé (2009).

In late-type stars, like the Sun, X-rays originate from the corona, which is heated to temperatures of some MK by reconnection of unstable magnetic fields, caused by rotation effects in the outer convective zone. The X-ray luminosity depends on rotation period ($L_X \propto P^{-2}$) and shows saturation at values of $L_X \lesssim 10^{31}$ erg s^{-1}. Late-type stars can show strong flares, where the plasma temperature exceeds 100 MK and the X-ray luminosity increases by a factor of up to 1000 on time scales of minutes to several days in the most extreme cases observed in pre-main-sequence stars. Maximum X-ray luminosities of some 10^{33} erg s^{-1} are reached (Favata 2002).

In OB stars, the energy transport in the outer layers is radiative and no dynamo effect can power X-ray emission. But shocks in strong stellar winds can heat the plasma, which leads to X-ray emission with luminosities of $L_X \propto 10^{-7} L_{bol} \lesssim 10^{33}$ erg s^{-1} (Berghoefer et al. 1997).

Galactic stars are foreground sources, homogeneously distributed in the SMC field. Due to the high galactic latitude of the SMC ($b \sim -44.5°$), the sample is expected to be dominated by late-type coronal-active stars. These are found as soft point-sources with possible time variability due to flares. The X-ray emission can be described by a plasma model with low absorption. Since stars emit predominantly at longer wavelengths than X-rays, the detection of an optical counterpart is expected.

Late-type stars in the SMC are not expected to be found in the XMM-*Newton* SMC survey, because even the highest fluxes during flares are below the detection limit. In some extreme cases, X-ray emission from early-type stars within the SMC can be observed with XMM-*Newton*. This is e. g. the case for Wolf-Rayet stars, i. e. evolved blue supergiants that have stripped off their outer hydrogen

envelope. These stars loose up to $10^{-5} M_\odot$ yr^{-1} in winds with velocities of some 10^3 km s^{-1}. In binary systems, wind collisions further heat the plasma, leading to temperatures of $>10^7$ K. Three sources in the SMC are reported so far (Guerrero & Chu 2008). Also, the cumulative X-ray emission of several OB stars was detected in the open cluster NGC 346 (Nazé et al. 2002).

The cumulative emission of point-sources below the detection limit can cause an apparently diffuse soft X-ray component. E. g. in deep *Chandra* observations of the Galactic Ridge region, such a component was resolved up to 80% into accreting WDs (see Sec. 2.4.5) and strong coronal active stars in binary systems with individual X-ray luminosities of $L_X \leq 10^{32}$ erg s^{-1} and $L_X \leq 10^{31}$ erg s^{-1}, respectively (Revnivtsev et al. 2006, 2009).

2.4.3. Supernova remnants

At the end of the life of a star with a zero-age-main-sequence mass of $M_{\mathrm{ZAMS}} > 8 M_\odot$, the pressure of the core cannot sustain gravity and the core collapse powers a supernova explosion. An exception are SN type Ia, which are powered by the thermonuclear explosion of an accreting WD reaching the so-called Chandrasekhar mass ($M_c = 1.44 M_\odot$). Both supernova types release kinetic energy of the order of 10^{51} erg (Woosley et al. 2002; Nomoto et al. 1984). Due to the supersonic ejecta velocities up to initially 10^4 km s^{-1}, the ejecta will be preceded by a shock wave. The surrounding medium will decelerate the ejecta by the propagation of a reverse[5] shock into the ejecta. Both shocks-waves propagate with high Mach numbers, heat the overrun medium to 10^{7-8} K and produce X-ray emission. Details about the X-ray emission of SNRs can be found in Vink (2012).

In a simplified picture, a SNR evolves as follows: During the first few hundred years the SNR is in the *ejecta-dominated phase*, where the expansion velocity is nearly constant and the ejecta dominate the chemical composition. The expanding shock wave sweeps up more and more ISM and as its mass becomes dominant, the remnant is in the adiabatic *Sedov-Taylor phase*. Here, the expansion can be described by the self-similar Sedov-Taylor equation (Taylor 1950), as the radiative energy losses have negligible influence and the kinetic energy is rather constant. The expansion depends on the initial explosion energy E and the density of the ISM ρ and can be described by

$$R(t) \propto E^{\frac{1}{5}} \rho^{-\frac{1}{5}} t^{\frac{2}{5}}. \tag{2.14}$$

With time the velocity and temperature decreases and the SNR is in the *radiative phase* when ions recombine and enable a more efficient cooling. In the final *merging phase*, the remnant cannot be discriminated from the hot phase of the ISM. The final size and age depends on the surrounding ISM density, but is in general less than 100 pc and several tens of kyrs (Badenes et al. 2010).

SNRs in the first two phases are luminous X-ray sources, radiating thermal X-rays with luminosities of 10^{35-37} erg s^{-1}. The spectra are characterised by a collisionally excited plasma, which is not in ionization equilibrium. In some cases – like the Crab nebula – synchrotron radiation can cause a dominant non-thermal component. This component is associated with a pulsar powered wind nebulae. But also from the SNR shells synchrotron emission can be observed in X-rays (Koyama et al. 1997).

All 26 known X-ray bright SNRs and candidates in the SMC have been observed with XMM-*Newton* (Badenes et al. 2010; Haberl et al. 2012a). Because of the small distance of the SMC, all SNRs are spatially resolved with XMM-*Newton*. Due to their extent, SNRs are constant X-ray sources on a long time scale, except the youngest ones like SNR 1987A (e. g. Sturm et al. 2009). Therefore, SNRs are used as calibration sources, as e. g. 1E0102.2-7219 in the SMC, which is observed regularly with XMM-*Newton* and other X-ray observatories.

[5] reverse in the forward-shock rest frame, but expanding outwards in the observer's rest frame.

Other features of SNRs are radio synchrotron emission with a typical spectral index[6] of $\alpha \sim -0.5$. In the optical, slower shock waves cause line emission of e. g. Hα, O III, and S II. For collisionally excited plasma, a Hα/[S II] ratio $\gtrsim 0.4$ is characteristic, in contrast to H II regions, which rather show Hα/[S II] ~ 0.1 due to a higher ionisation of sulphur (Filipović et al. 1998).

SNRs are important for our understanding of the evolution of galaxies. They strongly influence the morphology and evolution of the hot ISM, trigger the birth of new stars, and mix heavy elements, produced in the stellar nucleosynthesis, into the ISM. Due to the short life time of both massive stars and SNRs, they trace the most recent star formation in the SMC. By analysing the spectra of SNRs in the *adiabatic expansion phase*, the chemical composition of the swept up ISM can be constrained (e. g. Russell & Dopita 1992). As an example of a newly discovered SNR candidate XMMU J0056.5-7208 is discussed in Sec. 5.4.

2.4.4. Hot interstellar medium

Truly diffuse[7] emission can be produced by the hot ISM. The ISM is a non-linear system with several components (gas, dust, magnetic field, etc.) in different phases (cool, warm, hot). The hot phase of the interstellar medium fills most of the volume in a galaxy and has sufficiently high temperatures for X-ray emission. Besides of SN explosions (see Sec. 2.4.3), energy input is provided by stellar winds of massive stars. The energy release from stellar winds can be described analogous to SN explosions with similarity solutions, but with a steady mechanical energy release of $L_W = \frac{1}{2}\dot{M}v^2_{\mathrm{wind}}$ (Weaver et al. 1977). This leads to a turbulent patchy distribution of the individual phases of the ISM (e. g. de Avillez & Breitschwerdt 2005). Several SN explosions in an OB association will create enhancements of hot plasma, so-called super bubbles. The hot plasma will expand in the direction of smallest resistance and can escape the galaxy in fountains (Shapiro & Field 1976). Depending on the gravitational potential of a galaxy, this plasma will fall back to the galaxy, as assumed in the case of the Milky Way, or can escape, as it might be the case in dwarf galaxies (Mac Low & Ferrara 1999; Klein 2012).

The plasma can be assumed to be in CIE and has temperatures of some 10^6 K. Radiative losses are not energetically important, making the hot phase of the ISM a long-term constant X-ray source. In the direction of the SMC, X-ray emission from the hot ISM can originate from several places:

X-rays are observed from the local hot bubble (LHB, Paresce 1984) . The LHB is a region of hot plasma with a temperature of (50−90) eV (Miyaji et al. 1998) in the Galactic disc, where the solar system is currently passing through. This cavity has a low density of $\sim 4 \times 10^{-3}$ cm^{-3} and causes a void of H I (Snowden et al. 1997). This region is used to explain the local X-ray foreground, although nowadays, it is unclear, how much of the soft foreground emission is due to SWCX and the LHB (Welsh & Shelton 2009). The X-ray luminosity scales with the line-of-sight depth of the region, which is between 80 and 200 pc. Across the SMC field, this component can be assumed to be constant and can be handled as additional X-ray background component.

Another source of diffuse foreground emission originates from the Galactic halo. In contrast to local X-ray emission, this component is absorbed by the Galactic ISM in the foreground.

Also in the SMC, diffuse X-ray emission was found with ROSAT. The plasma shows X-ray emission with a total X-ray luminosity $L_{\mathrm{X}} = 1.1^{+1.1}_{-0.44} \times 10^{37}$ erg s^{-1} in the (0.1−2.4) keV band and temperatures of 10^{6-7} K (Sasaki et al. 2002). From more distant galaxies, a correlation of diffuse X-ray emission with star formation rate (SFR) was found (see e. g. Mineo et al. 2012b).

[6] defined by: $S_\nu \sim \nu^\alpha$

[7] i. e. not constituting from several faint point sources below the detection threshold.

2.4.5. X-ray binaries

In a very general sense, an X-ray binary consists of a binary star system with a compact object that accretes material from the companion star, which powers the X-ray emission. In a more common sense, the compact component is a neutron star or black hole, whereas accreting white dwarf systems are designated cataclysmic variables (CVs), novae, etc. CVs were known from optical astronomy already. The X-ray emission of CVs is in general below 10^{33} erg s^{-1}. Therefore, we do not expect to detect CVs in the XMM-*Newton* SMC survey. However, they can contribute to unresolved diffuse emission as discussed in Sec. 2.4.2. The exception of luminous SSSs, which are powered by nuclear burning, rather than gravitational energy release of accreted matter, will be discussed in Sec. 2.4.6. NS and BH X-ray binaries are classified according to the mass of the donor star as high-mass X-ray binaries ($M > 8M_\odot$, HMXB) and low-mass X-ray binaries ($M < 2M_\odot$, LMXB).

In LMXBs, the mass transfer occurs mainly via Roche-lobe overflow. Due to the long life time of low-mass stars, the size of a LMXB population of a galaxy is proportional to the integrated SFR or the stellar mass of the galaxy. The stellar mass of the SMC is smaller by a factor of 50−100 compared to the Galaxy. Therefore, one expects null to one LMXB in the SMC. So far, this is consistent with no known LMXB in the SMC (Coe et al. 2010a).

In contrast to the LMXB population, the population of HMXBs scales with the recent SFR of a galaxy (Grimm et al. 2003), because of the short life time of massive stars. A high recent star formation (Antoniou et al. 2010) and low metalicity (Dray 2006) are probably responsible for the remarkably high number of ∼90 known HMXBs in the SMC. The size of the SMC sample can be compared to the slightly larger Galactic sample (e. g. Coe et al. 2010a).

According to the mass-donating star, HMXBs are further subdivided into two classes: supergiant X-ray binaries (SgXRBs) and Be/X-ray binaries (BeXRBs). In SgXRBs, the optical counterpart is an early-type supergiant of luminosity class I or II. Mass transfer is mainly caused by the high-density wind ($10^{-8} - 10^{-6} M_\odot$ yr^{-1} with terminal velocities up to 2000 km s^{-1}). This enables accretion for some 10^4 yr. Depending on the orbit of the compact object, rather persistent luminosities up to 10^{36} erg s^{-1} are reached. In rare cases, like SMC X-1 (and Cen X-3, LMC X-4), mass transfer via Roche-lobe overflow causes luminosities of $\sim 10^{38}$ erg s^{-1}. Besides SMC X-1, other SgXRBs are not known in the SMC. In the Galaxy, at least one quarter of the known HMXBs are SgXRBs. Two further subclasses of SgXRBs are discussed since the launch of the INTEGRAL mission. One subclass are highly obscured SgXRB (Walter et al. 2006). These systems can show persistent or transient X-ray luminosities and are characterised by a large amount of local absorption with H I column densities above 10^{23} cm^{-2}, probably due to absorption in the stellar wind or a dust cocoon. The second subclass are supergiant fast X-ray transients (SFXTs, Negueruela et al. 2006). These systems show strong outbursts of $L_X = 10^{36-37}$ erg s^{-1} lasting typically only a few hours. The high variability is discussed to be caused by accretion of clumpy wind. In both subclasses, X-ray pulsations and spectral properties of SFXTs point to a NS as compact object.

In BeXRBs (e. g. Reig 2011) the optical counterpart is an O9−B5 dwarf to giant star of luminosity class III−V, which is not filling its Roche lobe and has a rather moderate wind. By a mechanism not well understood and in combination with high rotation, Be stars eject material in the equatorial plane, causing the build-up of a circumstellar decretion disc (Okazaki 2001; Ziolkowski 2002). Reprocessing of the UV and optical radiation from the Be star in this disc leads to an NIR excess and emission lines (e. g. Hα) that are not observed in normal B stars. The variability of both NIR excess and emission lines yield evidence for the instability of these discs. If a Be star is in a binary system with a compact object, mass transfer via this disc is possible. In most cases of classical BeXRBs, the compact object seams to be a NS. Systems with BH are not known. Be/WD systems will be discussed in Sec. 2.4.6.

The optical emission lines from Be stars can show double peaked line profiles, as expected for a rotating disc. Asymmetries between the violet and red peak are typical and show a quasi-periodic variability. These are interpreted as one-armed perturbations and these are significantly smaller in BeXRBs than in isolated Be stars. This points to a truncation of the decretion disc by the NS, which is supported by a correlation of NS orbit period and Hα line width in BeXRBs (Reig et al. 1997).

BeXRBs are subdivided into persistent and transient systems. The first show X-ray emission at $L_X \lesssim 10^{35}$ erg s^{-1} and generally have wide orbits ($P_{orb} > 200$ d). Owing to a supernova kick, the NS can be in a highly eccentric orbit ($e \geq 0.3$). Such binary systems show a transient behaviour, with *type-I* outbursts in X-rays, caused by enhanced accretion of matter onto the NS during periastron passage. These outbursts last for several days at typical luminosities of some 10^{36} erg s^{-1}. Other authors quote ~30% of the orbital period for the duration (Galache et al. 2008). If a Be stars looses its disc due to instability, the NS can accrete over a long time, causing *type-II* outbursts, which are not connected to an orbital period, reach luminosities of $\gtrsim 10^{37}$ erg s^{-1}, and can last for several binary orbits. In low X-ray state, the X-ray emission of these transient systems is ~10^{33} erg s^{-1}.

Variability in X-ray intensity of BeXRB can, besides of orbital motion and variable decretion disc, also be caused by the *propeller effect*. Most pulsars show spin-up during periods of high accretion caused by angular momentum transfer from the accretion disc (Ghosh & Lamb 1979; Coe et al. 2010b). But also spin down is observed sometimes, probably due to reverse torques. Depending on the accretion rate, matter that reaches the magnetosphere will be accelerated and ejected, if the magnetic field and rotation frequency of the NS are sufficiently high. This prevents accretion but also enables an efficient spin down of the NS. In the theoretical case of a constant accretion rate, the NS is expected to rotate at an equilibrium period. To explain the slowest rotating pulsars, a subsonic propeller phase is suggested (Ikhsanov 2007). In this case, accretion can occur only if

$$P_{spin} > P_{break} \approx 442\mathrm{s}\left(\frac{\mu}{10^{30}\mathrm{G\,cm^3}}\right)^{16/21}\left(\frac{\dot{M}}{10^{15}\mathrm{g\,s^{-1}}}\right)^{-5/7}\left(\frac{M_{NS}}{M_\odot}\right)^{-4/21} \tag{2.15}$$

with μ the magnetic moment of the NS and $\dot{M}$ the mass accretion rate.

In the energy band of XMM-*Newton*, most spectra of BeXRBs can be described by a power-law with photon index of $\Gamma \approx 1$ (Haberl & Pietsch 2004). Also Fe K$_\alpha$ fluorescent emission is found in some systems. A soft excess below 1 keV is observed only sometimes, either because of absence or because of absorption. In the latter case, the excess might be ubiquitous. Hickox et al. (2004) investigated several possible origins for the soft excess: (i) Only in X-ray bright ($L_X > 10^{36}$ erg s^{-1}) outbursts, the excess can be caused by reprocessing of hard X-rays from the NS in optically thick material like an accretion disc. (ii) In fainter systems, the excess may be caused by diffuse gas that is either collisionally heated or photoionised. (iii) Also thermal emission from the NS surface can contribute to the excess. At higher energies the X-ray spectra show a break in the power-law between 10 and 30 keV and cyclotron absorption lines between 10 and 100 keV, which are caused by electrons in magnetic fields of some 10^{12} G.

Due to the local accretion onto the magnetic poles, which does not have to be aligned with the rotation poles of the NS, the observed X-ray flux can show coherent variability. Typical pulse periods are 1 s to 1000 s. The spin period evolution depends on magnetic field, and therefore age of the NS, and the average angular momentum transfer during mass accretion. Roche-lobe-filling SgXRBs have very short spin and orbital periods, whereas wind-fed systems show rather long spin periods independent of orbital periods. For BeXRBs a correlation between spin and orbital period is known (Corbet 1984). The spin- and orbital-period distribution is likely bimodal, probably due to different kicks in different types of SN explosions (Knigge et al. 2011).

The relation of star formation history and HMXB density in the SMC was studied by Antoniou et al. (2010). In several fields in the SMC, they find a correlation of BeXRB density and SFR 25–60 Myr ago. By using a larger set of nearby galaxies, the HMXB populations were found to be describable by a luminosity function with universal shape. The number of HMXBs above a luminosity of $L_X > 10^{38}$ erg s^{-1} correlates with the star formation of that galaxy (Grimm et al. 2003). Therefore, the X-ray luminosity above 2.0 keV might be a useful SFR indicator in more distant galaxies. At lower luminosities ($L_X < 2 \times 10^{35}$), Shtykovskiy & Gilfanov (2005) found a turn over in the X-ray luminosity function to a flatter distribution, which might be caused by the propeller effect.

Further investigation of HMXB is important, to gain further insights in all the fields, mentioned above (accretion physics, SN kicks, connection with star formation). The SMC is ideally suited to investigate statistical properties of HMXBs, because of the large sample size and high density that allows to observe several sources simultaneously.

2.4.6. Super-soft X-ray sources

Super-soft X-ray sources (SSSs, Greiner 1996; Kahabka 2006) are a phenomenological class of X-ray point sources, defined by a very soft X-ray spectrum without significant emission above 1 keV. Therefore, these systems can only be detected in cases of low line-of-sight absorption. The general scenario for a SSS is thermonuclear burning on the surface of an accreting WD, which can be stable for certain accretion rates between $1.6 \times 10^{-8} M_\odot$ yr^{-1} and $6.2 \times 10^{-7} M_\odot$ yr^{-1} (Nomoto et al. 2007), depending on the mass of the WD. At lower accretion rates, the accreted material will be accumulated on the WD surface, until conditions for a thermonuclear runaway are reached, which causes a classical nova explosion. Material that is not ejected in the explosion will still undergo nuclear burning. As soon as the ejected material becomes transparent for soft X-rays, the WD can be observed weeks to years after the nova explosion (see e. g. Henze et al. 2011). Accreting WDs with SSS state are associated with CVs, symbiotic stars, planetary nebulae, and post-outburst optical novae. Less luminous super-soft X-ray emission is observed in some planetary nebulae, CVs, hot cooling isolated NSs, and hot cooling WDs, so-called PG 1159 stars.

But also Be star binaries are suggested to harbour accreting WDs. It is still under debate to what extent the generation of the Be phenomenon is related to close binary evolution or another mechanism (Gies 2000). In the case of close binary evolution, matter transfer causes a spin up of the gainer, becoming a Be star, whereas the donor turns into a He star, WD or NS. Binary system evolution models predict, that Be/WD systems might be more frequent than Be/NS systems (Pols et al. 1991; Raguzova 2001). Raguzova (2001) obtain an abundance ratio for He-star/NS/WD of 2/1/7, but only a few Be/WD systems are suggested so far, in contrast to the large number of Be/NS systems. The expected luminosity for stable thermonuclear burning is $L_X \sim 10^{36-38}$ erg s^{-1}.

Similar to an accreting NS, WDs in Be systems are expected to show hard X-ray emission powered by accretion, but at lower luminosity of 10^{29-33} erg s^{-1}, compared to 10^{34-38} erg s^{-1} for NSs (Waters et al. 1989). Suggested candidates are γ Cas like objects (Haberl 1995; Lopes de Oliveira et al. 2006). However, the expected luminosities are below the XMM-*Newton* SMC survey detection threshold. Alternatively, stable thermonuclear burning is suggested to power X-ray emission from Be/WDs. The very-soft emission is likely to be absorbed by the decretion disc of the Be star in most cases, complicating the discovery of such systems (Apparao 1991) and explaining the lack of detected systems. Only one Be/WD SSS system has been proposed so far in the LMC, XMMU J052016.0-692505 (Kahabka et al. 2006). The first candidate in the SMC was discovered during the investigations of this thesis (see Sec. 5.2).

The spectra of SSSs can be described by a black-body model with typical temperatures in the range

of (20−100) eV. These yield a useful approximation to WD atmosphere models if only CCD energy resolution is available, but should be regarded only as parametrisation of the spectrum (Henze et al. 2011). In high-resolution spectra, absorption and emission lines have been observed. SSSs can show a constant, variable or transient X-ray behaviour.

SSSs as an individual X-ray source class were discovered first in the Magellanic Clouds due to their short distance and low foreground absorption, and still today, the Magellanic Clouds offer a unique possibility to study these systems. A better understanding is necessary, e. g. to explain the integrated super-soft X-ray emission of galaxies and the effect of absorption on the observed population (e. g. compare Gilfanov & Bogdán 2010; Hachisu et al. 2010). Besides of WD mergers, accreting WDs are believed to be the main channel leading to SN of type Ia. This SN type is of special importance, as it can be used as *standard candle* to measure cosmological distances. Also most of the iron in the Universe is likely produced by SN Ia.

2.4.7. Active galactic nuclei

Galaxies with active galactic nucleus (AGN) are bright X-ray sources up to cosmological distances and are expected to provide the majority of X-ray sources in the XMM-*Newton* SMC field. Spectral properties of AGN strongly depend on the inclination of the AGN, as described by the unified picture of Urry & Padovani (1995). Evolution during the merging of galaxies is also discussed to have significant influence (Hopkins et al. 2008).

X-rays are caused by accretion onto a super-massive black hole ($M_{\mathrm{SMBH}} \sim 10^{7-9} M_{\odot}$) with luminosities up to 10^{47} erg s^{-1} and show hard power-law-like spectra with a typical photon index of $\Gamma = 1.7$ in the XMM-*Newton* band. X-rays are discussed to originate from a corona of hot electrons via inverse Compton scattering. Possible X-ray features are e. g. Fe K fluorescent emission or a soft excess, which can be caused by reprocessing of harder X-rays. The reverberation, found in Fe L emission, supports this picture (Fabian et al. 2009). Since AGN are accretion powered, they can show variability at all wavelengths and time scales (Grandi et al. 1992). Whereas AGN are observed as point sources in X-rays, radio lobes can originate from synchrotron emission of electrons in jets with sizes up to several 100 kpc. For small inclination angles, these radio galaxies are observed as point-like quasars. AGN are luminous in the UV and infrared, due to emission from the inner part of the accretion disc and a nearby dust torus, respectively.

In the optical, the identification of AGN behind the SMC is complicated by the high stellar density in the field. AGN candidates are selected by optical variability, IR photometry, or radio and X-ray emission. The first quasar behind the SMC was found in a radio investigation of SNRs (Mills et al. 1982). Another was reported in the catalogue of Wilkes et al. (1983). Later on, Tinney et al. (1997) confirmed further eight candidates, selected from ROSAT X-ray sources, with optical spectroscopy. Dobrzycki et al. (2003a,b) confirmed five X-ray selected candidates and five candidates selected due to their optical variability (Eyer 2002). Kozłowski & Kochanek (2009) selected 657 quasar candidates using *Spitzer* IR and NIR photometry. With follow-up spectroscopy Kozłowski et al. (2011) were able to confirm 29 of 268 observed candidates, rising the number of confirmed background AGN to ∼70.

AGN behind the SMC are a valuable sample of background sources. They provide a reference frame for astrometry, which is important for proper-motion studies of the Magellanic Clouds (e. g. Piatek et al. 2008), but also to reduce the systematic uncertainties in the positions of X-ray observations (e. g. Watson et al. 2009). Further, absorption of the radiation of an AGN by the ISM of the SMC might be used to probe the ISM with present or future X-ray missions (e. g. Haberl et al. 2001) or at other wavelengths. Besides, these sources can be studied themselves (e. g. Kelly et al. 2009) with multi-wavelength data from different epochs.

2.4.8. Galaxies

Galaxies from behind the SMC can be seen in X-rays, showing an unresolved combination of X-ray sources of the types discussed above (e. g. Tajer et al. 2005, and references therein). The X-ray emission of elliptical galaxies is often dominated by the thermal emission of the hot ISM. Spiral galaxies rather show emission of SNRs and X-ray binaries. Since most galaxies are believed to contain a super-massive BH in their centre, the emission of a central AGN can contribute to the emission as well. With increasing distance, these sources cannot be resolved and become blended into one X-ray source. Also hot intergalactic medium can contribute to the X-ray emission in galaxy groups. The X-ray emission of normal galaxies (i. e. without the contribution of an AGN) can reach luminosities up to $\lesssim 10^{42}$ erg s^{-1}. The density on the sky is $\sim$1 deg^{-2} at an X-ray flux limit of 10^{-14} erg cm^{-2} s^{-1}. So we expect only a few sources associated with background galaxies in the SMC field.

2.4.9. Cluster of galaxies

Clusters of galaxies (ClGs) are another class of X-ray sources behind the SMC. ClGs are the largest relaxed structures in the Universe and consist mainly of dark matter ($\sim$87%). Baryonic matter in the intracluster medium (ICM) accounts for $\sim$11%. The member galaxies of clusters are the optically brightest components, but constitute only $\sim$2% of the cluster mass. For a review, see Rosati et al. (2002) or Voit (2005).

During the gravitational collapse of $10^{14-15} M_\odot$ of matter distributed over several Mpc, adiabatic compression and shocks caused by the supersonic motion during virialisation heat the ICM to $kT = (2-15)$ keV, resulting in a thin, hot, and ionised plasma that can be assumed to be in CIE. The typical mean cluster metalicity is $Z \sim 0.3 Z_\odot$. ClGs are among the brightest X-ray sources in the Universe with X-ray luminosities of 10^{43-45} erg s^{-1}. The angular extent of the X-ray emission depends on the size and distance of the cluster. Whereas ClGs with low redshift have a measurable extent – as extreme case, the Virgo cluster has a diameter of several degrees on the sky (Böhringer et al. 1994) – more distant clusters are difficult to separate from point sources with XMM-*Newton*, but are also below the detection limit for the SMC survey.

As ClGs follow the gravitational collapse of primordial density perturbations, they probe the high-density tail of the cosmic density field. For a further investigation of ClGs, redshift measurements of member galaxies are necessary, which is challenging in fields with high stellar density, like the Magellanic Clouds. Therefore, studying ClGs behind the SMC might be less interesting. However the identification of these sources is important, to separate them from SNRs and avoid contamination when studying the diffuse emission in the SMC. So far, no X-ray selected clusters behind the SMC are reported in the literature.

2.4.10. Cosmic X-ray background

With decreasing flux, more and more extragalactic X-ray sources fall below the detection limit of individual X-ray observations. These sources constitute the unresolved cosmic X-ray background (CXB), which is diffuse and homogeneous, but absorbed by the Galactic ISM. Whereas below $\sim$1 keV the diffuse X-ray background is dominated by emission from the Galaxy and the LHB (Sec. 2.4.4), the cosmic X-ray background contributes most at higher energies.

Using XMM-*Newton*, De Luca & Molendi (2004) characterised the CXB by a power law with photon index of $\Gamma = 1.41 \pm 0.06$ and a normalisation of 2.46 ± 0.09 photons cm^{-2} s^{-1} sr^{-1} keV^{-1} at 3 keV translating to a (2−10) keV flux of $(2.24 \pm 0.16) \times 10^{-11}$ erg cm^{-2} s^{-1} deg^{-1}.

With deep XMM-*Newton* and *Chandra* observations of fields with low Galactic H I column density like e. g. the *Lockman hole*, (80−100)% of this component could be resolved into point sources like AGN in the (0.5−2.0) keV band (Hasinger et al. 2001; Worsley et al. 2005).

3. Observations and data reduction

3.1. XMM-Newton observations of the SMC

During the first ten years of the XMM-*Newton* mission, different kinds of sources in the SMC have been the subject of the X-ray observations. Examples are X-ray bright SNRs (e. g. IKT 5, IKT 18, and IKT 23), early-type stars (e. g. HD 5980), HMXBs (e. g. SMC X-1), and SSSs known from ROSAT (e. g. RX J0059.6-7138). Observations of 15 fields, mainly in the bar of the SMC were performed, to discover HMXBs and study their relation to star formation. All these observations became available in the public archive about one year after the observation.

Additionally, a few observations were triggered by transient sources. Observation 0311590601 was aimed to observe the Nova SMC 2005, but the source was not detected. Also a follow-up observation of the RXTE-detected pulsar XTE J0055-727 failed to localise the source. Recently, three triggered observations of RX J0049.0-725 and one observations of SXP 175 were performed. These target of opportunity (ToO) observations became public about six months after the observation.

Calibration observations of the SNR 1E0102.2-7219 (= IKT 22) are performed regularly every six months since the beginning of the mission. These observations constitute the deepest observed XMM-*Newton* field in the SMC. Calibration observations are public immediately.

The observations of the *large-programme SMC-survey* were chosen to fill the gaps, which were not covered at sufficient depth by previous observations and to cover the main body of the SMC as seen in Hα. The coverage of these observations is compared to an optical emission line image in Figure 3.1. The survey observations were executed with EPIC in *full-frame* imaging mode using the thin and medium filter for EPIC-pn and EPIC-MOS, respectively.

All these observations form a continuous field with an area of 5.58 deg^2, which we will refer to as the *main field*. The exposure distribution, accounting for vignetting and without time periods of proton flares, is presented in Figure 3.2. Apart from the deep field around 1E0102.2-7219, a relatively homogeneous coverage was archived (cf. Figure 3.3).

In addition to observations in the main field, observations further away from the SMC bar and wing were used, which still can contain sources located within the SMC. Also, these fields were used to measure the celestial X-ray background around the SMC.

To build an XMM-*Newton* point-source catalogue for the SMC field, I combined the data of the large-programme SMC survey, with all publicly available archival data until April 2010 (62 observations, 1.6 Ms exposure), from which 28 observations (850 ks exposure) are calibration observations of the SNR 1E0102.2-7219. The 33 observations of 30 different fields of the SMC large-programme survey have a total exposure of 1.1 Ms. From the outer fields, I included two observations of a field in the north and three fields in the south of the SMC main field (98 ks exposure in total). These are somewhat further away from the SMC bar and wing but can contain sources in the SMC like e. g. SSSs found by ROSAT. The total area covered by the observations used for the catalogue is 6.32 deg^2 and constitutes of observations inside the blue box in Figure 3.2. More recent observations (C29–32, A35–38, and O6–10) were used only for the mosaic image and to investigate the diffuse emission.

A list of all EPIC exposures, performed within a radius of 200′ of the position 1^{h} -72.°5 until the end of 2011, is given in Table B.2 in the appendix.

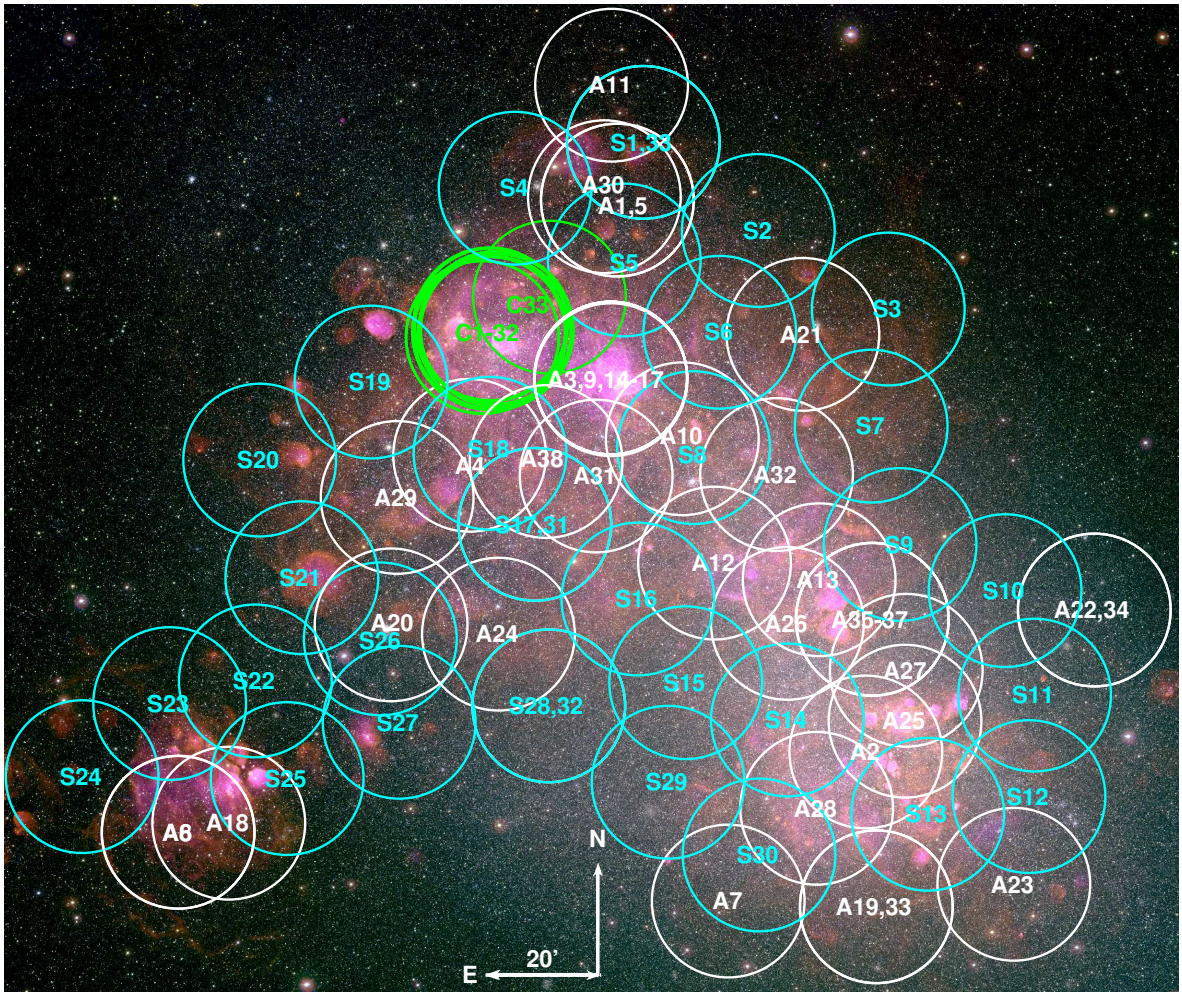

Figure 3.1. Colour image of the SMC from MCELS (e. g. Smith et al. 2000; Winkler et al. 2005) with Hα, [S II], and[O III] in red, green, and blue. The overlaid circles mark the observed XMM-*Newton* fields and have radii of 800″. Labels correspond to column 1 of Table B.2. Archival observations are plotted in white, calibration observations in green and large-programme survey observations in cyan.

In addition to scientific observations, calibration observations with closed filter wheel are performed regularly to measure the detector background. Merged event files from these observations are provided[1] by the XMM-*Newton* background working group.

3.2. Processing of the data

For the processing of the XMM-*Newton* SMC data, I build on a similar analysis pipeline as used for XMM-*Newton* observations of the Local Group galaxies M 31 (Pietsch et al. 2005; Stiele et al. 2011) and M 33 (Pietsch et al. 2004; Misanovic et al. 2006) that were developed in our research group. The analysis of point sources in these studies was similar as for the XMM-*Newton* Serendipitous Source Catalogue (2XMM, Watson et al. 2009), but compared to this catalogue, the M 31 and M 33 catalogues have an improved position accuracy by using astrometric boresight corrections based on

[1] available at http://xmm2.esac.esa.int/external/xmm_sw_cal/background/filter_closed/

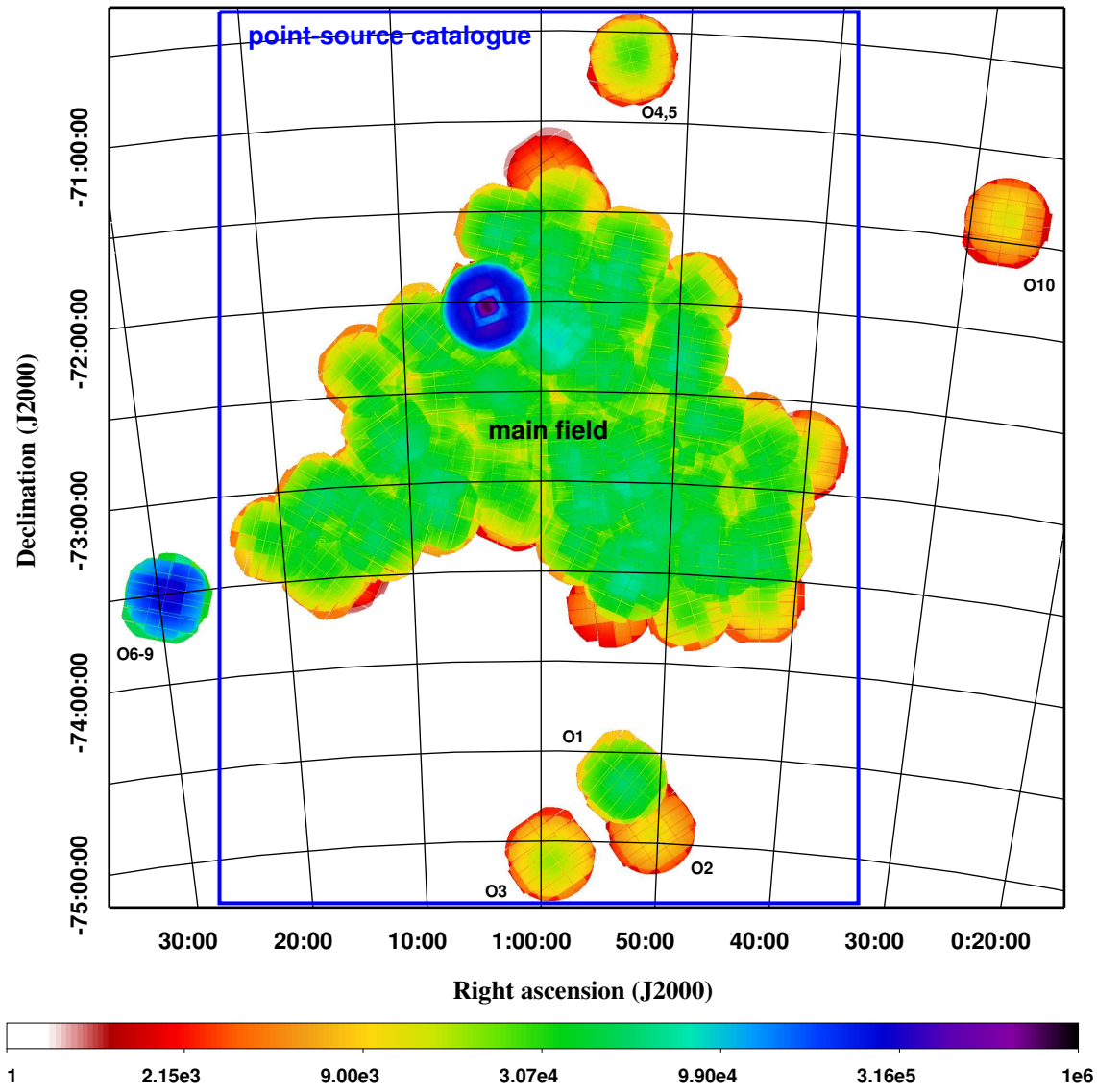

Figure 3.2. Combined vignetting-corrected and GTI-screened EPIC exposure map of the SMC main field and surrounding observations in units of seconds. EPIC-MOS1 and -MOS2 exposure is weighted by a factor of 0.4 relative to EPIC-pn to account for the lower effective area. The outer fields are labelled according to column 1 of Table B.2. The blue box marks the field, used to create the point-source catalogue. The allocation of individual observations of the main field is given in Figure 3.1.

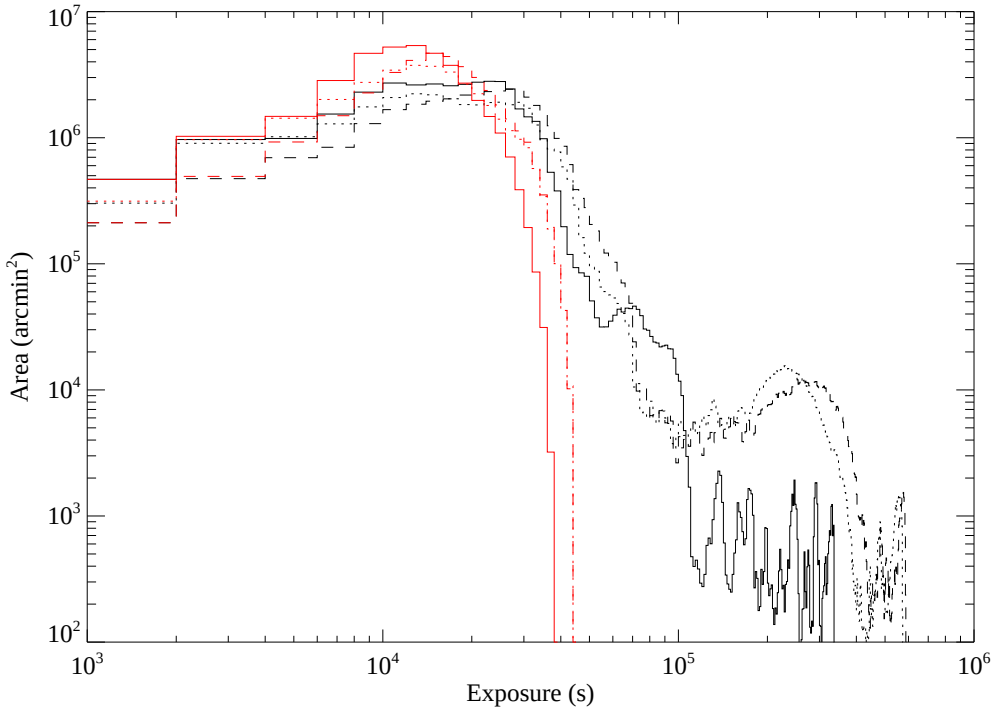

Figure 3.3. Vignetting corrected exposure of the main field for EPIC-pn (solid line), EPIC-MOS1 (dotted line) and EPIC-MOS2 (dashed line) in the (1.0-2.0) keV band, when summing all observations (black) and using the deepest observation at each position (red).

identified sources, and a comprehensive source screening.

The XMM-*Newton* Science Analysis Software (SAS)[2] was used to create the basic source products. The SAS is a collection of tasks specifically designed for XMM-*Newton* data and provided by ESA. For the analysis of source products, I used `ftools` (Blackburn 1995), `xspec` (Arnaud 1996), `stilts` (Taylor 2011) and `ds9` (Joye 2006). In addition, I developed more sophisticated `bash`, `sql`, and `idl` scripts for advanced data analysis as part of this thesis.

Before the data reduction, the existing pipeline was tested with the new SAS version and modified at several places. This pipeline creates eventfiles, produces images, performs source detection for the individual observations, and calculates a mosaic image. Due to the high number of observations and the nowadays available multi-core CPUs, I updated many scripts to allow a parallel execution. Also some scripts had to be optimised regarding their performance, e. g. by avoiding unnecessary or already calculated products. I basically reworked the scripts for the calculation of the mosaic image to allow a subtraction of the detector background and to create an image with excluded point sources for the study of the diffuse emission. Scripts for the extraction and analysis of source products (e. g. spectra of point sources), were optimised in order to minimise manual interaction. I developed scripts for the reduction of spectra of the diffuse emission and their analysis.

To provide a fast and comprehensive access to the analysis results for the SMC large-programme collaboration, a database was set up on a `MySQL` server. A pilot study of such a database was done by Eger (2008). This first version used only one table, which limits its capability (e. g. for each source, only one possible optical counterpart was stored). As part of this thesis, I developed a comprehensive

[2] http://xmm.esac.esa.int/sas/

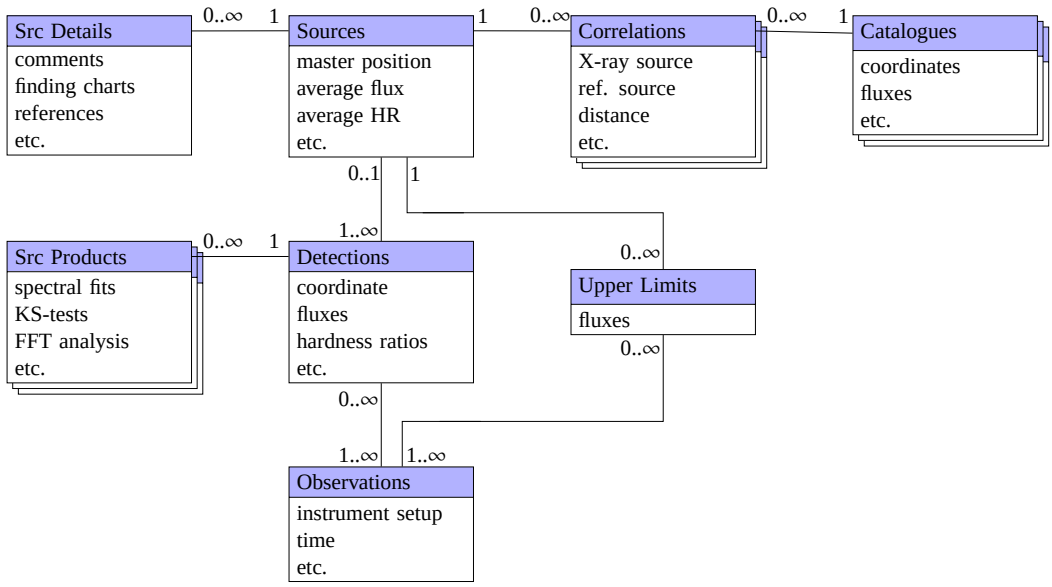

Figure 3.4. Simplified entity-relationship diagram for the SMC database. Boxes represent tables. Lines illustrate their connection and are labelled with the range of corresponding entries in the table.

database structure together with Jai Won Kim (see Figure 3.4), to combine the desired information e. g. from observations, X-ray sources, and counterparts. This makes the database a very powerful tool for data analysis. E. g. I developed `sql` scripts that allow source screening, cross-correlation, and classification inside the database. I loaded other catalogues completely[3] into the database and used correlation tables to assign counterparts. For the loading of `FITS` files into the database, I used the `fittablereader`[4]. To enable a comprehensive access to the data for the SMC large-programme collaboration, a web interface for this database was created by Jai Won Kim in close collaboration with me. The interface allows to run user defined `sql` queries on all tables and provides access to source products, like spectra or finding charts.

3.3. Data reduction

In the following the data reduction of the pipe-line and individual source products will be described.

3.3.1. Event lists

The XMM-*Newton* raw data is organised in observation data files (ODFs). The SAS task `odfingest` adds ancillary information from satellite housekeeping and calibration data, necessary to process the observations. To assign the most recent current calibration files (CCFs), a CCF index file (CIF) was created for each observation with `cifbuild`.

I processed all observations homogeneously with SAS version 10.0.0 and created EPIC event lists[5]

[3] Also reference sources without X-ray counter part were regarded, but for all-sky catalogues, only the field of the SMC was used.

[4] Developed by Jai Won Kim. Besides of loading a `FITS`-table into the database according to the `FITS` description, it allows to store the meta-data of `FITS` tables in the database, like e. g. units or descriptions of table columns.

[5] An event list is a table with one row per event registered by the instrument, containing all measured information like position, energy, frame time, event-pattern, and flag. The total number of events in SMC observations is 223 014 497.

using `epchain` or `emchain`, respectively. If preliminary boresight corrections could be determined, these were already used to correct the attitude file (see Sec. 3.3.7). I used `epreject` to correct for artefacts in the EPIC-pn offset map, which are caused by charged high-energy particles, hitting the detector during the offset-map calculation and causing a shift in the energy scale. This avoids the detection of spurious very-soft sources later on, but has the disadvantage of enhancing the effect of optical loading by optically bright stars. Therefore, I screened for bright stars as described in Sec. 3.3.6. The photon arrival times where randomised within their read-out frame.

3.3.2. Selection of good time intervals

To remove times of bad data, SAS tools use good time interval (GTI) files, which contain the start and end times of GTIs. *Standard GTIs*, which list usable time intervals for each CCD, are already created by `epchain` or `emchain` and appended to the event lists. Additional GTIs must be defined, to exclude time intervals affected by high background. Examples for two EPIC-pn background light-curves are presented in Figure 3.5. Both exhibit typical features of strong but sharp soft-proton flares (Figure 3.5a) and increased background at the end of the satellite orbit (Figure 3.5b) caused by the radiation belts.

To exclude time intervals of high background, I defined *background GTIs* when the background rate in the (7−15) keV band was below 8 and 2.5 cts ks^{-1} $arcmin^{-2}$ for EPIC-pn and EPIC-MOS, respectively, as shown by the blue line in Figure 3.5. Since soft proton flares affect all EPIC detectors, EPIC-pn and EPIC-MOS were allowed to veto each other, but it was assured, that EPIC-MOS exposure is used, when EPIC-pn was calculating the offset map at the beginning of the observation. Exceptions are the observations 0503000301, 0011450201, and 0412981301, where the count rate in the high energy band was significantly increased for EPIC-pn only, thus the EPIC-MOS data was used in these cases. For observations 0112780601, 0164560401, 0301170501, and 0135722201, the good-time exposure was below 1 ks and these observations were rejected. The resulting net exposures are given in Table B.2. For the observations used for the source catalogue, this good-time selection removed about 16% exposure from the survey data, 22% from the calibration observations, 34% from other archival data and 10% from the outer fields.

These *background GTIs* are suitable for source detection and the analysis of X-ray point and extended sources. But for the spectral analysis of faint diffuse emission as well as for the assembly of mosaic images, also weak flares can contribute considerably to the faint X-ray emission. Therefore, I defined additional, more restrictive *sigma-clipping GTIs* for each exposure with the SAS task `espfilt` (Kuntz & Snowden 2008). In this method, a count-rate histogram is created, fitted with a Gaussian profile to determine the peak of the quiescent count rate and only time intervals with a count rate of $\pm 1.5\sigma$ around the peak count rate are accepted. This method selects intervals with very low or no contamination, as plotted in green in Figure 3.5. Compared to above, this more restrictive temporal screening removes about 30% exposure from the survey data, 27% from the calibration observations, 57% from other archival data and 37% of the outer fields.

Another source of variable background contamination is SWCX (Sec. 2.4.1). Since this emission is variable on a longer time scale, a screening of this component is more complicated. Often the only way to exclude a significant contribution is the comparison of two separate observations of the same field. I created background light curves in the (400−800) eV band. Within the *sigma-clipping GTIs* I could not find variations, which would point to a significant contribution of SWCX emission.

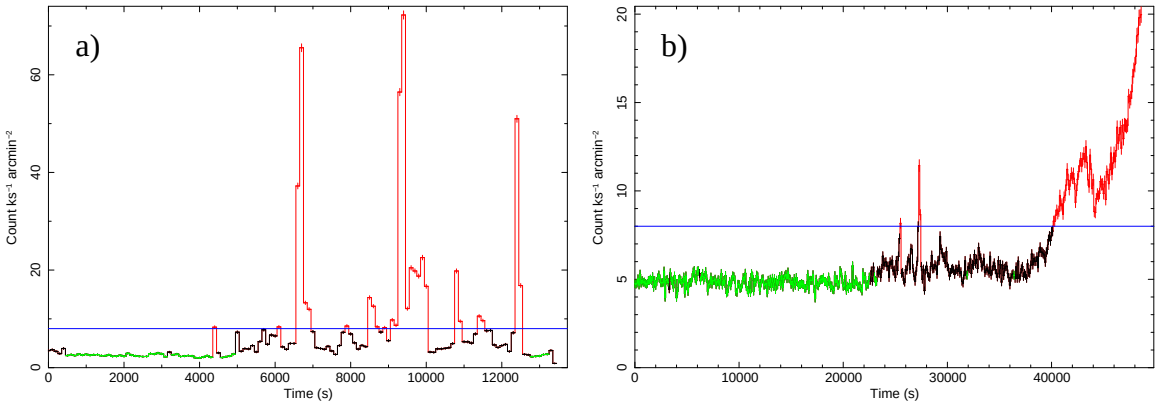

Figure 3.5. Examples for EPIC-pn background light curves in the (7.0−15.0) keV band. The threshold count rate which was used for GTIs is shown by the blue line. Rejected time intervals above that rate are plotted in red. Time intervals with very low background contribution, as defined by the sigma-clipping method are shown in green, others in black. [(a)] Observation 0142661001 is affected by three short strong flares and moderate proton contamination in between. [(b)] Observation 0601210501 shows increased background at the end of the satellite's orbit.

3.3.3. X-ray images

For the X-ray images, EPIC-pn events between 7.2 keV and 9.2 keV were discarded, since these are affected by background fluorescent emission lines inhomogeneously distributed over the detector area (Freyberg et al. 2004). In the lowest energy band of EPIC-pn, an additional screening of recurrent hot pixels was used and for a few columns with increased noise, events were rejected below individual energy-offsets between 220 and 300 eV.

I produced images with an image-pixel binning of $2'' \times 2''$ in the five XMM-*Newton* standard energy subbands (see Table 3.2). Single-pixel events were used for EPIC-pn in the (0.2−0.5) keV band, single- and double-pixel events for the other EPIC-pn bands, and single- to quadruple-pixel events for all EPIC-MOS bands. EPIC-MOS events were required to have `FLAG=0`. EPIC-pn events were selected with `(FLAG & 0xfa0000) = 0`, which, as opposed to `FLAG=0`, allows events in pixels, next to bad pixels or bad columns. This increases the covered area on the sky, but can also cause additional spurious detections, which needed to be taken into consideration (see Sec. 3.3.6). Exposure maps accounting for telescope vignetting were created with `eexpmap`. Merged, exposure-corrected, and smoothed ($10''$ FWHM) images of all observations can be found in Figure C.1 in the appendix.

3.3.4. Maximum-likelihood source detection

For each observation, I accomplished source detection on the X-ray images using the SAS task `edetect_chain`, which (i) searches for point sources with a sliding box detection method, (ii) creates a background image by fitting a two dimensional spline with 16 nodes to the observed image with point sources removed and adds in the case of EPIC-pn an *out-of-time* event image, (iii) assembles point-source candidates by a second sliding box detection run where the background image is used to determine the local background, and (iv) performs a maximum-likelihood fit, using `emldetect`, for each candidate in all energy bands and instruments (up to 3×5 images) simultaneously. For each source, the position and the counts in each image were fitted. In addition, a possible source extent was investigated by using a β-model, which approximates the brightness profile of galaxy clusters

(Cavaliere & Fusco-Femiano 1976) with

$$f(x,y) = \left(1 + \frac{(x-x_0)^2 + (y-y_0)^2}{r_c^2}\right)^{-3/2} \tag{3.1}$$

The core radius r_c is used as extent (*Ext*) with corresponding uncertainty and a likelihood of source extent ML_{ext}. Also, extended sources where tested to be fitted with two point sources. A detailed description of the detection procedure can be found in Watson et al. (2009). As in the case of their catalogue, detections with $ML_{det} = -\ln(P) \geq 6$ were accepted, where ML_{det} is the detection likelihood, normalised to two degrees of freedom, and P is the chance detection probability due to Poissonian background fluctuations.

3.3.5. Compilation of the point-source catalogue

To create a source catalogue for the SMC, I auto-correlated all 5236 non-spurious (Sec. 3.3.6) detections of point or moderately extended sources to identify detections originating from the same source in fields, which were observed several times. Correlations with a maximal angular separation of $d_{sep} < 7''$ and $d_{sep} < 3(\sigma_1 + \sigma_2)$ were accepted, where $\sigma_{1,2}$ is the positional uncertainty of the two sources (see Watson et al. 2009). This resulted in 3053 unique X-ray sources. Master source positions and source extent were calculated from the error-weighted average of the individual detection values. Detection likelihoods were combined and renormalised for two degrees of freedom.

3.3.6. Catalogue screening

Each observation was screened individually and a quality flag `QFLAG` was set manually to indicate if the detection was most likely not caused by a point source. Spurious detections can be caused by single reflections of SMC X-1 (`QFLAG=S`), or by OOT events of bright sources (`QFLAG=O`). The substructure of extended sources or residuals of the PSF of the brightest sources can lead to multiple detections (`QFLAG=M`). Also, sources with significant extent like supernova remnants and the largest clusters of galaxies were marked (`QFLAG=E`) and not used for the point-source catalogue.

Using a preliminary version of the source catalogue and the mosaic image, a second screening was performed taking full advantage of all X-ray information. Using a mosaic colour image of the SMC (see Sec. 3.3.14), I looked for wrongly correlated detections and not correlated detections obviously originating from the same source. This occurred e. g. in the case of bright sources with low statistical uncertainty, if the astrometric solution was not yet sufficiently accurate. In some observations EPIC-MOS CCDs were in *anomalous state* (Kuntz & Snowden 2008), where they show increased low energy ($\lesssim$1 keV) noise. Affected CCDs were identified with `emtaglenoise`. The data were used for source detection, but not for the mosaic image. To ensure that the detections in these noisy CCDs are real, I required that the detection likelihood for the noisy CCD in the (1.0–12.0) keV band is sufficient for an independent detection, or that the source is found by an instrument not in *anomalous state* within the same or another observation. If in addition no source is visible in the mosaic image, the detection was flagged with `QFLAG=N`. Detections found in regions with enhanced diffuse emission, where the reliability is doubtful, were flagged (`QFLAG=D`), if no clear point source was visible in the deep mosaic image. The task `eproject` abolishes EPIC-pn offset map corrections for optical loading caused by bright optical sources with $V < 12$ mag or $V < 6$ mag for observations with thin or medium filter, respectively[6]. I found 57 detections of 36 sources, which fulfil this criterion. If the source was

[6]M. J. S. Smith 2008, PN optical loading, XMM-*Newton* calibration technical note XMM-SOC-CAL-TN-0051 Issue 1.2,

Table 3.1. Screening of detections.

QFLAG	description	number
G	good (default)	5236
M	multiple detection	503
S	single reflection	232
E	extended source	207
P	hot pixel	129
N	MOS CCD in anomalous state	110
O	out-of-time events	22
D	diffuse emission	20
L	optical loading	4

not detected with a high level of significance by another instrument, in another observation, or in the EPIC-pn energy bands 2−5, this source was rejected (`QFLAG=L`). This caused a rejection of only 4 sources. All other 32 potentially affected sources show evidence for real X-ray emission. Sources, detected only in one observation and by only one instrument with detection likelihood $ML_{\rm det} > 10$ in energy band 1, but not detected above 1 keV, were checked for hot pixels, which might have been missed by `badpixfind` and flagged (`QFLAG=P`), if a bright pixel was found in the detector image or if the detection was close to a hot pixel or column and had a peculiar, non-PSF-like shape. All other detections have `QFLAG=G` by default. Only the G-flagged sources were included in the point-source catalogue. The flags and the number of occurrences are listed in Table 3.1.

3.3.7. Astrometric corrections

The accuracy of the astrometric frame of XMM-*Newton* can be improved since the position of bright sources has a higher statistical precision than the initial XMM-*Newton* attitude solution. However, the standard boresight correction, using a simple comparison with a complete optical reference catalogue, cannot be applied, because the number of random optical counterparts overwhelms the number of real counterparts in the SMC field.

If astrometric corrections were known already (e. g. Eger 2008), or if they could be determined easily by clearly identified sources (HMXBs or AGN), the attitude file was corrected before the event-file creation. I used this information to correct the spacecraft attitude for a linear boresight shift in right ascension and declination. These corrections have led to shifts of up to 4″, e. g. observation 0500980101 and thus improve the quality of the images and cross correlations.

Using the autocorrelated detection list, I further controlled and improved the coordinates of individual source detections. I selected optical counterparts, mainly from Zaritsky et al. (2002), of identified HMXB and spectroscopically confirmed AGN as well as identified foreground stars from the Tycho-2 catalogue, as described in Sec. 4.3. In the latter case, known proper motions were taken into account. The positions of all detections of the individual observations were corrected in this second iteration. The overall applied boresight corrections for all observations are listed in Table B.2. As I only used identified sources instead of a general correlation with a reference catalogue, I also accepted coordinate corrections if only one identified source was available in the FoV of an observation. This allowed a coordinate improvement for all observations and a systematic position uncertainty of $\sigma_{\rm sys} = 0.5''$ (Pietsch et al. 2005) is assumed uniformly. The total position uncertainty was estimated by $\sigma = (\sigma_{\rm sys}^2 + \sigma_{\rm stat}^2)^{1/2}$, where $\sigma_{\rm stat}$ is the statistical uncertainty from the maximum likelihood fit.

http://xmm2.esac.esa.int/docs/documents/CAL-TN-0051-1-2.ps.gz

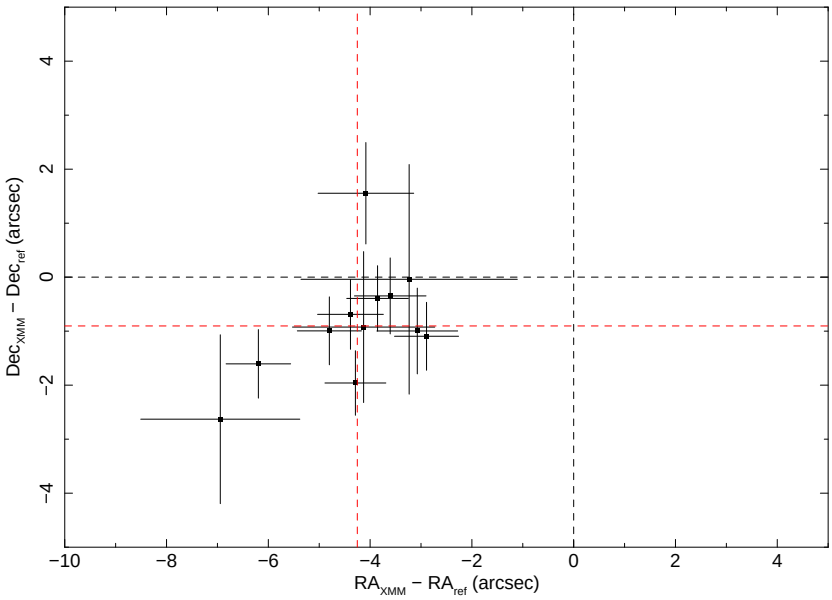

Figure 3.6. Example for source offset for observation 0500980101. Dashed red line gives the estimated correction for the pointing direction. Dashed black lines indicates the initial astrometric solution.

3.3.8. Spectral characterisation

To investigate the spectral properties of all sources, hardness ratios HR_i ($i = 1, 2, 3, 4$) and corresponding uncertainties ΔHR_i were used, defined by

$$HR_i = \frac{R_{i+1} - R_i}{R_{i+1} + R_i} \tag{3.2}$$

$$\Delta HR_i = 2\frac{\sqrt{(R_{i+1}\Delta R_i)^2 + (R_i \Delta R_{i+1})^2}}{(R_{i+1} + R_i)^2} \tag{3.3}$$

where R_i is the count rate in energy band i (see Table 3.2). To increase statistics in the individual energy bands, the count rates of all three instruments were added and the uncertainties were propagated quadratically. For sources detected in several observations, average count rates were calculated. Also here, the uncertainty of counts was propagated quadratically. The dependence of the relative count rates on the instrumental setup is smaller than the rate uncertainty in most cases. HR_i is not given, if both rates R_i and R_{i+1} are null or if the 1σ uncertainty of ΔHR_i covers the complete HR interval from -1 to 1.

3.3.9. Flux calculation

To convert an individual count rate R_i of each energy band i into an observation setup independent observed flux F_i, I assumed a universal spectrum for all sources, described by a power-law model with a photon index of $\Gamma = 1.7$ and a photoelectric foreground absorption by the Galaxy of $N_{\mathrm{H,Gal}} = 6 \times 10^{20}$ cm^{-2} (average for SMC main field in H I map of Dickey & Lockman 1990). I calculated energy conversion factors (ECFs) $f_i = R_i/F_i$, by simulating this spectrum with standard EPIC redistribu-

tion matrix files (RMFs)[7]. This universal spectral shape is only a rough assumption. But since the correction is from counts to detected flux, i. e. not corrected for absorption, and since the fluxes are calculated independently for each of the relatively narrow energy bands, deviations from the global source spectrum are reduced. Therefore, the calculated fluxes give a good approximation within 20% of the true detected flux in most cases (see also Pietsch et al. 2004).

For EPIC-MOS, increased redistribution of measured photon energies is known to occur around the EPIC-pn and RGS prime pointing position, where most targets are placed (Read et al. 2006). This has some effect on the ECFs for the energy bands 1 and 2. I decided to use the *off-patch* single to quadruple event RMF, since in the case of the SMC survey, the majority of detections lies outside this patch area. The differences between *on*- and *off-patch* ECFs is <10% for energy band 1 and lower for the other bands. For EPIC-pn, the dependence of the spectral resolution on the detector position has an even smaller influence on the ECFs (<2%) and the RMF for CCD rows 81-100 was used as average. It was ensured that the RMFs were based on the same pattern selection as used to create the images. The dependence of the ECFs on data mode is <2% (Watson et al. 2009) and the *full-frame* RMFs was used for all instruments. The ancillary response files (ARFs) were calculated with `arfgen` for each filter and instrument and do not contain corrections, which have already been applied by `emldetect`. For EPIC-pn, f_5 is corrected for the removed (7.2−9.2) keV sub-band, thus translating to full (4.5−12.0) keV fluxes. The derived ECFs are listed in Table 3.3. Since energy band 5 does not contribute substantially to the total flux but rather increases its uncertainty in most cases, it is not used for the so-called XID flux[8]. To calculate XID fluxes, the energy bands $1-4$ were added for each instrument and their uncertainties were added quadratically. The final flux in the (0.2−4.5) keV band was determined, by calculating the error-weighted average from all available instruments, similar as in previous studies of M 31 and M 33. For sources with several detections, the catalogue includes the minimum, maximum and error-weighted average of the flux.

Table 3.2. Energy bands.

Name	$E_{\rm min}$	$E_{\rm max}$
total	0.2	12.0
soft	0.2	2.0
hard	2.0	12.0
XID	0.2	4.5
band 1	0.2	0.5
band 2	0.5	1.0
band 3	1.0	2.0
band 4	2.0	4.5
band 5	4.5	12.0

Table 3.3. Energy conversion factors.

Detector	Filter	f_1	f_2	f_3	f_4	f_5
pn	thin	11.150	8.132	5.839	1.943	0.463
	medium	9.976	7.897	5.758	1.926	0.465
	thick	6.329	6.071	4.964	1.824	0.459
MOS1	thin	2.118	1.937	2.064	0.744	0.144
	medium	1.891	1.883	2.029	0.735	0.144
	thick	1.273	1.530	1.807	0.705	0.142
MOS2	thin	2.117	1.938	2.070	0.748	0.152
	medium	1.886	1.884	2.034	0.740	0.152
	thick	1.264	1.530	1.812	0.710	0.150

Notes. Energy conversion factors f_i in units of 10^{11} cts cm^2 erg^{-1} for the standard bands 1−5 (Table 3.2).

3.3.10. Estimation of sensitivity

To estimate the completeness of the catalogue, I calculated sensitivity maps for each observation with `esensmap` for the individual energy bands and instruments, as well as for combinations of them. Assuming Poissonian count statistics, detection limits for each position were calculated from the

[7] Available at http://xmm2.esac.esa.int/external/xmm_sw_cal/calib/epic_files.shtml
[8] In other studies, the XID band is defined as (0.5−4.5) keV band (e. g. Watson et al. 2009).

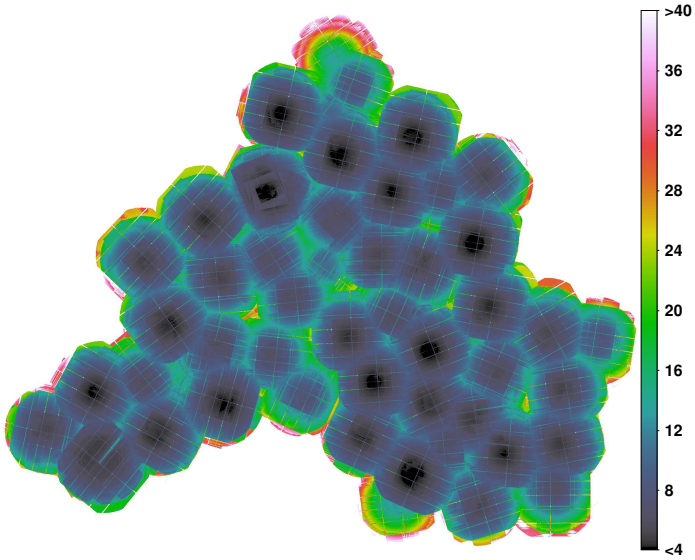

Figure 3.7. The sensitivity map for the main field in the (2.0−12.0) keV band in 10^{-15} erg cm^{-2} s^{-2}.

exposure and background maps. In the case of combined energy bands or instruments, the background images were added and the exposure maps were averaged, weighted by the expected count rate for the adopted universal spectrum of Sec. 3.3.9. The individual observations were combined, by selecting the observation with highest sensitivity at each position. An example is plotted in Figure 3.7. I note that, depending on the individual source spectra, the detection limits deviate from this estimated value, but a detailed simulation of the detection limit goes beyond the scope of this thesis.

3.3.11. Long-term time variability

An important characteristic of X-ray sources is their long-term time variability between the individual observations. It allows to discriminate between transient, variable, and long-term constant X-ray sources.

In addition to the fluxes for each detection (Sec. 3.3.9), I calculated flux upper limits $F_{\rm UL}$ for each observation and source, if the source was covered but not detected in the individual observation. Analogously to the initial source detection, I used `emldetect` with the same parameters as above to fit sources, but kept the source positions fixed (`xidfixed=yes`) at the master positions of the sources and accepted all detection likelihoods to get an upper limit for the flux. To assure that all sources are fitted in order of decreasing brightness, a second `emldetect` run was performed, based on the results from the first run.

Following Primini et al. (1993), Misanovic et al. (2006), and Stiele et al. (2008), for the characterisation of the observed variability of sources covered by various XMM-*Newton* observations, I calculated the variability V and its significance S from

$$V = \frac{F_{\rm max}}{F_{\rm min}} \tag{3.4}$$

$$S = \frac{F_{\rm max} - F_{\rm min}}{\sqrt{\sigma^2_{\rm max} + \sigma^2_{\rm min}}} \tag{3.5}$$

where $F_{\rm max}$ and $\sigma_{\rm max}$ are the source flux and 1σ uncertainty in the (0.2–4.5) keV band of the detection, for which $F - \sigma$ is maximal among all detections with a significance of $F > 2\sigma$. In a similar way, $F_{\rm min}$ and $\sigma_{\rm min}$ were chosen from the detection, for which $F + \sigma$ is minimal among all detections with $F > 2\sigma$. In cases of $F < 2\sigma$, I considered $F_{\rm min} = 3\sigma$ as possible lower limit. Analogously, the minimum upper limit flux $F_{\rm UL}$ was selected from the observations, where the source was not detected. If the minimum $F_{\rm UL}$ was smaller than $F_{\rm min}$ defined above, I used it instead to calculate V.

3.3.12. Short-term time variability

To investigate the flux variability within the individual observations, I used KS-tests to compare the photon arrival time distribution with the expected distribution from a constant source. This method is also applicable to sources with poor statistics, where background-subtracted binned light curves cannot be obtained.

I extracted time series of events, i. e. a list of photon arrival times, of the EPIC-pn and both EPIC-MOS in the (0.2–4.5) keV band. The same flag and pattern selection was used as described in Sec. 3.3.3. Source counts were selected within an ellipse that approximates the PSF of the source at a surface brightness (in cts pix^{-1}) equal to the background surface brightness, as defined by the SAS task `region`. All events have to be within the *background GTI* of the soft-proton flare screening (Sec. 3.3.2) and the standard GTIs of all EPIC instruments. I merged the event lists of the individual EPIC instruments to obtain higher statistics. To estimate the background variability caused for example by residual soft-proton flares, I assumed a spatial independence of the background time variability. Time series of background events were extracted in a similar manner, but excluding regions around each point source where the PSF brightness is larger than 10% of the background value.

In most cases, the KS-test works well by using a linear increasing function during GTIs and a constant otherwise. In some cases, the background time series exhibits significant variability. For bright sources, the contribution of the background is negligible. To ensure that this has no influence on the variability estimate of faint sources, I created a reference function, combining the background and constant source distribution. The expected relative background contribution was estimated from the background maps (Sec. 3.3.4). Since the statistics of the background time series is high compared to that of faint sources, it can be used as a quasi-continuous function. I added this cumulative light curve to the constant-source function and performed a one-sample KS-test. The resulting probability, Cst, that the temporal photon distribution can be explained by a constant source was calculated for each detection. For sources with several detections, the catalogue includes the minimum of Cst over all detections. Sources that can be considered variable show values of $Cst < 0.5\%$ (see Sec. 4.4.5).

3.3.13. Products for bright point sources

In spring 2011, version 11.0.0 of SAS became available and was used to extract the data products of bright sources.

To define extraction regions for the individual sources, I created images in the (0.2−10.0) keV band with `FLAG=0` and single to double or to quadruple events for EPIC-pn and EPIC-MOS, respectively, and taking into account the *standard* and *background GTIs*. This is the same selection, as used for the source products later on.

To estimate the contribution of the background, events are selected from a region near the source extraction region. The background regions were defined manually for all three instruments. Ideally, the region should fulfil the following criteria: (i) a point source free area on the sky; (ii) a location on the same CCD as the source extraction region, to avoid systematic differences in the detector

background; (iii) a similar off-axis angle as the source region, to have same vignetting; (iv) an area of at least the same size as the source selection region, to have similar statistics of the background contribution in both regions; (v) in the case of EPIC-pn the OOT stripes of the source must be avoided, since this would lead to a contribution of source counts; (vi) the OOT stripes of other bright sources in the FoV must be avoided, since otherwise this source would contribute to the background; (vii) avoid regions of increased detector background, e. g. close to the read-out edge of EPIC-pn; (viii) the same location on the sky for the background regions of all three instruments. Of course, only for very few sources, it is possible to define regions fulfilling all criteria and compromises had to be made.

To select events from an individual source, a region centred on the source was defined. The SAS task `eregionanalyse` was used to determine the radius of a circular extraction region by optimising the signal-to-noise ratio. E. g. for brighter sources, larger extraction radii can be used, until the contribution of the background becomes dominant. It was ensured that the source extraction regions have a distance of $>10''$ to other detected sources.

Energy spectra of the source and background region as well as response matrices were created with `especget`. Three versions of EPIC-pn spectra were created using single, double, and single and double events. For EPIC-MOS, single to quadruple events were used. Event times must be inside the *background GTIs* and `FLAG=0` was required. I binned the spectra to a signal-to-noise ratio of 5 for each energy bin.

For timing analysis, I created time series of events. I did a temporal selection first, where I combined the *standard GTIs* of all involved CCDs (source and background region) and the *background GTIs*. After this temporal screening, the photon arrival times were recalculated for the solar barycentre with `barycen`, to correct for the motion of the satellite and Earth. I selected events with single to double or to quadruple events for EPIC-pn and EPIC-MOS, respectively. This was done for the (0.2−10.0) keV energy band, as well as for the soft, hard and all sub bands. Since the photon arrival times do not depend on instrumental properties, one can merge time series from all available EPIC instruments, to increase the statistics for the timing analysis. This was done analogously to above, but only selecting events within GTIs of all instruments simultaneously, i. e. the light curve covers only intervals with good data common to all available instruments.

Light curves, binned to have 30 cts bin^{-1} on average, were created using the SAS tasks `etimeget` and corrected for background, vignetting, and point-spread-function losses by `epiclccorr`. The same event selection was used as for the time series.

3.3.14. Mosaic image

To produce a mosaic image of the SMC, I used EPIC-pn observations in full-frame or extended-full-frame mode only. EPIC-MOS observations were used in all modes, as the outer CCDs are always in imaging mode. I excluded the observations 0011450201, 0112780601, 0135722201, 0311590601, 0412981301, and 0301170501 for the mosaic image, because they suffer high background or are affected SMC X-1 in bright state.

To create a mosaic image of the SMC, the image coordinates of all events were recalculated to a common coordinate grid. Images in the individual subbands were created with the same selection criteria as described in Sec. 3.3.3, but applying the more restrictive *sigma-clipping GTIs*. I did not use data from EPIC-MOS CCDs in *anomalous state*. Exposure maps were calculated in mosaic size and corrected for vignetting.

In addition to these images, I analogously extracted images from the merged eventfile of observations with filter wheel closed (FWC) and from the EPIC-pn OOT eventfiles. OOT images were multiplied with the OOT event fraction $f_{\rm oot}$ according to Table 2.2. Following Bauer (2004), I assumed

that events in the detector corners are caused primarily by detector background, as these regions are shielded from the X-ray telescopes. The FWC images of each energy band were scaled by a factor f_{fwc}, that is calculated from the counts in the shielded detector corners of the image, the OOT image, and the FWC image, respectively:

$$f_{\mathrm{fwc}} = \frac{C_{ima} - f_{\mathrm{oot}} C_{\mathrm{oot}}}{C_{\mathrm{fwc}}} \tag{3.6}$$

Single reflections of photons from SMC X-1 cause strong artefacts (arc-like features) in the mosaic images. Their position on the sky depends on the off-axis angle of SMC X-1. Therefore, affected regions can be covered without single reflections in another observation. For individual exposures, I defined rough regions that are affected by single reflections and a region-dependent cut-off for the surface brightness. An image of this region was created, smoothed with a Gaussian kernel with a FWHM of 10″. A mask was created from these images, using the individual cut-off to exclude the brighter arcs. This mask was applied to the images and exposure maps of this observation.

The images of the individual observations where added, to create stacked images for the individual subbands (1–5), instruments (EPIC-pn, -MOS1, and -MOS2), and image types (images, oot-images, fwc-images and exposure maps). I added the subbands 1–4 (XID band) of all instruments and subtracted the OOT and FWC images. This image was used to estimate the statistics at each position, to define a smoothing template with `asmooth`. The smoothing was calculated adaptively, such that regions with high statistics are less smoothed. E. g. a bright source is smoothed with a minimum of 10″ (FWHM), whereas photons of diffuse emission are smoothed with a wider kernel. Also in the deep field around 1E0102.2-7219, the high statistics results in a minimal smoothing in the complete field. I calculated the smoothing template to produce an image with an approximate signal to noise ratio of 5. Using this template, all stacked images were smoothed homogeneously. Individual smoothing templates according to the statistics in the individual bands would prohibit a comparison of these images.

The stacked and smoothed images were combined according to

$$I = \frac{I_{\mathrm{pn}} - I_{\mathrm{pn,oot}} - I_{\mathrm{pn,fwc}} + I_{\mathrm{m1}} - I_{\mathrm{m1,fwc}} + I_{\mathrm{m2}} - I_{\mathrm{m2,fwc}}}{E_{\mathrm{pn}} + f_{\mathrm{m1}} E_{\mathrm{m1}} + f_{\mathrm{m2}} E_{\mathrm{m2}}} \tag{3.7}$$

The exposure maps of EPIC-MOS were weighted with a factor of $f_{\mathrm{m1}} = f_{\mathrm{m2}} = 0.4$ relative to EPIC-pn ($f_{\mathrm{pn}} = 1$) to account for the lower effective area. Finally, I applied a mask, to assure that the combined exposure is above 7200 s, which corresponds to an exposure time of 4000 s, if all three instruments are available.

The resulting image is presented in Figure C.2 in the appendix and reveals extended sources and diffuse emission.

3.3.15. Products for diffuse emission

For a spectral investigation of the diffuse emission of the SMC, I used the EPIC-pn data of full-frame and extended full-frame observations. This was motivated by two aspects: (i) The higher effective area of EPIC-pn is more suited to measure the faint diffuse emission component of the SMC, although the energy resolution of EPIC-MOS is higher. Further, EPIC-pn is more stable, improving the background estimation. (ii) Only few studies of diffuse X-ray emission are based on EPIC-pn. Also, the XMM-*Newton* Extended Source Analysis Software was initially developed for EPIC-MOS and the EPIC-pn tasks are still preliminary. The analysis of the EPIC-pn data will provide new insight for the EPIC-pn background behaviour.

For spectral reduction, single-pixel events were selected from EPIC-pn in the (0.2−12.0) keV band with `FLAG=0`. I used the *sigma-clipping GTIs* to reduce soft-proton contamination as far as possible. Regions of point sources were excluded down to a 10% contribution of the PSF brightness. As input, I used the detection list of the individual observation (Sec. 3.3.4). To further reduce the contribution of X-ray point sources that were not detected in the individual observation but in another observation of the same field, I also excluded all positions of the point-source catalogue with a radius of 15″. To exclude SNRs and ClGs, additional extended regions were defined manually, based on the mosaic image (Sec. 3.3.14). For each observation, I created an image of the resulting selection, which was screened for any kind of feature. If necessary, additional regions were removed from this individual observation. In this way, I account for single reflections of SMC X-1, the OOT-event stripes of the brightest sources, and sources and hot pixels, missed by the pipeline processing.

To test for variable background contamination, e. g. caused by SWCX, I created light curves for each observation in the (0.4−0.8) keV, (2.0−7.0) keV, and (7.0−15.0) keV band. Here I did not find any indication of variability, that is left after the temporal screening.

Spectra were extracted for the complete FoV of each observation. To have a higher spatial resolution, I defined a grid of box-shaped regions spanning the whole *main field*. I used a box size of approximately $0.15^\circ \times 0.15^\circ$, which is a compromise to have sufficient counts in each box, but to avoid strong variations of the diffuse X-ray emission or the H I column density within the boxes. As the boxes are defined for equatorial coordinates (RA and Dec), the box size in right ascension is slightly varying, depending on the declination.

To account for the contribution of OOT events, I created spectra with the same selection from the OOT event file. Since these spectra contain events from different types of sources, it is not straight forward to model these spectra. As their contribution is only a few percent and as the spectral shape is well determined from the OOT event file, they can be subtracted from the spectrum of the diffuse emission, after scaling the OOT spectrum with f_{oot}.

Analogously, spectra from the merged FWC eventfile have been extracted. These spectra were used to constrain a model for the detector background. A direct subtraction of the FWC spectra from the diffuse-emission spectra would not account for temporal variations in the detector background.

Spectra were only used, if they contain more than 1000 counts. All spectra were binned to have a signal to noise ratio of at least 6 for each bin. I decided to calculate individual response matrices for each observation and field, rather than adding all events in a field into an average spectrum and using some average response. This was motivated by two facts. (i) The archival observations of the SMC were done in different filter and science modes. An average response would not account for this. (ii) To account for different vignetting of individual observations, a weighting of the events would be necessary before creating the spectra. In this way, also events of detector background would be weighted, although these are not affected by vignetting.

The responses were calculated, using detector maps, to average the response over the used detector area. The size of the extraction region was calculated with `backscal`, taking into account CCD gaps, bad pixels, parts outside the FoV, and excluded regions. I assured, that these corrections are not included in the ARF.

3.3.16. Finding charts for detected sources

For each X-ray source, I created $\sim 3' \times 3'$ finding charts, using the publicly available *R*-band images of the Digitized Sky Surveys 2. These are useful to inspect identifications and for follow-up observations. The recently published mosaic image of the *Spitzer* survey of the SMC (Gordon et al. 2011) allowed the creation of IR finding charts, which can be used to identify the counterparts of AGN.

4. The point-source population in the SMC field

In this Chapter, the XMM-*Newton* point-source catalogue of the SMC is described and its statistical properties are discussed. The cross-correlation with other catalogues and the classification of sources is presented. This study has been submitted to A&A (Sturm et al. 2012a). The catalogue will be provided to the community via CDS[1].

4.1. Catalogue description and characterisation

The catalogue contains a total of 3053 X-ray sources based on 5236 detections, either from the large-programme SMC survey between May 2009 and March 2010 or in re-analysed archival observations between April 2000 and April 2010, publicly available in April 2010. For 927 sources, detections at different epochs are available. Some SMC fields were observed up to 36 times.

4.1.1. Description

The source catalogue contains the following information:
(1) = unique source id;
(2) = XMM name;
(3) = number of detections of the source;
(4) = number of observations of the source;
(5) = combined maximum detection likelihood normalized for two degrees of freedom;
(6-7) = J2000 coordinates in degrees;
(8) = position uncertainty for 1σ confidence (99.7% of all true sources positions are expected within a radius of 3.439σ);
(9-22) = averaged fluxes and uncertainties in the five standard bands, in the combined band (0.2−12.0) keV and the XID band (0.2−4.5) keV, all in erg cm^{-2} s^{-1};
(23-24) = maximum of all detected fluxes of this source in the XID band in erg cm^{-2} s^{-1} and the corresponding uncertainties;
(25-26) = minimum or upper limit of all detected fluxes (as described in Sec. 3.3.11) in the XID band in erg cm^{-2} s^{-1};
(27-34) = hardness ratios between the standard bands and corresponding uncertainties;
(35-37) = averaged source extension, corresponding uncertainty and likelihood of extent;
(38) = KS-test probability Cst, that the source was constant in all observations (the minimum value of all detections is taken, corresponding to the highest observed variability);
(39-40) = source variability V between individual observations and corresponding significance S;
(41) = source classification;
(42) = name of identified sources.
Additional parameters for instrumental setup of the individual observations are listed in Table B.2.

[1]Centre de Données astronomiques de Strasbourg, http://cdsweb.u-strasbg.fr/

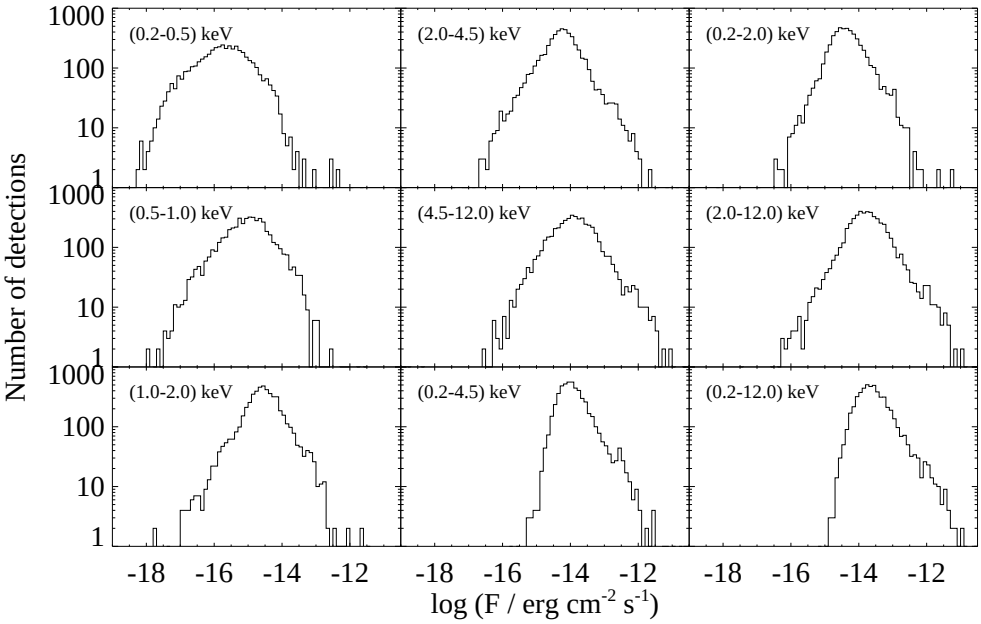

Figure 4.1. Flux distribution of individual detections in various energy bands. The source detection was performed simultaneously in the individual subbands, causing a wider flux distribution in the subbands than in the total band.

4.1.2. Completeness, confusion, and spurious detections

In Figure 4.1, the flux distribution of all individual source detections in several energy bands is presented. In the (0.2−4.5) keV and (0.2−12.0) keV band, we see a decreasing number density for fluxes lower than 10^{-14}erg cm^{-2} s^{-1} and $\sim 2\times10^{-14}$erg cm^{-2} s^{-1}. Thus we estimate the average detection threshold of the catalogue for sources in the SMC to be $\sim 5\times10^{33}$ erg s^{-1} and 10^{34} erg s^{-1}, respectively. However, the inhomogeneous exposure time of the individual observations must be considered.

In the field around the calibration source 1E0102.2-7219, we can compare the catalogue with a deep XMM-*Newton* mosaic image (Figure 4.2, left). Sources from the catalogue are overplotted with circles of 3.4σ radii. Detections of 1E0102.2-7219 were screened, due to the high extent of this SNR. It is usually fitted with ∼5 sources. Other examples of identified sources (see Sec. 4.3) in the field are an AGN (№ 53), a HMXB (№ 227), a Wolf-Rayet star in the SMC (№ 1212), a Galactic star (№ 231), a SSS candidate (№ 235), and a cluster of galaxies (ClG, № 1174). Sources that are not clearly visible in the mosaic image can be caused by weak variable sources. Also, spurious detections in this field accumulate from 28 observations, since for each observation an independent source detection was performed. From the estimated number of spurious detections (see below) we expect ∼7 spurious sources in this image. A few additional sources appear in the deep mosaic image that are not listed in the catalogue, e. g. two sources left of № 251. The flux of these sources is below the detection limit of individual observations.

Since *Chandra* performs similar calibration observations of 1E0102.2-7219, we compare the XMM-*Newton* catalogue with a deep *Chandra* ACIS image (Figure 4.2, right). It was created by merging 107 observations with the CIAO (version 4.3) task `merge_all` and adaptively smoothed. The exposure time is ∼920 ks decreasing with distance to 1E0102.2-7219, as the outer fields are not covered in all calibration observations. XMM-*Newton* sources are overplotted with radii of 10″ in white and red for detection likelihoods of $ML_{\rm det} \geq 8$ and $ML_{\rm det} < 8$, respectively. We see that source confusion is

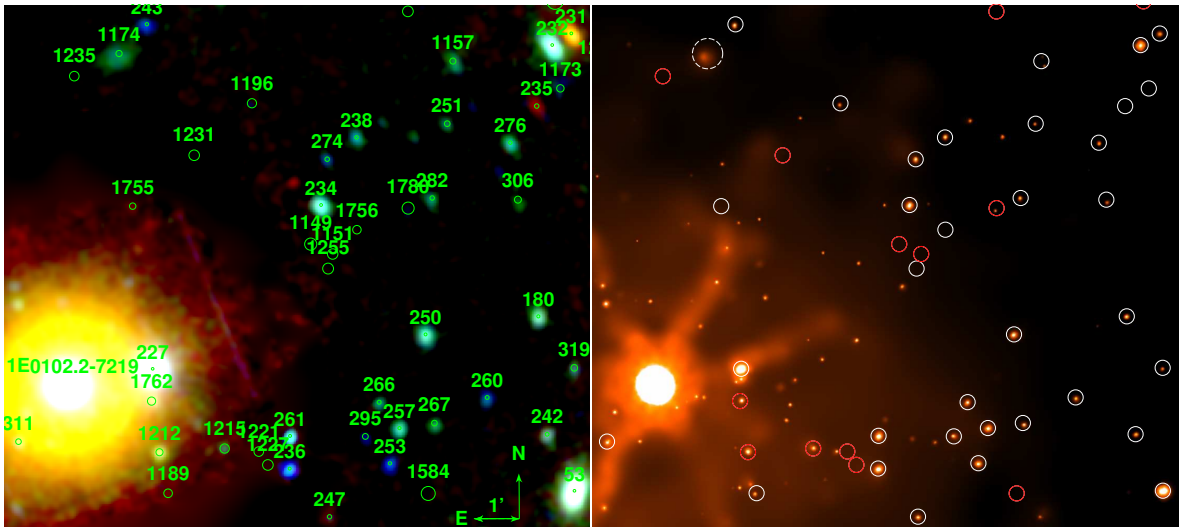

Figure 4.2. *Left:* XMM-*Newton* mosaic image of the deepest field in the SMC overplotted with the point-source catalogue. The image is background subtracted. Colours (red/green/blue) give logarithmically scaled intensities in the (0.2–1.0)/(1.0–2.0)/(2.0–4.5) keV bands. The brightest source is the oxygen-rich SNR 1E0102.2-7219. *Right:* Comparison with a deep *Chandra* image of the same region. The false-colour image gives logarithmically scaled intensities in the (0.2–10.0) keV band. Sources with low detection likelihood ($ML_{\rm det} < 8$) are plotted in red, others in white.

only relevant near the brightest sources (cf. the surrounding of 1E0102.2-7219) and in some rare cases of close-by sources (e. g. source № 1157 might consist of two weak sources seen by *Chandra*). Source № 1174 is extended in the *Chandra* image further supporting the ClG classification. We see that most sources with $ML_{\rm det} \geq 8$ are clearly visible in the *Chandra* image. № 235 is not found, due the the very soft spectrum and time variability (see Sec. 5.2). For sources with $ML_{\rm det} < 8$, a corresponding source in the *Chandra* image is not always obvious.

To quantify spurious detections, I compared the XMM-*Newton* catalogue with two deep *Chandra* SMC fields, where source lists are available (Laycock et al. 2010). All XMM-*Newton* sources, which were detected more than once or have a detection likelihood of $ML \gtrsim 8$ are also listed in the *Chandra* catalogue. Only 3 of 12 XMM-*Newton* sources with $ML_{\rm det} < 8$ and one source with $ML_{\rm det} = 8.2$ were not detected by *Chandra*. Some non-detections might be due to variability and the lower effective area of *Chandra* at highest and lowest energies, but in general, as for the 2XMM catalogue, a fraction of detections with $ML_{\rm det} < 8$ is expected to be spurious and should be regarded with care. In total, the XMM-*Newton* catalogue contains 418 sources with $ML_{\rm det} < 8$. From the former comparison, we roughly estimate around one hundred spurious detections among those, i. e. about one per observation.

4.1.3. Accuracy of source parameters

The angular separation of identified sources before and after the astrometric correction (Sec. 3.3.7) is presented in Figure 4.3a. The median of the total position uncertainty of all source positions is 1.3″. In Figure 4.3b, the distribution of angular separation r scaled by the total uncertainty $\sigma = (\sigma_{\rm sys}^2 + \sigma_{\rm sta}^2 + \sigma_{\rm ref}^2)^{1/2}$ is shown, where $\sigma_{\rm ref}$ is the position uncertainty of the reference source. The blue line shows the expected distribution according to a Rayleigh probability density function:

$$f(r,\sigma) = \frac{r}{\sigma^2} \exp\left(-\frac{r^2}{2\sigma^2}\right) \tag{4.1}$$

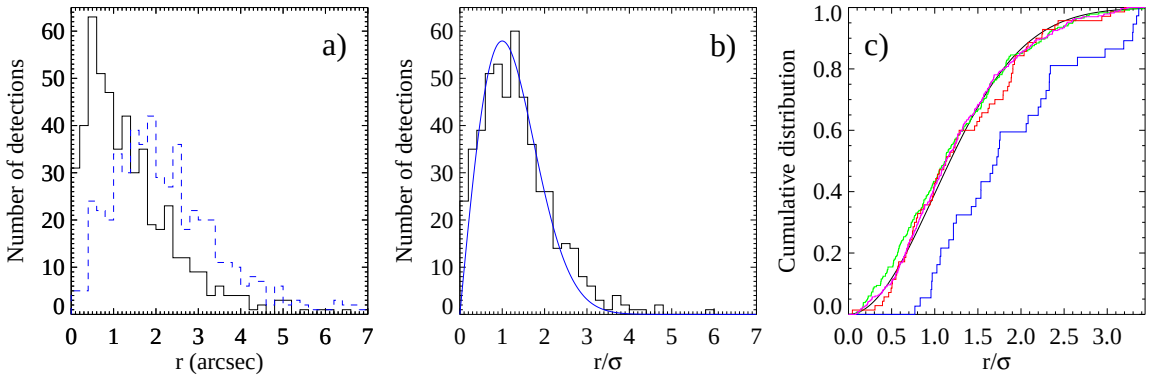

Figure 4.3. (a) Angular separation of X-ray and reference position of identified sources before (dashed blue line) and after (solid black line) bore-sight correction. (b) Distribution of r/σ, compared with a Rayleigh distribution (blue line). (c) Cumulative distribution of angular separation between the XMM-*Newton* SMC catalogue and the *Chandra* catalogues of McGowan et al. (2008) in green, Laycock et al. (2010) in red, Nazé et al. (2003) in blue, and Evans et al. (2010) in orange. The cumulative Rayleigh distribution is shown by the black line.

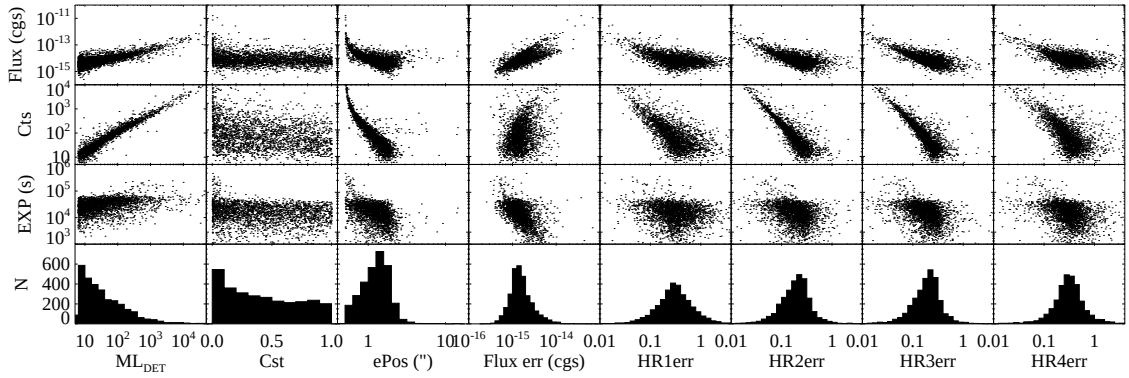

Figure 4.4. Dependence of detection maximum likelihood $ML_{\rm det}$, probability for time constancy Cst and uncertainty of position ePos, flux in the (0.2–4.5) keV band and hardness ratios HR on flux, counts, exposure, and number of sources.

The comparison justifies the estimation of the systematic error of $\sigma_{\rm sys} = 0.5''$. Since the same sample was used to determine the boresight corrections, some deviations from the Rayleigh distribution are expected. For example, for all observations containing only one identified source, the angular separation will be reduced to 0 due to the boresight shift.

To further test the positional accuracies with a statistically independent sample, we compared the final catalogue with available *Chandra* catalogues. These are close to a one-to-one correlation with a negligible number of chance coincidences (see Sec. 4.2 and Table 4.1). Sources, that have been used for boresight correction were excluded from this comparison. In Figure 4.3c, the cumulative distribution yields a good agreement with the *Chandra* wing survey (McGowan et al. 2008), the deep fields of Laycock et al. (2010), and the *Chandra* source catalogue (Evans et al. 2010) with KS-test statistics of 22%, 47%, and 77%, respectively. Only for the deep field of Nazé et al. (2003), an unexpected distribution of angular separations is found, with a KS-test statistic of 0.097%. In a further investigation, I found a systematic offset of the *Chandra* positions relative to the XMM-*Newton* positions by ∼1.7″. The offset is also evident when comparing the *Chandra* coordinates to the Tycho-2 position of HD 5980 and the MCPS positions of SXP 152 and SXP 304. This suggests

that the coordinates of these *Chandra* sources are wrong by a systematic offset.

An overview of the distribution of source parameter uncertainties and probabilities for existence $ML_{\rm det}$ and constancy Cst as well as their dependence on observational parameters is shown in Figure 4.4. The number of counts is the main quantity on which they depend. For 2378 and 2635 sources, the detection maximum likelihood is $ML_{\rm det} > 10$ and >8, respectively. The relative uncertainties of fluxes in the (0.2−4.5) keV band have a median of 22%. For the uncertainties of the hardness ratios 1 to 4, the medians are of 0.30, 0.20, 0.20, and 0.31, respectively.

4.2. Cross-correlation with other catalogues

To classify and identify individual sources, I correlated the boresight-corrected positions of the XMM-*Newton* SMC point-source catalogue with publicly available catalogues. The correlations with X-ray catalogues from previous studies allows to study the evolution of X-ray luminosity with time. Other wavelength catalogues add ancillary information, enabling a multi-frequency analysis. The catalogues used are listed in Table 4.1 together with statistical properties of the correlations. The result of all correlations were loaded into the database and are accessible by the web interface.

4.2.1. Selection of counterparts

The uncertainties of the XMM-*Newton* source coordinates are radially symmetric, as it is the case for most of the other catalogues. For some catalogues with higher positional accuracy, elliptical errors are given (e. g. 2MASS). Since here the XMM-*Newton* positional uncertainty is dominant, I assumed radial symmetric uncertainties for all catalogues, for simplicity, and used the semi-major axis as the radius if elliptical errors are given. When confidence levels for the positional uncertainty are given, I recalculated the positional uncertainty of the reference catalogue $\sigma_{\rm ref}$ for 1σ confidence. In some cases, the uncertainties had to be estimated. Following Watson et al. (2009), I consider all correlations, having an angular separation of $d \leq 3.439 \times (\sigma^2_{\rm sys} + \sigma^2_{\rm sta} + \sigma^2_{\rm ref})^{1/2}$ as possible counterparts. This corresponds to a 3σ (99.73%) completeness when we assume a Rayleigh distribution (Equation 4.1). The resulting number of matched XMM-*Newton* and reference sources, $N_{\rm XMM}$ and $N_{\rm ref}$, is given in Table 4.1 for all correlated catalogues.

4.2.2. Estimation of chance correlations

Depending on the source density and positional uncertainty, the numbers of chance coincidences, $C_{\rm XMM}$ and $C_{\rm ref}$, has to be considered. These numbers were estimated by shifting one catalogue in right ascension and declination by multiples of the maximal possible correlation distance between two sources in both catalogues and using the same correlation criterion as above. I performed several of these correlation runs to investigate variations of chance coincidences.

Examples for the dependence of the number of chance-correlations $C_{\rm XMM}$ on the shifting distance are given in Figure 4.5. In the case of the 2MASS catalogue, we see only a small systematic decrease with increasing offset that is negligible, compared to the standard deviations. If the coordinate shift becomes too large, a variable source-density can affect the number of correlations. This is the case for catalogues with inhomogeneously distributed sources e. g. due to the SMC morphology or a limited SMC-specific field of the catalogue. By investigating the dependence of the number of correlations on shifting distance, I found no significant variations on a scale of a few shifts, with the exception of the correlation with the Einstein catalogue. The variations found for the Einstein catalogue are caused by relatively large positional uncertainties that require a large coordinate shift.

Table 4.1. Reference catalogues used for cross-correlation.

Catalogue	Type	Ref.	$\sigma_{\rm ref}('')$	$N_{\rm cat}$[a]	$N_{\rm ref}$[b]	$N_{\rm XMM}$[c]	$C_{\rm ref}$[d]	$C_{\rm XMM}$[e]
Einstein	X-ray	1	40[f]	50	48	154	45.1±1.6	131±13
Einstein[g]	X-ray	1	40[f]	50	26	27	6.1±2.1	6.5±2.4
ROSAT PSPC	X-ray	2	10[i]	353	282	353	40.9±4.5	55.5±7.4
ROSAT PSPC[h]	X-ray	2	10[i]	353	236	264	15.3±4.0	17.9±4.6
ROSAT HRI	X-ray	3	2.6[i]	109	76	78	2.4±1.8	2.4±1.8
ASCA	X-ray	4	18.6[f]	83	69	111	33.1±4.2	42.5±6.1
Chandra wing Survey	X-ray	5	1.02[i]	393	242	240	2.3±1.6	2.3±1.5
Chandra deep fields	X-ray	6	0.66[i]	394	85	85	1.8±1.4	1.7±1.3
Chandra NGC 346	X-ray	7	0.30[i]	75	41	41	0.58±0.64	0.63±0.70
CSC (release 1.1)	X-ray	8	1.30[i]	496	368	373	8.2±2.4	9.4±3.4
MCPS	opt.	9	0.3	2872224	10484	2604	10082±75	2431±21
Tycho-2	opt.	10	0.078[i]	321	41	41	1.5±1.1	1.5±1.2
GSC (version 2.3.2)	opt.	11	0.43[i]	855524	3476	2099	3045±42	1752±20
2MASS	NIR	12	0.15[i]	159491	923	743	565±27	427±17
2MASX	NIR	12	4.4[i]	223	26	26	8.5±2.4	9.0±2.7
DENIS MC	NIR	13	0.47[i]	94357	609	540	364±19	303±15
DENIS (3rd release)	NIR	14	0.3	438517	2058	1043	1477±55	737±18
IRSF Sirius	NIR	15	0.1	1855973	8426	2407	6500±110	1914±22
S^3MC	IR	16	1, 3, 6[j]	400735	3403	1711	2193±40	1108±17
ATCA RCS	radio	17,18	1.0	301	31	31	1.6±1.2	1.6±1.2
SUMSS (version 2.1)	radio	19,20	3.0[i]	246	46	47	5.3±2.2	5.5±2.3
MA93	Hα	21	2.0[f]	1805	63	62	18.6±3.0	18.2±3.4
Murphy2000	Hα, [O III]	22	3.5, 4.4	286	12	12	7.4±2.6	7.3±2.7
2dF SMC	stars	23	0.5[f]	2874	31	31	8.8±3.4	8.7±3.4
6dF GS	galaxies	24	1.0[f]	16	6	6	0.04±0.20	0.04±0.20
Kozlowski2009	AGN	25	1.0[f]	655	146	148	3.9±2.2	3.8±2.1
Bica2008	star cluster	26	26.6[k]	409	41	45	29.0±6.1	32.1±6.6
Bonatto2010	star cluster	27	33.7[k]	75	11	14	7.8±2.9	9.4±3.2

Notes. [a] Number of reference-catalogue sources inside the XMM-*Newton* survey field. [b] Number of reference-catalogue sources matching at least one XMM-*Newton* source. [c] Number of XMM-*Newton* sources matching at least one reference-catalogue source. [d] Expected number of reference sources matched by chance. [e] Expected number of XMM-*Newton* sources matched by chance. [f] Value estimated. [g] Compared with a subset of XMM-*Newton* sources brighter than 5×10^{-14} erg cm^{-2} s^{-1}. [h] Compared with a subset of XMM-*Newton* sources brighter than 10^{-14} erg cm^{-2} s^{-1}. [i] Catalogue contains individual position uncertainties for each source, value gives the average of the used sample. [j] Uncertainty is 3″ for sources detected at 24 μm or higher, 6″ for sources detected at 70 μm only, 1″ otherwise. [k] This is the average of the semi-mayor axis extent.

References. (1) Wang & Wu (1992); (2) Haberl et al. (2000); (3) Sasaki et al. (2000); (4) Yokogawa et al. (2003); (5) McGowan et al. (2008); (6) Laycock et al. (2010); (7) Nazé et al. (2003); (8) Evans et al. (2010); (9) Zaritsky et al. (2002); (10) Høg et al. (2000); (11) Lasker et al. (2008); (12) Skrutskie et al. (2006); (13) Cioni et al. (2000); (14) DENIS Consortium (2005); (15) Kato et al. (2007); (16) Bolatto et al. (2007); (17) Filipović et al. (2002); (18) Payne et al. (2004); (19) Bock et al. (1999); (20) Mauch et al. (2003); (21) Meyssonnier & Azzopardi (1993); (22) Murphy & Bessell (2000); (23) Evans et al. (2004); (24) Jones et al. (2009); (25) Kozłowski & Kochanek (2009); (26) Table 3 of Bica et al. (2008); (27) Bonatto & Bica (2010).

In order to estimate the variation of the number of chance coincidences, I used 24 shifted correlations of a 5×5 grid. All these samples result from coordinate shifts between $d_{\max}$ and $\sqrt{8}d_{\max}$. Only the comparison with the Einstein catalogue was done with a 3×3 grid. The averaged numbers of chance coincidences for the XMM-*Newton* catalogue C_{XMM} and the reference catalogue C_{ref} are given in Table 4.1. Their uncertainties are estimated, using their standard deviation. By comparing these values with the number of real correlations, we can estimate the contribution of chance coincidences. The number of multiple coincidences can be estimated by comparing the number of matched sources in the XMM-*Newton* catalogue N_{XMM} to the number of matched sources of the reference catalogues N_{ref}. E. g. the correlations with radio and *Chandra* X-ray catalogues are close to a one-to-one correlation, whereas for dense optical catalogues four times more reference sources are found than X-ray sources. In the case of the MCPS catalogue (Zaritsky et al. 2002), 74% of the matched XMM-*Newton* sources have more than one, and 53% have more than two counterparts.

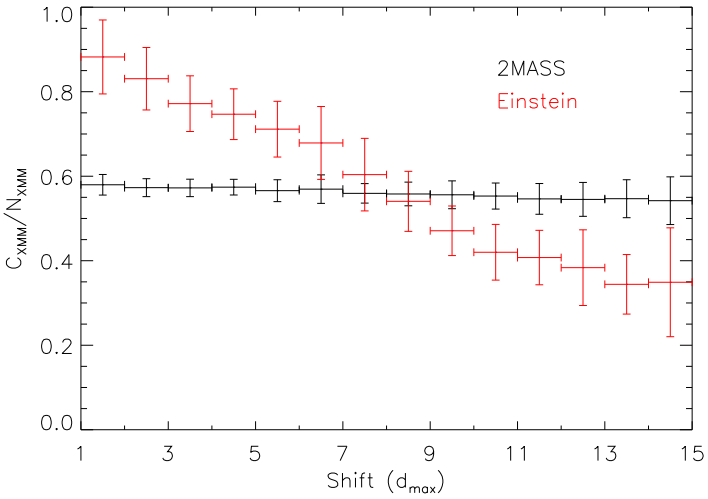

Figure 4.5. Examples for the chance-correlation dependence on offset. The data points are binned in units of maximal correlation distance ($d_{\max}$). For each bin, the average of chance-correlation C_{XMM} is given, normalised to the number of correlations N_{XMM} with unshifted coordinates. The error bars give the standard deviation for each bin.

4.2.3. Correlation with other X-ray catalogues

I correlated the XMM-*Newton* catalogue with X-ray catalogues from previous studies: From earlier epochs, I used X-ray sources detected with the Einstein observatory between 1979 and 1980 (Wang & Wu 1992), ROSAT sources from Haberl et al. (2000) and Sasaki et al. (2000) detected between 1990 and 1998, and ASCA sources from observations between 1993 and 2000 (Yokogawa et al. 2003). Due to the high positional uncertainties of the Einstein catalogue and the higher sensitivity of XMM-*Newton* the correlation is dominated by chance coincidences. Most Einstein sources cannot be assigned uniquely to an XMM-*Newton* source. A more unambiguous correlation can be achieved if a set of the brightest XMM-*Newton* sources with fluxes $> 5 \times 10^{-14}$ erg cm^{-2} s^{-1} is used. Similarly, one finds an improvement for the correlation with the ROSAT PSPC catalogue with a restriction to sources with fluxes $> 10^{-14}$ erg cm^{-2} s^{-1}. These results are also listed in Table 4.1.

Based on *Chandra* observations since 1999, there are several catalogues from the same era as the XMM-*Newton* data but covering only some part of the SMC main field: fields in the SMC wing (McGowan et al. 2008), deep fields in the SMC bar (Laycock et al. 2010), and sources around NGC 346 (Nazé et al. 2003). Additional sources were taken from the *Chandra* Source Catalogue (CSC, Evans et al. 2010). In general for comparable exposures, these catalogues offer more precise positions but

Table 4.2. Spectral classification of the X-ray source sample.

spectrum	classified	selection criteria
super soft	18	$(8HR_1 + 3HR_2 < -3$ or $(HR_1 < -0.75$ && HR_2 not def.)) && $F_1 > 3\Delta F_1$ && $F_3 < 3\Delta F_3$ && $F_4 < 3\Delta F_4$ && $F_5 < 3\Delta F_5$
soft	298	$8HR_2 + 3HR_3 < -3$ or $(HR_2 < -0.75$ && HR_3 not def.)
hard	2711	$(8HR_2 + 3HR_3 > -3$ or $(HR_2 > 0$&&HR_3 not def.)) && not super soft
ultra hard	945	$8HR_3 + 3HR_4 > -1.4$ or $(HR_3 > 0.2$&&HR_4 not def.) && not soft && not super soft
unclass.	8	–

have fewer counts per detection compared to XMM-*Newton* detections. The correlation between the XMM-*Newton* and *Chandra* sources is close to a one-to-one correlation with less then 2% of chance coincidences.

4.2.4. Correlation with catalogues at other wavelength

For the determination of optical counterparts I used the MCPS catalogue (Zaritsky et al. 2002), providing stellar photometry in *U*, *B*, *V* and *I* down to magnitudes of ~20–22 mag. Due to the high source density compared to the XMM-*Newton* resolution, the cross-correlation is dominated by chance coincidences. To identify bright foreground stars, which are not listed in the MCPS, I used the Tycho-2 catalogue (Høg et al. 2000), which has a completeness of 99% for $V \sim 11.0$ mag and provides proper motions and B_T and V_T magnitudes. Since the MCPS does not cover all parts of the XMM-*Newton* field and some stars around $V \sim 12$ mag are too faint for the Tycho-2 catalogue but too bright for the MCPS, I used the Guide Star Catalogue (GSC, Lasker et al. 2008) in these cases, which gives B_J and R_F magnitudes down to ~21 mag. For 129 X-ray sources, which do not have a counterpart in either of the MCPS and Tycho-2 catalogues, I found a counterpart in the GSC.

Near-infrared sources in *J*, *H*, and K_S were taken from the Two Micron All Sky Survey (2MASS, Skrutskie et al. 2006), the Deep Near Infrared Survey (DENIS, Cioni et al. 2000; DENIS Consortium 2005), and the IRSF Sirius catalogue of Kato et al. (2007). Since these catalogues contain measurements from different epochs, they allow to estimate the NIR variability of X-ray sources, which is especially interesting for HMXBs.

Infrared fluxes at 3.6, 4.5, 5.8, 8.0, 24, and 70 μm are taken from the *Spitzer* Survey of the SMC (S^3MC, Bolatto et al. 2007). Radio sources were taken from the ATCA radio-continuum study (Payne et al. 2004; Filipović et al. 2002), with ATCA radio point-source flux densities at 1.42, 2.37, 4.80, and 8.64 GHz, and from the Sydney University Molonglo Sky Survey at 843 MHz (SUMSS, Mauch et al. 2003). These correlations enable a classification of background sources.

Furthermore, I compared the XMM-*Newton* sources with some individual catalogues providing emission-line sources (Meyssonnier & Azzopardi 1993; Murphy & Bessell 2000), stellar classification (Evans et al. 2004), galaxies confirmed by redshift measurements (Jones et al. 2009), and IR selected AGN candidates (Kozłowski & Kochanek 2009). For the correlation with the catalogues of star clusters (Bica et al. 2008; Bonatto & Bica 2010), I used the semi-major axis of the cluster extent as a 3σ uncertainty for the reference position.

4.3. Source identification and classification

Besides X-ray sources within the SMC, the observed field contains Galactic X-ray sources and background objects behind the SMC. To distinguish between these, I identified and classified individual

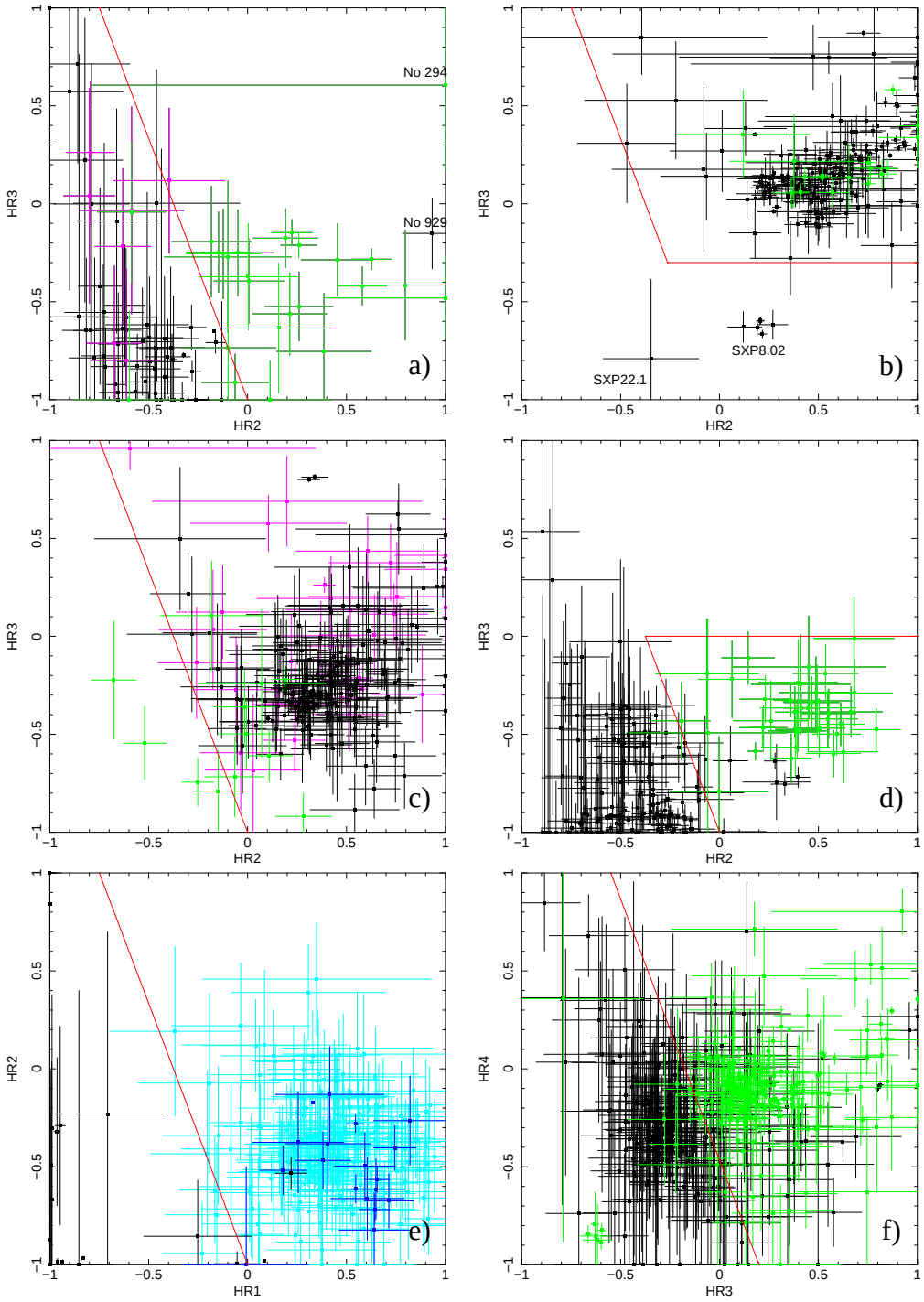

Figure 4.6. Hardness-ratio diagrams for XMM-*Newton* detections. Red lines show HR-selection cuts as used for source classification. [(a)] Detections with optical counterparts in the Tycho-2 catalogue. Galactic stars are shown in black and magenta, SMC-stars in green. Details are given in Sec. 4.3.1. [(b)] Detections of known pulsars (black) and identified HMXBs (green). See Sec. 4.3.3. [(c)] Detections of spectroscopically confirmed AGN (black), radio background sources (magenta) and galaxies (green). See Sec. 4.3.4. [(d)] Detections of sources, screened due to their extent. SNRs are shown in black, other sources in green. See Sec. 4.3.6. [(e)] Comparison of detected SSSs in the SMC and LMC (black) with identified (blue) and classified (cyan) stars in the HR_1-HR_2-plane. See Sec. 4.3.2. [(f)] Comparison of AGN and radio sources from c) (black) with pulsars and HMXBs from b) (green) in the HR_3-HR_4-plane. See Sec. 4.3.3.

Table 4.3. Source classification criteria.

class	classification criteria	identified	classified
ClG	hard && HR_3<0 && Ext>ΔExt && $ML_{\rm Ext}$>10	12[(a)]	13
SSS	super soft && no opt. loading && $ML_{\rm det} > 10$ && ($N_{\rm det} > 1$ or ($ML_{\rm pn} > 4$ && ($ML_{\rm m1} > 2$ or $ML_{\rm m2} > 2$)))	4	8
fg-star	soft && $\log(f_X/f_o) < -1$ && ($B-V > 1.2$ or ($B-V > 0.3$&&$V > 17$))	34	128
AGN	hard && appropriate radio (r), infra red (i), X-ray (x) or optical (o) counterpart	72	2106
HMXB	ultra hard && $13.5 < V < 17.0$ && $-0.5 < B-V < 0.5$ && $-1.5 < U-B < -0.2$ && no AGN id	49	45

Notes. Sixteen additional sources were identified with other source classes. 581 sources are unclassified. [(a)] Not in this catalogue, see Table 3 of Haberl et al. (2012a).

sources. For identification, I searched the literature as described below and selected secure cases only.

Unidentified sources were classified following the M 33 investigation of Pietsch et al. (2004). However, different properties of the SMC and the larger sample size of the SMC catalogue required a modification of the classification criteria that I developed with an empirical approach. Classification criteria were derived from the parameters of individual detections of identified sources as seen with XMM-*Newton* with the applied processing. The usage of individual detections, instead of averaged source values, increases the statistics, accounts for spectral variability and was chosen, since ~70% of the XMM-*Newton* sources were only detected once. Classifications are marked by angle brackets (<*class*>). I note, that classes give likely origins for the X-ray emission, but have to be regarded with care.

First, I distinguished between point sources and sources fitted with small, but significant, extent. Most of these sources were classified as clusters of galaxies (<ClG>, see Sec. 4.3.6 and Table 4.7). Sources with extent too large to be modelled properly by `emldetect` as one single source (e. g. SNRs with substructure), were flagged beforehand and were not included in the final catalogue. An overview of these sources can be found in Haberl et al. (2012a). The example for a new SNR candidate is given in Sec. 5.4.

The remaining point sources were classified, using X-ray hardness ratios and multi-wavelength properties. Using the selection criteria given in Table 4.2, I divided the sample in super-soft, soft, hard, and ultra-hard sources. I selected super-soft X-ray sources first. They are classified only, if detector noise as origin is unlikely. Soft X-ray sources are classified as foreground stars if they have an appropriately bright optical counterpart that is unlikely to be within the SMC on the basis of its colours. Also depending on the counterpart, hard X-ray sources were classified as AGN or HMXB. An overview of the classification criteria and results is presented in Table 4.3. The hardness ratios of identified sources are compared in Figure 4.6. Details for each source class are given in the following.

4.3.1. X-rays from non-degenerate stars

Shocks in the wind of OB stars, coronal activity from F to M stars, accretion processes in T Tau stars and interaction of close-binary stars can cause X-ray emission from non-degenerate stars (see Sec. 2.4.2). Because stars are weak X-ray sources, most stars in the SMC are below the sensitivity limit of the survey. Galactic stars are foreground sources, which are expected to be homogeneously distributed in the XMM-*Newton* SMC field. Compared to more distant Local-Group galaxies, the identification of Galactic stars in front of the SMC is challenging, because luminous SMC stars and faint Galactic stars can have a similar brightness.

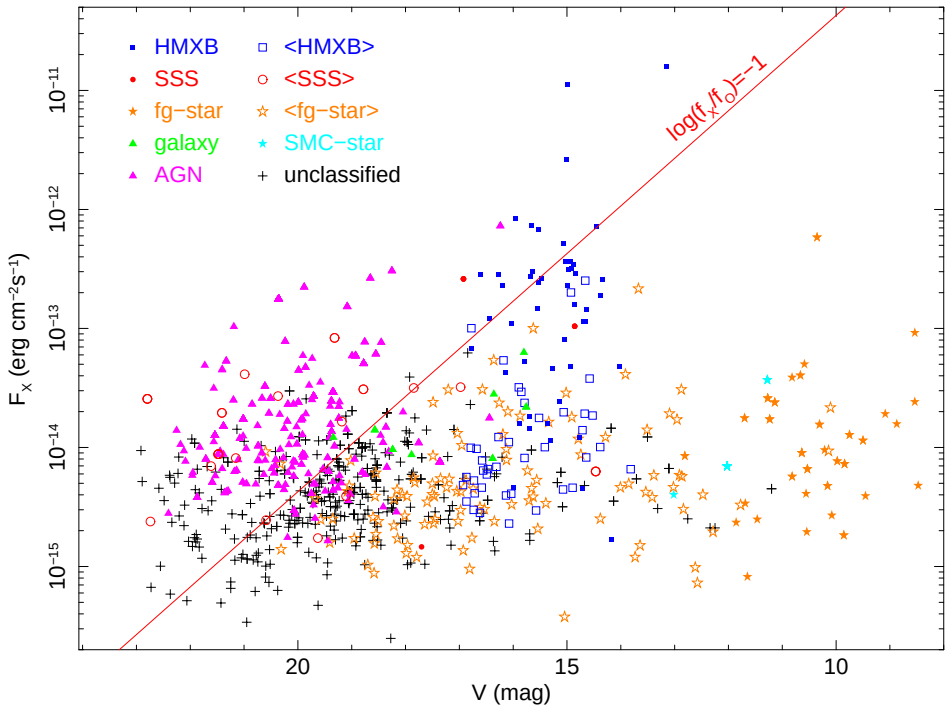

Figure 4.7. Optical *V*-band magnitude vs. the detected X-ray flux in the (0.2–4.5) keV band. For foreground stars, the brightest counterpart is plotted. For HMXB we selected the counterparts as in Sec. 4.3.3. For all other sources, the nearest optical counterpart is plotted.

Identification of Galactic stars

To identify the brightest ($V < 11$ mag) foreground stars, I used the correlation with the Tycho-2 catalogue, where we expect one or two chance coincidences. 40 individual X-ray sources with a Tycho-2 counterpart resulting in 84 XMM-Newton detections with determined HR_2 and HR_3 are plotted in Figure 4.6a. One additional X-ray source has $HR_2 \leq -0.9$, but an undetermined HR_3. This holds also for three detections of the previous 40 sources.

There are 33 Tycho-2 sources with significant (>3σ) proper motions that are all >8 mas yr^{-1}. These are obviously foreground stars (fg-star). Two more counterparts are stars with a late-type main-sequence classification (Wright et al. 2003). X-ray detections of these 35 confirmed foreground stars are plotted in black in Figure 4.6a. Twenty-five detections of three Tycho-2 sources, correlating with SMC-stars (see Sec. 4.3.1), are plotted in green. The remaining three matches (№ 140, 2008, and 2158) were classified as candidates for Galactic stars (<fg-star>, plotted in magenta). Source № 929 shows harder X-ray colours than the remaining foreground stars and is therefore not classified. The optical and X-ray emission might correlate by chance, but also a foreground CV is possible.

Classification of Galactic stars

To classify an X-ray source as foreground star candidate (<fg-star>), I demand four criteria:

(i) Using the Tycho-2 set of 35 confirmed foreground stars, I defined a cut (red line in Figure 4.6a) for the X-ray colour selection of fg-star candidates, which separates them from hard X-ray sources, such as AGN and HMXBs (see below and cf. Figure 4.6b and c). For faint soft sources with a low HR_2 value, the count rate R_4 will not be well determined, leading to an unconstrained HR_3. The selection

allows a less precise determined HR_3 for sources with lower HR_2. From similar source samples, a correlation between X-ray plasma temperature and spectral type is not found (Wright et al. 2010). Therefore, a bias in the selection method is not expected, although the selection criteria on X-ray hardness ratios are defined using the Tycho-2 catalogue that contains only the brightest stars in the *B* and *V* bands. The catalogue contains 258 unidentified soft X-ray sources.

(ii) For stars with fainter optical magnitudes, it becomes more complicated to discriminate between stars in the Galaxy and the SMC. In addition to soft X-ray colours, the source must have a sufficiently bright optical counterpart. Following Maccacaro et al. (1988), I calculated

$$\log(f_X/f_o) = \log(F_{(0.2-4.5)\mathrm{keV}}) + \frac{V}{2.5} + 5.37 \tag{4.2}$$

for the MCPS counterparts and

$$\log(f_X/f_o) = \log(F_{(0.2-4.5)\mathrm{keV}}) + \frac{R+B}{2\times 2.5} + 5.37 \tag{4.3}$$

for GSC counterparts, where the X-ray flux is in units of erg cm^{-2} s^{-1}. Sources are classified as foreground-star candidates only, if they have an optical counterpart with $\log(f_X/f_o) < -1$. 197 of the 258 sources have a sufficiently bright optical counterpart in the MCPS. The dependence of X-ray flux on optical *V* magnitude is plotted in Figure 4.7. For most foreground stars one expects to find an optical counterpart with the given sensitivity of the MCPS.

(iii) Since true optical counterparts are still outnumbered by chance correlations with stars of the SMC, I used a colour selection to exclude most of them. The colour-magnitude and colour-colour diagram of all possible optical counterparts of X-ray sources with measured *U*, *V*, and *B* magnitudes in the MCPS (black points) is shown in Figure 4.8. To avoid main-sequence and horizontal-branch stars of the SMC, I only selected optical counterparts to the right of the blue dashed line, which have $V < 17$ mag and $B-V > 0.3$ mag or $B-V > 1.2$ mag without any magnitude selection. This reduces the fg-star sample to 107 sources.

For source №548, one finds a Tycho-2 colour of $B-V = -0.38$ mag, which would suggest an early-type star. However, this source is identified with the Galactic star Dachs SMC 3-2 and other catalogues give $B-V = 0.70$ mag (e. g. Massey 2002). The Tycho-2 colour is regarded as outlier and corrected with the magnitudes of Massey (2002) for Figure 4.8.

(iv) To avoid random correlations, I did not classify X-ray sources with a positional uncertainty of more than 3″ (4 sources).

This allows to classify 103 candidates for foreground stars. To estimate the number of chance coincidences, I shifted the coordinates of one catalogue. For 25.5±4.9 of the 249 unidentified soft X-ray sources with $ePos < 3''$ one finds at least one counterpart compatible with the selection criteria for stars by chance. Taking into account that some true correlations cause chance correlation when their coordinates are shifted,

$$N_{\mathrm{true}} = \frac{N_{\mathrm{correlations}} - N_{\mathrm{chance}}}{1 - \frac{N_{\mathrm{chance}}}{N_{\mathrm{total}}}} \tag{4.4}$$

we estimate that ∼(16.1±3.6)% of the classified foreground stars are chance coincidences. In addition, using the GSC in cases where the X-ray source did not have a counterpart in the Tycho-2 or MCPS catalogues, 17 X-ray sources were classified as foreground stars.

However, the X-ray emission of stars can become harder during flares (e. g. Güdel et al. 2004), so that the hardness-ratio selection criteria can be violated. Similarly, as the X-ray flux increases the f_X/f_o criteria might be violated. This causes some overlap with AGN in hardness ratios and f_X/f_o.

Table 4.4. Faint SSS candidates in the SMC.

No.	RA[(a)]	Dec[(a)]	ePos[(b)]	HR_1	HR_2	F[(c)]	$ML_{\rm det}$[(d)]	comment
235	01 01 47.58	-71 55 50.7	0.85	-0.3±0.1	-0.8±0.1	6.0±0.6	146.5	WD/Be?
1198	01 01 24.19	-72 00 37.9	1.82	-0.4±0.2	-1.0±0.5	2.5±0.7	16.2	
1531	00 39 45.58	-72 47 01.4	1.58	-1.0±0.1	0.8±0.4	1.8±0.4	28.6	star?
1549	00 38 58.74	-72 55 10.4	1.68	-1.0±0.2	–	3.6±0.9	18.3	star?
2132	00 57 45.29	-71 45 59.7	0.93	-0.4±0.1	-0.5±0.2	4.1±0.5	121.1	
2178	00 55 37.71	-72 03 14.0	0.74	-0.9±0.0	0.2±0.4	6.7±0.5	391.5	
2218	00 55 08.45	-71 58 26.7	1.38	-0.2±0.2	-0.9±0.4	1.3±0.3	14.0	WD/Be?, star?
3235	00 55 03.65	-73 38 04.1	0.64	-0.9±0.0	0.2±0.2	13.6±0.8	787.0	

Notes. [(a)] Sexagesimal coordinates in J2000. [(b)] Positional uncertainty in arcsec. [(c)] Detected flux in the (0.2–1.0) keV band in 10^{-15} erg cm^{-2} s^{-1}. [(d)] Source detection likelihood.

To investigate this possibility, I searched for sources with short-term variability $Cst < 0.5\%$ and $f_X/f_o < 0$. To exclude HMXBs and the bulk of AGNs, I also demanded $HR_2 < 0.2$ and $HR_3 < -0.3$. Five additional sources (№ 146, 1998, 2041, 2740, and 3059) were selected as candidates (<fg-star>).

For 61 stars, which have a 2MASS counterpart in the MCPS catalogue, Despina Hatzidimitriou derived a spectral classification from the $J-K$ colour (see Bonfini et al. 2009). The resulting distribution of the spectral types is shown in Figure 4.9 and follows the expected distribution, peaking around early M stars.

Stars within the SMC

In some extreme cases, X-ray emission from early-type stars within the SMC can be observed with XMM-*Newton*, e. g. from stellar-wind interaction of a Wolf-Rayet star in a binary system with an OB star. Guerrero & Chu (2008) found X-ray emission from SMC-WR5, SMC-WR6, and SMC-WR7 (Massey et al. 2003), which are the sources № 150, 237, and 1212 in the XMM-*Newton* catalogue (cyan stars in Figure 4.7 and Figure 4.8, left). № 1212 is visible in the images of Figure 4.2.

For completeness I note, that source № 145 is close to SMC-WR3, but due to a distance of 3.29″ (2.73σ), this correlation is doubtful. Also, sources № 294, 1031, and 2963 correlate formally with the SMC stars AzV 369 (4.6″, 3.1σ), AzV 222 (4.1″, 2.8σ), and 2dFS 3274 (1.8″, 1.0σ).

In the centre of the star-cluster NGC 346 we see an unresolved convolution of X-ray bright stars (see Nazé et al. 2002, 2004), which is source № 535 in the XMM-*Newton* catalogue. Source № 2706 has similar X-ray colours and correlates with the star-cluster Lindsay 66. Also № 294 can be associated with the star-cluster Bruck 125. From the correlation with the star-cluster catalogue of Bica et al. (2008), one expects around 13±6.6 X-ray sources to be correlated with star clusters. About half of these sources can be explained by HMXBs, which might have formed in these clusters (Coe 2005).

4.3.2. Super-soft X-ray sources

SSSs are a phenomenological class of X-ray sources, defined by a very soft thermal X-ray spectrum with no emission above 1 keV. Luminous SSSs are associated with CVs, planetary nebulae, symbiotic stars, and post-outburst optical novae. Less luminous SSSs can be observed in some CVs, cooling neutron stars and PG 1159 stars. For more details, see Sec. 2.4.6.

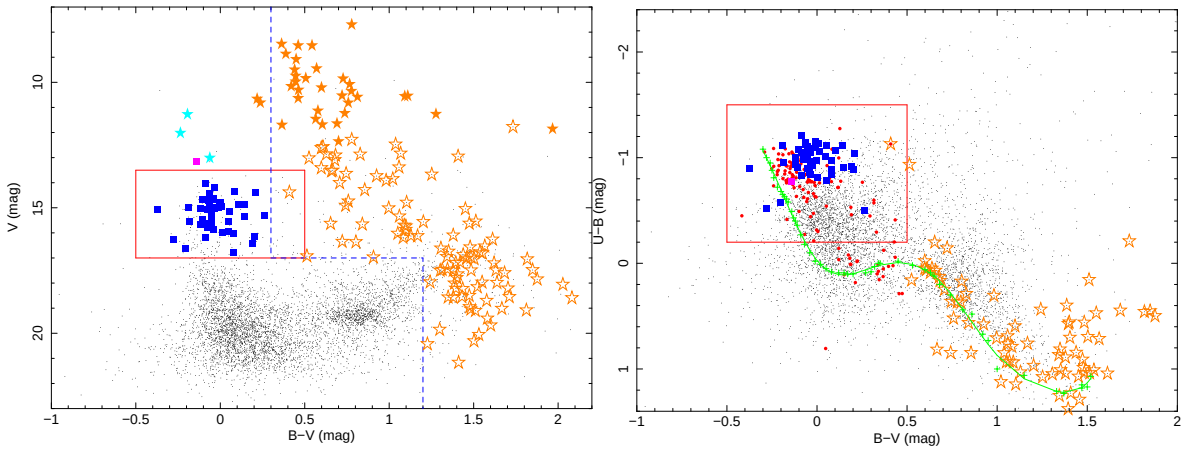

Figure 4.8. Colour-magnitude (*left*) and colour-colour (*right*) diagram. Black points show all possible optical counterparts of X-ray sources with measured U, V, and B magnitudes in the MCPS found inside the 3σ positional uncertainty. Counterparts for Galactic foreground star candidates were selected redwards of the blue dashed line only. The red boxes mark the selection region of counterparts for BeXRBs in both plots. Identified foreground stars (filled orange stars), classified foreground stars (open orange stars), identified BeXRBs (blue squares) are marked. WR stars in the SMC and SMC X-1 are shown by cyan stars and the magenta square. Red dots in the right diagram mark all sources (black dots) within the red box of the left diagram. The green line gives the colours for the unreddened main sequence according to Fitzgerald (1970).

Identification of super-soft X-ray sources

Two bright SSSs in the SMC, the planetary nebula SMP SMC 22 (№ 686) and the symbiotic nova SMC3 (№ 616), were observed during the survey (Mereghetti et al. 2010; Sturm et al. 2011b). In addition, Mereghetti et al. (2010) confirmed SMP SMC 25, that was discovered with ROSAT as a faint SSS by Kahabka et al. (1999), in the XMM-*Newton* survey data (№ 1858). Other SSSs known from ROSAT (RX J0059.1-7505, RX J0059.4-7118, RX J0050.5-7455), were previously observed with XMM-*Newton* (Kahabka & Haberl 2006). The first source is the symbiotic star LIN 358 (№ 1263), the second was discussed to be a close binary or isolated neutron star (№ 324), for the third source Kahabka & Haberl (2006) gave an upper limit. In the survey analysis, this last source is detected (№ 1384), but is most likely associated with the Galactic star TYC 9141-7087-1 and affected by optical loading. Other ROSAT sources from Kahabka & Pietsch (1996) are the transient SSS RX J0058.6-7146 and the candidate SSS RX J0103.8-7254. For neither a source in found in the XMM-*Newton* catalogue. The position of the variable SSS 1E 0035.4-7230 is not covered by any XMM-*Newton* observation yet. The position of the super-soft transient MAXI J0158-744 (Li et al. 2012) was not covered with XMM-*Newton*. New luminous SSS transients were not found during the XMM-*Newton* SMC survey.

Search for faint SSS candidates

The XMM-*Newton* survey enables a search for faint SSSs. Analogously to the division into soft and hard X-ray sources in Sec. 4.3.1, I separate super-soft from soft X-ray sources in the HR_1-HR_2-plane, as shown in Figure 4.6e. Detections of identified SSSs from Sec. 4.3.2, are plotted in black. To increase the reference sample, I also used detections of identified SSSs in the LMC (see Kahabka et al. 2008, and references therein), from an identical data processing as used for the SMC data. In general, HR_1 is negative for SSSs and depends strongly on photoelectric absorption. HR_2 is expected to be close to -1, but due to low count rates in the energy bands 2 and 3, HR_2 is only poorly determined

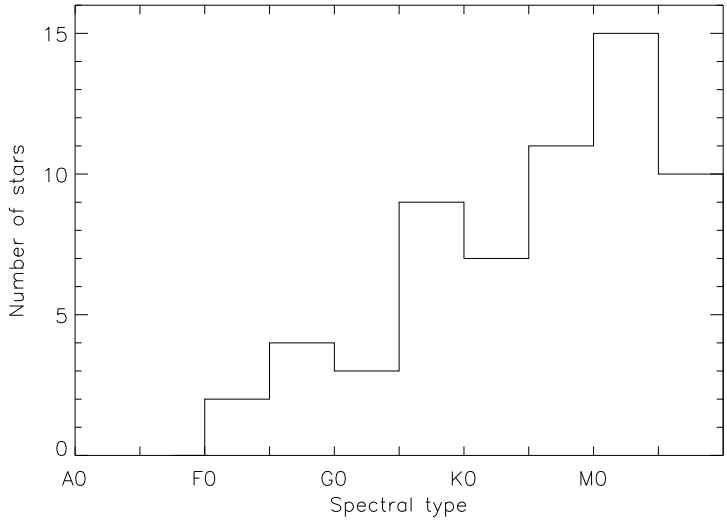

Figure 4.9. Distribution of spectral classes of X-ray emitting stars. Courtesy of Despina Hatzidimitriou.

for weak SSSs. I also demand no significant (<3σ) emission in the energy bands 3–5, but significant emission in the energy band 1, to designate the spectrum as super soft. The two LMC SSSs outside the selection area, are CAL 87 and RX J0507.1-6743, which are both affected by high absorption (Kahabka et al. 2008) causing a HR_1 of 0.087 ± 0.003 and 0.22 ± 0.08, respectively. Identified Tycho-2 stars (Sec. 4.3.1), which are not affected by optical loading are plotted in blue. In cyan, I show all sources, which fulfil the selection criteria for candidate foreground stars, have a detection likelihood of $ML_{\rm det} > 10$ and are not affected by optical loading. Three of these sources fulfil the selection criteria of both SSS and stars. Here a X-ray spectral analysis is necessary.

Unfortunately, optical loading and detector noise cause spurious detections with characteristics similar to SSS. EPIC-MOS is less sensitive below 500 eV by a factor of 6 compared to EPIC-pn (cf. Figure 2.4a). Therefore, I demanded a conservative total detection likelihood of $ML_{\rm det}$ >10 and rejected candidates affected by optical loading in EPIC-pn. Further, I required that the source has at least a slight detection in another instrument or observation. The selection procedure yielded a total of 8 candidate faint SSSs, which are listed in Table 4.4. Source №235 was analysed in more detail (Sec. 5.2) and is proposed to be a binary system consisting of a white dwarf and a Be star. Source №2218 may be another candidate, as it has a possible optical counterpart with a separation of 4.6″ (3.2σ) and with typical colours for B stars in the SMC (see Sec. 4.3.3).

Search for Be/WD candidates

The search criteria from above were optimised to find standard SSS with low absorption. However, a detailed analysis of the faint SSS candidate №235 (Sec. 5.2) shows that the source can be explained by absorbed SSS emission. In general, the lack of observed SSSs in Be systems might be explained by absorption in the decretion disc of the Be star (Apparao 1991). I studied the possibility of intermediate and strongly absorbed but more luminous Be/WD systems. Assuming a black-body model with kT = 100 eV (as found for №235, Sec. 5.2), one would expect hardness ratios of $HR_1 = 0.81$ and $HR_2 = -0.68$ for an absorbing column density of $N_{\rm H}^{\rm smc} = 10^{22}$ cm^{-2}.

I found 10 additional candidates, listed in Table 4.5, with $HR_2 + \Delta HR_2 < 0$ and correlating with an early-type SMC star from the MCPS (see Sec. 4.3.3). I used the same optical colour selection as derived for BeXRBs (see Sec. 4.3.3). Three of the counterparts are emission-line objects in the list

Table 4.5. Absorbed SSS candidates with possible early-type star counterpart in the SMC.

No	X-ray RA (J2000)	Dec (J2000)	ePos (″)	HR_1	HR_2	MCPS d (″)	U (mag)	B (mag)	V (mag)	MA93 d (″)	No	comment
235	01 01 47.6	-71 55 51	0.9	-0.3±0.1	-0.8±0.1	1.4	13.3	14.4	14.5	1.7	1284	SSS?
935	01 17 40.4	-73 30 51	1.3	0.6±0.2	-0.3±0.2	1.3	13.3	14.1	14.2	0.4	1845	HMXB
1219	01 05 16.1	-72 00 25	2.1	0.9±0.2	-1.0±0.1	5.2	14.9	15.8	16.0	–	–	–
1565	00 59 54.6	-72 15 31	1.8	1.0±0.2	-0.7±0.2	4.4	15.8	16.8	16.9	–	–	–
1702	00 49 13.5	-73 25 60	1.8	0.3±0.2	-0.7±0.2	0.8	14.6	15.4	15.4	–	–	–
1784	01 01 05.0	-72 04 44	3.3	0.3±0.2	-0.7±0.2	5.5	15.3	16.2	16.4	–	–	Gal. star?
1828	00 53 55.6	-72 26 44	2.1	0.7±0.3	-0.5±0.2	1.3	13.6	14.6	14.7	–	–	HMXB
1839	00 51 52.5	-72 31 48	1.6	0.5±0.2	-0.5±0.2	3.1	13.7	14.8	14.4	3.4	506	Gal. star?
2211	00 55 07.3	-72 08 26	1.7	-0.1±0.3	-0.6±0.3	3.9	16.0	16.8	16.9	–	–	HMXB?
2218	00 55 08.5	-71 58 27	1.4	-0.2±0.2	-0.9±0.4	4.6	14.2	15.2	15.4	–	–	–
2219	00 54 15.0	-72 14 43	3.4	1.0±0.5	-1.0±0.5	5.3	15.8	16.5	16.6	12.0	744	–

Notes. ePos: 1σ X-ray position uncertainty, including the systematic error. *HR*: X-ray hardness ratios. *d*: Angular distance to the counterpart from MCPS (Zaritsky et al. 2002) and MA93 (Meyssonnier & Azzopardi 1993).

of Meyssonnier & Azzopardi (1993). Using the same method as above, I estimate ~4.3 coincidences by chance. Since also stars fall into the X-ray selection criteria, the relative number of chance coincidences is higher, compared to the correlation with SSS candidates. Three sources correlate with known Be/NS systems, which apparently were detected in a relatively soft low-luminosity state.

4.3.3. High-mass X-ray binaries

The SMC hosts a remarkably large population of HMXBs. HMXBs have been introduced in Sec. 2.4.5. With the exception of SMC X-1 (SgXRB, source № 1) and SXP8.02 (anomalous X-ray pulsar, source № 48, Tiengo et al. 2008) all known X-ray pulsars in the SMC are presumably BeXRBs.

Search for SgXRB candidates

From the X-ray sources correlating with bright SMC stars (Sec. 4.3.1) only № 1031 might also be explainable by a supergiant HMXB from optical and X-ray colours. A search for supergiant systems resulted in no further candidate.

Identification of Be/X-ray binaries

We identified 49 HMXBs listed in literature (e. g. Haberl & Sasaki 2000; Galache et al. 2008). During the survey, two pulsars were newly discovered (Coe et al. 2011; Sturm et al. 2011a) as well as two further bright Be/X-ray binary transients (sources № 2732 and 3115, Coe et al. 2012). Although detected with XMM-*Newton*, the catalogue does not contain the source SXP11.5, since it was not observed in the nominal field of view and therefore not accessible to the processing (Townsend et al. 2011). The same holds for SXP1062, which was recently discovered in the outer wing of the SMC (Hénault-Brunet et al. 2012; Haberl et al. 2012b) after the data processing. All other pulsars with known position are within the main field. A detailed analysis of the observed Be/X-ray binary population will be discussed in a forthcoming study. The XMM-*Newton* catalogue contains 200 detections of 42 pulsars. X-ray pulsations confirm the neutron-star nature of the accreting object. Hardness ratios

for all X-ray pulsars are shown in Figure 4.6b in black. All other 17 detections of 8 HMXBs with unknown pulse period are plotted in green.

Search for Be/X-ray binary candidates

Sources are classified as HMXB candidates (<HMXB>), if they fulfil the following criteria:

(i) Because of the power-law-like X-ray spectrum with a typical photon index of $\Gamma \approx 1$ (Haberl & Pietsch 2004), HMXBs can easily be discriminated from soft X-ray sources, by using the same dividing line as in Figure 4.6a. In general, HMXB show a harder X-ray spectrum than AGN ($\Gamma \approx 1.7$), thus providing a lower limit for HR_3 at -0.3 (see Figure 4.6b). There is a notable exception, SXP8.02, all detections of this pulsar lie outside the selection region of Figure 4.6b. This can be explained on the basis of the anomalous X-ray pulsar (AXP) nature of this object (Tiengo et al. 2008). The X-ray colours of SXP22.1 (№ 935) have large uncertainties. In total 1536 XMM-*Newton* sources, which are not identified as HMXB or AGN (see Sec. 4.3.4), are hard (see Table 4.2) X-ray sources with $HR_3 > -0.3$.

(ii) To avoid chance correlations with sources having a high positional uncertainty, I only used X-ray sources with a positional uncertainty <2.5″. This excludes 33 X-ray sources.

(iii) In addition to the selection of X-ray colours, an early-type star is required as counterpart. I used the loci of the confirmed BeXRBs (shown with blue squares) on the colour-magnitude and colour-colour diagram of Figure 4.8, to define the selection area for candidate BeXRB systems. The loci are indicated with red boxes and correspond to 13.5 mag< V <17 mag and colours of -0.5 mag < $B-V$ <0.5 mag and -1.5 mag< $U-B$ <-0.2 mag. The MCPS catalogue comprises 16 605 entries, which fulfil these criteria and are in the XMM-*Newton* field.

(iv) To further improve the separation of AGN and HMXB, I use a third dividing line in the HR_3-HR_4-plane (Figure 4.6f), where the difference in average power-law photon index has most effect. I note, that the separation between the BeXRB and AGN populations is not clear-cut: Highly obscured AGN are shifted towards larger HR_3, and there are also some detections of HMXB on the left side of the cut. 34 sources fulfil the criteria i−iv. By using subsamples of XMM-*Newton* and MCPS sources fulfilling the criteria i−iv and shifting the coordinates of one catalogue as described in Sec. 4.2.2, ~16.6±3.4 chance coincidences are estimated.

(v) Moreover, two weak candidates (№ 154 and 1408) correlate with an emission line object. This also confirms a possible HMXB nature of the source.

Five sources that fulfil the criteria i−iii, but violate criteria iv or v are considered as weak candidates, marked with "?". In addition, I found one source, № 66, in the young star-cluster NGC 330. Due to the high stellar density, no optical counterpart could be identified in the MCPS at this position, but the source correlates with the Be star NGC 330:KWBBe 224 (Keller et al. 1999). The hardness ratios and short-term variability further support the HMXB nature for this source. Source № 1605 is in the star-cluster NGC 376 and was rejected because of a $B-V$=0.71 in the MCPS. However, this colour might be influenced by confusion with other stars in the cluster. One finds $B-V=-0.15$ in the OGLE catalogue (Udalski et al. 1998) and a classification of B2e by Martayan et al. (2010). Source № 823 was rejected because of a $B-V$ colour of 2.4 mag in the MCPS. However, this source was classified as B1-5 III e by Evans et al. (2004) and has $B-V=-0.13$ in the OGLE catalogue. Source № 3003 is outside the MCPS field. The X-ray properties and optical colours from Massey (2002) are consistent with a HMXB. Evans et al. (2004) classified the star to B1-3 III. Therefore, I also add these four sources to the catalogue of HMXB candidates.

All 45 candidate HMXBs (<HMXB>) are listed in Table 4.6. This list includes also the weak candidates as it is useful to set an upper limit to the BeXRB luminosity function.

Table 4.6. BeXRB candidates in the SMC.

No	X-ray RA (J2000)	Dec (J2000)	ePos (″)	MCPS d (″)	V (mag)	$B-V$ (mag)	$U-B$ (mag)	MA93 d (″)	No	Comments and references
12	01 19 38.94	-73 30 11.4	0.7	0.3	15.8	-0.1	-0.8	0.9	1867	H00,S05
65	00 57 23.66	-72 23 55.8	0.8	1.7	14.7	-0.1	-1.0	–	–	?, S05,A09
66	00 56 18.85	-72 28 02.7	0.7	–	–	–	–	–	–	in NGC 330, S05
94	00 55 07.72	-72 22 40.3	0.9	0.8	14.4	-0.1	-1.0	–	–	
117	00 48 18.73	-73 20 59.9	0.6	0.2	16.2	0.3	-0.8	–	–	S05,A09,K09
133	00 50 48.06	-73 18 17.6	0.9	0.3	15.1	0.1	-1.0	2.8	396	S05,A09
137	00 52 15.06	-73 19 16.3	0.6	2.2	15.9	-0.1	-1.0	5.7	552	L10
154	01 00 30.26	-72 20 33.1	1.0	0.7	14.6	-0.1	-1.0	0.3	1208	S05
160	01 00 37.31	-72 13 17.4	0.9	2.4	16.7	-0.2	-0.9	–	–	N03,S05
247	01 02 47.51	-72 04 50.9	0.8	0.5	16.0	-0.3	-1.1	–	–	
259	01 03 28.54	-72 06 51.4	0.7	1.9	16.5	-0.2	-0.9	–	–	S05
287	01 01 55.89	-72 10 27.9	0.9	0.9	15.1	-0.2	-0.9	–	–	
337	00 56 14.65	-72 37 55.8	0.8	0.7	14.6	0.1	-1.3	1.9	922	S05
474	00 54 25.99	-71 58 24.1	0.8	2.4	16.6	-0.1	-0.8	–	–	?
562	01 03 31.73	-73 01 44.4	1.0	1.5	15.4	-0.2	-1.1	–	–	
823	01 00 55.85	-72 23 20.3	1.0	1.1	15.6	2.4[a]	–	–	–	B1-5 III e
1019	00 49 02.67	-73 27 07.4	1.6	3.5	15.8	-0.2	-0.9	–	–	
1189	01 03 33.62	-72 04 17.5	1.7	4.9	16.1	-0.1	-1.0	–	–	
1400	00 53 41.76	-72 53 10.1	0.8	2.2	14.7	0.1	-1.1	–	–	
1408	00 54 09.28	-72 41 43.2	1.4	1.3	13.8	-0.0	-0.7	1.0	739	
1481	00 42 07.77	-73 45 03.4	0.7	1.5	16.8	-0.1	-0.5	–	–	
1524	00 45 00.20	-73 42 46.7	1.7	1.5	15.6	0.0	-0.3	–	–	
1605	01 03 55.08	-72 49 52.7	1.5	3.7	16.2	0.7[a]	-0.6[a]	–	–	in NGC 376
1762	01 03 38.00	-72 02 15.5	1.6	4.5	16.3	-0.2	-0.8	–	–	
1817	00 54 08.68	-72 32 07.5	1.4	1.1	16.9	-0.1	-0.3	–	–	
1820	00 53 18.52	-72 16 17.6	1.6	2.3	16.6	-0.2	-0.8	–	–	
1823	00 53 14.81	-72 18 47.6	1.7	4.9	16.6	-0.0	-0.8	–	–	
1826	00 52 35.29	-72 25 20.8	1.6	5.7	14.9	-0.2	-0.9	–	–	
1859	00 48 55.55	-73 49 46.4	0.6	1.3	14.9	-0.2	-0.7	–	–	S05
1955	00 55 35.02	-71 33 40.9	1.3	4.7	16.1	-0.1	-0.8	–	–	
2100	01 04 48.54	-71 45 41.5	1.6	4.3	16.9	0.4	-0.2	–	–	
2208	00 56 05.48	-72 00 11.1	2.0	1.3	16.7	-0.1	-0.9	–	–	N11
2211	00 55 07.25	-72 08 25.7	1.7	3.9	16.9	-0.1	-0.7	–	–	
2300	00 56 13.87	-72 29 59.7	1.0	0.7	14.5	0.0	-1.0	–	–	
2318	00 56 19.02	-72 15 06.1	1.8	5.2	16.1	-0.1	-0.9	4.7	928	
2497	00 43 15.87	-73 24 39.2	1.5	2.7	16.7	-0.1	-0.8	–	–	
2569	00 51 46.12	-73 07 04.3	1.1	2.9	16.7	-0.0	-0.7	–	–	?
2587	00 52 59.47	-72 54 02.1	2.1	1.7	16.8	0.2	-0.5	–	–	
2675	00 55 49.77	-72 51 27.1	1.5	1.0	16.5	-0.0	-0.6	–	–	
2721	01 06 00.78	-72 33 03.7	1.9	2.0	16.3	-0.1	-0.9	–	–	
2737	01 08 20.18	-72 13 47.1	0.7	2.2	14.7	-0.1	-0.7	–	–	?
3003	01 23 27.46	-73 21 23.4	1.1	1.3[b]	15.5[b]	-0.1[b]	-0.9[b]	–	–	B1-5 III
3052	01 11 08.59	-73 16 46.1	0.7	0.1	15.5	-0.1	-1.0	–	–	SXP31.0 ?
3271	00 51 33.27	-73 30 12.2	1.5	4.4	16.6	0.1	-0.8	–	–	
3285	01 04 29.42	-72 31 36.5	1.3	1.4	15.8	-0.2	-1.1	–	–	

Notes. [a] Colour questionable. [b] Source is outside MCPS area. Values are from Massey (2002).

References. (H00) Haberl & Sasaki (2000); (S05) Shtykovskiy & Gilfanov (2005); (K09) Kozłowski & Kochanek (2009); (A09) Antoniou et al. (2009); (N03) Nazé et al. (2003); (L10) Laycock et al. (2010); (N11) Novara et al. (2011) .

4.3.4. Active galactic nuclei

Galaxies with an active galactic nucleus (AGN, see Sec. 2.4.7) are bright X-ray sources at cosmological distances, and constitute the majority of point sources in the catalogue. X-rays are caused by accretion onto a super-massive black hole.

Identification of AGN

Forty seven spectroscopically confirmed quasars could be identified in the catalogue, mainly from Véron-Cetty & Véron (2006) and Kozłowski et al. (2011). All XMM-*Newton* detections of these sources are plotted in Figure 4.6c in black. Point sources, emitting X-rays and radio, are also dominated by AGN. I identified 25 X-ray sources, which correlate with a radio background source of Payne et al. (2004). In this case the number of expected chance correlations is low. These sources are marked with an additional `r` behind their classification. In Figure 4.6c, detections of these sources are plotted in magenta.

Classification of AGN

AGN can be separated well from stars in the HR_2-HR_3-plane (Figure 4.6c). I selected AGN candidates (<AGN>) among hard X-ray sources, where I use the same cut as for stars to discriminate between soft and hard X-ray sources (red line in Figure 4.6c). I could classify 16 AGN, which have a SUMSS radio counterpart (noted with `r`), but no correlation with a radio source of the SMC or foreground in Payne et al. (2004). 110 hard X-ray source correlate with an infra-red selected AGN candidate of Kozłowski & Kochanek (2009, noted with `i`), in addition to the already identified AGN. Using the *Chandra* wing survey (McGowan et al. 2008), the optical counterpart can be determined more precisely, and I found 126 hard X-ray sources, correlating with a source, classified as AGN by McGowan et al. (2008, noted with `x`).

In general, one expects for the optical and X-ray flux of an AGN a ratio of $-1 < \log(f_X/f_O) < 1$ (Maccacaro et al. 1988). Another 1861 X-ray sources were classified with <AGN>, if the source has an optical counterpart with $\log(f_X/f_O) > -1$ in the MCPS (noted with `o`). I stress, that this last classification is very general, because of the high source density in the MCPS. *Chandra* correlations with stars in the SMC can fulfil the same $\log(f_X/f_O)$ criterion. Also, for weak X-ray sources, the optical luminosity of the AGN can be below the completeness limit of the MCPS. Since the bulk of hard X-ray sources is expected to be of AGN class, this classification will be correct in most cases (cf. Sec. 4.4.2), but some sources may be of a different nature. Therefore, AGN classifications based only on the optical criterion are marked with a "?".

4.3.5. Galaxies

Galaxies behind the SMC (Sec. 2.4.8) can be seen in X-rays, showing an unresolved combination of X-ray sources as e. g. X-ray binaries, diffuse emission and a contribution of a central AGN. In the 6dFGS catalogue (Jones et al. 2009), one finds 6 entries, correlating with X-ray sources (№ 365, 376, 645, 1726, 2905, and 3208). These sources were classified as galaxies, with the exception of № 365 (6dFGS gJ005356.2-703804), which was identified as AGN in the previous section. Source № 1711 was fitted as an extended source in X-rays and also has a counterpart in the 2MASS extended source catalogue (2MASX, Skrutskie et al. 2006), similar to the nearby source № 1726. There is an indication of diffuse emission in the mosaic image connecting both sources. Also sources № 708 and № 709 are inside a cluster of galaxies (ClG) and have 2MASX counterparts. Therefore, I also

classified these sources as galaxies. Sources, classified as galaxies are plotted in green in Figure 4.6c. In the SMC bar, no redshift-confirmed galaxies are found.

4.3.6. Clusters of galaxies

Clusters of Galaxies and galaxy groups contribute to the background sources (see Sec. 2.4.9). Just like SNRs in the SMC, ClGs have an extent detectable with XMM-*Newton*. Since the temperature of SNRs is significantly lower, these two source classes can be separated by hardness ratios. The hardness ratios of all detections, which were flagged as significantly extended (`QFLAG=E`) in the X-ray images are plotted in Figure 4.6d. Only SNRs, super bubbles, and ClGs are expected as X-ray sources with such a large extent in the SMC field. Diffuse emission of the hot interstellar medium in the SMC is modelled by spline maps and treated as background. Identified SNRs and new candidates of Haberl et al. (2012a) are plotted in black. They have similar soft X-ray colours as stars. All other sources are plotted in green and show X-ray colours typical of ClGs in the mosaic image (cf. Haberl et al. 2012a). The red line marks the selection cut for the ClG classification. The only SNRs within this cut are IKT 2, IKT 4 and IKT 25. The spectra of these SNRs show high absorbing column densities ($N_H \gtrsim 4 \times 10^{21}$ cm^{-2}, van der Heyden et al. 2004). In addition to X-ray colours, I demand a significant extent of the X-ray source of $Ext > \Delta Ext$ and a maximum likelihood for the extent of $ML_{\rm ext} > 10$. Using these criteria, I classified 13 of 19 sources with significant extent as ClG candidates (<ClG>), in addition to the 11 ClGs not included in the point-source catalogue (because of their very large extent). All catalogue sources with significant extent are listed in Table 4.7.

4.3.7. Other source classes

The search for additional source classes is more extensive and goes beyond the scope of this thesis. This includes faint low-mass X-ray binaries or bright cataclysmic variables in the SMC that are at the detection limit of the deepest XMM-*Newton* observations. Extended sources, such as SNRs and ClGs, which are not included in the catalogue, are presented in Haberl et al. (2012a). A search for highly absorbed X-ray binaries in the survey data was presented by Novara et al. (2011). A specific source class was assigned to some individual sources: Source №48 as an anomalous X-ray pulsar (AXP, Tiengo et al. 2008), source №54 as a pulsar wind nebula or micro quasar (PWN?/MQ?, Owen et al. 2011), source №324 as an isolated neutron star candidate (INS?, Kahabka & Haberl 2006), source №551 as PWN candidate (PWN?, Filipović et al. 2008), and source №535 as a star cluster (Cl*, Sec. 4.3.1).

4.3.8. Comparison with other X-ray catalogues

55 ROSAT sources of Haberl et al. (2000) have an XMM-*Newton* counterpart, where the XMM-*Newton* classification is in agreement with the ROSAT classification. In addition 187 unclassified ROSAT sources have an XMM-*Newton* counterpart, which is identified or classified now. Comparing the derived classification with sources also listed in the ROSAT PSPC catalogue, I find a corresponding XMM-*Newton* source with foreground star classification for all sources marked as “stellar” and “fg-star” in Haberl et al. (2000), with the exception of the ROSAT sources 204, 404, and 618. These correspond to the sources №57, №2434, and №1074 in the XMM-*Newton* catalogue, respectively. Only, №2434 shows soft X-ray emission compatible with a foreground star, but it was not classified as such because of the large distance to the likely optical counterpart. For the sources 204 and 618, one can reject a “stellar” classification, based on the XMM-*Newton* X-ray colours.

Also the comparison with the classification of *Chandra* sources by McGowan et al. (2008) shows good agreement. Of the sources common in both catalogues, 142 have the same classification and 34 sources are unclassified in both catalogues. Only the four sources №1726, №640, №1732, and №3185 have a contradictory classification. These sources were classified as stars by McGowan et al. (2008), whereas here the first source was identified as a galaxy and the latter three were classified as AGN candidates (<AGN> o?), due to their hardness ratios. Sources №46 and 2785 are unclassified in the XMM-*Newton* catalogue but classified as stars by McGowan et al. (2008). They have bright optical counterparts, but show hard X-ray colours in the XMM-*Newton* catalogue. It should be pointed out that these *Chandra* detections have fewer then 7 counts in the *Chandra* data.

4.4. General characteristics of the data set

With the XMM-*Newton* catalogue of the SMC, the central field is covered completely down to luminosities of 5×10^{33} erg s^{-1} in the (0.2-4.5) keV band, for the first time with an imaging X-ray telescope. The comparison with previous ROSAT and *Chandra* surveys as well as with the XMM-Newton Serendipitous Source Catalogue shows that ~1200 sources have been detected for the first time during the large-programme SMC survey. Some basic properties of the data set will be discussed in the following.

4.4.1. Spatial distribution

The spatial distribution of individual source classes in the main field is shown in Figure 4.10. In Figure 4.10a, sources identified as Galactic stars (red) or classified as candidates for Galactic stars (blue) are marked. The distribution is homogeneous over the entire field. SSSs as well as SSS candidates (Figure 4.10b) are found in the outer regions of the bar, especially in the northern part. None are found in the SMC wing. As expected, HMXBs and their candidates follow the SMC bar (Figure 4.10c). Since the bar harbours most of the blue main-sequence stars, also most of the chance correlations with background AGN that contribute to the HMXB candidates are found here. AGN show a homogeneous distribution over the observed field (Figure 4.10d). Infrared selected AGN candidates are restricted to the smaller *Spitzer* SMC field, AGN candidates from *Chandra* are only in the *Chandra* wing fields. Clusters of galaxies that could be identified or classified, are shown in the Figure 4.10e. Unclassified sources are marked in Figure 4.10f. Here, we see some enhancement at the eastern rim, where the MCPS does not cover the field, and around SMC X-1, which may cause some spurious detections due to its brightness. Also around 1E0102.2-7219, an enhancement of unclassified sources is observed as expected, due to the high number of observations, which lead to a higher number of spurious detections.

4.4.2. Luminosity functions

I constructed the luminosity functions of the various classes of objects detected in the SMC fields. For sources with high long-term time variability, taking the average or maximal flux would not represent the source luminosity distribution of the galaxy at one time. For each source, I selected the flux from the observation with the highest sensitivity at this position, i. e. with minimal detection-limit flux. If the source was not detected in this observation, the source was not taken into account for the luminosity function. None of the selected detections is from an observation that was triggered by an outburst of the corresponding source. Therefore, this method selects one of several measured fluxes of transient sources in a quasi-random manner and thus represents the flux distribution as measured

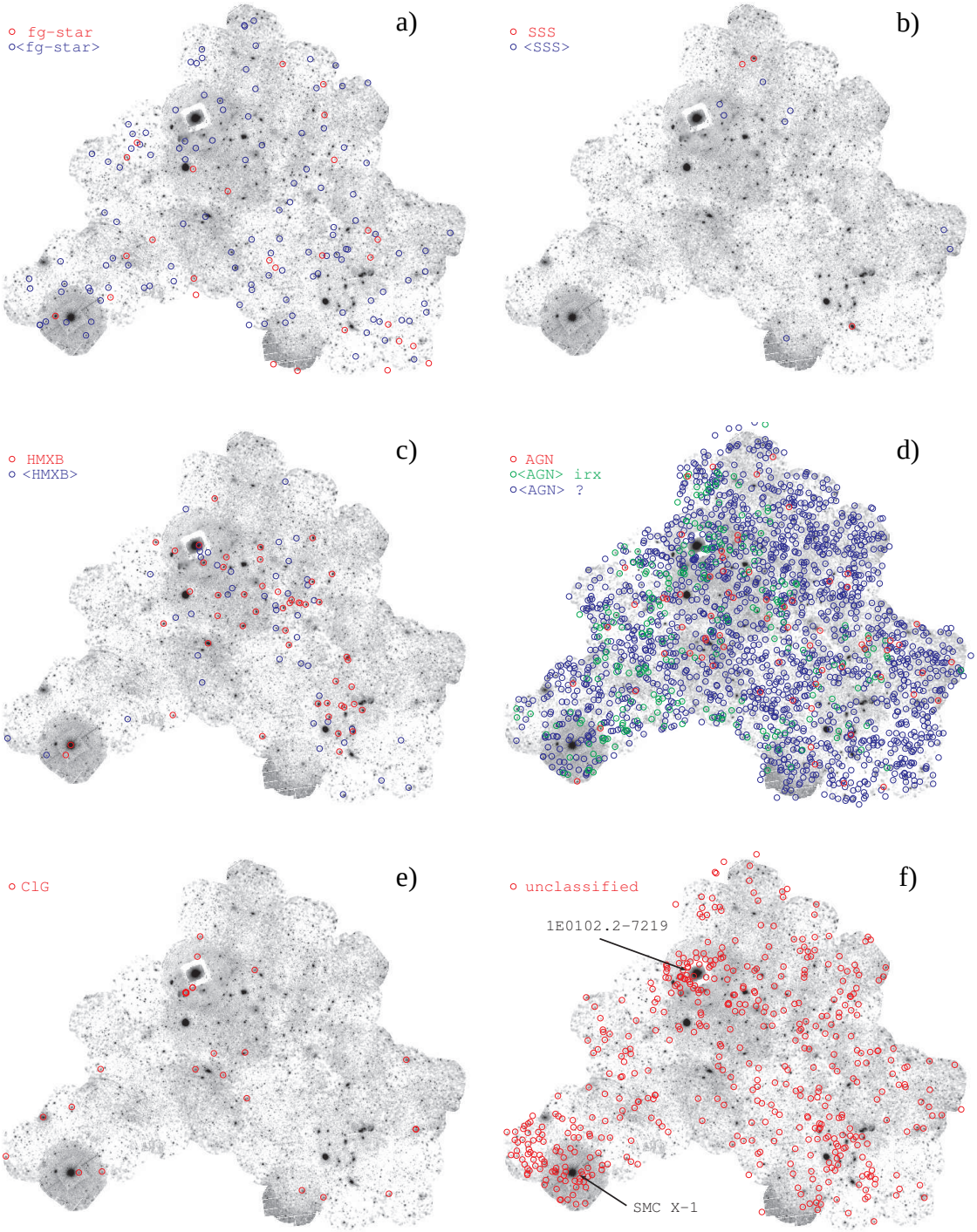

Figure 4.10. Spatial distribution of identified and classified X-ray sources in the SMC main field. The underlying mosaic image shows logarithmically scaled intensities in the (0.2–4.5) keV band. North is up, east is left.

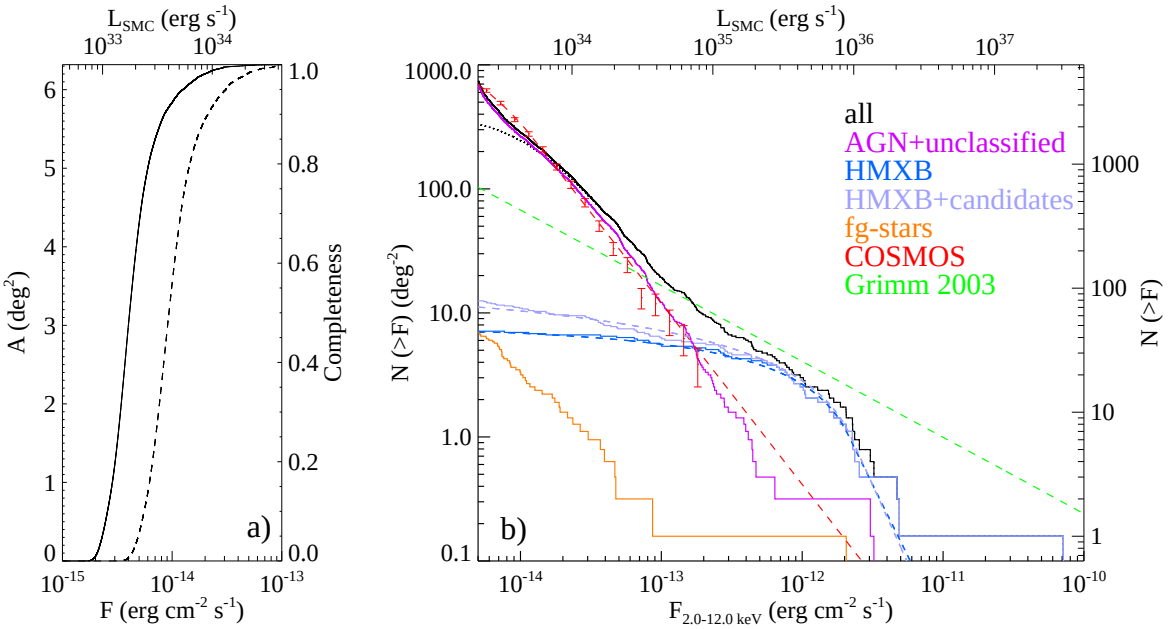

Figure 4.11. (a) The sky coverage as function of flux is shown for the (0.2–12.0) keV and (2.0–12.0) keV band by the solid and dashed line, respectively. (b) Cumulative luminosity function for sources in the XMM-*Newton* catalogue (solid lines) and models (dashed lines) as described in Sec. 4.4.2.

in one single observation of the whole galaxy. Also, this method minimizes the effect of spurious detections at higher fluxes, since the source has to be detected in the most sensitive observation.

Depending on exposure time and observation background, the sensitivity varies between individual observations. Diffuse emission and vignetting also cause a spatial dependence of the sensitivity within each observation. The calculation of sensitivity maps is described in Sec. 3.3.10. To estimate the sky coverage, I merged all sensitivity maps, by selecting the observation with highest sensitivity at each position. The corresponding completeness function is presented in Figure 4.11a.

Especially for background sources, the completeness for the full energy band is clearly overestimated, since the ECFs, adopted from the universal spectrum (Sec. 3.3.9) only account for Galactic absorption, but not for absorption in the SMC, reaching line-of-sight column densities of up to 1.4×10^{22} cm^{-2}. To minimise this effect, I use the (2.0−12.0) keV band in the following. The flux reduction by Galactic absorption ($\sim 6 \times 10^{20}$ cm^{-2}) is 0.5% for the assumed universal spectrum. The absorption by the ISM of the SMC causes a flux decrease in the (2.0–12.0) keV band by 1.2% and 2.4% when crossing a column density of 5 and 10 $\times 10^{21}$ cm^{-2}, respectively. Analogously, one would expect a decrease by 35% and 51% in the (0.5−2.0) keV band for an AGN with negligible intrinsic absorption. Therefore the observed fluxes in the (2.0–12.0) keV band are used in the following. The completeness-corrected cumulative distribution of all sources is shown by the solid black line in Figure 4.11b. Following Cappelluti et al. (2009), the completeness-corrected cumulative distribution is calculated by

$$N(>F) = \sum_{i=1}^{N_F} \frac{1}{A_i} \tag{4.5}$$

with N_F the number of detected sources with fluxes greater than F and A_i the sky coverage for the

flux F of source i. The correction mainly affects the number of sources with fluxes below $\sim 3 \times 10^{-14}$ erg cm^{-2} s^{-1} as can be seen by the uncorrected distribution (dotted line in Figure 4.11b).

For HMXBs, we see a break around 10^{-12} erg cm^{-2} s^{-1}, similar to that inferred by Shtykovskiy & Gilfanov (2005). As suggested by these authors, this can be caused by the propeller effect, which can inhibit accretion at low accretion rates. Using C statistics (Cash 1979), I parametrise the flux distribution of the total (i. e. not normalised by area) HMXB populations by fitting a broken power law to the unbinned source counts

$$n(F) = \frac{dN}{dF} = \begin{cases} N_1 F^{-\alpha_1} & \text{if} \quad F \leq F_b \\ N_2 F^{-\alpha_2} & \text{if} \quad F > F_b \end{cases} \tag{4.6}$$

with the faint and bright end slopes α_1 and α_2, the normalisation $N_2 = N_1 F_b^{\alpha_2 - \alpha_1}$, and the break flux F_b and flux F in 10^{-12} erg cm^{-2} s^{-1}. For HMXBs, I obtain $\alpha_1 = 0.64^{+0.13}_{-0.17}$, $\alpha_2 = 3.30^{+2.17}_{-1.38}$, $F_b = 2.09^{+0.74}_{-1.21} \times 10^{-12}$ erg cm^{-2} s^{-1}, and $N_1 = 11.9^{+7.5}_{-3.5}$. Including the HMXB candidates as well, I obtain $\alpha_1 = 0.87^{+0.08}_{-0.10}$, $\alpha_2 = 3.52^{+1.91}_{-1.64}$, $F_b = 2.25^{+0.62}_{-1.49} \times 10^{-12}$ erg cm^{-2} s^{-1}, and $N_1 = 13.9^{+7.6}_{-3.4}$. Uncertainties are for 90% confidence. These models are shown by the blue dashed lines in Figure 4.11b and give an upper and lower limit for the luminosity function.

The bright-end slope is significantly steeper than found for HMXB populations of nearby galaxies above a luminosity of 10^{38} erg s^{-1} ($\alpha = 1.61 \pm 0.12$, Grimm et al. 2003). The extrapolation of this model to lower luminosities is shown by a dashed green line in Figure 4.11b, where I used a star-formation rate of $\mathrm{SFR_{SMC}} = 0.15\ \mathrm{M_\odot\ yr^{-1}}$ (as in Grimm et al. 2003) and a correction factor of 1.24 (as expected for a photon index of $\Gamma = 1$) to obtain fluxes in the (2.0–12.0) keV band.

The universal luminosity function for HMXBs of Grimm et al. (2003) was derived from observations of nearby galaxies with distances up to 35 Mpc. With respect of the Milky Way and the Magellanic Clouds, the optical counterparts of HMXB cannot be constrained well and the discrimination from other hard X-ray sources must be done statistically. E. g. the LMXB population must be estimated from the stellar mass of the galaxy. Also the flux limits for more distant Galaxies are higher. Therefore, the universal HMXB luminosity function of Grimm et al. (2003) was derived for X-ray sources above a luminosity of 10^{38} erg s^{-1}. However, Mineo et al. (2012a) suggested that the universal shape is valid down to a luminosity of 10^{35} erg s^{-1}. So the differences seen for the SMC might not be caused by different sensitivity limits.

The luminosity of HMXBs depends on several parameters. Especially in BeXRBs, the accretion rate can be highly variable, depending on orbital period and eccentricity, and decretion disc variability. Therefore, it is reasonable to assume different shapes for the luminosity functions of SgXRBs and BeXRBs. If one compares the HMXB population of the SMC and the Milky Way, the SMC has a higher ratio of BeXRBs to SgXRBs (e. g. Coe et al. 2010a), which is likely caused by different star-formation histories. Strong star formation in the SMC occurred ~60 Myr ago. SgXRBs that formed in this burst have already ended their lives in SN explosions of the donor star and we see only the BeXRBs today. Most BeXRBs have luminosities of $\lesssim 3 \times 10^{36}$ erg s^{-1}, whereas for more distant galaxies due to higher flux limits only the brightest HMXBs can be detected. The luminosity bias can further increase the fraction of SgXRBs which are more persistent and can contain a black hole instead of a neutron star. The presence of one supergiant system in the SMC, SMC X-1, is consistent with the Grimm model. This scenario suggests, that the luminosity function of HMXB depends on the ratio of BeXRBs and SgXRBs and therefore on the star formation history. In this context, also the turn over might be interpreted as the transition from transient to persistent BeXRBs. I will not discuss the luminosity function below $\sim 2 \times 10^{-14}$ erg cm^{-2} s^{-1}, as we have only 3 sources here and run into incompleteness.

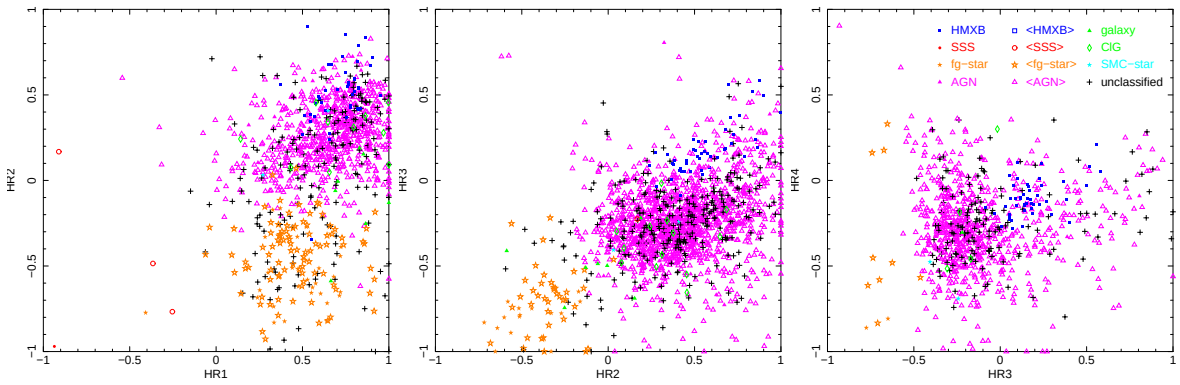

Figure 4.12. Hardness-ratio diagram of sources with respective uncertainties of $\Delta HR_i < 0.25$.

To investigate background sources, the sources of the SMC field are compared with the XMM-*Newton* COSMOS field (Hasinger et al. 2007) population. The COSMOS-field source counts and broken power-law model of Cappelluti et al. (2009) is shown in red in Figure 4.11b. As these values are given in the (2.0–10.0) keV band, I applied a factor of 1.14 to estimate fluxes for the (2.0–12.0) keV band, as expected for a power law with photon index of $\Gamma = 1.7$. We see a general agreement with the distribution of unidentified and AGN sources (magenta line in Figure 4.11b). Therefore, most hard sources in the catalogue are indeed AGN behind the SMC. Small deviations can be explained by the slightly different data processing. The contribution of Galactic stars (orange line in Figure 4.11b) is negligible above 2 keV.

4.4.3. Spectral properties

To characterise the spectral properties of the source sample, I calculated hardness ratios as described in Sec. 3.3.8. Hardness-ratio diagrams of sources with well measured hardness ratios ($\Delta HR_i < 0.25$) are presented in Figure 4.12. Of course, the classified sources follow the selection criteria (cf. Figure 4.6). In total, I find 436 hard unclassified sources. Presumably, these are mainly background AGN, where we expect a faint optical counterpart. If we assume a completeness of the MCPS catalogue of $V \approx 21$ mag, optical counterparts of AGN with $\log(f_x/f_o) = 1$ can be missed, if they are fainter than $F_x = 10^{-12.7}$ erg cm^{-2} s^{-1}. Nearly all of the unclassified hard sources have such a low X-ray luminosity. A few hard sources might be caused by foreground flare stars, where the X-ray photon statistics is insufficient to detect variability. Also, the comparison with the COSMOS field (Fig. 12) seems to be consistent with most of these sources being background. Sources in the upper left of the HR_3-HR_4-plane are good candidates for highly absorbed AGN (Brightman & Nandra 2012), where the absorption can exceed $N_H > 10^{24}$ cm^{-2}, which is significantly higher than expected from the interstellar medium of the SMC along the line of sight. From 130 unclassified soft sources, 67 have a detection likelihood of $ML_{det} < 10$. Here we expect most of the spurious detections. Other soft X-ray sources might originate from distant K or G stars that cannot be distinguished well from bright SMC stars and violate criterion iii of the foreground star selection.

4.4.4. Source extent

Table 4.7 lists all sources, fitted with a significant extent with $Ext > \Delta Ext$ and a likelihood for the extent of $ML_{ext} > 10$. Most of them are consistent with a ClG classification. Three other sources are inside or behind an extended X-ray source. In the case of SMC X-1 (№ 1), the source extent is caused

Table 4.7. Sources with significant extent.

SRC	RA	Dec	Ext (″)	ML_{ext}	HR_2	HR_3	class	comment
1	01 17 05.2	-73 26 36	6.34 ± 0.02	69614.5	0.3 ± 0.0	0.2 ± 0.0	HMXB	pile-up
307	01 03 28.6	-71 45 48	8.74 ± 0.95	11.6	0.3 ± 0.1	-0.2 ± 0.1	<ClG>	
362	00 53 08.7	-72 34 45	10.90 ± 1.63	12.8	-0.3 ± 0.1	-0.4 ± 0.2		in B0050-72.8
566	01 01 25.0	-72 46 34	14.20 ± 1.84	13.2	0.3 ± 0.2	-0.0 ± 0.1	<ClG>	
571	01 04 08.1	-72 43 54	20.24 ± 1.46	24.8	0.7 ± 0.1	-0.3 ± 0.1	<ClG>	
604	00 52 53.4	-73 00 09	3.74 ± 0.61	12.7	-0.3 ± 0.1	-0.7 ± 0.1	<fg-star>	multiple stars?
638	01 09 53.3	-72 21 47	31.89 ± 2.87	20.4	-0.3 ± 0.1	-0.4 ± 0.2		extent spurious?
799	00 59 04.1	-72 56 45	8.51 ± 1.05	29.0	0.3 ± 0.1	-0.5 ± 0.1	<ClG>	
916	01 16 15.3	-73 26 57	11.94 ± 1.11	46.0	0.5 ± 0.1	-0.6 ± 0.1	<ClG>	
937	01 13 53.2	-73 27 08	8.51 ± 1.00	11.7	0.3 ± 0.1	-0.4 ± 0.1	<ClG>	
1174	01 03 45.9	-71 54 36	14.79 ± 2.04	12.6	0.7 ± 0.2	-0.2 ± 0.1	<ClG>	
1305	01 01 26.3	-75 05 06	9.12 ± 1.40	18.4	0.1 ± 0.1	-0.5 ± 0.2	<ClG>	
1436	00 53 03.5	-70 47 34	12.48 ± 2.12	10.2	0.2 ± 0.2	-0.3 ± 0.2	<ClG>	
1505	00 44 19.4	-73 36 24	13.15 ± 1.90	12.3	0.1 ± 0.1	-0.3 ± 0.2	<ClG>	
1562	00 58 22.2	-72 17 59	19.94 ± 2.38	15.5	0.1 ± 0.2	-0.5 ± 0.2	<AGN> o?	in IKT 16
1711	01 09 00.6	-72 29 03	8.56 ± 1.03	23.6	-0.3 ± 0.1	-0.7 ± 0.1	galaxy	in ClG?
2695	01 02 18.3	-72 37 03	12.57 ± 1.55	22.0	0.4 ± 0.1	-0.3 ± 0.1	<ClG>	
2889	01 13 26.3	-72 42 19	13.25 ± 1.64	26.8	0.1 ± 0.1	-0.4 ± 0.2	<ClG>	
3030	01 23 32.1	-73 17 10	8.35 ± 1.35	17.6	0.5 ± 0.1	-0.7 ± 0.1	<ClG>	

Notes. This table does not contain sources, with extent too large for the source detection. See Haberl et al. (2012a).

by pile-up. For №604, the hardness ratios point to a star. In the optical, several bright counterparts are found. The extent might be due to a superposition of two or more stars. №638 was detected as an extended source only in one of three detections. Therefore, the extent might be spurious. I note that 13 additional sources were fitted with extent at lower likelihood or with high uncertainty.

4.4.5. Source variability

Intra-observational variability

To estimate the variability of sources during the individual observations, I used KS-tests as described in Sec. 3.3.12. This allows the estimation of the source variability also for sources with poor statistics. Some examples of cumulative count distributions, as used for the KS-test, are presented in Figure 4.13. A bright star (№2041, Figure 4.13a) showing a flare and a variable HMXB (№335 = RX J0054.9-7245, Figure 4.13b) are shown. A foreground star candidate (№255, Figure 4.13c), detected with only 29 counts also exhibits a flare. As an example for a constant source, the SNR 1E0102.2-7219 is given in Figure 4.13d. In the case of high variability, the photon time distribution of the source (black line) shows a difference to the reference distribution for a constant source (red line), that is unlikely to be caused by statistical fluctuations.

The distribution of probabilities Cst for constancy during individual observations is presented in Figure 4.14 for various source classes. Here, we see a uniform distribution, with the exception of stars and HMXBs. These are expected to show variability whereas extended sources can be assumed to have a constant X-ray luminosity on short time scales. All 89 sources with $Cst < 0.5\%$ are listed in Table 4.8. Assuming a uniform distribution one would expect ~15 catalogue sources to be found with $Cst < 0.5\%$ by chance. Whereas 15.4% of all HMXB detections and 9.3% of all foreground-star detections have $Cst < 0.5\%$, this occurs only for 0.8% of the remaining detections.

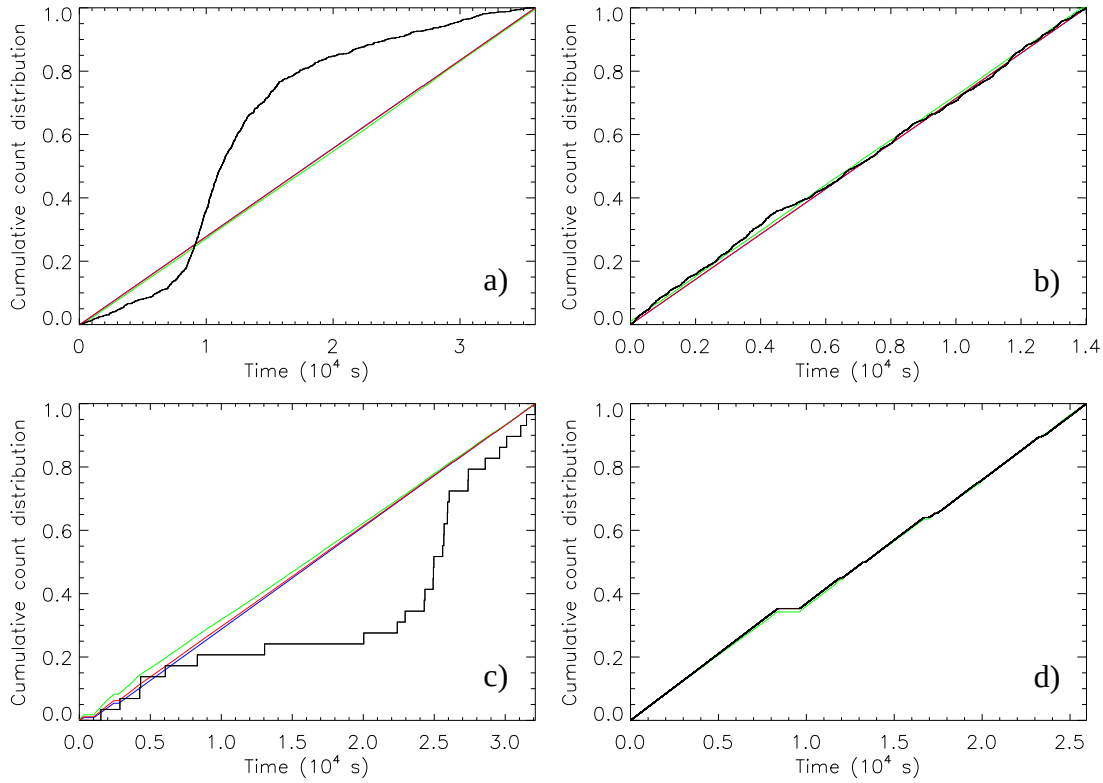

Figure 4.13. Cumulative photon arrival time distributions as used for the KS tests. Source counts are plotted in black, the background light curve is shown in green. The distribution, expected from a constant source is shown in blue and the reference distribution in red. In case of a constant source and background light curve, all lines are blended. [(a)] The bright foreground star № 2041. [(b)] The HMXB RX J0054.9-7245 (№ 335). [(c)] The foreground star candidate № 255. [(d)] The SNR 1E0102.2-7219.

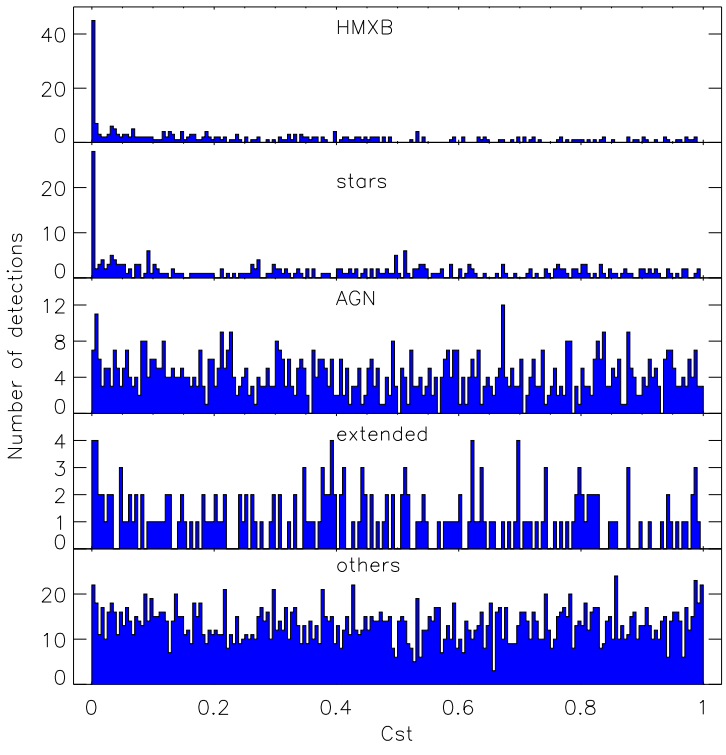

Figure 4.14. Histogram of probability that the source flux was constant within the observation. The bin size is 0.005. Note the number of stars and HMXB showing short-term variability with $Cst < 0.5\%$.

Table 4.8. X-ray sources in the SMC field with significant short-term variability.

SRC	class	$\log(Cst)^{(a)}$	$N^{(b)}$	SRC	class	$\log(Cst)^{(a)}$	$N^{(b)}$
1	HMXB	<-40	316817	851	<fg-star>	-13.06	290
2	fg-star	-39.36	13873	852	AGN	-5.51	1008
7	<fg-star>	-3.63	171	884	<fg-star>	-17.02	2022
9	<AGN> o?	-3.08	153	885	<fg-star>	<-40	1067
37	<fg-star>	-2.58	280	888		-9.01	211
51	HMXB	-3.73	1081	905	<fg-star>	-15.30	290
61	HMXB	-4.67	505	923		-4.18	55
63	HMXB	-3.37	463	934	<AGN> o?	-2.97	10
66	<HMXB>	-2.70	214	937	<ClG>	-2.38	119
92	HMXB	-8.26	1160	948		-13.49	33
112	HMXB	-31.48	7094	1032	<fg-star>	-4.87	21
113	HMXB	-6.92	10189	1041	fg-star	<-40	241087
137	<HMXB>	-4.97	387	1194	<AGN> o?	-8.93	63
146	<fg-star>	-13.08	214	1199	<fg-star>	-2.59	11
149	HMXB	<-40	6024	1399	HMXB	-5.35	1551
165		-2.47	22	1462	<AGN> o?	-2.40	219
183	<fg-star>	-3.36	20	1481	<HMXB>	-6.64	315
184	HMXB	-6.16	999	1483	<AGN> o?	-2.35	131
187	HMXB	-2.63	1322	1500	<fg-star>	-8.80	29
197	<AGN> ox	-3.20	189	1525	<AGN> o?	-2.50	28
216	HMXB	-7.85	1948	1560	<AGN> o?	-4.48	428
227	HMXB	-9.15	7426	1617	<AGN> o?	-2.51	19
228	HMXB	-3.57	235	1700	<AGN> o?	-2.31	30
231	<fg-star>	-8.88	199	1702	<fg-star>	-2.51	21
239	<fg-star>	-2.74	65	1755		-17.86	36
255	<fg-star>	-4.26	29	1802	HMXB	-2.32	2592
256		-2.34	22	1998	<fg-star>	-4.35	28
287	<HMXB>	-2.95	28	2002	<AGN> o?	-2.54	42
335	HMXB	-3.58	3038	2041	<fg-star>	<-40	1014
352	<AGN> o?	-2.32	10	2381	AGN r	-17.31	606
392	<AGN> o?	-2.55	19	2454	<AGN> o?	-2.42	27
402	<AGN> o?	-2.94	580	2601		-5.50	154
407	fg-star	-2.44	352	2651	<AGN> o?	-4.05	14
487	<fg-star>	-4.39	451	2735	fg-star	<-40	708
542	<AGN> oi	-2.66	31	2738	AGN r	-2.66	332
556	<AGN> oi	-2.90	23	2740	<fg-star>	-3.49	204
562	<HMXB>	-2.49	19	2845	<fg-star>	-9.22	524
615	HMXB	-2.83	223	2846	<fg-star>	-11.28	304
636	<AGN> o?	-2.62	16	3059	<fg-star>	-9.03	103
654	HMXB	-3.16	2149	3115	HMXB	-11.24	811
668	<AGN> o?	-2.52	51	3167	<AGN> o?	-3.35	27
674	HMXB	-14.16	6464	3186	<AGN> o?	-2.31	127
730		-2.64	81	3190	<fg-star>	-2.64	79
760	<fg-star>	-2.79	173	3267	<AGN> o?	-6.26	214
812	<AGN> o?	-15.07	1087				

Notes. [(a)] Probability Cst that the source is constant during the observation. Minimum of all detections of the source is given. [(b)] Number of source counts of the detections with the given value of Cst.

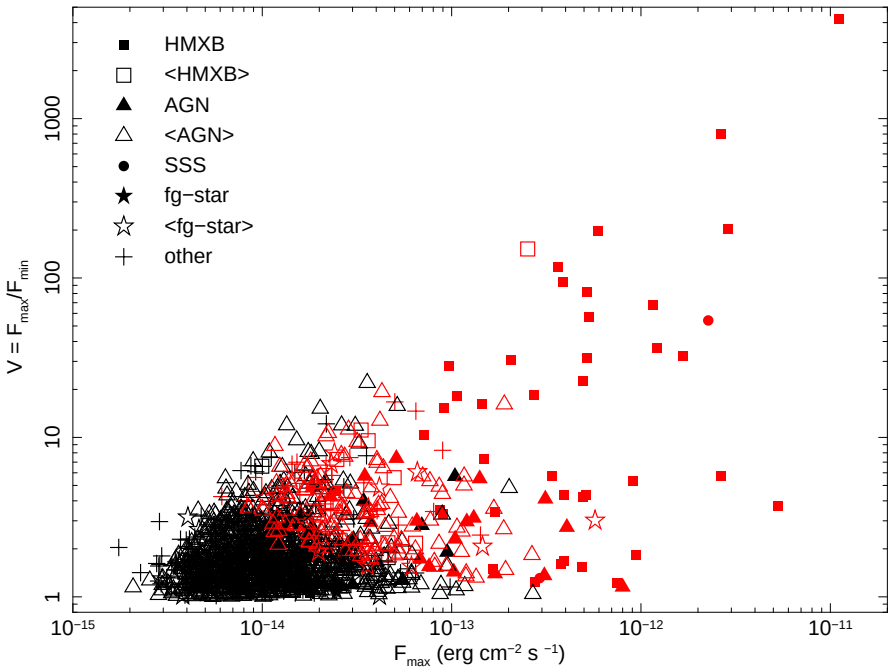

Figure 4.15. Variability of SMC sources as observed with XMM-*Newton* in the (0.2-4.5) keV band. Sources with a significance of variability greater (less) than 3 are plotted in red (black).

Inter-observational variability

For sources which were observed several times, the long-term variability was calculated as described in Sec. 3.3.11. The dependence of variability on the maximal detected flux is plotted in Figure 4.15. For sources with $F_{\rm max} < 10^{-14}$ erg cm^{-2} s^{-1}, the variability is uncertain. The calculation results in a significant ($S \geq 3$) variability measurement for most sources with $F_{\rm max}$ above 10^{-13} erg cm^{-2} s^{-1}.

Sources with high variability of $V \geq 10$ are listed in Table 4.9. As expected, most of these sources are HMXBs. For two HMXB candidates, the high variability supports their classification. In addition, we find the symbiotic nova SMC 3, which has a known 1600 day variability, one Galactic star, possibly observed during a flare in one observation, and six more sources, unclassified or with AGN classification. Sources № 1560 and № 1907 were only detected once with $ML_{\rm det} < 10$. The other four show clear variability, which is rather high but possible for AGNs. E. g. № 186 is classified as AGN from X-ray and radio correlations. Another explanation of such high variabilities might be given by an X-ray binary nature, but these sources do not have bright optical counterparts, needed for a HMXB classification. In the case of LMXBs, one would not expect an optical counterpart. Only very few LMXBs are expected in the SMC, as this population scales with the stellar mass of the galaxy. So far, none is known. These X-ray variable sources might be considered as candidates.

The spatial distribution of the highly variable sources is presented in Figure 4.16. Obviously, it is more likely, to find variable sources in fields, which were observed more frequently. Specifically, long-term variability cannot be measured in fields observed only once. Since most variable sources are HMXBs, the distribution follows the bar of the SMC.

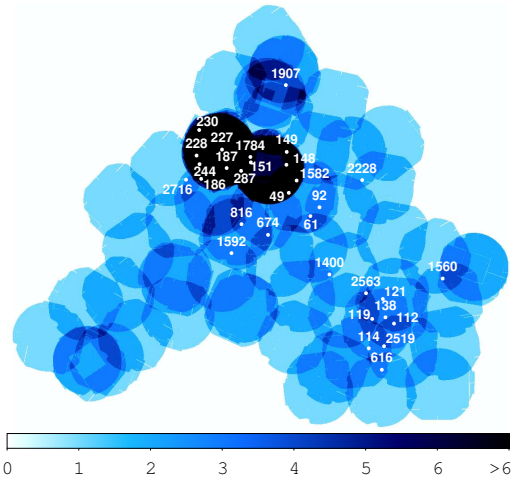

Figure 4.16. The number of observations per field is compared with the distribution of significant long-term variable sources ($V \geq 10$ and $S \geq 3$), shown by white dots. Labels give the source numbers.

Table 4.9. X-ray sources in the SMC field with high variability between individual observations.

No	name	class	$V^{(a)}$	$S^{(a)}$	F_{max} ($10^{-14}\times$ erg cm^{-2} s^{-1})
49	SXP565	HMXB	196.5	6.5	59.43 ± 9.06
61	SXP645	HMXB	18.6	25.0	27.35 ± 0.91
92	CXOU J005446.2-722523	HMXB	30.5	27.7	20.67 ± 0.70
112	SXP264	HMXB	36.6	66.7	121.60 ± 1.74
114	SXP756	HMXB	22.5	38.5	49.36 ± 1.09
119	SXP892	HMXB	16.1	17.0	14.48 ± 0.74
121	RX J0048.5-7302	HMXB	15.2	11.8	9.11 ± 0.69
138	SXP25.5	HMXB	18.1	14.3	10.74 ± 0.69
148	SXP152	HMXB	57.3	37.2	53.40 ± 1.38
149	SXP280	HMXB	32.4	50.9	167.23 ± 2.68
151	SXP304	HMXB	31.7	21.3	51.57 ± 2.25
186		<AGN> oxr	16.2	14.6	18.97 ± 1.16
187	SXP348	HMXB	95.0	31.1	38.86 ± 1.22
227	SXP1323	HMXB	67.8	63.1	115.24 ± 1.79
228	SXP726	HMXB	28.3	13.4	9.74 ± 0.68
230			14.6	8.9	6.47 ± 0.66
244		<AGN> o?	12.8	7.5	4.18 ± 0.50
287	2MASS J01015608-7210288	<HMXB>	11.1	6.6	3.33 ± 0.45
616	SMC3	SSS	54.1	197.5	226.66 ± 1.09
674	SXP202.5	HMXB	201.6	67.0	286.88 ± 4.23
816	SXP7.92	HMXB	10.4	14.4	7.17 ± 0.39
1400	2MASS J00534219-7253096	<HMXB>	152.1	10.3	25.21 ± 2.43
1560		<AGN> o?	19.3	3.1	4.29 ± 1.33
1582		<AGN> o?	11.2	3.9	2.85 ± 0.66
1592	SXP6.85	HMXB	4232.7	166.8	1110.92 ± 6.66
1784			16.7	4.6	5.02 ± 1.01
1907		<AGN> o?	10.2	3.2	2.17 ± 0.61
2228	SXP91.12	HMXB	81.6	50.9	51.75 ± 0.98
2519	SXP11.87	HMXB	800.7	99.5	263.98 ± 2.65
2563	SXP214	HMXB	117.9	32.9	36.40 ± 1.09
2716		<AGN> o?	10.7	3.5	2.23 ± 0.57

5. Individual X-ray sources in the SMC

5.1. A new X-ray view of the symbiotic binary SMC 3

During the survey observation 0601211301, the symbiotic binary SMC 3 was found at its highest X-ray luminosity as observed until now. This detection enables spectral analysis of the EPIC-pn data with unprecedented statistical quality. Four spectra from different intensity states allow to study the spectral evolution of the hot component of SMC 3. The light curve starting with the first ROSAT detection in 1990 is used to investigate the nature of the variability seen from this system. This study was published in Sturm et al. (2011b).

5.1.1. Previous studies of SMC 3

The symbiotic star SMC 3 (Morgan 1992) in the SMC was discovered as a SSS during the ROSAT all sky survey (Kahabka & Pietsch 1993). It is thought to be an interacting binary system, consisting of a cool M0 giant and a hot WD in a wide orbit. In this model accretion from the stellar wind of the giant donor onto the WD leads to steady hydrogen burning on the WD surface that powers the high X-ray luminosity (Kahabka & van den Heuvel 1997).

A series of ROSAT observations covering ~6 years (from October 1990 to November 1993 with the PSPC and from April 1994 to November 1996 with the HRI), revealed high X-ray variability (a factor of ≥80 in ROSAT PSPC count rate), which was explained by an eclipse of the WD by the donor star (Kahabka 2004). This scenario needs obscuration of the X-ray emission region by the dense stellar wind close to the giant to account for the shape and the long duration of several months of the eclipse ingress and egress.

An optical outburst between December 1980 and November 1981 of up to 3 mag in the *U*-band was reported by Morgan (1992). During this outburst no changes were detected in the *I*-band, and therefore, its origin was assigned to the hot stellar component. It is not clear whether the non-detection of SMC 3 with the Einstein satellite was due to X-ray inactivity before the optical outburst or to insufficient sensitivity (Kahabka 2004). The enrichment of nitrogen also suggests that there is evidence of a thermonuclear event (Vogel & Morgan 1994). Results from modelling multi-wavelength data of SMC 3 with non-LTE models under the assumption of a constant X-ray source were presented in Orio et al. (2007) and Jordan et al. (1996). Orio et al. (2007) find that the variability cannot be caused by photoelectric absorption and suggested a “real” eclipse by the red giant.

5.1.2. Observations and data reduction

SMC 3 was serendipitously observed four times with XMM-*Newton* at off-axis angles between 8′ and 14′. Table 5.1 lists details of the observations with the EPIC instruments operated in full-frame mode. In addition to the observation in October 2009 from the large-programme SMC survey, I analysed three archival observations from 2006 and 2007. The first observation in March 2006 revealed SMC 3 in a high intensity state, but suffered from very high background. These data were used in the study of

Table 5.1. XMM-*Newton* EPIC-pn observations of SMC 3.

ObsID	Date	Filter	Net Exp [s]	Net cts. (0.2−10.0 keV)	Bg[(a)]	Net cts. (0.2−1.0 keV)	Bg[(a)]	R_{sc}[(b)] [″]	R_{bg}[(b)] [″]
0301170501	2006 Mar 19	medium	10446[(c)]	8287	12%	8246	2%	19	30
0404680301	2007 Apr 11-12	thin	13986	170	13%	137	5%	16	50
0503000201	2007 Oct 28	medium	16607	451	9%	407	4%	21	40
0601211301	2009 Oct 3	thin	26535	39456	2%	39338	1%	69	55

Notes. [(a)] Ratio of background count rate to source count rate in the same energy band. [(b)] Radius of the source and background extraction region. [(c)] No GTI screening was applied.

Orio et al. (2007). The two observations in April and October 2007 showed the source at low intensity. The detection of the source in the later observation was noted by Zezas & Orio (2008).

To process the data, I used XMM-*Newton* SAS 10.0.0 with calibration files available until 17 June 2010, including the latest refinement of the EPIC-pn energy redistribution. Spectra were created as described in Sec. 3.3.13. X-ray images of the four observations, with marked selection regions are presented in Figure 5.1. For the observation in 2006, the EPIC-pn background count rate was between 500 and 2500 cts ks^{-1} $arcmin^{-2}$ (to be compared to the standard cutoff at 8 cts ks^{-1} $arcmin^{-2}$) and in order to retain any data, no background screening was applied. Since soft-proton flares usually show a rather hard spectrum, the contribution to the super-soft spectrum of SMC 3 was still acceptable (cf. Table 5.1). Since the MOS-spectra have lower statistical quality by a factor of 10 for such soft spectra and to avoid cross calibration effects between the EPIC instruments[1], this study is focusing on the EPIC-pn spectra. In the following, EPIC-pn spectra of single-pixel events are used.

5.1.3. Spectral analysis of the EPIC-pn data

I used `xspec` version 12.5.0x for spectral fitting. For all models, the Galactic photoelectric absorption was fixed at a column density of $N_{H,gal} = 6{\times}10^{20}$ cm^{-2} (Dickey & Lockman 1990) and elemental abundances according to Wilms et al. (2000), whereas the SMC column density was a free parameter with abundances at 0.2 for elements heavier than helium. At first, I investigated the recent EPIC-pn spectrum of 2009, which has unprecedented statistics compared to previous X-ray observations. For black-body emission, I obtain a best fit with $\chi^2/\mathrm{dof} = 213/74$ with the best-fit parameters: $N_{H,SMC} = 7.84^{+0.44}_{-0,24} \times 10^{20}$ cm^{-2}, $kT = (33.9 \pm 0.5)$ eV, and a bolometric luminosity of $L_{bol} = 6.25^{+1.08}_{-0.86} \times 10^{38}$ erg s^{-1}. This luminosity is super-Eddington (and leading to a WD radius $\sim 5-10$ times larger than expected for a 1 $M_\odot$ WD), which is often caused by the black-body approximation, as well as an overestimated temperature (see e. g. Greiner et al. 1991; Kahabka & van den Heuvel 1997, and references therein). The residuals around 500 eV (cf. Figure 5.2) suggest contribution of nitrogen line emission, as observed in post-nova X-ray spectra of SSS (e. g. Rohrbach et al. 2009). The quality of the fit was improved to $\chi^2/\mathrm{dof} = 119/72$ by including two Gaussian lines with fixed energy at 431 eV (N VI) and 500 eV (N VII) and line widths fixed to 0. The equivalent widths of -19 eV and -32 eV for the N VI and N VII lines, respectively, are physically plausible, but the residuals could at least partially be also caused by calibration uncertainties. Alternatively, allowing the oxygen abundance in the SMC absorption component as free parameter also improved the fit ($\chi^2/\mathrm{dof} = 123/73$), resulting in an oxygen abundance of $9.9^{+4.5}_{-2.7}$ times solar with an $N_{H,SMC} = 4.39^{+0.66}_{-0.79} \times 10^{20}$ cm^{-2}. A hard spectral component, which could possibly be caused by the wind nebula, is not seen in the spectrum. Adding

[1]EPIC Calibration Status Document, http://xmm2.esac.esa.int/external/xmm_sw_cal/calib/index.shtml

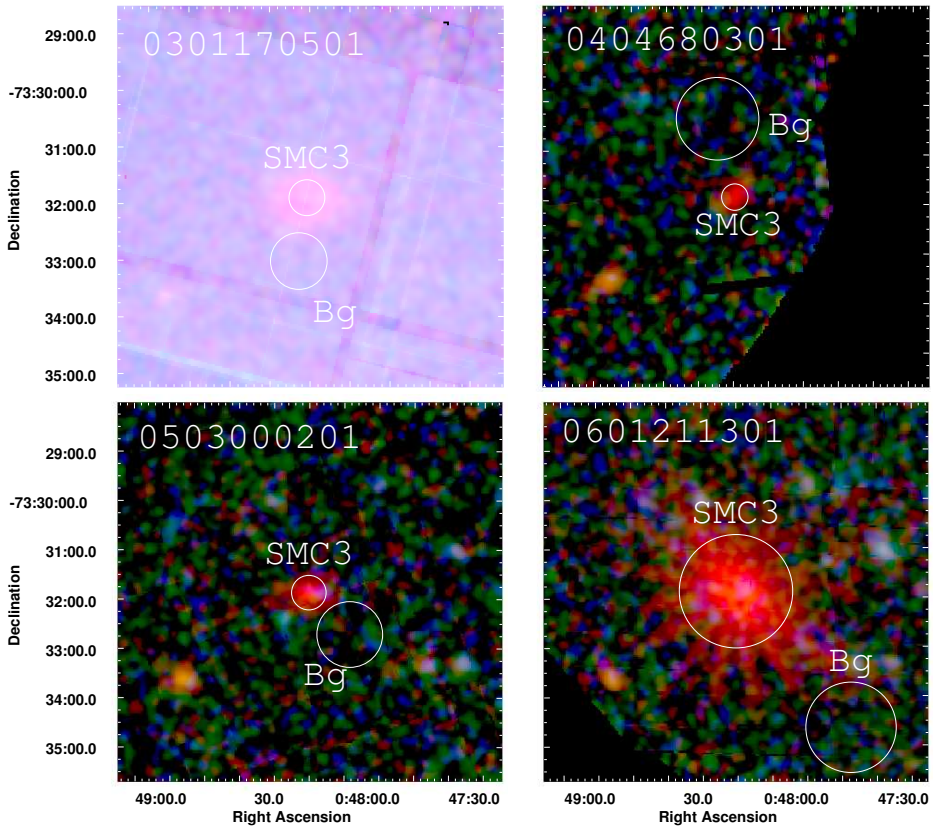

Figure 5.1. Combined EPIC colour images of SMC 3 from the four XMM-*Newton* observations. Red, green, and blue colours denote X-ray intensities in the (0.2−1.0) keV, (1.0−2.0) keV, and (2.0−4.5) keV bands. Circles indicate the extraction regions. In the upper left, the background is increased at higher energies.

an apec plasma emission component to the black-body emission, with fixed temperature of $kT = 500$ eV and SMC-abundances, yields an upper limit for the emission measure of $EM = 8.6 \times 10^{57}$ cm^{-3}.

The derived values for the absorption $N_{H,SMC}$ are well below the total SMC absorption in the direction of SMC 3 (~5×10^{21} cm^{-2}; see Stanimirović et al. 1999). This suggests that the symbiotic system is located on the near side of the large amount of H I present in the SMC bar.

I also tested non-local thermal equilibrium models provided by Thomas Rauch[2] (Rauch & Werner 2010). The best fit (χ^2/dof = 220/74) was found for a pure helium atmosphere with WD surface gravity log g = 5, $N_{H,SMC} = 2.4 \times 10^{20}$ cm^{-2}, kT=6.9 eV, and $L^{\rm unabs.}_{0.2-1.0{\rm keV}} = 1.57 \times 10^{37}$ erg s^{-1}. For a pure hydrogen atmosphere with log g = 9 the best fit results in χ^2/dof = 261/74 with $N_{H,SMC} = 1.1 \times 10^{21}$ cm^{-2}, kT=8.1 eV, and $L^{\rm unabs.}_{0.2-1.0{\rm keV}} = 2.59 \times 10^{38}$ erg s^{-1}. If the spectrum in fact contains emission lines, this might be the reason of the inferior fit of the non-LTE models, which produce spectra that are dominated by absorption lines from the WD atmosphere. Since the black-body spectrum resulted in a better fit, we decided to use this model in the further investigations.

To study the spectral evolution of SMC 3, I fitted the EPIC-pn spectra of all four epochs simultaneously with a set of models based on absorbed black-body emission. In each model only one individual parameter for each spectrum and two common parameters for all spectra were allowed to vary (see below). Since the statistical quality of the high-flux spectrum is far better than for the other spectra,

[2]http://astro.uni-tuebingen.de/~rauch/

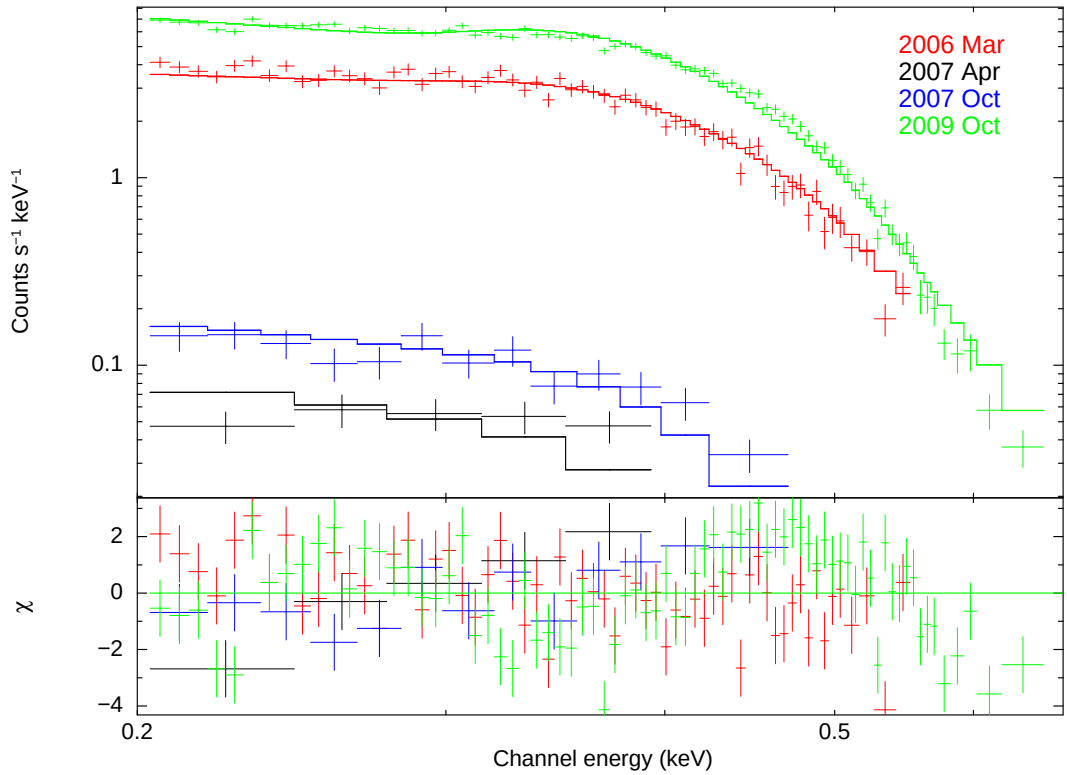

Figure 5.2. EPIC-pn spectra of SMC 3 together with the best-fit black-body model 3 with variable temperature. No significant emission is seen above 0.7 keV.

it also dominates the resulting χ^2. This leads to relatively bad fits for the simple black-body models. Adding emission lines would improve the fits (see above). However, given the limited spectral resolution of the EPIC-pn instrument it is not clear if the lines have any physical meaning. Because we were mainly interested in the evolution of spectral parameters, we decided to use the simplest model.

The first model (model 1 in Table 5.2) assumes temperature and luminosity not varying with time, while the absorbing column density can change with time. This corresponds to the eclipse model with varying absorption by the dense donor wind, as suggested by Kahabka (2004). This model gives an insufficient fit to the data (see Table 5.2). Although, the fit is statistically dominated by the two high-flux spectra, the spectral shape of the low-flux spectra cannot be reproduced by a high column density which predicts much less flux at lowest energies (cf. Figure 2.5).

For model 2, I fixed the spectral shape (same temperature and absorption) and allowed the luminosity to change (i. e. fitting individual normalisations, which corresponds e. g. to a variable size of the emission area). This fits the data much better (Table 5.2). Within the systematic uncertainties the spectral parameters are in agreement with the black-body model of Orio et al. (2007).

An even better fit was achieved by the third model with varying source temperature. The corresponding black-body luminosities were related to the temperature ($L_{\rm bol} \propto T^4$). The results for this model are again described in Table 5.2 and the individual spectra with the model fit are plotted in Figure 5.2.

Table 5.2. Results from the simultaneous black-body fit to the EPIC-pn spectra.

Model 1 T and $L_{\rm bol}$ constant with time $N_{\rm H}$ variable	Model 2 $N_{\rm H}$ and T constant with time $L_{\rm bol}$ variable	Model 3 $N_{\rm H}$ constant with time T variable, $L_{{\rm bol},i} = L_{\rm bol,1}(T_i/T_1)^4$
$kT = (32.5 \pm 0.5)$ eV	$N_{\rm H} = (0.77 \pm 0.04) \times 10^{21}$ cm^{-2}	$N_{\rm H} = (0.77 \pm 0.02) \times 10^{21}$ cm^{-2}
$L_{\rm bol} = (8.8 \pm 1.6) \times 10^{38}$ erg s^{-1}	$kT = (33.7 \pm 0.5)$ eV	$L_{\rm bol,1} = (5.5 \pm 0.3) \times 10^{38}$ erg s^{-1}
$N_{\rm H,1} = (1.08 \pm 0.05) \times 10^{21}$ cm^{-2}	$L_{\rm bol,1} = (4.43 \pm 0.78) \times 10^{38}$ erg s^{-1}	$kT_1 = (32.7 \pm 0.2)$ eV
$N_{\rm H,2} = (6.75 \pm 0.48) \times 10^{21}$ cm^{-2}	$L_{\rm bol,2} = (0.12 \pm 0.02) \times 10^{38}$ erg s^{-1}	$kT_2 = (24.3 \pm 0.3)$ eV
$N_{\rm H,3} = (6.91 \pm 0.23) \times 10^{21}$ cm^{-2}	$L_{\rm bol,3} = (0.18 \pm 0.03) \times 10^{38}$ erg s^{-1}	$kT_3 = (25.3 \pm 0.2)$ eV
$N_{\rm H,4} = (0.81 \pm 0.05) \times 10^{21}$ cm^{-2}	$L_{\rm bol,4} = (6.47 \pm 1.15) \times 10^{38}$ erg s^{-1}	$kT_4 = (33.8 \pm 0.4)$ eV
χ^2/dof = 940/154 = 6.10	χ^2/dof = 383/154 = 2.49	χ^2/dof = 365/154 = 2.37

5.1.4. The long-term X-ray light curve of SMC 3

To analyse the temporal behaviour of the system, I reconciled the X-ray light curve of SMC 3 starting from the first detection by ROSAT in 1990. To convert the ROSAT count rates, provided by Kahabka (2004), into fluxes, I simulated a ROSAT PSPC spectrum based on the spectral model derived from the simultaneous fit with variable normalisation and the PSPC detector response. This yields a conversion factor of 1.54×10^{-11} erg cm^{-2} cts^{-1}. All fluxes are computed for the (0.2−1.0) keV band. Because of the dominant statistics of the XMM-*Newton* high-flux spectrum in the model fit, this factor rather corresponds to the high-flux state. Using the model with variable temperature, the conversion factor for the low flux can be lower by a factor of $\lesssim$2. Analogously, for the ROSAT HRI, this simulation yields a conversion factor of 4.63×10^{-11} erg cm^{-2} cts^{-1}.

I searched the *Swift* archive for observations covering SMC 3. The source was detected in observation 00037787001 with ∼3 ks exposure on 18 August 2008. The source and background spectrum was extracted with `xselect` and the effective area file was created using `xrtmkarf`. The resulting spectrum contains 135 net counts, which is insufficient to distinguish between the above described models. Thus I fitted only the normalisation and assumed the spectral shape according to the simultaneous fit to the EPIC-pn spectra with variable normalisation. This fit yields a flux of $2.61^{+0.26}_{-0.15} \times 10^{-12}$ erg cm^{-2} s^{-1}.

To derive XMM-*Newton* fluxes, I integrated the best-fit model with variable temperature as described above. The source flux during a *Chandra* observation in February 2003 was deduced from the parameters of the best-fit black-body model reported by Orio et al. (2007).

Figure 5.3 shows the X-ray light curve of SMC 3 since the first detection by ROSAT in 1990. By modelling the light curve with several eclipses, we find, that (i) the transition from high to low intensity occurs over a long time period and that (ii) the time scales of the duration of the high and low intensity intervals are of the same order. Thus, instead of eclipses the light curve may also be interpreted by several periodic outbursts. For demonstration, the dashed line in Figure 5.3 shows a fit with a sine function. To account for uncertainties in the flux conversion and cross calibration between the different instruments I included a 20% systematic error on the flux. As best-fit ephemeris for the X-ray minimum I then obtain (90% confidence errors):

$$\mathrm{MJD}_{\rm min,x} = (49382 \pm 10) + \mathrm{N} \times (1634 \pm 7) \text{ days.}$$

The relatively high flux measured in the last XMM-*Newton* observation might suggest possible changes in the amplitude of the modulation.

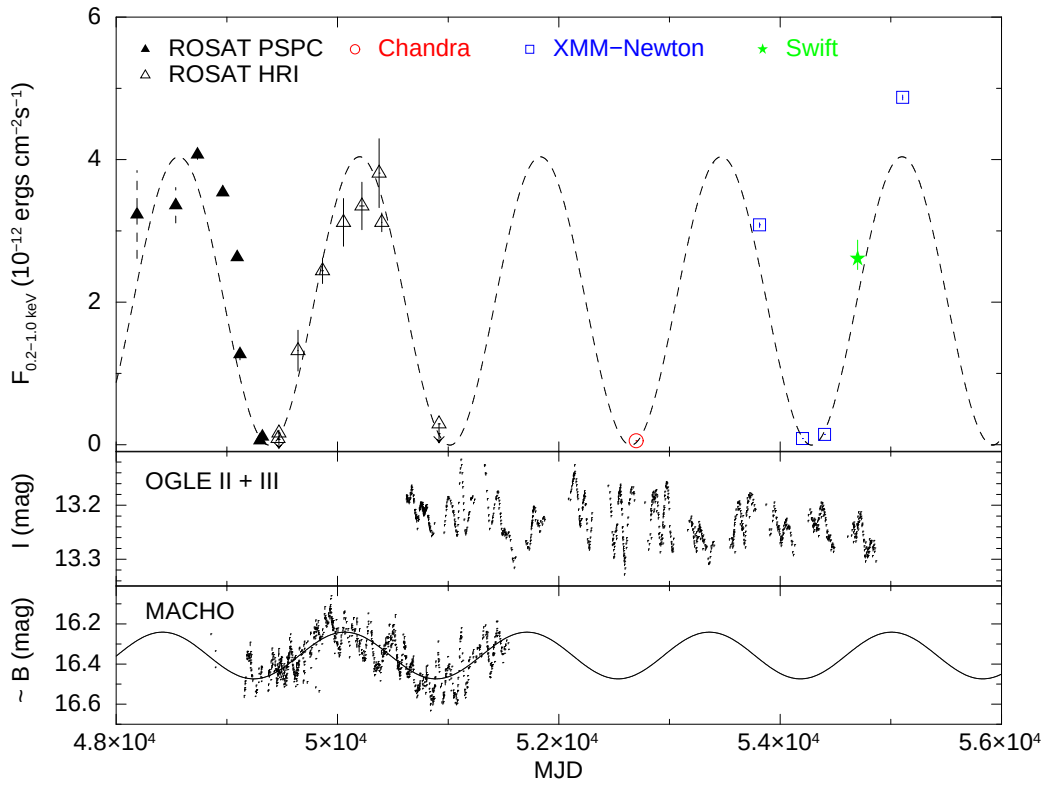

Figure 5.3. The (0.2−1.0) keV X-ray light curve of SMC 3 (upper panel), the light curves in the *I*-band (OGLE, middle panel) and the approximate *B*-band (MACHO, lower panel). The dashed line shows the best-fit sine function to the X-ray light curve and the solid line the best-fit sine function to the MACHO light curve (see text).

5.1.5. MACHO and OGLE data

The OGLE II (Udalski et al. 1997) and OGLE III (Udalski et al. 2008) *I*-band as well as the MACHO *B*-band light curves are shown in the lower two panels of Figure 5.3. The calibrated MACHO light curve was shifted in magnitude to match its average *B* magnitude with that measured by Zaritsky et al. (2002). In the *I*-band of OGLE II and the *B*-band of MACHO, Kahabka (2004) found correlating quasi-periodic oscillations with periods around 110 days, which might be related to pulsations of the red giant star. These short variations are also present in the OGLE III data. With the OGLE III data, which cover a much longer time interval, we can now rule out a significant variation with the 1630 day cycle as suggested by the X-ray light curve. As noted by Kahabka (2004), the MACHO light curve shows a quasi sinusoidal modulation with a period of ~4 years, in addition to shorter variations. A fit of a sine function to the MACHO *B*-band data (solid line in Figure 5.3), results in an ephemeris for the optical minimum of

$$\mathrm{MJD}_{\mathrm{min,B}} = (49242 \pm 9) + \mathrm{N} \times (1647 \pm 24)\ \mathrm{days}.$$

To account for the short-term variations I added a systematic error of 0.05 mag to the *B*-band magnitudes. Formally, the fits to X-ray and MACHO light curves indicate a phase shift of (140 ± 14) days (optical preceding the X-rays) while the periods agree within the uncertainties. However, it should be noted that the MACHO light curve covers only ~1.5 cycles and is superimposed by the short-term variations, which may influence the results.

5.1.6. Discussion

SMC 3 was observed with XMM-*Newton* at four epochs, covering the super-soft X-ray source twice at high and twice at low intensity. A strong variation in the X-ray flux by a factor of more than ∼50 between minimum and maximum intensity is found in the (0.2−1.0) keV band. I showed that the light curve can qualitatively be described by a sine function with a period of 1633 days. This simple model can only be a crude approximation of the light curve, but the ∼20 year coverage indicates a high regularity of the period with similar duration of high- and low-intensity intervals. The regularity of the X-ray light curve, with meanwhile four observed minima, strongly supports the interpretation of the 4.5 year period as the orbital period of the binary system. Assuming masses of 2 $M_\odot$ and 1 $M_\odot$ for the M-giant and the white dwarf, respectively, the orbital period implies a semi-major axis of the binary system of 3.9 AU.

I analysed the spectral evolution and found, that the variability of the X-ray flux cannot be explained by photoelectric absorption by neutral gas with varying column density. To avoid the strongly energy-dependent attenuation of soft X-rays, Kahabka (2004) discussed absorption due to highly ionised gas. In this picture, the strong X-ray source ionises the stellar wind around it. Compton scattering on free electrons would then reduce the X-ray flux along the line of sight most efficient when looking through the dense innermost regions near the M-star. This mimics variable intensity with little energy dependence (no significant change of spectral shape). Using a Compton scattering model (`cabs` in `xspec`), instead of variable normalisation, would require a column density of $>4.8 \times 10^{24}$ cm^{-2} (completely ionised absorber) to reduce the X-ray intensity from maximum to minimum. In this picture, scattering of X-rays into the line of sight is neglected or at least assumed not to change significantly between the two states. Using the estimated mass, size and density of the ionised wind region as given by Orio et al. (2007) yields a column density to its centre of 5.8×10^{23} cm^{-2}. This is a factor of ∼8 lower than the estimate from Compton scattering and may be explained by the simplified assumption of a constant wind density while the line of sight during the low intensity observations should pass through the denser wind regions near the giant star. In this picture, most of the stellar wind must be ionised, consistent with the fact that we do not see a variable contribution of photoelectric absorption by neutral gas. In this model, the low intensity can still be explained by an eclipse of the X-ray source by the giant star *and* its stellar wind. An eclipse by the star only would be short (∼10% of the orbital period) with sharp ingress and egress, while the dense inner wind regions cause a long gradual eclipse ingress (and egress) by increasing (decreasing) Compton scattering along the line of sight. This geometric model with scattering in the circum-stellar material is consistent with both the gradual ingress/egress of the X-ray light curve and the spectral changes (no significant variation in photoelectric absorption). The exact shape of the light curve should then depend on the geometry of the binary system and the distribution of free electrons in the stellar wind.

The spectral analysis shows, that the X-ray variability can alternatively be dominated by temperature changes, varying between 24 and 34 eV. Assuming a constant size of the emitting area, this corresponds to a variation in $L_{\rm bol}$ (for spherically symmetric emission) by a factor of 4.3. The larger variation in observed instrumental count rates would then be caused by shifting the spectra with lower temperature out of the sensitive energy band of EPIC. This behaviour is independent of the model used. The spectra show clear softening, which is parametrised by a temperature change (similar if black-body or atmosphere models are used). A possible scenario might be an elliptical orbit of the white dwarf around the M-giant or equatorial mass ejection with inclined WD orbit, causing accretion at different rates. Variable accretion, even at low level, can lead to large temperature changes in the burning layer (Paczynski & Rudak 1980). Similar scenarios were used to explain X-ray variability in other SSS (e. g. AG Dra, Greiner et al. 1996). However, I note, that in those cases usually an

anti-correlation of X-ray and optical luminosity is observed, whereas in the case of SMC 3 these two are clearly correlated.

Assuming the same temperature and absorption (and no change in Compton scattering) for the low and high intensity spectra, the inferred radii would be different by a factor of ∼8 to account for the factor of 60 difference in $L_{\rm bol}$. In general for stable shell burning on the WD surface, an increase of the hydrogen burning envelope (e. g. due to a higher accretion rate) leads to an increase of both temperature and radius (Fujimoto 1982). Increasing temperature and declining Compton scattering both lead to an increasing X-ray luminosity. It depends on the orientation of the orbit with respect to the observer, how much the two effects act in phase. Additional temperature variations may therefore reduce or increase the amount of Compton scattering required to explain the X-ray luminosity variations.

Superimposed on the general long term variation in the X-ray light curve, we probably see effects imposed by the donor star. The ∼110 days brightness variations seen in the *I*-band suggests changes in the stellar wind, which can lead to variations in the mass accretion rate onto the white dwarf. Since the 1630 day X-ray period is not visible in the *I*-band, it is unlikely that this period is caused by the cool stellar component, which seems to remain rather unaffected by the process producing this variation. In the *B*-band, both modulations are seen, the 1630 day period derived from the X-rays and the ∼110 day variations which correlate with the *I* mag (as already pointed out by Kahabka 2004). Therefore, the cool companion star and the region where the X-ray emission is produced most likely both contribute to the *B*-band. If viewing effects produce the variation in the *B*-band in a similar way as in the X-rays (by changing extinction) or if heating of the cool star by the X-ray source is causing this variation remains unclear: While Kahabka (2004) finds X-ray heating insufficient to account for the observed *B*-band modulation, Orio et al. (2007) discuss irradiation effects influencing the mass outflow as very important.

5.2. The Be/white dwarf candidate XMMU J010147.5-715550

One of the newly found super-soft X-ray source candidates (№ 235, Table 4.4) correlates with the emission-line star AzV 281 in the SMC. Binary-system evolution models predict, that Be/WD systems might be seven times more frequent than Be/NS systems (Raguzova 2001), but no Be/WD system is known so far in the SMC in contrast to the large number of Be/NS systems (∼90). Only one Be/WD SSS system has been proposed previously, XMMU J052016.0-692505 (Kahabka et al. 2006) in the LMC. I analysed the X-ray data and the optical counterpart to further investigate this system. This study was published in Sturm et al. (2012b).

5.2.1. Analyses of X-ray data and results

The source was detected three times in images of calibration observations of the supernova remnant 1E0102.2-7219 at off-axis angles of ∼10.5′ on MJD 51650, 51651, and 52014. The error weighted average of the astrometric boresight corrected best-fit positions is RA (J2000)=$01^{\rm h}\ 01^{\rm m}\ 47\overset{\rm s}{.}58$ and Dec (J2000)=$-71^\circ\ 55'\ 50\overset{''}{.}7$ with a 1σ uncertainty of 0.85″.

There is no star within 10″, sufficiently bright to cause optical loading, which might fake a SSS. The multiple detections rule out detector effects for spurious detections and confirm the veritableness of the X-ray source. The source is also listed in the XMM-*Newton* incremental source catalogue (2XMM J010147.5-715550, Watson et al. 2009).

Detected fluxes *F*, detection likelihoods *ML* and net exposures of the individual observations are

Table 5.3. X-ray observations of XMMU J010147.5-715550.

ObsID	MJD	F in (0.2–1.0) keV (10^{-16} erg cm^{-2} s^{-1})	ML	Exp. (ks)
0123110201	51650.9	92.8 ± 11.9	88.0	17.9
0123110301	51651.3	74.3 ± 13.7	31.5	11.7
0135720601	52014.1	99.3 ± 16.6	36.0	13.4
0135720801†	52269.0	32.0 ± 10.5	5.8	27.6
0135720901	52385.0	25.1 ± 11.1	6.6	10.1
0135721001	52412.5	12.4 ± 8.8	2.1	9.4
0135721001†	52412.7	66.1 ± 29.8	2.9	7.5
0135721101†	52560.3	15.1 ± 11.8	0.0	23.1
0135721301†	52622.3	< 11.1	0.2	28.4
0135721401†	52749.8	< 12.4	0.1	30.4
0135721501	52939.5	< 9.7	0.1	24.2
0135721701	52959.4	< 7.4	0.0	25.2
0135721901†	53123.5	< 12.3	0.2	33.0
0135722001†	53304.5	< 11.2	1.4	31.6
0135722101	53316.3	8.6 ± 5.0	0.6	24.0
0135722301†	53317.1	< 26.5	0.0	14.0
0135722401†	53292.6	< 20.8	0.0	30.4
0135722501‡	53478.1	< 15.0	0.0	23.8
0135722601†	53679.5	< 7.9	0.0	29.0
0135722701‡	53845.3	17.5 ± 10.9	1.3	30.2
0412980101†	54044.2	< 9.2	0.1	31.0
0412980201‡	54215.7	< 11.8	0.0	19.6
0412980301†	54399.6	12.0 ± 6.7	0.1	35.0
0412980501‡	54575.6	< 16.7	0.0	22.0
0412980701†	54785.0	< 13.9	0.0	28.6
0412980801‡	54934.2	< 15.3	0.0	6.5
0412980901†	55125.5	15.4 ± 10.0	0.5	28.6
0412981001‡	55307.2	27.2 ± 16.6	0.2	27.3

Notes. Combined EPIC-pn and EPIC-MOS source detection. Fluxes are calculated from count rates by assuming the best-fit black-body model. Uncertainties are for 1σ. For observations marked with †, the source was not covered by EPIC-pn, but both MOS cameras. For observations, marked with ‡, the source was in the FoV of EPIC-MOS2 only. In all other observations, the source was observed with all EPIC instruments.

summarised in Table 5.3. In later calibration observations, the source was marginally detected on MJD 52269, 52385, and 52412 and not detected above a detection likelihood $ML > 2$ in any of the 21 observations after this date. In the later observations, the source was mostly not covered by EPIC-pn.

I merged the EPIC-MOS1 and -MOS2 data of these latter observations and measured counts in circular source and background regions with 20″ radius. This yields 18±16 and 23±18 net counts in the (0.2−1.0) keV band. For vignetting corrected exposures of 182 ks from MOS1 and 235 ks from MOS2, this translates into a 3σ flux limit of 10.2 $\times 10^{-16}$erg cm^{-2} s^{-1} and indicates a significant source variability of a factor of at least ∼10.

Hardness ratios (see Sec. 3.3.8) were used to characterise the source spectrum. For the first three observations, the point-source catalogue gives $HR_1 = -0.10 \pm 0.12$, -0.69 ± 0.15, and -0.13 ± 0.16 and $HR_2 = -0.85 \pm 0.11$, -0.09 ± 0.42, and -1.00 ± 0.13. Based on hardness ratio criteria, the source was classified as SSS in Sec. 4.3.2. The 2XMM catalogue gives $HR_1 = -0.45 \pm 0.07$ and $HR_2 = -0.93 \pm 0.07$, consistent with the SSS classification.

I extracted EPIC-pn source and background spectra from the first three observations as describe in

Sec. 3.3.13, but in the (0.15−2.0) keV band and with the XMM-Newton SAS version 10.0.0. The EPIC-pn single- and double-pixel spectra were used in the following. The spectra have 55, 27, and 15 net counts in the (0.15−2.0) keV band. I fitted black-body (bb), power-law (pl), thermal-plasma emission (apec), and several non-local thermal-equilibrium (nlte, Rauch & Deetjen 2003) models using `xspec` version 12.6.0k with C statistic (Cash 1979). The photoelectric absorption is described by a Galactic component with column density fixed to a maximum of $N_H^{gal} = 6{\times}10^{20}$ cm^{-2} (Dickey & Lockman 1990) and elemental abundances according to Wilms et al. (2000) and an additional (SMC and source intrinsic) absorption with free column density and abundances set to 0.2 for elements heavier than helium (Russell & Dopita 1992). To test for a Be/X-ray binary with soft excess, I fitted the combination of a black-body and power-law model (bb+pl).

Fitting the three EPIC-pn spectra simultaneously by assuming a common black-body temperature, I found no significant differences for the fluxes (relative: 1.0, $0.91^{+0.50}_{-0.36}$, and $0.93^{+0.61}_{-0.41}$). Thus, I fitted the same models to all three spectra. The co-added spectrum, rebinned to 3σ significance per bin for better illustration, together with the best-fit bb model is shown in Figure 5.4. The detected flux in the (0.2−1.0) keV band is $(9.4 \pm 2.4) \times 10^{-15}$ erg cm^{-2} s^{-1}. The best-fit model parameters are listed in Table 5.4. Statistical uncertainties and limits are for 90% confidence. To estimate the goodness of the fit, in addition to the C statistics, also the χ^2 statistics is given, which is derived by fitting the models to spectra, binned to a minimum of 10 cts bin^{-1}. These fits result in similar parameters as those given in Table 5.4 derived with C statistics. Most models give an acceptable fit. Possible physical scenarios for these models are discussed in Sec. 5.2.3. To demonstrate the parameter dependence on modelling, the best-fit values for two nlte models are listed, for surface gravity $\log(g) = 9$ with solar (nlte_S, $Z = Z_\odot$) and halo (nlte_H, $Z = 0.1Z_\odot$) abundances.

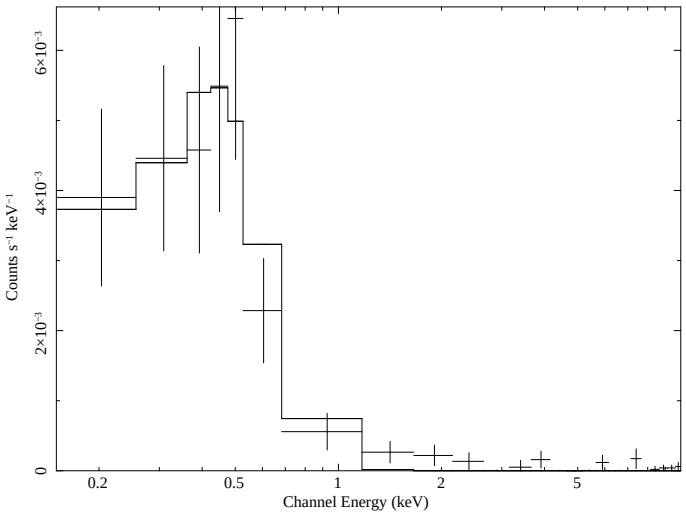

Figure 5.4. Co-added spectrum of three EPIC-pn observations of XMMU J010147.5-715550 together with the best-fit black-body model.

5.2.2. The optical counterpart

The MCPS (Zaritsky et al. 2002) lists two possible counterparts within the X-ray position uncertainty. The fainter one ($V = 17.0$ mag), with angular separation of 2.1″, has a proper motion of ∼580 mas yr^{-1} in the USNO-B1.0 catalogue (Monet et al. 2003). It is therefore a Galactic foreground star.

The brighter counterpart at a distance of 1.4″, has $U = (13.26 \pm 0.03)$ mag, $B = (14.40 \pm 0.02)$ mag, $V = (14.47 \pm 0.04)$ mag, and $I = (14.30 \pm 0.04)$ mag. This star (AzV 281) was classified as a B0 star in the SMC by Azzopardi et al. (1975) and as O7III by Massey (2002). The star corresponds

Table 5.4. Spectral fitting results for several models.

model	N_H^{gal}	N_H^{smc}	kT	Γ	F	C	χ^2_{red}
bb	$6^{(f)}$	<9	97^{+15}_{-21}	–	22	90.6	0.95
$nlte_S$	$6^{(f)}$	<3	80^{+3}_{-6}	–	22	91.2	1.02
$nlte_H$	$6^{(f)}$	53^{+7}_{-6}	26^{+2}_{-1}	–	170000	91.7	0.74
apec	<46	–	92^{+97}_{-65}	–	35	107.9	1.72
pl	$6^{(f)}$	<15	–	$5.0^{+2.3}_{-1.2}$	120	89.5	0.97
bb+pl	$6^{(f)}$	<14	88^{+17}_{-24}	$1.0^{(f)}$	23+8	86.6	0.95

Notes. N_H in 10^{20} cm^{-2}, kT in eV, unabsorbed flux F in the (0.2–1.0) keV band in 10^{-15} erg cm^{-2} s^{-1}. Fixed values are marked with $^{(f)}$.

to the Hα emission-line object [MA93] 1284 and LIN 384 (Meyssonnier & Azzopardi 1993; Lindsay 1961). Therefore, the optical counterpart most likely is an O7IIIe–B0Ie star. An *I*-band image from OGLE III (Udalski et al. 2008) of the surroundings of this star (OGLE III SMC113.5 8) is shown in Figure 5.5.

The *I*-band OGLE III light curve of AzV 281 is compared to the X-ray light curve in Figure 5.6. It exhibits an increasing trend in brightness superimposed by sinusoidal variations. A fit of a linear plus sine function (solid line in Figure 5.6) results in a constant flux increase of (-0.01687±0.00005) mag yr^{-1}, a sine amplitude of (0.0240±0.0002) mag, and a period of (1264±2) days. Uncertainties are given for 1σ confidence. A Lomb-Scargle (Lomb 1976; Scargle 1982) periodogram did not reveal any further significant variability from the source.

The star is included in the NIR 2MASS catalogue (Skrutskie et al. 2006, ID 01014789-7155512, $J = (14.24 \pm 0.03)$ mag, $H = (14.21 \pm 0.03)$ mag, $K = (14.04 \pm 0.05)$ mag, on MJD 51034) and in the IRSF/SIRIUS catalogue (Kato et al. 2007, ID 01014790-7155512, $J = (14.44 \pm 0.02)$ mag, $H = (14.36 \pm 0.01)$ mag, $K = (14.24 \pm 0.03)$ mag, on MJD 52535, magnitudes are converted to the 2MASS system). In Figure 5.7, the optical and NIR fluxes, corrected for $E(B-V) = 0.08$, are compared to Kurucz stellar atmosphere models for a B1V and an O7V star both normalised to the dereddened *U*-band flux. The NIR excess and NIR variability provide further evidence for a Be star. Remarkably, the NIR flux decreased significantly during or before the time of the X-ray detections.

5.2.3. Discussion

I analysed XMM-*Newton* X-ray data and OGLE III photometry of XMMU J010147.5-715550. In the following I will discuss possible classifications of the source:

A Galactic star can produce soft coronal X-ray emission. In this case the fainter object could be the true counterpart. But the emission of stars extends to higher energies than we see from the SSS causing a positive HR_1 in general (Pietsch et al. 2004; Stiele et al. 2011). Also, the derived χ^2_{red} of the apec model suggests formally that a description of the spectrum by a thermal plasma is less likely than by the other models.

A cooling isolated compact object, i. e. a NS or PG 1159 star, can emit super-soft X-rays. We would not expect to see an optical counterpart. In both cases, we cannot explain the variability, seen in the X-ray light curve.

For an *AGN* with very soft X-ray emission and with a faint undetected optical counterpart, we expect to see the Galactic and total SMC absorption in the line of sight. The total SMC column density in the direction of the source is $N_{H,SMC} = 5.1 \times 10^{21}$ cm^{-2} (Stanimirović et al. 1999). For the power-law

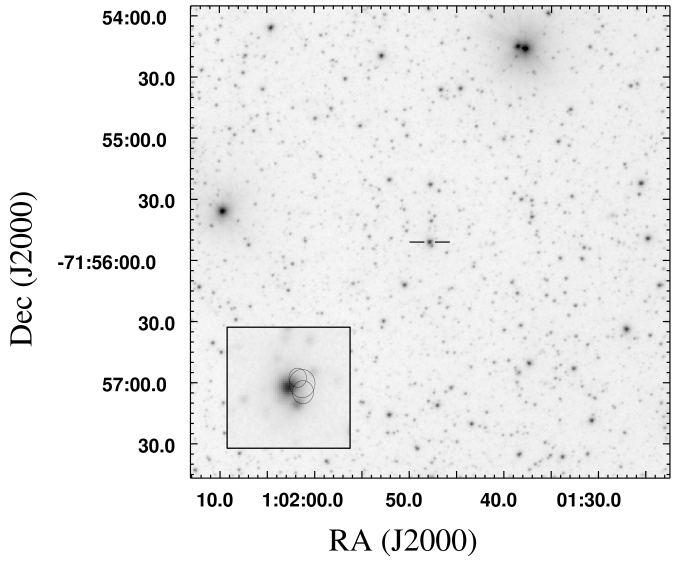

Figure 5.5. *I*-band finding chart from OGLE. Lines mark OGLE III SMC113.5 8. The zoom-in shows the optical counterpart over plotted with the positions of the three X-ray detections with 1σ radii.

model an $N_{H,SMC} < 1.5 \times 10^{21}$ cm^{-2} is derived, which seems to contradict the AGN assumption.

A CV in the SMC, which by chance correlates with AzV 281, can account for the super-soft emission. However, there is no accretion powered system known with super-soft emission exceeding 10^{33} erg s^{-1}, which is below the observed luminosity of XMMU J010147.5-715550 for the distance of the SMC. In the case of nuclear surface burning, higher luminosities can be reached (e. g. CAL 83 in the LMC). This would need a highly obscured WD, as discussed below. Another possibility for variable super-soft X-ray emission would be the rare case of a nova explosion. Here, super-soft emission is observed up to 2–5 years (Henze et al. 2011) after outburst. However, a nova explosion in this system is not known, which of course could have been missed. Due to the low nova rate in the SMC (only 3 novae were discovered during the last 10 years) this is an unlikely scenario.

A Galactic CV cannot be excluded with the available data. E. g. the Galactic star could contain a WD companion. In this case, a soft intermediate polar (Haberl & Motch 1995) could account for the spectral properties, but only a handful of these systems is known in the Galaxy so far.

To estimate the chance for a random coincidence of a SSS or SSS candidate (14 in total) with a blue emission-line star, I used a subset of early-type SMC stars ($V < 17$ mag, -0.5 mag $< B - V < 0.5$ mag, -1.5 mag $< U - B < -0.2$ mag, see Sec. 4.3.3) from the MCPS which correlate with an emission-line object from MA93. This sample (1748 sources inside the observed XMM-*Newton* field) was correlated with X-ray sources, which fulfil the criteria for super-soft X-ray emission and whose coordinates were shifted by multiples of the maximal correlation distance (Sec. 4.2.2). Correlations were accepted with an angular separation of $d \leq 3.439 \times (\sigma_1^2 + \sigma_2^2)^{1/2}$, where σ was estimated to $0.3''$ and $2.0''$ for the MCPS and MA93 sources, respectively. The XMM-*Newton* sources have source-individual position uncertainties of $\sim 1''$. In 440 runs, only 3 chance correlations were found. Analogously, using a set of USNO-B1.0 sources with proper motions >50 mas yr^{-1} (134780 sources) results in 773 chance coincidences. This further affirms AzV 281 as the most likely optical counterpart. Also the coincidence of the X-ray emission with the NIR-flux minimum further supports the identification of the super-soft X-ray source with AzV 281.

From a *Be/NS system* one would expect outbursts with hard X-ray emission during accretion, which has not been observed for this system, although it was monitored regularly since 2000. Also, observing only super-soft X-ray emission is atypical for a Be/NS system, as dominant hard emission is

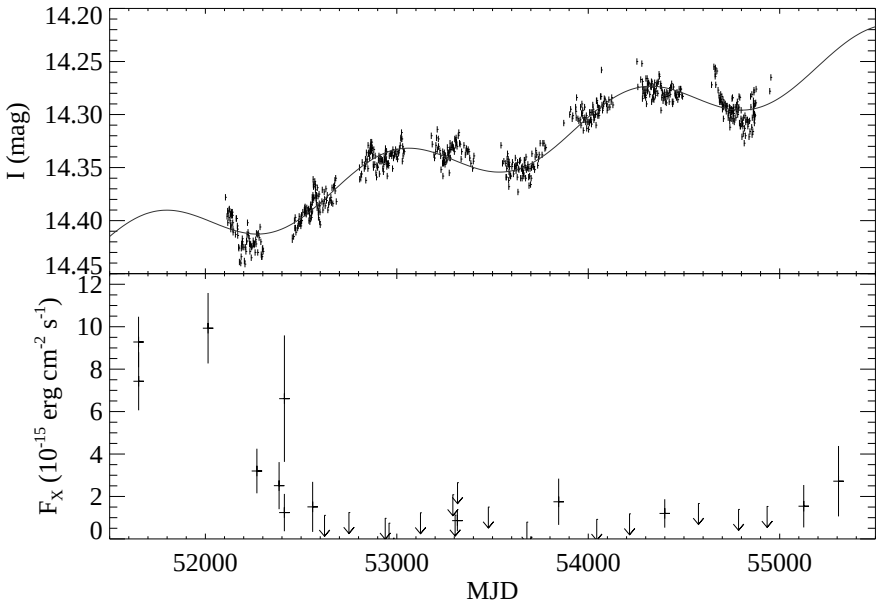

Figure 5.6. *Top: I*-band light curve from OGLE III. *Bottom:* X-ray flux in the (0.2−1.0) keV band.

expected in addition to a soft excess (Hickox et al. 2004). Even in the extreme case of an outburst of RX J0103.6-7201 (Eger & Haberl 2008), a hard X-ray component is present and the soft component extends to higher energies. From the bb+po model, a limit for $L_{\rm bb}/L_{\rm X}$ of >0.5 is derived in the (0.15−10.0) keV band, proofing the dominance of the thermal component. Therefore, the system is less likely a classical Be/X-ray binary.

In contrast to the former possibilities, a *WD/Be system* can account for both the super-soft X-ray emission and the variability. Black-body emission is a crude approximation to the spectra of SSSs (Rauch & Werner 2010). Physically more meaningful are NLTE models, but higher statistics and high resolution spectra would be necessary to constrain the parameters. To demonstrate the parameter dependence on elemental abundances two NLTE models are listed in Table 5.4. Solar abundances result in similar parameters as the black-body model with an emission radius of (73−106) km compared to (19−75) km from the bb model. Halo abundances result in a higher absorption, higher luminosity and an emission radius of (90 000−190 000) km. For an object in the SMC, abundances between solar and halo values ($Z_{\rm smc} \approx 0.2 Z_{\odot}$, Russell & Dopita 1992; Dias et al. 2010) are expected. Therefore, the black-body emission radius is rather a lower limit. This further demonstrates, that luminosity and absorption cannot be determined uniquely for XMMU J010147.5-715550 and that the spectra might be compatible with absorbed emission from a WD and luminosities sufficiently high for surface burning. The presumable optical counterpart shows properties typical for a Be star. This makes the system the second candidate for a SSS Be/WD binary after XMMU J052016.0-692505 in the LMC (Kahabka et al. 2006).

The X-ray turn-off around MJD 52500 can be caused by an exhaustion of the nuclear burning on the WD, as it occurs for post-nova SSSs, if the accretion rate is too low for stable nuclear burning. In the case of ongoing mass transfer, reignition of nuclear burning on the WD is possible in a nova explosion, followed by another super-soft X-ray emission state. More likely, the decrease in soft X-rays in the later observations might be explained by increasing photoelectric absorption due to a build-up of the

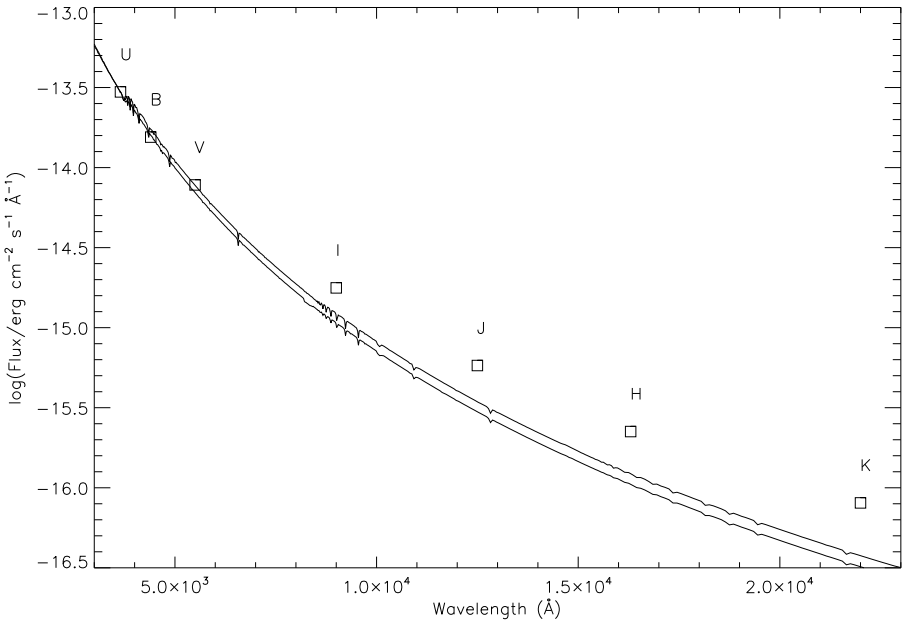

Figure 5.7. Dereddened optical (Zaritsky et al. 2002) and NIR (Kato et al. 2007) fluxes (squares) compared to a Kurucz model atmosphere for a B1V (upper line) and an O7V (lower line) star both normalised to the *U*-band flux. Courtesy of Malcolm Coe.

decretion disc around the Be star. An additional absorbing column density of $N_H \gtrsim 10^{22}$ cm^{-2} would be required for a non-detection of XMMU J010147.5-715550 in the merged images. Be stars can loose and rebuild their discs on a time scale of some years including intervals without a disc of some hundred days (Reig 2011; Wisniewski et al. 2010). The decrease of the NIR flux before or during the X-ray active phase and the low photoelectric absorption during the three X-ray detections suggest this scenario. The X-ray detections have only a small overlap with the optical light curve, but since X-ray turn-off, the *I*-band shows an increase in flux, which can be caused by the recreation of a disc. I note, that the optical light curve of XMMU J052016.0-692505 (cf. Fig. 4 in Kahabka et al. 2006) has similar characteristics of both a long-term increase in the *I*-band and a periodicity around one thousand days.

The low X-ray absorption suggests a location of the system on the near side of the SMC bar. Also, the system intrinsic absorption along the line of sight must have been low during the X-ray detections. If the 1264 d period is caused by binarity, we get a relatively large separation of 5.7 AU ($\sim 140 R_*$) for $M_{\rm WD} = 1 M_\odot$ and $M_* = 15 M_\odot$. But the realness and nature of the periodicity are uncertain, since the OGLE light curve covers only about two cycles. While Raguzova (2001) argue that most Be/WD systems are not detectable in X-rays due to absorption by the decretion disc, truncation of the disc, as it is known from Be/NS systems with low excentricity (Okazaki & Negueruela 2001) might only allow accretion during disc instabilities. Also, the absorption by the SMC has to be low, to be able to observe such systems in X-rays. The completeness in the SMC catalogue in the (0.2−1.0) keV band is estimated to a flux limit of $2.5{\times}10^{-15}$erg cm^{-2} s^{-1}, which would require a SMC absorption of less than 3×10^{21} cm^{-2} for the best-fit black-body model. Therefore, XMMU J010147.5-715550 might be the tip of the iceberg of the SMC Be/WD system population.

5.3. Discovery of the 11.866 s Be/X-ray binary pulsar XMMU J004814.0-732204

The XMM-*Newton* large-programme survey revealed four new BeXRBs. In this section, the analysis of the newly discovered BeXRB pulsar SPX11.87 is described as an example for a BeXRB. Optical follow-up observations and their analysis was done by Malcolm Coe and is included here for completeness. This study was published in Sturm et al. (2011a). I contributed the analysis of XMM-*Newton* data of five further BeXRBs in the SMC to the papers of Townsend et al. (2011), Coe et al. (2011), Coe et al. (2012), and Haberl et al. (2012b). Further, an outburst of the BeXRB IGR J05414-6858 in the LMC was discovered within the *Swift* UV-survey of the LMC (Sturm et al. 2011c) and the results of an XMM-*Newton* follow-up ToO observation are presented in Sturm et al. (2012c).

5.3.1. Observations and data reduction

The new transient was discovered on 2009 October 3, during observation 13 (ObsID 0601211301) of the XMM-*Newton* large-programme SMC survey. The source was located near the border of CCD 1 (partly spread onto CCD 4) of the EPIC-pn instrument and on CCD 2 of EPIC-MOS2. There are no MOS1 data for this source because it was located on CCD 6, which has been switched off since XMM-*Newton* revolution 961. The soft-proton background was at a very low level during the whole observation. Therefore, background-screening did not remove time intervals, resulting in net exposure times of 30 779 s and 32 368 s for EPIC-pn and EPIC-MOS2, respectively.

I used XMM-Newton SAS 10.0.0 to process the data. The data reduction was done as described in Sec. 3.3.13. The extraction regions are plotted on the X-ray image in Figure 5.8. The EPIC-pn single-event spectrum was used in the following. The EPIC-pn and EPIC-MOS2 spectra contain 9286 and 8054 background-subtracted counts, respectively. For the timing analysis, I used the merged event list from both instruments, containing 25 945 cts (without background subtraction).

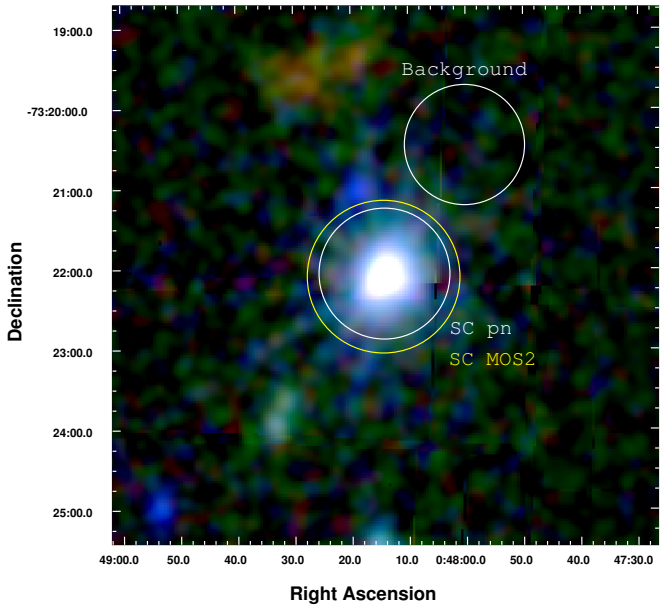

Figure 5.8. EPIC colour image of XMMU J004814.0-732204 combining pn and MOS data. The red, green, and blue colours represent the X-ray intensities in the (0.2−1.0), (1.0−2.0), and (2.0−4.5) keV energy bands. Circles indicate the extraction regions (with radii of 49″ and 57″ for pn and MOS2 source regions and 45″ for the background).

5.3.2. X-ray data analysis and results

X-ray coordinates

I identified sources in the FoV for astrometric boresight correction by comparison with the MCPS and obtained a shift of ΔRA=$-0.15''$ and ΔDec=$-1.23''$. This was done here, without using the identification of XMMU J004814.0-732204, to have an independent position. The corrected position of the transient as found by `emldetect` is R.A. = $00^h48^m14\overset{s}{.}07$ and Dec. = $-73°\ 22'\ 04\overset{''}{.}4$ (J2000), with a statistical uncertainty of $0.06''$ and a systematic uncertainty of $\sim 0.5''$ (1σ confidence).

Spectral analysis of the X-ray data

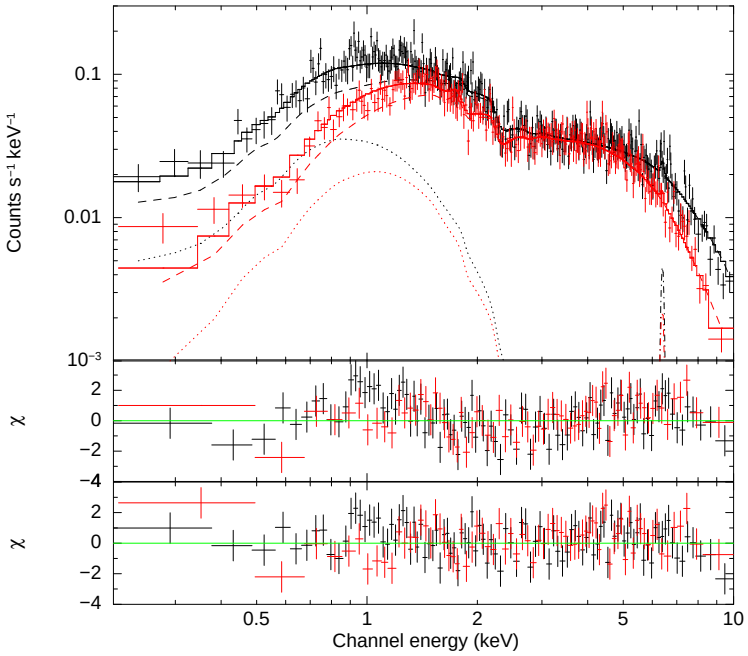

Figure 5.9. EPIC spectra of XMMU J004814.0-732204. The top panel shows the EPIC-pn (black) and EPIC-MOS2 (red) spectra, together with the best-fit model (solid line) of an absorbed power law (dashed line) plus black-body (dotted line) and iron fluorescent line (dash-dotted line). The residuals (re-binned for better comparison by an additional factor of three) are plotted for this model (bottom panel) and for the best-fit single power-law model (middle panel).

I used `xspec` version 12.5.0x for spectral fitting. The two EPIC spectra were fitted simultaneously with a common set of spectral-model parameters and only a relative normalisation factor was allowed to vary to account for instrumental differences. The spectrum (Figure 5.9) was modelled first with an absorbed power law. I fixed the Galactic photoelectric absorption at a column density of $N_{H,gal}$ = $6{\times}10^{20}$ cm^{-2} with abundances according to Wilms et al. (2000), whereas the SMC column density was a free parameter with abundances for elements heavier than helium fixed at 0.2. The best-fit parameters are summarised in Table 5.5 where uncertainties denote 90% confidence.

The extraction of the EPIC-pn spectrum is hampered by the CCD gap cutting the extraction region. The missing area is taken into account in calculating effective area by `arfgen`. However, we noticed that when using the default spatial resolution (parameter `badpixelresolution` = $2.0''$) the flux derived from the EPIC-pn spectrum is higher by (21 ± 3)% compared to MOS. The flux discrepancy reduces to 7% for `badpixelresolution` = $1.0''$. This is within the expected systematic uncertainties in the presence of gaps. Extracting the EPIC-pn spectrum from a smaller source region with radius $6''$, so that the complete source region is placed on CCD 1, yields a flux that only differs by $\sim$1% from the MOS2 value. The spectral shape is not affected by the CCD gap, but the number of source counts for the smaller extraction region is a factor of two lower.

Table 5.5. Spectral fit results.

Model[(a)]	SMC N_H (10^{21}cm^{-2})	Γ	kT (eV)	R[(b)] (km)	EW_{Fe} (eV)	Flux[(c)] (erg cm^{-2} s^{-1})	L_x[(d)] (erg s^{-1})	χ^2/dof
PL	1.72±0.25	0.66±0.03	–	–	–	(9.0±0.3)×10^{-12}	4.0×10^{36}	570/523
PL+BB	2.32±0.44	0.52±0.05	279±43	12.2±1.4	–	(9.3±0.5)×10^{-12}	4.2×10^{36}	524/521
PL+BB+Fe	2.34±0.45	0.53±0.05	277±40	12.2±1.4	-35±30	(9.6±0.5)×10^{-12}	4.2×10^{36}	520/520
PL+DiskBB	2.99±0.54	0.52±0.06	383±97	>5.9±3.5	–	(9.3±0.7)×10^{-12}	4.2×10^{36}	528/521

Notes. [(a)] For definition of spectral models see text. [(b)] Radius of the emitting area (for BB) or inner-disc radius (DiskBB, for the definition see text). [(c)] Observed (0.2−10.0) keV flux. [(d)] Source intrinsic X-ray luminosity in the (0.2−10.0) keV band (corrected for absorption) for a distance to the SMC of 60 kpc.

In principle, this fit is formally acceptable and additional components are not required. However, soft excesses and fluorescent emission from iron are known to contribute to the X-ray emission of some BeXRBs (e. g. Eger & Haberl 2008; La Palombara et al. 2009; Hickox et al. 2004). To investigate these possibilities I first added a black-body emission component to the model (Table 5.5). This component contributes ∼2% to the observed flux and ∼3% to the absorption-corrected luminosity. The bolometric luminosity is $(1.40 \pm 0.35) \times 10^{35}$ erg s^{-1}. Compared to the single power law, the reduced χ^2 improved from 1.09 to 1.01, which corresponds to an F-test chance probability of 2.6×10^{-10} and formally proves the significance of this component (but see Protassov et al. 2002, for limitations of the F-test). An additional emission line with fixed energy at 6.4 keV and unresolved line width (fixed at 0) yielded a line flux of $4.6 \pm 4.0 \times 10^{-6}$ photons cm^{-2} s^{-1} corresponding to the equivalent width given in Table 5.5. Substituting the 6.4 keV line by a 6.7 keV line for ionised Fe XXV resulted in an upper limit for the equivalent width of -41 eV.

Replacing the black-body component by a multi-temperature disc black-body model (diskbb in `xspec`), a lower limit for the inner-disc radius of $R_{\rm in} = 5.9^{+3.5}_{-2.2}$ km is derived (for a disc inclination of $\Theta = 0$ with $R_{\rm in} \propto 1/\sqrt{cos\Theta}$). Following Hickox et al. (2004) to estimate the inner-disc radius, yields $R_{\rm in} = \sqrt{L_{\rm X}/(4\pi\sigma T^4)} = 39$ km.

Timing analysis of the X-ray data

I corrected the event's arrival times to the solar system barycentre using the SAS task `barycen` and searched for periodicities in the X-ray light curves using fast Fourier transform (FFT) and light-curve folding techniques. The power-density spectra derived from light curves in various energy bands from both EPIC instruments showed a periodic signal at 0.084 Hz. To increase the signal-to-noise ratio, I then created light curves from the merged event list of EPIC-pn and EPIC-MOS2 (delimited to common time intervals). Figure 5.10 shows the inferred power-density spectrum from the (0.2−10.0) keV energy band with the clear peak at a frequency of 0.084 Hz. Following Haberl et al. (2008), I used a Bayesian periodic signal detection method (Gregory & Loredo 1996) to determine the pulse period with 1σ uncertainty to (11.86642 ± 0.00017) s. The background-subtracted pulse profiles folded with this period in the EPIC standard energy bands (Table 3.2) are plotted in Figure 5.11 along with hardness ratios (Sec. 3.3.8). Assuming a sinusoidal pulse profile, I determined a pulsed fraction of (7.5 ± 1.0)% for the (0.2−10.0) keV band. The profiles suggest some evolution from a single-peaked to a double-peaked structure with increasing energy, causing the variations in hardness ratios HR_3 and HR_4. A strong dependence of the pulse profiles on energy (e. g. Wilson et al. 2003; Haberl et al. 2008) and luminosity (e. g. Bildsten et al. 1997) is seen from a number of high-mass X-ray binaries.

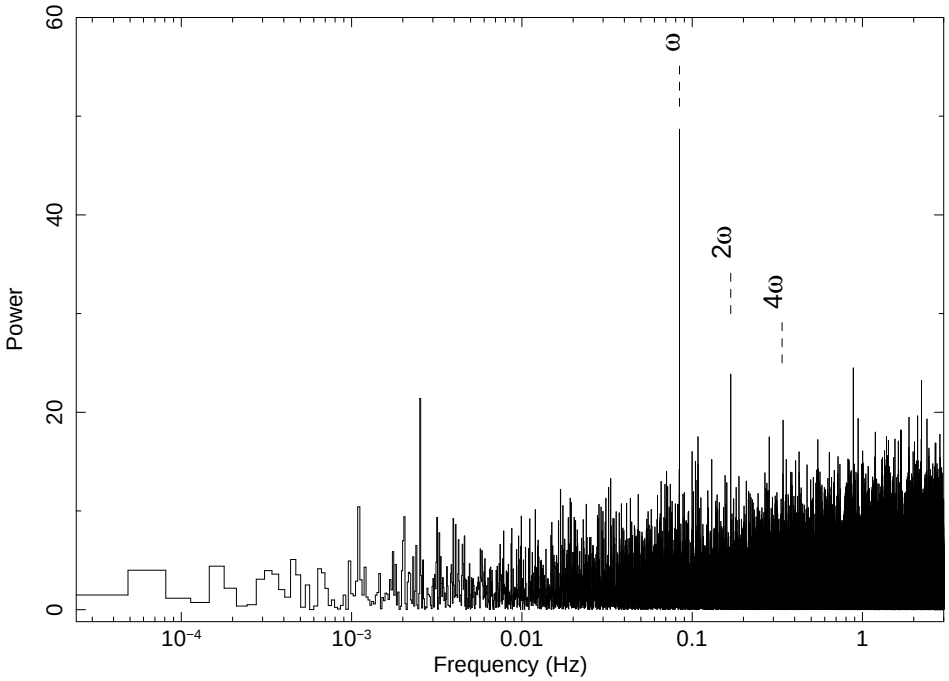

Figure 5.10. Power-density spectrum created from the merged EPIC-pn and EPIC-MOS2 data in the (0.2−10.0) keV energy band. The best-fit frequency of $\omega = 0.084$ Hz and its harmonics are marked with dashed lines. The time binning of the input light curve is 0.1176 s.

Long-term X-ray variability

The position of XMMU J004814.0-732204 was covered in two previous XMM-*Newton* observations on 2000 October 15 (ObsID: 0110000101) and 2007 April 11 (ObsID: 0404680301) with a background-screened net exposure of 21.6 ks and 17.6 ks, respectively. In the later observation, the source position was only covered by the EPIC-MOS2 FoV. In both observations, no source was detected above a likelihood threshold of 6. Using sensitivity maps, I derived 3σ upper limits of 2.5×10^{-3} cts s^{-1} and 2.7×10^{-3} cts s^{-1}, respectively. Assuming the same spectrum as during the outburst, this corresponds to a flux limit of 1.7×10^{-14}erg cm^{-2} s^{-1} (from October 2000, measured by EPIC-pn) and 6.1×10^{-14}erg cm^{-2} s^{-1} (April 2007, EPIC-MOS2) in the (0.2−10.0) keV band and to luminosity limits of 7.6×10^{33} erg s^{-1} and 2.7×10^{34} erg s^{-1}, respectively.

Also in a *Chandra* ACIS-I observation (Observation ID 2945) on 2002 October 2, this position was covered with a 11.8 ks exposure, and no source was detected. I used the CIAO (Version 4.2) task `aprates` to estimate a 3σ upper limit of 5.1×10^{-4} cts s^{-1}. Assuming the same spectrum as above, this corresponds to a flux limit of 1.6×10^{-14}erg cm^{-2} s^{-1} in the (0.2−10.0) keV band and a luminosity of 7.1×10^{33} erg s^{-1}.

The upper limits derived from the previous XMM-*Newton* and *Chandra* observations show that XMMU J004814.0-732204 increased in brightness at least by a factor of 560 during its outburst. RXTE monitoring of the SMC has been carried out for nearly a decade (Galache et al. 2008) and XMMU J004814.0-732204 has frequently fallen within the pointing direction of the telescope, often at a collimator response of ≥60%. Unfortunately, the time of the XMM-*Newton* detection on MJD 55107 falls into the gap in the RXTE monitoring (MJD 55080 – 55138) when the spacecraft was temporarily disabled, so there is no simultaneous RXTE coverage. Within the envelope of the last 9.5 years there are no possible detections of this source in the periods of time (approximately 6.5 years)

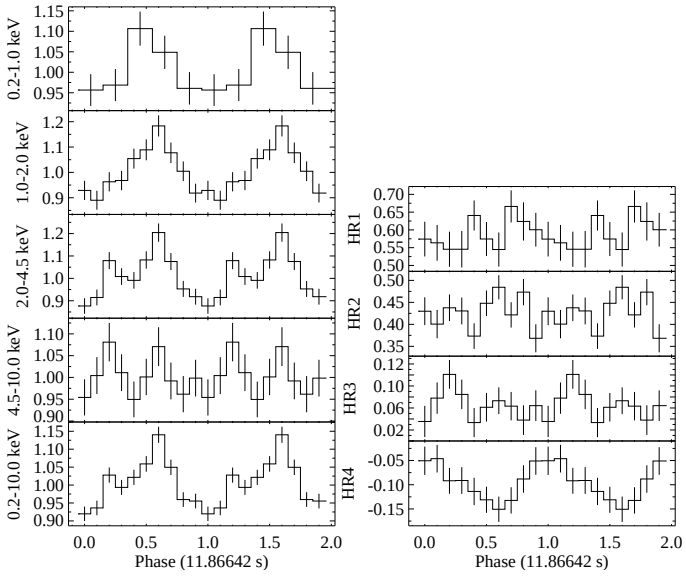

Figure 5.11. Left: Pulse profiles obtained from the merged EPIC data in different energy bands (for better statistics the first two standard energy bands were combined in the top panel, the bottom panel shows all five energy bands combined). The profiles are background-subtracted and normalised to the average count rate (0.116, 0.228, 0.249, 0.207, and 0.801 cts s^{-1}, from top to bottom. Right: Hardness ratios as a function of pulse phase derived from the pulse profiles in two neighbouring standard energy bands.

when the source was above a 0.6 collimator response. The RXTE pulse monitoring is sensitive to detections with a pulsed amplitude in excess of 0.15–0.2 cts s^{-1} PCU^{-1}. This approximately translates into ∼0.5–1.0 cts s^{-1} PCU^{-1} – depending on the collimator response and pulsed fraction (which is not very high for XMMU J004814.0-732204) – or a luminosity limit of $\sim 2\times10^{36}$ erg s^{-1} for a source in the SMC.

5.3.3. The optical counterpart

Identification of the optical counterpart

Searching optical catalogues of the MCPS (Zaritsky et al. 2002), MACHO, and OGLE, we found three stars that are located near the XMM-*Newton* source. Their positions and magnitudes from Zaritsky et al. (2002) and their OGLE III names are listed in Table 5.6. A finding chart produced from OGLE III data is shown in Figure 5.12.

The star closest to the X-ray position (OGLE III 14642) has colours and brightness consistent with an early B star. Its position on the $U - B$ vs. $B - V$ diagram (Figure 4.8) is also entirely consistent with it being the counterpart of a BeXRB. This candidate also appears as number 10287 in the survey list of Massey (2002). The $B - V$ colour index from that catalogue is $B - V = (-0.12 \pm 0.01)$ mag. Correcting for an extinction to the SMC of $E(B - V) = 0.09$ (Schwering & Israel 1991, also used for the spectral type estimates hereafter) gives an intrinsic colour of $B - V = (-0.21 \pm 0.01)$ mag. From Wegner (1994), this indicates a spectral type in the range B1.5V − B2.5V, which is typical of optical counterparts to BeXRBs in the SMC (McBride et al. 2008). However, care must always be taken when interpreting colour information as a spectral type in systems that clearly have circumstellar discs contributing some signal to the *B* and *V*-bands.

Optical photometry was performed at the Faulkes Telescope South (FTS) on 2009 November 25 (MJD 55160). The telescope is located at Siding Spring, Australia and is a 2 m, fully autonomous, robotic Ritchey-Chrètien reflector on an alt-azimuth mount. The telescope employs a robotic control system. The telescope was used in real time interface mode for the observation of XMMU J004814.0-732204. All the observations were pipeline-processed (flat-fielding and de-biasing of the images). The *I*-band magnitude of the optical counterpart was determined to be (15.30±0.02) mag by comparison

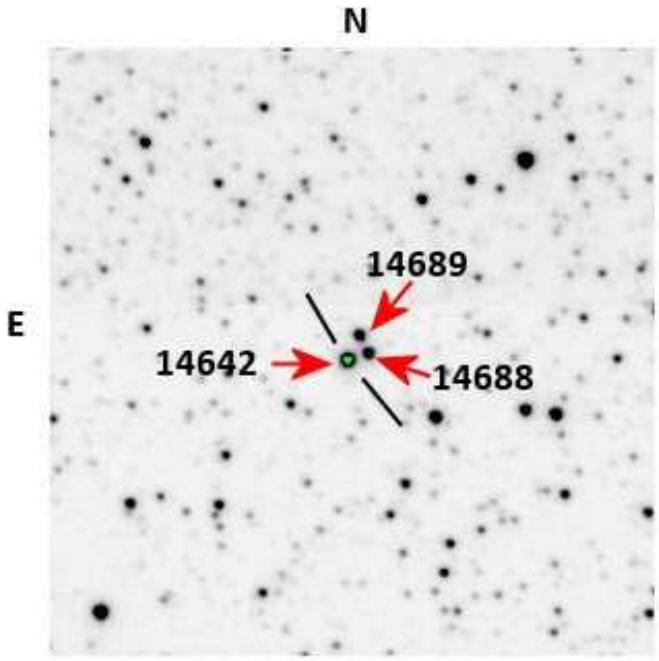

Figure 5.12. Finding chart of SXP11.87. The *I*-band image from OGLE II shows the 3 close objects near the X-ray position marked with their OGLE III identification (arrows). The two lines further mark the likely counter part. The image size is 1.′5 by 1.′5. Courtesy of Malcolm Coe.

with several other nearby stars on the same image frame and in the OGLE database. These comparison stars have not exhibited any significant variability in the last eight years of OGLE monitoring.

Figure 5.13 shows optical and NIR photometry of OGLE III 14642 taken at the different epochs (see Table 5.7 for the actual values). The earliest optical data come from Massey (2002) and were recorded on 1999 January 8. These data are combined with NIR measurements taken on 2002 August 31 with the Sirius camera on the 1.5 m IRSF telescope in South Africa (Kato et al. 2007). Also included is the OGLE *I*-band measurement taken simultaneously with the Sirius NIR data set. These early data are compared to a *B*, *V*, *R*, and *I* photometric data set recorded on 2009 November 25 from the FTS.

For comparison, a stellar atmosphere model (Kurucz 1979) representing a B2 V star ($T_{\rm eff}$ = 22 000 K and $\log(g) = 4.0$) is also shown where the model has been normalised to the most recent *B*-band measurement. It is very clear that the recent data taken around the time of the XMM-*Newton* detection represent the source in a much lower activity state than the earlier data. Furthermore, the shape of the model atmosphere indicates clear evidence of a significant NIR excess in the past, almost certainly arising from the circumstellar decretion disc of the system. But in late 2009, the disc had diminished significantly, to the extent where there is only small NIR excess. This is supported by the very weak Hα emission (see below).

The other two bright stars have a large separation to the XMM-*Newton* source of more than 5σ. The star OGLE III 14688 is probably a red (K to M) giant according to its OGLE colours. The light curve shows small variations of the order of 0.1 mag in the *I*-band, but no evidence of any coherent fluctuations. There is an object from the 2MASS survey (Skrutskie et al. 2006) – 2MASS J00481347-7322030 – which is closest to the position of this star, with J = 14.76 mag, H = 14.13 mag, and K = 14.04 mag, which rather points towards a K2 star. OGLE III 14689 is likely a late B-type star (B5–B9) from the OGLE colours. The OGLE light curve shows fluctuations of the order of 0.05 mag and evidence of a strong modulation at a period of 2.19 days. The folded light curve appears sinusoidal, which is probably evidence of non-radial pulsations in the star (Diago et al. 2008). The position, optical magnitudes, and colours make the star OGLE III 14642 the most likely counterpart.

Table 5.6. Possible optical counterparts of XMMU J004814.0-732204

RA[(a)] (J2000)	Dec[(a)] (J2000)	dist.[(b)] ($''$)	U[(a)] (mag)	B[(a)] (mag)	V[(a)] (mag)	I[(a)] (mag)	OGLE III
00 48 14.10	-73 22 03.6	0.76	13.96±0.03	14.90±0.02	15.02±0.05	15.25±0.13	14642
00 48 13.52	-73 22 02.8	2.86	–	18.90±0.07	17.26±0.07	15.88±0.04	14688
00 48 13.78	-73 22 00.5	4.07	15.20±0.03	15.93±0.03	15.90±0.03	16.00±0.04	14689

Notes. [(a)] According to Zaritsky et al. (2002). [(b)] Distance of the Zaritsky et al. (2002) positions to the bore-sight corrected XMM-*Newton* position.

Table 5.7. Optical and IR photometry of OGLE III 14642.

	M2002[(a)] 1998 Jan 8 MJD 51186	K2007[(b)] 2002 Aug 31 MJD 52517	FTS[(c)] 2009 Nov 25 MJD 55160	Sirius[(c)] 2009 Dec 15 MJD 55180
B	14.54±0.01	–	14.87±0.20	–
V	14.66±0.01	–	14.86±0.03	–
R	14.66±0.01	–	14.87±0.03	–
I	–	14.70±0.01	15.30±0.02	–
J	–	14.67±0.01	–	15.46±0.01
H	–	14.62±0.01	–	15.47±0.02
K	–	14.53±0.02	–	15.49±0.07

Notes. [(a)] Massey (2002). [(b)] Kato et al. (2007). [(c)] This work.

Long-term variability of OGLE III 14642

The identification of XMMU J004814.0-732204 with OGLE III 14642 is supported by the MACHO and OGLE light curves. This star shows strong outbursts repeating on time scales of ∼1000 days. Figure 5.14 shows the light curves of the proposed optical counterpart in approximate *B* and *R* magnitudes derived from MACHO data (ID 212.15846.31) and in the *I*-band from OGLE II and OGLE III. The *I*-band data point, which we obtained at FTS, was added to the OGLE light curve. The MACHO light curve shows two outbursts around April 1995 and January 1998, while OGLE observed six consecutive outbursts between June 1997 and December 2008.

The X-ray flux of the source is not obviously correlated with the optical outburst activity. The first XMM-*Newton* non-detection was during maximum optical brightness. The *Chandra* non-detection was close to the maximum optical brightness, the last XMM-*Newton* non-detection later in the optical decline, while the detection could have happened at the decline or already in optical low-state (see Figure 5.14).

Optical spectrum

Spectroscopic observations of the Hα region were made on 11 December 2009 (MJD 55176) using the 1.9 m telescope of the South African Astronomical Observatory (SAAO). A 1200 lines mm^{-1} reflection grating blazed at 6800 Å was used with the SITe CCD, which is effectively 266×1798 pixels in size, creating a wavelength coverage of 6200 Å to 6900 Å. The pixel scale in this mode was 0.42 Å pix^{-1}. The data were reduced using IRAF standard routines and the resulting spectrum is shown in Figure 5.15. The peak is at 6566 Å, which is consistent with the corresponding rest wavelength of the Hα line corrected for the motion of the SMC. In this mode the spectral resolution is ∼0.2 nm for

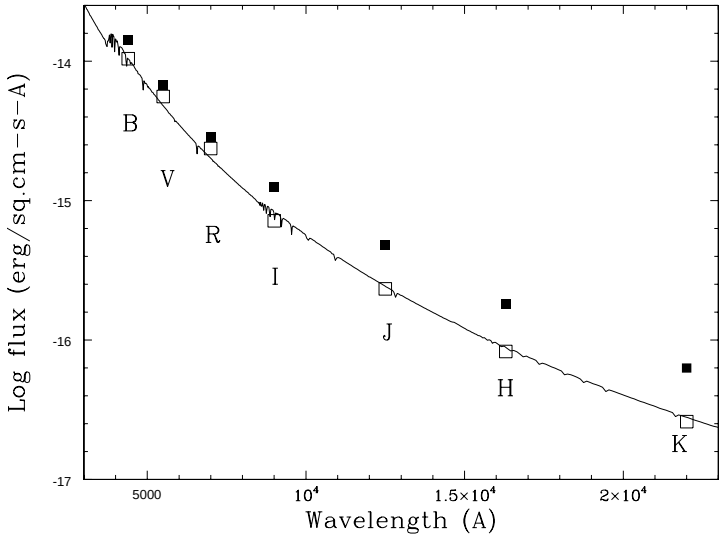

Figure 5.13. Combined optical-NIR flux for the counterpart OGLE III 14642 at two epochs: A historical data set (1999−2002) shown by solid symbols and a data set from the time of outburst (Nov−Dec 2009) presented by open symbols. See text for details of the observations. Both data sets are compared to a Kurucz model atmosphere for a B2 V star in which this stellar model has been normalised to the outburst *B*-band point. Courtesy of Malcolm Coe.

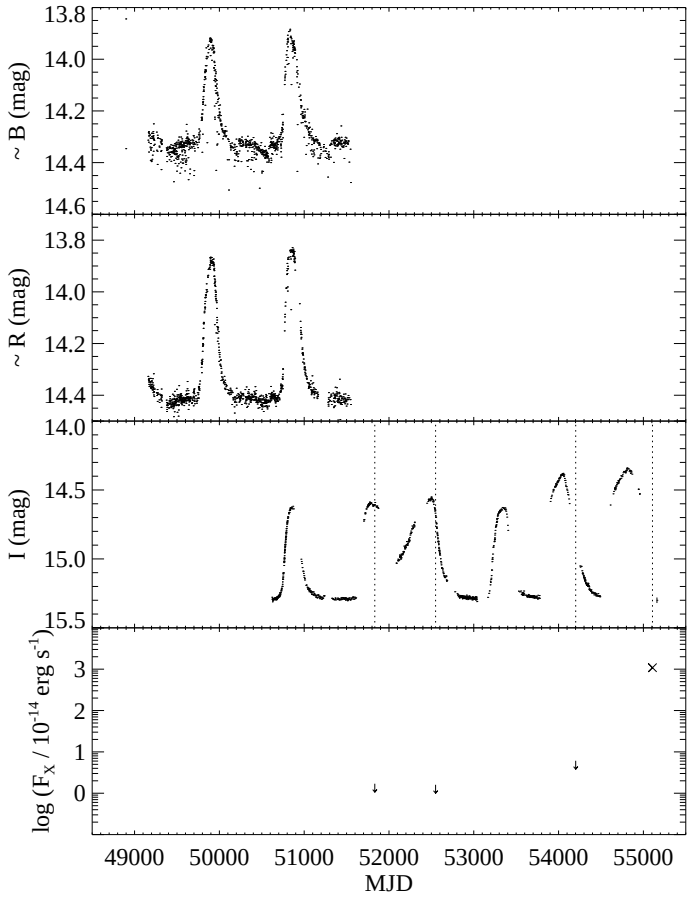

Figure 5.14. Multi-wavelength light curves of the XMMU J004814.0-732204 / OGLE III 14642 system. The upper two panels show the MACHO *B*- and *R*-bands. In the third panel, the OGLE III *I*-band light curve is plotted, with the last data point indicating the measurement using the Faulkes telescope (see text). Dashed lines indicate the times of X-ray measurements, as shown in the bottom panel. Arrows mark upper limits (XMM-*Newton*, *Chandra*, and XMM-*Newton* in chronological order), the cross indicates the XMM-Newton detection.

the signal-to-noise of ∼10. We measured an Hα line equivalent width of $EW = (-3.5 \pm 0.6)$ Å, the uncertainty being calculated using the prescription given in Howarth & Phillips (1986).

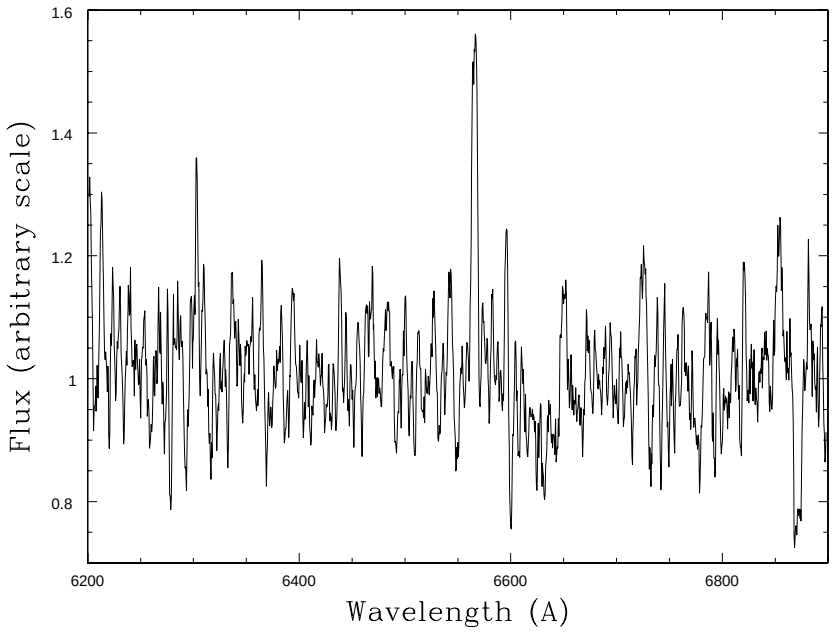

Figure 5.15. Hα spectrum of OGLE III 14642 taken 2009 December 11 at SAAO. Courtesy of Malcolm Coe.

5.3.4. Discussion

One of the first XMM-*Newton* observations of the SMC survey revealed the new high-mass X-ray binary pulsar XMMU J004814.0-732204 with a pulse period of 11.866 s (following Coe et al. 2005, we give it the alternative name SXP 11.87). Its X-ray behaviour and the properties of the optical counterpart (star with OGLE III ID 14688) are typical of a BeXRB. In particular its appearance as an X-ray transient (a factor of at least 560 brighter during the outburst on October 2009 as compared to non-detections from archival XMM-*Newton* and *Chandra* observations), the hard power-law shape of the X-ray spectrum, the pulse period, the optical brightness, variability, colours (indicating an early B star), and finally the Hα emission line in the optical spectrum clearly confirm XMMU J004814.0-732204 as another BeXRB in the SMC.

The power-law photon index derived from the EPIC spectra of 0.53−0.66 (depending on the spectral modelling of the soft part of the spectrum by including an additional soft model component or not) is on the hard side of the distribution of photon indices for BeXRBs in the SMC, which shows a maximum at ∼0.9−1.0 (Haberl et al. 2008; Haberl & Pietsch 2004). The range of values obtained for XMMU J004814.0-732204 is similar to the index of 0.35−0.54 reported for the 6.85 s pulsar XTE J0103−728 (also using XMM-*Newton* data in the same energy band; Haberl & Pietsch 2008). It should be noted, that the later, also called SXP 6.85, was detected at energies up to 35 keV with RXTE and INTEGRAL during a long type-II outburst (Townsend et al. 2010) showing that the hard spectrum extends to energies beyond the sensitivity of XMM-*Newton*. SXP 11.87 and SXP 6.85 also show similarities in their spectra at energies below 2 keV, indicating a soft X-ray excess. However, the energy resolution of the CCD instruments is not sufficient to determine the exact nature of this component. Some constraints can be inferred by using different models for the soft component. If one assumes a black-body component, a temperature of ∼280 eV and a black-body radius of ∼13.4 km is derived for SXP 11.87. While this could still be compatible with the size of the neutron star, the corresponding black-body radius for SXP 6.85 is too large (30 km, Haberl & Pietsch 2008). Therefore, these au-

thors conclude that the soft excess more likely originates near the inner edge of an accretion disc as expected for intermediate X-ray luminosities. The very similar parameters derived for a soft excess emission suggest the same picture for SXP 11.87, although the inferred black-body or inner-disc radii seem to be smaller than the corresponding values for SXP 6.85. However, emission by diffuse gas through collisional heating or photoionisation is also possible for both cases (Hickox et al. 2004).

The MACHO and OGLE light curves of the optical counterpart of XMMU J004814.0-732204 show prominent outbursts repeating on a time scale of about 1000 days. Very similar behaviour was reported from the optical counterpart of the 18.37 s BeXRB pulsar XMMU J004911.4-724939, which showed two outbursts separated by about 1300 days in MACHO and OGLE I data (Haberl et al. 2008). Such outburst behaviour is also observed from other isolated Be stars (Mennickent et al. 2002). Because of this and the fact that the outbursts do not repeat strictly periodically, it is unlikely that they are related to the orbital period of the binary system. Moreover, from the Corbet relation between neutron star spin period and the orbital period (Corbet 1984), a much shorter orbital period of about 20−200 days is expected (see Laycock et al. 2005; Corbet et al. 2009, for more recent versions of the P_s vs. P_{orb} diagram).

5.4. The SNR candidate XMMU J0056.5-7208

The background-subtracted EPIC mosaic image of the SMC revealed three new candidates for SNRs with low surface brightnesses and low temperatures (Haberl et al. 2012a). This increases the number of larger SNRs and affects the size distribution of SNRs in the SMC. The low statistics and low energy resolution of the data only allow a crude analysis. As an example, XMMU J0056.5-7208 will be presented in the following.

In the EPIC mosaic image, enhanced emission is clearly seen in the (0.2−1.0) keV band (Figure 5.16). The SNR nature of the new candidate XMMU J0056.5-7208 is affirmed by a corresponding optical emission-line structure. The Hα/[S II] intensity ratio at the rim of the shell structure reaches values of 0.4, which is at the lower limit of the expected values for SNRs in the SMC. However, X-ray emission is mainly seen from the northern part of the elliptical optical structure. It remains unclear, if we see two blended circular structures, or if the X-ray emission in the south is fainter. In radio, only a marginal detection at 843 MHz with flux densities of $S \approx 1$ mJy is seen, pointing to a steep spectral index (Miroslav Filipović, privat communication).

Source and background X-ray spectra of XMMU J0056.5-7208 were extracted by Joseph DeRose within a RISE-DAAD internship for the support of PhD students under my supervision. We used the EPIC-pn data of observation 0601210601 with a reduction as described in Sec. 3.3.13, but the ARF was calculated for an extended source. Due to the low surface brightness, the background spectrum is fitted simultaneously with a background model rather than subtracted from the source spectrum. The background model comprises an unconvolved exponential decay function (electronic readout noise), an unconvolved power law (detector background), a Gaussian line (Al fluorescent line), an apec model (thermal foreground emission), and a power law (CXB). The background model shape is assumed to be the same for the background and source spectrum, but we allowed a different normalisation of the contribution to both spectra. The spectrum of XMMU J0056.5-7208 is fitted with a `sedov` model (Borkowski et al. 2001) with $Z = 0.2 Z_\odot$ in addition to the background as shown by the green line in Figure 5.17. The best fit resulted in a $\chi^2_{\rm red}/{\rm dof} = 1.04/165$. The spectra and best-fit model are presented in Figure 5.17.

For the sedov model, we obtain an absorbing column density of $N_{\rm H} < 1.2 \times 10^{21}$ cm^{-2}, a plasma temperature of $kT = 0.52^{+1.18}_{-0.26}$ keV, an ionisation time of $\tau = 1.23^{+11.1}_{-0.93} \times 10^{11}$ s cm^{-3}, and an emission

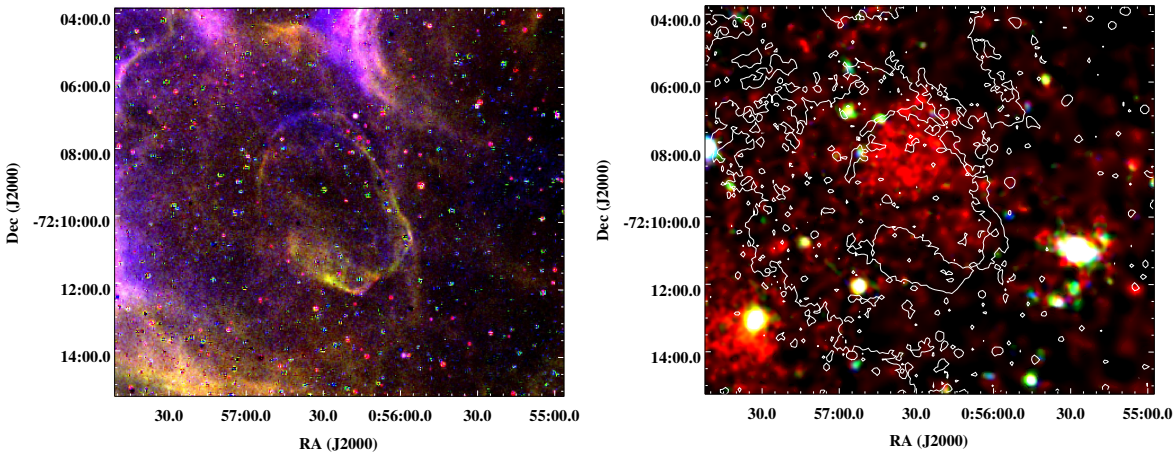

Figure 5.16. Comparison of the continuum subtracted emission-line image from MCELS with the EPIC mosaic image of XMMU J0056.5-7208. Colours give linearly scaled intensities between for Hα (red), [S II] (green), and [O III] (blue). In the right, the EPIC mosaic image is shown with linearly scaled intensities in the (0.2−1.0) keV (red), (1.0−2.0) keV (green), and (2.0−4.5) keV (blue). The contours mark the summed Hα, [S II], and [O III] intensity at 8×10^{-16} erg cm^{-2} s^{-1}.

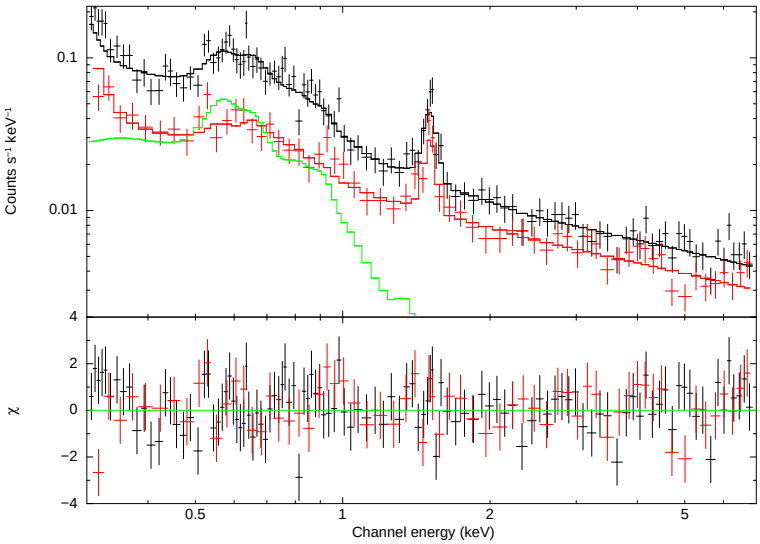

Figure 5.17. EPIC-pn spectrum of XMMU J0056.5-7208 (black) and a nearby background region (red) together with the best-fit model. The sedov model component is drawn in green. The lower panel shows the residua.

measure of $EM = 1.8^{+2.9}_{-0.8} \times 10^{57}$ cm^{-3}. Uncertainties are for 90% confidence. The observed flux in the (0.2−2.0) keV band is $\sim 5.3 \times 10^{-14}$ erg cm^{-2} s^{-1} corresponding to an unabsorbed luminosity of $\sim 3 \times 10^{34}$ erg s^{-1}.

The results of the spectral analysis are consistent with an SNR nature of the object, but can poorly constrain the plasma parameters. Deeper observations are needed to further investigate this and other SNR in the SMC with low surface brightness.

6. The diffuse X-ray emission

We see clear evidence for diffuse X-ray emission in the background-subtracted XMM-*Newton* mosaic image. To further investigate the diffuse emission, I developed a method for the spectral characterisation of diffuse emission with low surface brightness with EPIC-pn. In total, 647 spectra of diffuse emission in 240 subregions with a size of $0.15^\circ \times 0.15^\circ$ have been extracted (Sec. 3.3.15). After describing the spectral analysis, I will compare the results with the morphology of the brightness distribution and discuss the origin of the diffuse emission and its connection to star formation.

6.1. Development of a method for spectral analysis

To study the diffuse emission from hot gas in the SMC, several contributions to the measured X-ray spectra need to be taken into account. These originate from detector background, soft protons entering through the telescopes, and celestial X-rays. To fit the spectra, I characterised these background components using observations of the SMC and observations with closed filter wheel. This comprehensive set of about one hundred observations is distributed over the first 10 years of the XMM-*Newton* mission. New insights into the EPIC-pn background will be useful for other studies as well, but should be investigated with a complete set of all available XMM-*Newton* observations.

6.1.1. Soft-proton flares

As described in Sec. 2.2.4, low-energy particles can enter the detector via the telescopes and contribute significantly to the detected signal. Characteristic for this component is a flaring behaviour, but also a quiescent contribution is possible.

In general, it is assumed, that soft protons cannot reach the shielded corners of the EPIC CCDs. I found that this assumption is not valid for EPIC-pn. An example of a background light curve of an observation of the Vela SNR is shown in Figure 6.1. The SNR illuminates the entire FoV with X-rays. In the first part of the observation (green) the flaring component was at a low level or absent, in the latter part, the background increased (red). Surprisingly, I find also an increase in the shielded area (blue light-curve) of EPIC-pn (upper panel), but not in EPIC-MOS (lower panel). This is evidence for a different behaviour of EPIC-MOS and EPIC-pn in the detector corners. In Figure 6.2, we compare images from the two intervals. Illumination by particles, but not by X-rays, is obvious in the detector corners of EPIC-pn. Using an SMC observation (ObsID 0301170501) with very high background and without any flare removal, we see the same effect. I note, that this observation was performed between orbital phases of the satellite of 0.62 and 0.73 at altitudes above 90 000 km, i. e. not at the beginning or end of the orbit. In the case of the EPIC-MOS detector corners, the flat light curve points to an effective shielding against both particles and X-rays. Note, that in the case of EPIC-pn, OOT events have been subtracted from the light curves, images, and spectra.

The radial profiles along the blue boxes from Figure 6.2 are compared in Figure 6.3a. In the case of X-ray illumination, a sharp drop appears at the rim of the shielded area, while particles show only a moderate decrease, which is somewhat stronger, than the vignetting of this component inside the FoV.

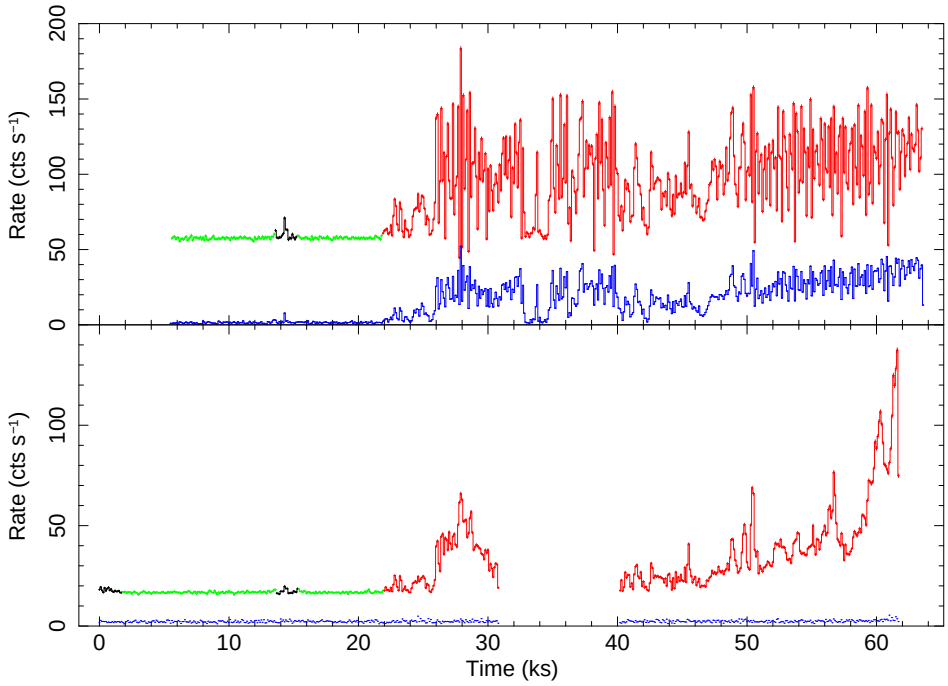

Figure 6.1. EPIC-pn (upper panel) and EPIC-MOS2 (lower panel) light curves of observation 0153750701. Time intervals, used for the images (Figure 6.2) are indicated in green (quiet selection) and red (flares). The light curves extracted form the corners are plotted in blue and multiplied by a factor of ten. For the corner light curve of EPIC-pn, the OOT light curve is subtracted. The time binning is 100 s. For high count rates, EPIC-pn is affected by counting mode gaps.

The spectrum of observation 0301170501 inside the FoV and from the detector corners is presented in Figure 6.3b. In both cases, one finds a continuum, which roughly follows an exponential function ($\exp(-KE)$). For the corners, the exponential factor is $K = (0.161 \pm 0.002)$ keV^{-1}, compared to ~0.11 keV^{-1} for the compete FoV. This is likely caused by the energy dependent vignetting of protons (cf. Fig. 17 of Kuntz & Snowden 2008).

For observations, which are only partly affected by flares, one can subtract the X-ray component, resulting in a clean flare spectrum. This was done for all SMC observations. Following Kuntz & Snowden (2008), I used a model for the "photon" spectrum $S(E) = dN/dE$ consisting of two exponentials, where the parameters of the second are coupled to the first by polynomials.

$$S_{\mathrm{SP}} = A_0 \exp(-B_0 E) + A_1 \exp(-B_1 E) \tag{6.1}$$

$$A_1 = a_0 + a_1 A_0 + a_2 A_0^2 \tag{6.2}$$

$$B_1 = b_0 + b_1 B_0 + b_2 B_0^2 \tag{6.3}$$

To avoid negative normalisations and allow a vanishing soft-proton contribution, I constrain $a_0 = 0$ and $a_{1,2} \geq 0$. Fitting this function to 55 flare spectra from observations of the SMC that were significantly affected, results in $a_1 = 1.59(2)$, $a_2 = 0.00000(3)$, $b_0 = -0.40(2)$, $b_1 = 9.6(3)$, and $b_2 = -15.0(9)$. The values for B_0 are found between 0.057 keV^{-1} and 0.3 keV^{-1}. The fit statistics is χ^2_{red}/dof = 1.44/79615, which is a significant improvement compared to the simple exponential model that results in χ^2_{red}/dof = 3.12/79620. I note that some flare spectra still show systematic residua. Intervals of strong flare activity have been removed in the background screening (Sec. 3.3.2) and the model developed above is used to account for the remaining contamination. This model allows to describe

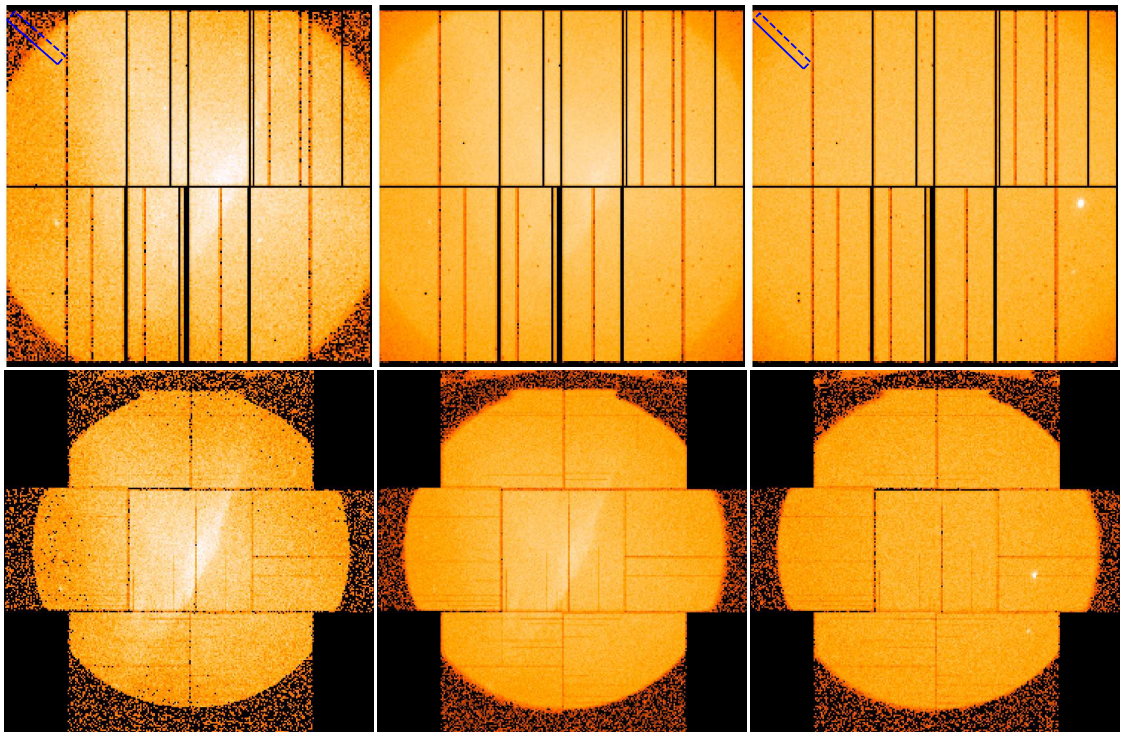

Figure 6.2. Images from EPIC-pn (upper panel) and EPIC-MOS2 (lower panel) of the time intervals with quiescent background of the Vela observation 0153750701 (left), the flare-affected time interval (middle), and the background dominated observation 0301170501 without GTI filtering (right). The false-colour images give logarithmically scaled intensities. OOT events in the EPIC-pn images are subtracted. The images are scaled to have the same number of counts in the outer FoV (1′). Blue boxes mark the area used for the projection (see Figure 6.3a).

the soft-proton contribution with only two parameters A_0 and B_0, i. e. with the same number as a single exponential model, when the coefficients a_i and b_i are determined. For EPIC-MOS an energy dependence was found, with the flare spectrum becoming harder for stronger flares (Kuntz & Snowden 2008). Since the residual flares in the GTI-screened SMC spectra may be softer, I constrained the exponential factor to be $0.05\ \mathrm{keV}^{-1} \leq B_0 \leq 0.5\ \mathrm{keV}^{-1}$.

6.1.2. Detector background

The detector background of EPIC-pn is composed of several components, as discussed by Strüder et al. (2000). Events caused by minimum ionising particles (MIPs) are already removed on board and by the SAS task `epchain`. From an unrecognised remaining component of MIPs and energetic electrons and γ-rays that can be produced by MIPs, a quiescent particle background is observed with a continuous energy distribution (Lumb et al. 2002). Additionally, MIPs cause X-ray fluorescent emission from material around the detector, which will be detected by the CCDs and cannot be separated from focused celestial X-rays. At lowest energies, electronic read-out noise also contributes significantly. The last three components are well measured in filter wheel closed observations. The merged event-files of these observations are provided by the background working group[1]. The spectrum of single-pixel events with `flag=0` from all full-frame observations is shown in Figure 6.4. Here I excluded flares at the end of observations from satellite revolution 822, 895, and 1393, as well as the

[1] available at http://xmm2.esac.esa.int/external/xmm_sw_cal/background/filter_closed/

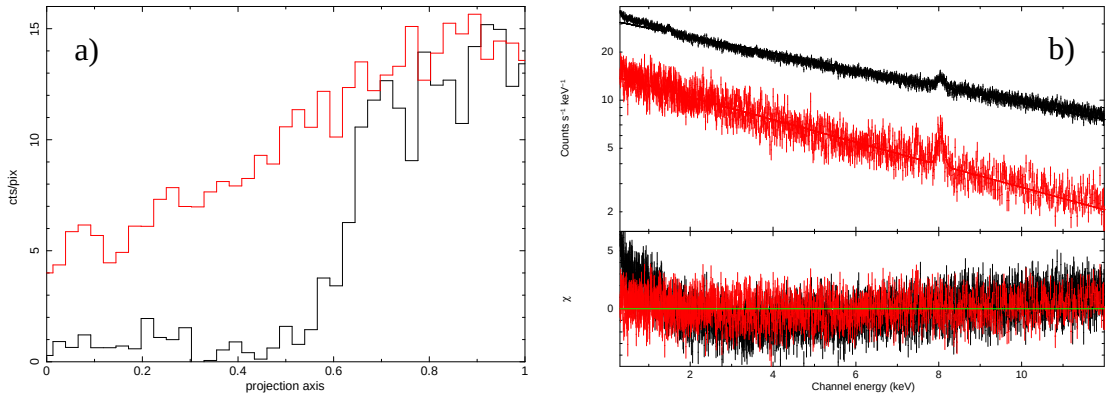

Figure 6.3. (a) Count distribution from the projections along the blue boxes in Figure 6.2. The X-ray dominated case is shown in black, the particle background dominated case in red. (b) Spectrum of single events of observation 0301170501 extracted from the FoV (black) and the corners (red). The corner spectrum is multiplied by a factor of ten. Using a diagonal response, the spectra are fitted with a simple model, consisting of an exponential function and a Gaussian line at 8.04 keV. The Gaussian represents an X-ray fluorescent line from Cu. The FoV spectrum might be contaminated by X-rays at energies below 2 keV. Only two bright sources have been excluded.

complete revolution 1561.

To describe the detector background for EPIC-pn, I developed an empiric model for the merged FWC spectrum. A basic description of the continuum is given by a power law with photon index of $\Gamma = 0.4957^{+0.0036}_{-0.0038}$, not convolved by the instrumental response[2]. The fluorescent lines were modelled with Gaussians as given in Table 6.1. Since I found similar residua for the strongest lines with instrumental and flat response, I decided to develop the model completely for a flat response. The read-out noise at lowest energies was modelled by an additional exponential function, which is motivated by a similar study, invoking also double pixel events. This study is focusing on the analysis of the soft emission from the SMC. Because the read-out noise of double pixel events contributes significantly up to ~0.5 keV, only single events were used. The high statistics in the FWC data allowed some further improvements to reduce residua. The exponential function was modified by multiplying a spline function to better represent the real shape of the spectrum. I also added two smeared absorption edges to the continuum at $0.539^{+0.015}_{-0.018}$ keV (K edge of oxygen) and at $1.387^{+0.024}_{-0.032}$, which is significantly lower than the Si K edge and may rather be interpreted as redistribution of the Al line. However, adding a model edge reduces the residua and we are not interested in a physical interpretation in first place. To improve the modelling of the two strongest fluorescent lines (Al and Cu), I added a second Gaussian for each line with the same central energy but a higher line width to improve the representation of the line spread function. The final model is presented in Figure 6.4 and results in a $\chi^2_{\mathrm{red}} = 1.09$ for 2312 degrees of freedom. There are still indications of missing components in the residua, as at the low energy tail of the Al line, some weak unresolved lines around 2 keV and a possible line at 5.9 keV. But with the current statistics, these components cannot be determined sufficiently well. They will have negligible effect on the investigation of single observations.

To investigate long term temporal evolution of the detector background, I fitted the detector-background model to spectra reduced from FWC observations between revolution 266 and 780 (phase A) and between revolution 1430 and 2027 (phase B). In phase A and B the detector background was at a low and high level, respectively, showing a transition in between. The increase is likely related to the solar cycle. The individual spectra of both phases can be described well, by using the detector-background model from above and fitting only two normalisations, one for the read-out noise, and

[2] A normalised diagonal response must be used in `xspec`.

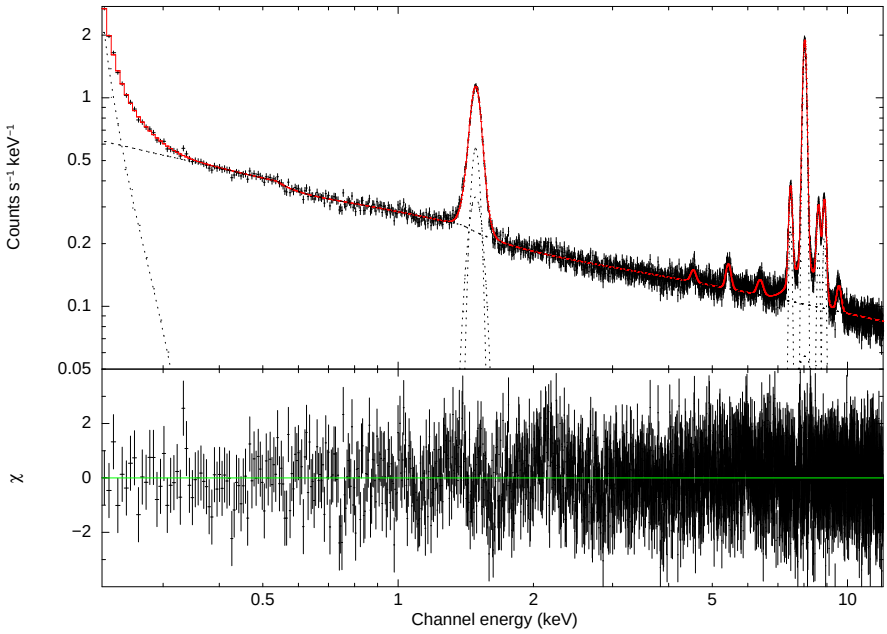

Figure 6.4. Screened FWC spectrum (black) of EPIC-pn with the best-fit model (red). Individual model components are shown as dashed lines. The lower panel gives the residua.

one for the continuum and the fluorescent lines. For the individual observations, the ratios of the normalisation of read-out noise and fluorescent lines to the normalisation of the continuum are plotted relative to the value of the average FWC spectrum in Figure 6.5. An independent evolution of the fluorescent lines and the continuum is not observed. For the read-out noise, one finds a systematic increase with time and fluctuations between the individual observations of up to 37% relative to the continuum. The normalisation of the fluorescent lines show only moderate variations up to 8.6% relative to the continuum.

Since the flux of each fluorescent line depends on the position in the detector (Freyberg et al. 2004), it is necessary to adjust the detector background model, when only a part of the FoV is used for spectral reduction. My approach is to extract a spectrum from the FWC data, selected from the same region on the detector as used for the spectrum of the investigated source. The statistics of the current FWC data corresponds to ∼1800 cts arcmin^{-2}. This allows to determine the emission lines, and shape of the read-out noise individually.

I tested the method for temporal variations. Therefore, I extracted spectra from each CCD and from three subregions divided by `RAWY=75` and `RAWY=140`. The spectral shape was determined for each subregion, by fit the detector-background model to the merged data set. Only weak features, i. e. the 4 weakest lines and the energy of the absorption edges, could not be determined individually for subregions. Due to the lower statistic, I only used spectra from phase A and B but not the individual observations. I find a good description of the spectra by the models derived from the merged FWC data in the according subregion, when only two normalisations are used. For all spectra I derive $\chi^2_{\rm red}$ between 0.70 and 1.16.

Other studies use the shielded areas of the detector corners to constrain the contribution of the detector background. There can be a remaining soft proton contamination within GTIs (cf. Fig. 13 of Kuntz & Snowden 2008) which might also contribute to the corners of EPIC-pn (Sec. 6.1.1). Since the diffuse celestial X-ray emission in the SMC field dominates below ∼2 keV only, whereas above

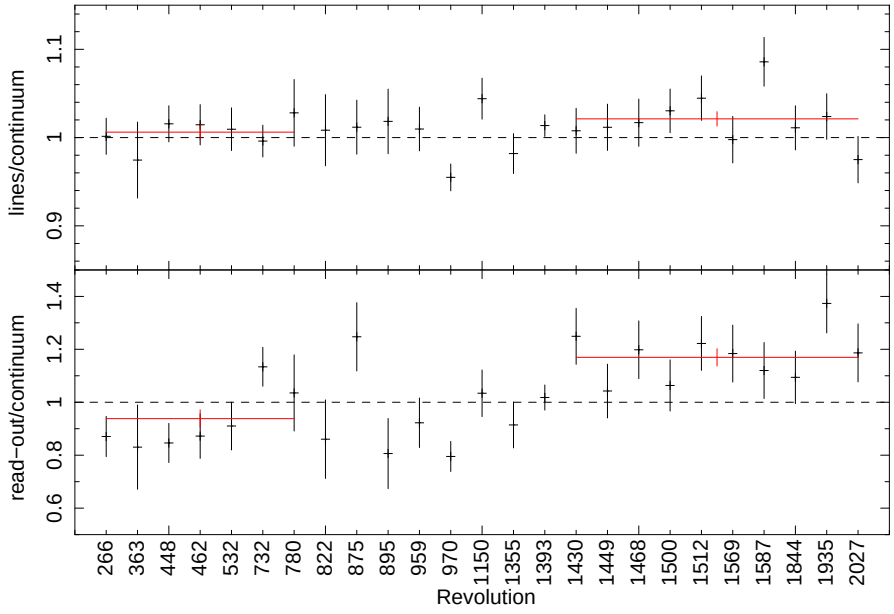

Figure 6.5. Evolution of individual detector components. Error bars indicate 90% confidence.

this energy the detector background and soft protons are relevant, I decided for this study to fit the detector background normalisation to the spectra. These two components can be distinguished by their different spectral shapes (power law vs. exponential). In addition, the detector background is constrained by the fluorescent lines.

6.1.3. X-ray fore- and background

Celestial X-ray emission in front of or behind the SMC is expected from thermal emission in the local hot bubble, thermal emission from the Galactic halo, and the cosmic X-ray background. In the following, I use "X-ray background" for the emission for all components.

In Figure 6.6, I show the large-scale diffuse X-ray emission around the SMC from the ROSAT all-sky survey. The XMM-*Newton* survey field and surrounding pointings are indicated by white lines. In the ROSAT 1/4 keV band, which covers approximately (0.12−0.284) keV band, there are intensity variations in the X-ray emission around the SMC, but a contribution from the Magellanic Clouds is not obvious. The comparison with the foreground H I column density map of Dickey & Lockman (1990), where the SMC and LMC column density is not included, yields an anti-correlation of H I column density and X-ray intensity. This points to an origin of this soft emission outside the local hot bubble and suggests that the variations are primarily caused by different absorbing column densities. In the 3/4 keV band (0.47−1.21 keV) and the 1.5 keV band (0.76−2.04 keV), I see diffuse emission from the LMC (lower left) and an enhancement in the SMC bar. Other structures are caused by individual ROSAT scans, causing strip-like structures converging at the ecliptic pole close to the LMC. The intensity in the higher energy bands shows no spatial variations close to the SMC. This is expected, as the emission in these energy bands is primarily originating from the hot Galactic halo and the extragalactic cosmic X-ray background and because absorption has less effect at these energies.

The modelling of the celestial X-ray background is challenging, since especially the thermal emission from the Galactic halo is expected to have similar X-ray characteristics as the diffuse emission from the SMC. Based on the ROSAT images, I assume, that the X-ray emission of the fore- and

Table 6.1. Modelling of fluorescent lines.

Element	$E_{\rm centre}$ [eV]	σ [eV]	flux [10^3 cm^{-2} s^{-1}]
Al	$1487.98^{+0.62}_{-0.52}$	$36.1^{+3.8}_{-5.0}$	54^{+25}_{-24}
	1487.98[(a)]	$58.8^{+12.0}_{-6.1}$	52^{+24}_{-24}
Ti	4532^{+15}_{-14}	$61.1^{+15.0}_{-12.2}$	$3.02^{+0.67}_{-0.60}$
Cr	$5425.2^{+7.5}_{-7.8}$	$70.9^{+8.8}_{-7.4}$	$7.00^{+0.74}_{-0.67}$
Fe	6382^{+16}_{-15}	96^{+23}_{-17}	$5.11^{+0.88}_{-0.75}$
Ni	$7466.5^{+2.3}_{-1.1}$	$65.2^{+1.5}_{-1.5}$	$40.47^{+1.02}_{-0.94}$
Cu	$8026.78^{+0.47}_{-0.41}$	$78.0^{+0.5}_{-0.4}$	$344.6^{+3.4}_{-2.5}$
	8026.78[(a)]	485^{+28}_{-25}	$71.3^{+3.2}_{-3.4}$
Zn	$8615.3^{+2.7}_{-3.1}$	$78.2^{+2.8}_{-2.8}$	$35.6^{+1.2}_{-1.2}$
Cu	$8878.2^{+2.3}_{-2.5}$	$80.5^{+2.4}_{-2.2}$	$44.1^{+1.3}_{-1.2}$
Zn, Au	9562^{+10}_{-10}	$108.7^{+10.5}_{-9.8}$	$8.60^{+0.73}_{-0.74}$

Notes. [(a)] Coupled to previous line.

background components are not varying over the SMC field and that the observed emission is only modified by absorption.

I describe the celestial X-ray background by four components. (i) To account for X-rays from the local hot bubble, I used an unabsorbed plasma model.

The plasma emission was calculated with the astrophysical plasma emission code (apec, Smith et al. 2001) that predicts emission line and continuum spectra for an optically thin plasma in CIE. (ii) Emission from the cooler plasma in the Galactic halo was modelled with an apec plasma model, which is affected by absorption of the Galactic ISM. This component accounts for the variable structures, seen in the ROSAT 1/4 keV band image. (iii) Analogously, emission from the hot Galactic halo was modelled with an apec model of higher temperature. (iv) Emission from the cosmic X-ray background was modelled with a power-law, that is absorbed by the ISM of the Galaxy and the SMC. With a line-of-sight column density up to 10^{22} cm^{-2}, the ISM of the SMC efficiently absorbs the CXB at lower energies. The photon index was set to $\Gamma = 1.41$ (De Luca & Molendi 2004). The normalisation of this component depends on the level to which point sources are resolved. As the XMM-*Newton* observations have a similar exposure, I assume a constant normalisation for all spectral components.

$$S_{\rm XRB} = S^{\,i}_{\rm apec} + e^{-\sigma(E)\rm N_H^{gal}}(S^{\,ii}_{\rm apec} + S^{\,iii}_{\rm apec} + e^{-\sigma(E)\rm N_H^{smc}} N_{iv} E^{-\Gamma}) \tag{6.4}$$

For the X-ray emitting plasma, as well as for the absorbing matter, I assumed abundances according to Wilms et al. (2000) for the Galactic ISM and abundances of $Z_{\rm smc} = 0.2 Z_\odot$ for all elements heavier than helium in the ISM of the SMC (Russell & Dopita 1992). For each field in the SMC, the absorbing column density can be derived from 21 cm H I maps. For the column density of the ISM of the SMC, $\rm N_H^{smc}$, I used the map of Stanimirović et al. (1999). A map of the Galactic foreground $\rm N_H^{gal}$ based on the data of Staveley-Smith et al. (1997) was kindly provided by Erik Muller (see also Stanimirović et al. 1999; Muller et al. 2003).

To constrain the X-ray emitting components, I used observations around the SMC main field (white circles in Figure 6.6). Observations in the east were excluded, since these can be affected by diffuse X-ray emission of the SMC wing, as well as one of the observations in the south that pointed on the

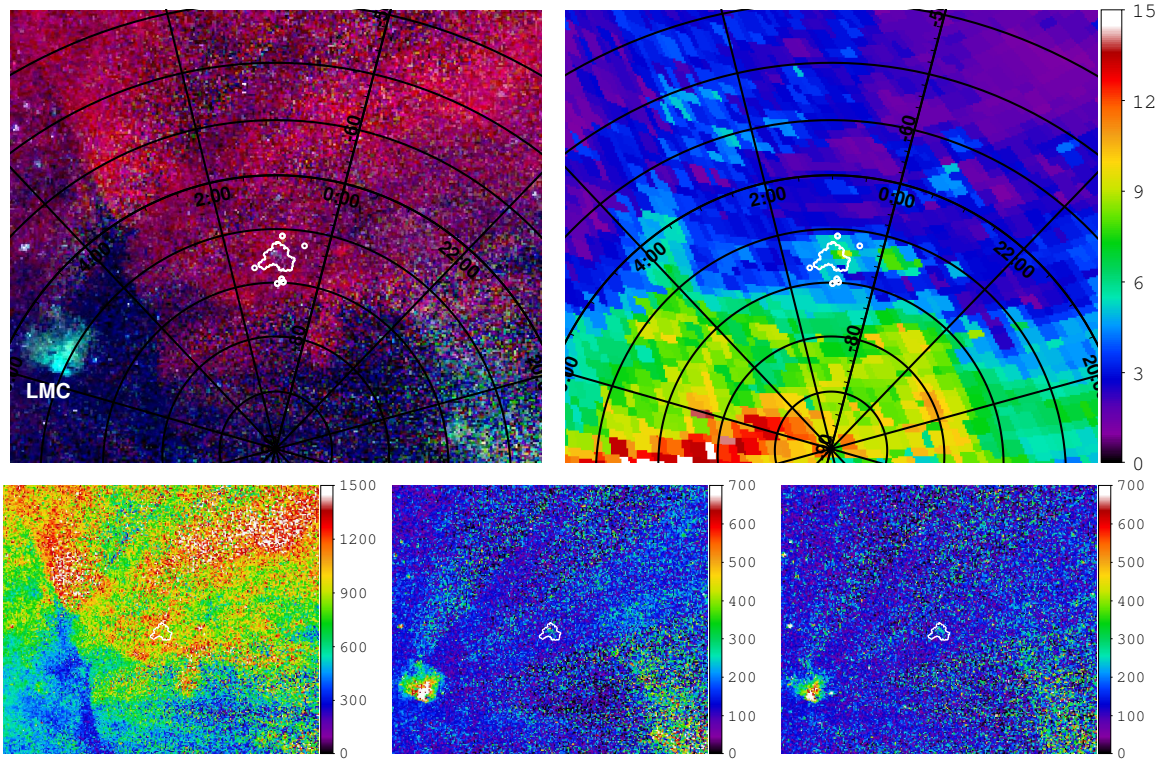

Figure 6.6. *Upper left:* ROSAT true-colour images (Snowden et al. 1997) of the diffuse X-ray background around the SMC. Red, green, and blue give logarithmically scaled intensities in the 1/4 keV, 3/4 keV and 1.5 keV band. White lines mark the observed XMM-*Newton* fields (cf. Figure 3.2). *Upper right:* H I column density map from Dickey & Lockman (1990) in units of 10^{20} cm^{-2}. *Lower panel* gives false-colour images of the 1/4 keV, 3/4 keV and 1.5 keV ROSAT bands in units of 10^{-6} cts s^{-1}, from left to right, respectively.

X-ray bright foreground star CF Tuc, which might contribute significantly also in the outer FoV of the observation.

Fitting the X-ray background model, including the detector-background and soft-proton model, to five observations in outer fields, I find a good description with a reduced $\chi^2_{\rm red}$ of 1.13 for 1752 degrees of freedom. For the apec plasma models the fit yields temperatures of $kT_i = 108.1^{+3.8}_{-4.6}$ eV, $kT_{ii} = 21^{+21}_{-15}$ eV, and $kT_{iii} = 248^{+20}_{-10}$ eV and normalisations of $N_i = 10.8^{+1.6}_{-2.2}$, $N_{ii} = 282^{+20603}_{-254}$, and $N_{iii} = 2.17^{+0.22}_{-0.35}$, all given in units of $10^{-24}(4\pi D_{\rm A}^2)^{-1} EM$ arcsec^{-2}, where EM is the emission measure of the plasma (Equation 2.10) in cm^{-3} and $D_{\rm A}$ is the distance to the plasma in cm. For the power law, I obtain a normalisation of $N_{iv} = 2.19^{+0.06}_{-0.12} \times 10^{-10}$ photons keV^{-1} cm^{-2} s^{-1} arcsec^{-2} at 1 keV. The temperature of the cooler absorbed plasma component is low, compared to other studies, which give ~0.1 keV (Kuntz & Snowden 2000). This leads to a lower contribution to the XMM-*Newton* energy band than the ROSAT band, as most of the emission falls below 0.2 keV. A cooler plasma will also be affected stronger by absorption, consistent with the spatial variability, seen in the ROSAT images of Figure 6.6.

6.1.4. X-ray emission from the SMC

Due to the moderate contribution of the SMC emission to the overall EPIC-pn spectrum, one can only fit a simple model. The real emission of the SMC will likely have a distribution in temperature and absorbing column density within the area of individual boxes and along the line of sight, but this

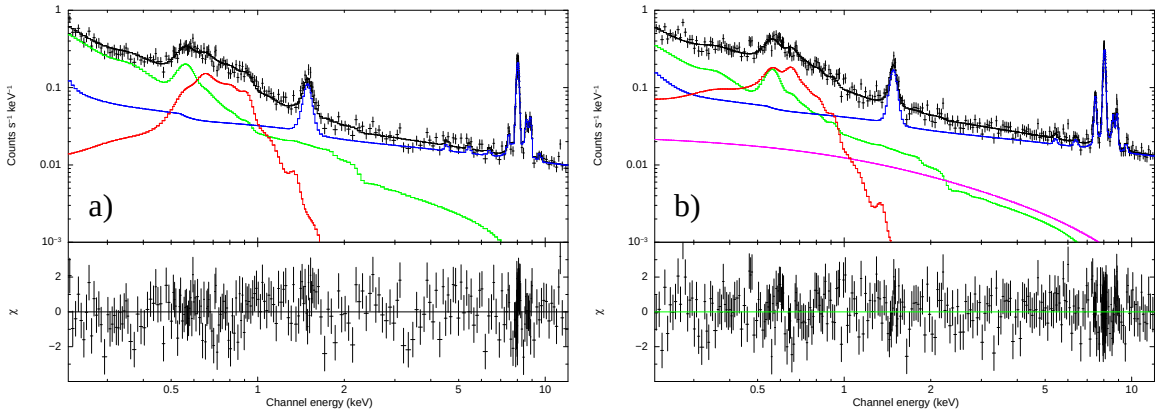

Figure 6.7. Examples for spectra and best-fit model. The X-ray fore- and background is plotted in green, detector background in blue, soft-proton contribution in magenta, and SMC emission in red and the summed model in black. The lower panel gives the residua. (a) Spectrum extracted from observation 0404680201 in the field of box 7-6. The absorption is $N_H^{smc*} = 7.9 \times 10^{21}$ cm^{-2} (b) Spectrum extracted from observation 0601210901 in the field of box 6-8. The absorption is $N_H^{smc*} = 6.5 \times 10^{20}$ cm^{-2}

would introduce too many parameters.

To characterise the diffuse emission of the SMC, I used an apec model, which is absorbed by the Galactic foreground and by a part of the ISM of the SMC, i. e. the column density of the SMC N_H^{smc*} was constrained to be $0 \leq N_H^{smc*} \leq N_H^{smc}$. I used $Z = 0.2 Z_\odot$ for the X-ray emitting plasma and the absorbing ISM as described above. N_H^{gal} and N_H^{smc} were set according to the H I maps as discussed above. This model,

$$S_{SMC} = e^{-\sigma(E) N_H^{gal}} e^{-\sigma(E) N_H^{smc*}} S_{apec}(T_{smc}, N_{smc}) \tag{6.5}$$

was fitted in combination with the previously discussed model components to all extracted spectra from the subregions of SMC observations. Spectra of the same subregion were fitted simultaneously, such that the parameters for the emission of the SMC (N_{smc}, T_{smc}, and N_H^{smc*}) were the same. Examples of two spectra are given in Figure 6.7. The results for each box are given in Table B.1 in the appendix.

6.2. Discussion

6.2.1. Morphology of the surface-brightness distribution

The XMM-*Newton* mosaic images, with and without point sources and extended sources (SNRs and ClGs), are compared with the mosaic image of ROSAT pointed observations (Haberl et al. 2000) in Figure 6.8. Here I also show a mask, visualising the distribution of XMM-*Newton* observations. Diffuse emission is clearly seen in the north-eastern part of the bar in the (0.5−1.0) keV band. I expect that most of the substructures in the XMM-*Newton* image are real features. This becomes evident, when we compare the XMM-*Newton* mosaic with the ROSAT image. The basic structures in both images coincide. The ROSAT point spread function strongly depends on off-axis angle, which makes it difficult to distinguish between faint sources in the SMC bar and diffuse emission. With XMM-*Newton*, we can better separate point and extended sources from the diffuse emission. Only a few artefacts possibly result from the bright sources SMC X-1 and 1E0102.2-7219.

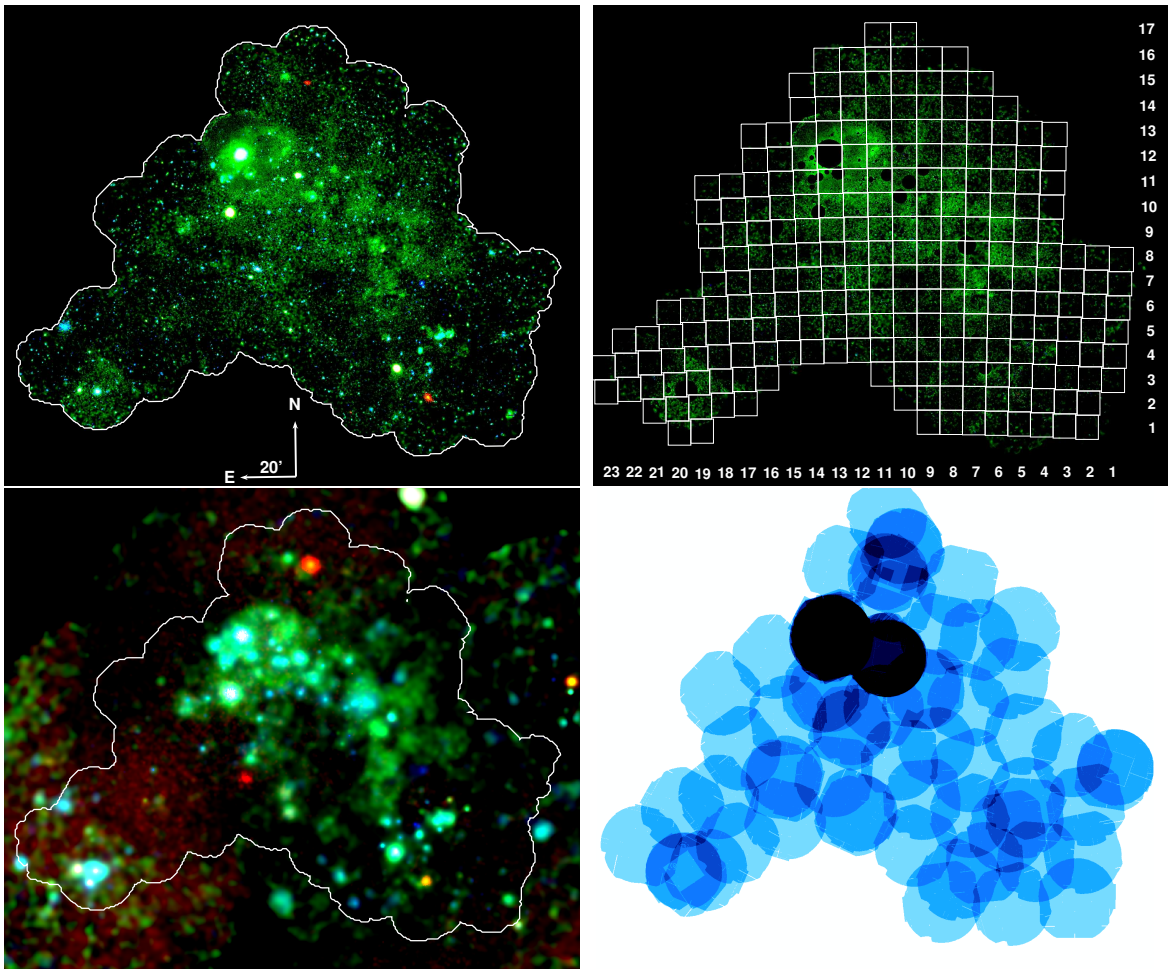

Figure 6.8. *Upper left:* XMM-*Newton* mosaic image of the SMC centred on RA=15$^{\rm h}$ Dec=-72.°6. Red/green/blue corresponds to intensities in the energy bands 0.2–0.5/0.5–1.0/1.0–2.0 keV. *Upper right:* Same image, but point and extended sources were excluded. White boxes mark the extraction regions for the spectral analysis of the diffuse emission. *Lower left:* The ROSAT mosaic from Haberl et al. (2000) in the 0.1–0.4/0.5–0.9/0.9–2.0 keV energy bands. *Lower right:* Distribution of XMM-*Newton* observations.

The observed surface brightness is especially high at the north-western rim of the north-eastern part of the bar and shows substructures with scales of some 100 pc in size. In Figure 6.9, the X-ray mosaic image, excluding point and extended sources, is compared to the H I (Stanimirović et al. 1999) and Hα (Winkler et al. 2005) emission of the SMC. Diffuse X-ray emission predominately originates in regions with high Hα and low H I emission. Especially at the north-western rim of the bar, the diffuse X-ray emission anticorrelates with the H I emission. The anticorrelation can be caused by the separation of hot and cold ISM as it is e. g. observed in the LMC. Keeping in mind the large depth along the line of sight of the SMC, the anticorrelation can also be caused by photoelectric absorption, if a sufficient amount of neutral ISM exists in front of the X-ray emitting regions.

Absorption can also explain the lack of diffuse X-ray emission in the south-western end of the bar. Here, several SNRs are located, pointing to the presence of a hot ISM. Also the spectra of the SNRs in this region show higher absorbing column densities than in other parts of the SMC (e. g. van der Heyden et al. 2004). In the south-western bar, the H I column density is highest in the SMC, with values up to 1.4×10^{22} cm^{-2}. Such high amounts of H I absorb X-rays up to 1 keV efficiently. E. g. the

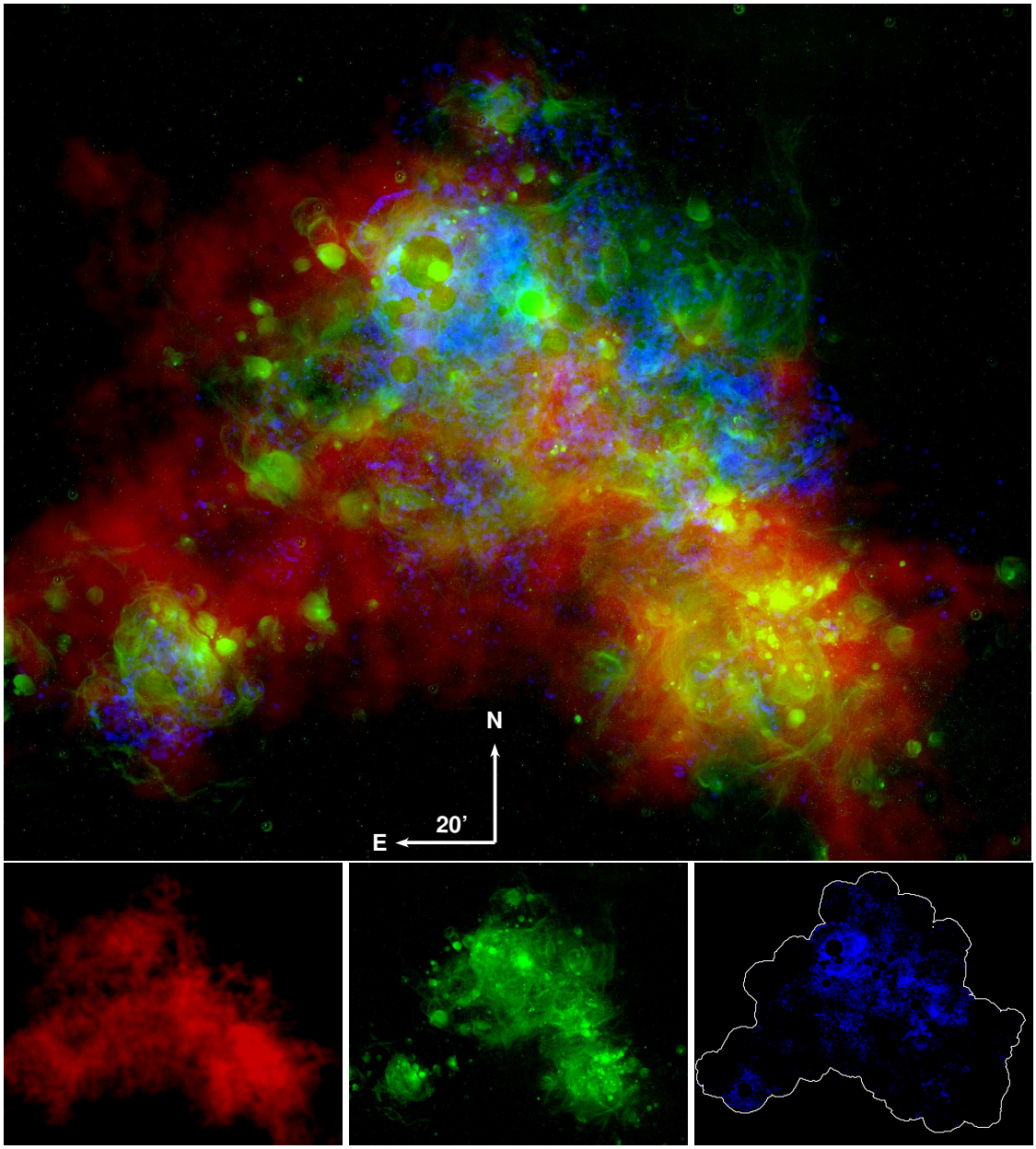

Figure 6.9. RGB image (*upper panel*) of the SMC centred on RA=15$^{\rm h}$ Dec=-72°.6 composed of logarithmically scaled emission in H I (red), Hα (green), and (0.2–1.0) keV X-rays (blue) as shown separately in the *lower panel*.

(0.5–1.0) keV flux of a plasma with a temperature of $kT = 0.2$ eV and SMC abundances ($Z = 0.2Z_{\odot}$) will be reduced to 54%, 23%, or 7% of the initial flux by passing a H I column density of 0.2, 0.5, or 1.0×10^{22} cm^{-2}, respectively. Thus, if the plasma is highly absorbed, a detection with XMM-*Newton* will be prevented completely, as the detector and cosmic background are dominant above 1 keV.

6.2.2. Spectroscopy

The results of the spectral analysis are presented in Figure 6.10. For most fields, the fit-statistics indicate a good description of the data by the model (Figure 6.10e). The high $\chi^2_{\rm red}$ values in the area of

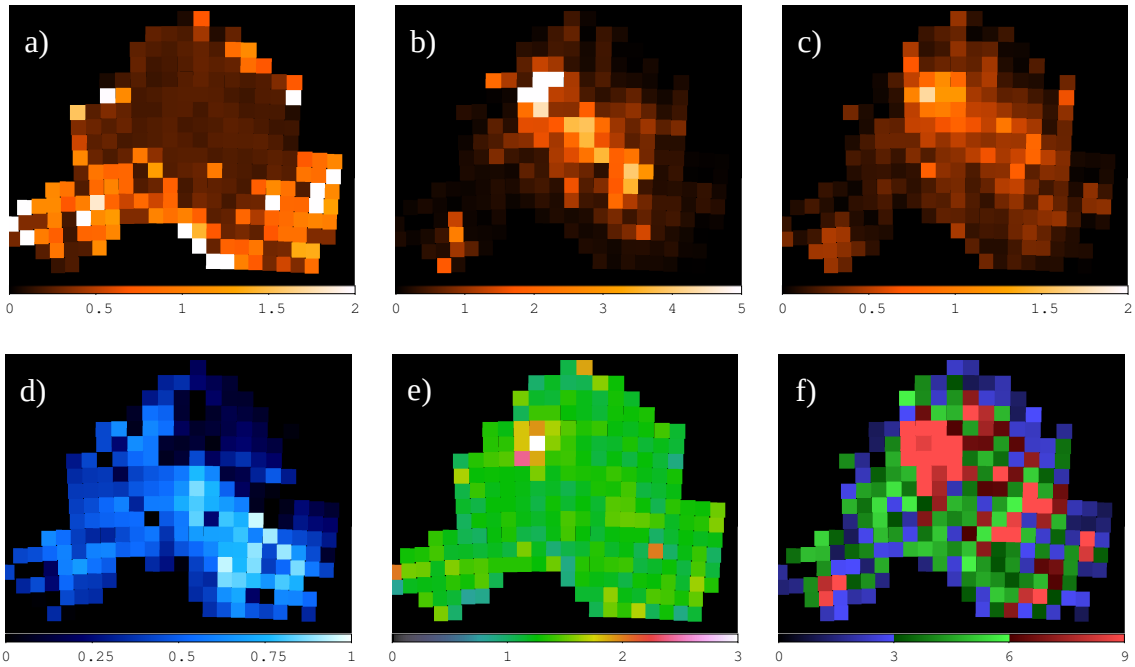

Figure 6.10. Distribution of parameters of the diffuse emission as obtained from the spectral fits (Section 6.1.4). [(a)] Temperature in keV. [(b)] Unabsorbed surface luminosity in 10^{30} erg s^{-1} arcsec^{-2}. [(c)] Detected surface brightness in 10^{-18} erg cm^{-2} s^{-1} arcsec^{-2}. [(d)] Absorbing column density N_H^{smc*} in 10^{22} cm^{-2}. [(e)] Reduced χ^2_{red}. [(f)] Significance of the SMC emission in σ.

1E0102.2-7219 point to some residual emission in this region. The significance of the SMC plasma emission was estimated by dividing the normalisation by the lower-limit 1σ confidence interval (see Figure 6.10f). Along the northern part of the bar, diffuse X-ray emission of the SMC is evident. In the outer parts of the bar and the wing of the SMC, low significances are derived, thus one cannot verify the presence of faint diffuse X-ray emission from the SMC here.

The spectral results confirm the scenario derived from the investigation of the morphology seen in the mosaic image. The resulting detected flux is high at the north-western rim of the bar (Figure 6.10c), whereas the unabsorbed luminosity, as derived from the spectral fitting, is following the bar of the SMC (Figure 6.10b). In the bar, high values are found for the absorbing column density N_H^{smc*} in contrast to the north-western rim, where the derived absorption is lower (Figure 6.10d). The fits often result in the maximal or minimal allowed value for N_H^{smc*}, as it is poorly constrained by the spectra. The two spectra, presented in Figure 6.7, give examples for a highly ($N_H^{smc*} = 7.9 \times 10^{21}$ cm^{-2}) and a moderately ($N_H^{smc*} = 6.5 \times 10^{20}$ cm^{-2}) absorbed SMC plasma, both having a temperature around 0.2 keV. As can be seen, absorption has most influence at lowest energies, but below 0.5 keV the emission of the X-ray foreground is dominant.

Within the northern part of the bar, a relatively constant temperature is found around $kT_{smc} \approx 0.2$ keV (Figure 6.10a). Around this region, the spectral analysis yields indication of plasma with higher temperature (0.7−1.1 keV) but low emission measure. Due to the low significance, the existence of such a component is doubtful and needs further investigation. In Figure 6.11a, a histogram is presented, where the luminosities of individual boxes for several temperature intervals are added. With ROSAT, Sasaki et al. (2002) found regions with higher temperatures (up to 0.8 keV), correlating with some SNRs, especially in the southern bar. This might be caused by some residual emission of these SNRs. Such a temperature distribution is not found from the spectral analysis of the EPIC-pn

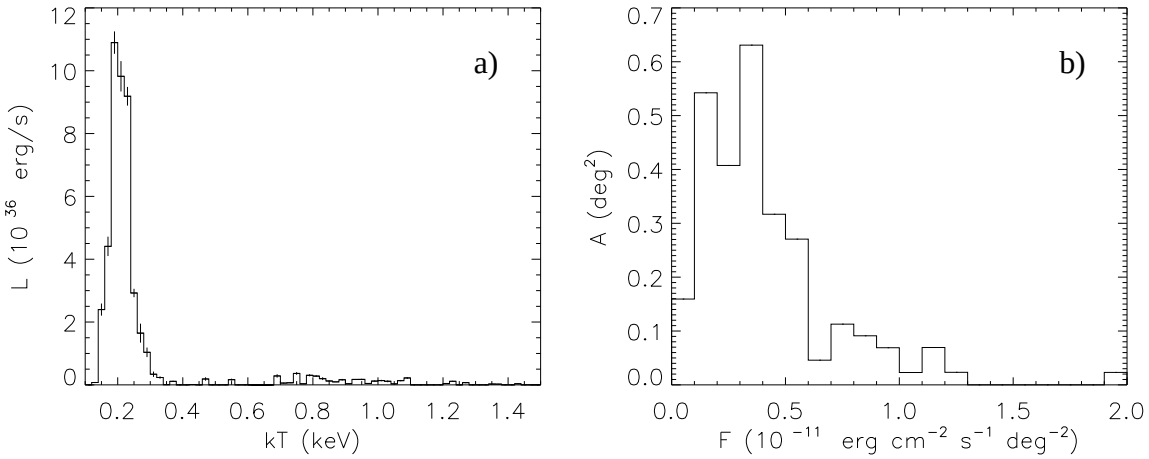

Figure 6.11. (a) Integrated unabsorbed luminosity as function of temperature. (b) Area covered by the emission as function of the surface brightness in the (0.5−1.0) keV band for boxes with significance $\geq 3\sigma$ and 0.15 keV $\geq kT \geq$ 0.3 keV.

data and also, we see no indication of spectral hardening in the mosaic image as would be expected for hotter plasma.

In Figure 6.11b, a histogram illustrates the area that is covered by the X-ray emitting plasma with temperature between 0.15 and 0.3 keV as function of the measured (absorbed) surface brightness in the (0.5−1.0) keV band. Typical values for the surface brightness are $2-5\times10^{-12}$ erg cm^{-2} s^{-1} deg^{-2} with a few regions reaching values up to 1.3×10^{-11} erg cm^{-2} s^{-1} deg^{-2}. Lower values often result in an insignificant SMC contribution and the distribution will be incomplete here. The X-ray background in the same band accounts for $\sim6.3\times10^{-12}$ erg cm^{-2} s^{-1} deg^{-2}, depending on SMC absorption.

By integrating over all boxes with a significance of $\geq 3\sigma$, I obtain an unabsorbed and absorbed luminosity of the SMC plasma in the (0.2−2.0) keV band of $3.95^{+0.05}_{-0.07}\times10^{37}$ erg s^{-1} and $7.08^{+0.06}_{-0.06}\times10^{36}$ erg s^{-1}, respectively, where the errors denote statistical uncertainties. However, systematic uncertainties will be higher, especially at lower energies, where absorption has most effect and the foreground emission is dominating. In the (0.5−1.0) keV band, one can derive a better constrained absorbed luminosity of $5.05^{+0.03}_{-0.03}\times10^{36}$ erg s^{-1}. The uncertainty of the measured X-ray fore- and background flux will contribute most to the systematic uncertainty with $\sim 2.8\times10^{35}$ erg s^{-1}.

Sasaki et al. (2002) derived a total unabsorbed luminosity of $L = 1.1^{+1.1}_{-0.44}\times10^{37}$ erg s^{-1} in the (0.1−2.4) keV band with ROSAT. For an apec plasma with $kT = 0.2$ and $Z = 0.2Z_{\odot}$, this translates to a luminosity of $L = 8.5\times10^{36}$ erg s^{-1} in the (0.2−2.0) keV band and $L = 4.2\times10^{36}$ erg s^{-1} in the (0.5−1.0) keV band. The unabsorbed luminosity found with XMM-*Newton* is higher by a factor of ∼4.6 compared to the value derived with ROSAT, which might be caused by the higher absorption found with XMM-*Newton*.

6.2.3. Origin of the diffuse X-ray emission

Diffuse X-ray emission can originate from the cumulative emission of weak soft X-ray sources below the detection threshold of the individual observations. From studies of the Galactic Ridge region such a component was resolved up to 80% into CVs and active binaries with individual luminosities of $L_X \leq 10^{32}$ erg s^{-1} (see Sec. 2.4.2). The average spectral shape of such a component is expected to be much flatter and extending to higher energies than the observed emission with characteristic temperature of 0.2 keV. E. g. Mineo et al. (2012b) used a power law with photon index of $\Gamma = 2$. Also

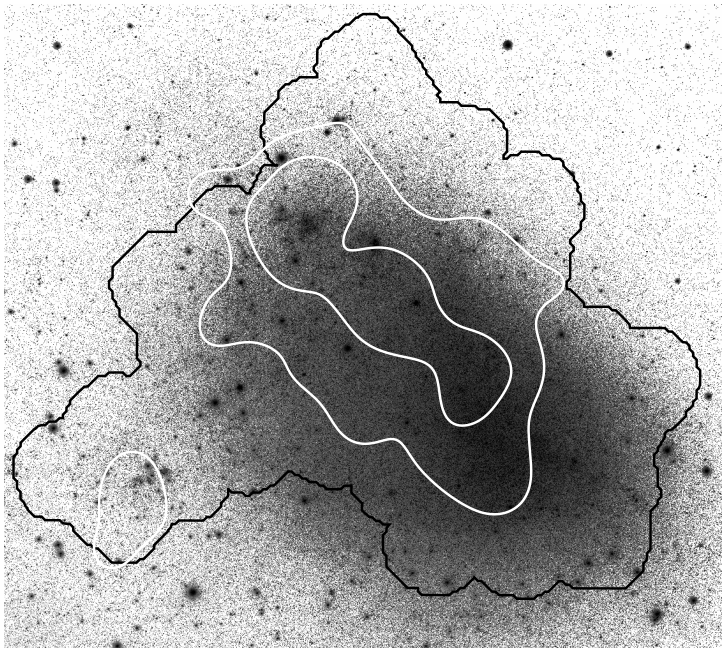

Figure 6.12. Logarithmically scaled *R*-band image from MCELS overlaid with contours of the luminosity of the diffuse emission (white) and the XMM-*Newton* main field (black).

the observed spatial distribution is not compatible with such a component, which is expected to follow the stellar population (Figure 6.12), but not the diffuse Hα emission (see below). One would expect a similar amount of diffuse emission in the outer south-western parts of the bar as in the northern bar. A CV/active binary component would be less affected by absorption and contribute above 1 keV. This is not seen in the mosaic images (Figure 6.8). Therefore, the observed diffuse X-ray emission cannot be produced by CVs and active binaries.

In contrast to this, the luminosity of the diffuse SMC emission clearly correlates with SFR indicators in the northern part of the bar, as shown in Figure 6.13. The X-ray emission of unresolved and faint young stellar objects cannot explain the observed temperature, since one would expect a harder X-ray spectrum with typical temperatures above 1 keV (Winston et al. 2007). The observed 0.2 keV temperature is typical for plasma in the hot phase of the ISM. The correlation to star formation is caused by the mechanical energy input by shock waves from stellar winds and SN explosions.

The SFR in the SMC is estimated to values between 0.05 and 0.4 $M_\odot$ yr^{-1} depending on different indicators (Shtykovskiy & Gilfanov 2005, and references therein). Lower values are derived from UV, Hα and FIR emission, whereas the higher values have been derived from stellar isochrone fits and the SNR population. This relates the observed luminosity in the (0.2−2.0) keV band to star formation by a factor of $2 - 14 \times 10^{37}$ erg s^{-1} per $M_\odot$ yr^{-1}. In other studies of nearby galaxies (e. g. Owen & Warwick 2009; Mineo et al. 2012b), higher values for L_X/SFR have been derived in the range of $0.25 - 5 \times 10^{39}$ erg s^{-1} per $M_\odot$ yr^{-1}. However, UV and reprocessed Hα and FIR emission is predominantly caused by the most massive stars with life times of some 10^6 yr. Since the life time of early B stars ($M = 8 - 20 M_\odot$) is in the range of 10−40 Myr (Bertelli et al. 2009), it takes longer for diffuse X-ray emission to reach maximum luminosity by SN explosions of stars with masses down to $8 M_\odot$ (Mas-Hesse et al. 2008). For the SMC, the spatially resolved star-formation history was derived by Harris & Zaritsky (2004) from isochrone fits to a photometric catalogue of the SMC divided into $12' \times 12'$ fields. I combined regions covered by the XMM-*Newton* survey according to the derived X-ray luminosity and SMC morphology to several larger fields as shown in Figure 6.13d. The star-formation history in these fields was derived by averaging the values of the subregions from Harris

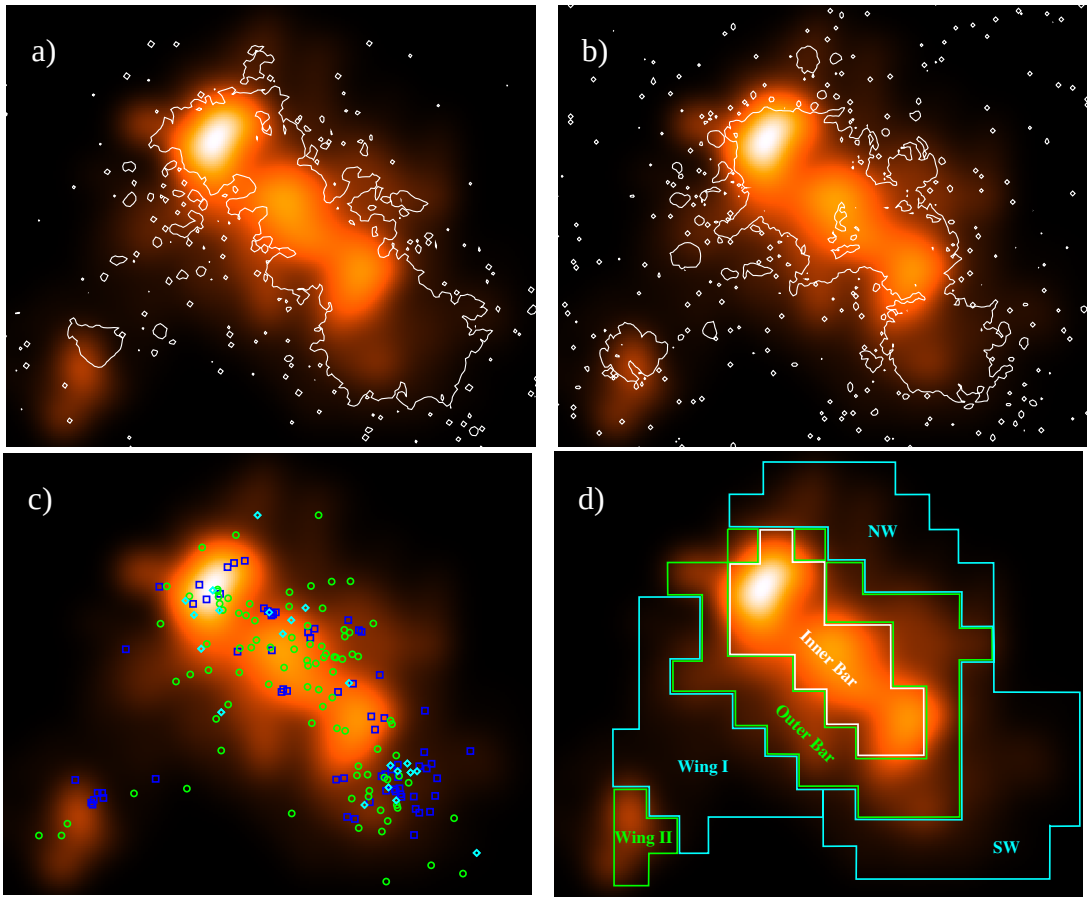

Figure 6.13. Same as Figure 6.10b but smoothed and overplotted with: [(a)] Contours of the 24 μm *Spitzer*/MIPS image at 0.1 MJy/sr (Gordon et al. 2011). [(b)] Continuum subtracted Hα contours at 5×10^{-16} erg cm^{-2} s^{-1} from MCELS (Winkler et al. 2005). [(c)] X-ray bright supernova remnants from Haberl et al. (2012a, cyan diamonds), high-mass X-ray binaries and candidates from the XMM-*Newton* catalogue (Section 4.3.3, green circles), and H II regions from Payne et al. (2004, blue boxes). [(d)] Regions used for the calculation of star-formation history from Harris & Zaritsky (2004).

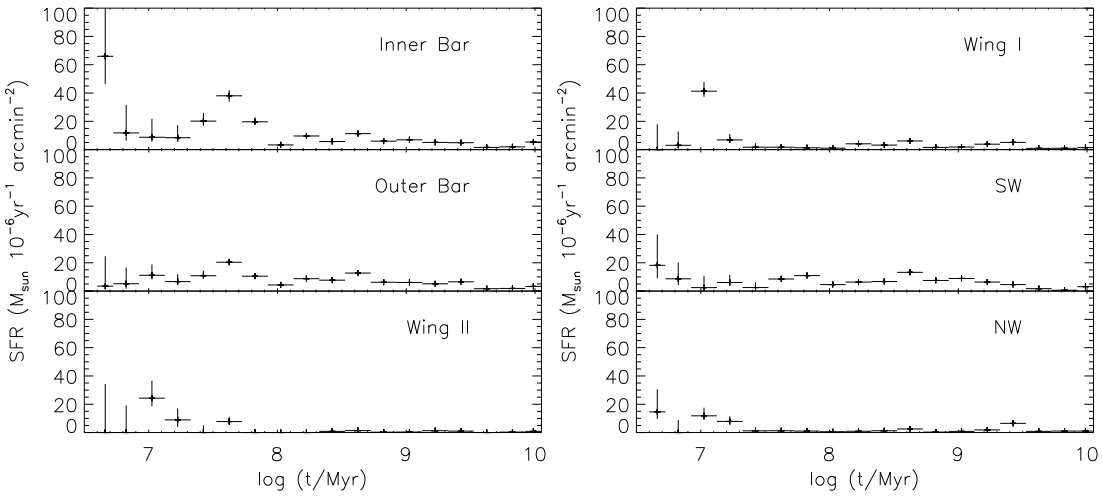

Figure 6.14. Star-formation history in the individual regions shown in Figure 6.13d.

& Zaritsky (2004) and adding the individual metallicity populations used by these authors. For each field, the star-formation history is plotted in Figure 6.14 as function of time. For the field with high X-ray luminosity (Inner Bar), a star-formation burst is found about 40 Myr ago. This is in good agreement with the time needed for stars of $8 M_{\odot}$ to evolve and explode in a SN. The total SFR in this area was $0.11 \pm 0.01 M_{\odot}$ yr^{-1} 40 Myr ago. For the inner bar, the unabsorbed $L_{0.2-2.0\mathrm{keV}}/\mathrm{SFR}_{40\mathrm{Myr}}$ ratio can be estimated to $2.5^{+0.85}_{-0.7} \times 10^{38}$ erg s^{-1} per $M_{\odot}$ yr^{-1} with this study. The high value of the most recent star formation in the inner bar originates within only three $12' \times 12'$ subregions of Harris & Zaritsky (2004) and unlikely causes the observed diffuse X-ray emission. In the regions with moderate X-ray luminosity (Outer Bar, Wing II) some indication of SF at 40 Myr is found as well. Regions with low X-ray luminosity do not show SF at this time. Only in the SW region, star formation is seen 40 Mys ago, but originates from regions, were diffuse X-ray emission might be absorbed completely. In the "Wing I" region, a burst of star formation is evident ∼10 Myr ago with $0.15^{+0.02}_{-0.01} M_{\odot}$ yr^{-1}. Here no strong diffuse X-ray emission is found.

Using Equation 2.8, we can roughly estimate the shock wave velocity to $v_{\mathrm{sh}} \approx 400$ km s^{-1}. This velocity is easily reached in stellar winds and SN explosions. The velocity of the heated plasma is expected to be $0.75 \mathrm{v}_{\mathrm{sh}} \approx 300$ km s^{-1} (Equation 2.5). If this velocity exceeds the escape velocity, the plasma might blow out into the halo. Also the X-ray luminosity might be high enough for outflows. By assuming an efficiency of 5% for the conversion of mechanical energy into X-ray emission, the mechanical luminosity of $\sim 8 \times 10^{38}$ erg s^{-1} would be sufficient to cause a blow out in dwarf galaxies with masses up to several $10^9 M_{\odot}$ as derived with hydrodynamic simulations by Mac Low & Ferrara (1999). Therefore, it is possible that we see outflows of the hot plasma at the north-western edge of the bar. For the distance of the SMC, 300 km s^{-1} corresponds to 1° per 40 Myr. As the X-ray luminosity scales with n^2, the expansion in the outer regions will prevent an detection at current depth of the observations. Deeper X-ray observations with higher spectral resolution are needed to further test this scenario.

7. Summary and conclusions

With the unprecedented effective area of ESA's X-ray space observatory XMM-Newton, the main body of the SMC is covered for the first time in the (0.2−12.0) keV band with imaging X-ray optics down to fluxes of 2×10^{-14} erg cm^{-2} s^{-1}. X-ray sources in the SMC are revealed down to luminosities of $\sim10^{34}$ erg s^{-1}. This allows to study HMXBs, SSSs, SNRs and the diffuse emission. In this thesis, I analysed XMM-*Newton* observations of the SMC from the large-programme XMM-*Newton* survey, performed between May 2009 and March 2010, and from archival data taken since September 2000. I was focussing on the point-source population, new transient sources discovered in the survey, other individual interesting sources, and the diffuse X-ray emission of the SMC.

To characterise the point-source population, I created the most comprehensive catalogue of X-ray sources in the SMC, using 91 XMM-*Newton* pointings covering the SMC bar and eastern wing with an area of 5.6 deg^2 and a total net exposure of ∼2 Ms. Detection of sources in the EPIC images was accomplished with sliding-box and maximum-likelihood techniques. The final catalogue contains 3053 unique X-ray point sources based on 5236 detections in the SMC field. X-ray sources are characterised by fluxes in individual energy bands, hardness ratios, source extent, as well as inter- and intra-observational variability. For the brightest sources, spectra and time series were extracted, as well as finding charts were created for all sources. In collaboration with Jai Won Kim, I developed a database system that is accessible by a web interface. This allows a powerful analysis of the data and provides access for the project collaboration members to the source catalogue and individual source products.

Due to the low distance of the SMC, point sources can be resolved and separated from regions with diffuse emission to a higher completeness than in more distant galaxies. However, the large extent on the sky leads to a relatively low surface brightness of the diffuse emission compared to detector and celestial X-ray background. For the analysis of the diffuse emission, a mosaic X-ray image of the SMC was created. The subtraction of detector background allowed a correction for telescope vignetting and revealed structures with low surface brightness, like new SNR candidates. In a second version of the mosaic image, I excluded point and extended sources, revealing the structure of the diffuse emission. To further investigate the spectral characteristics of the diffuse emission, I divided the main body of the SMC in subregions ($0.15^\circ \times 0.15^\circ$) and developed a method for the spectral analysis of these regions. Here, evidence for a contribution of the flaring background in the shielded detector corners of EPIC-pn was found, in contrast to EPIC-MOS.

To analyse the point-source catalogue, the data set and its uncertainties are described. The typical uncertainty for coordinates is 1.3″ (1σ confidence). Confusion of X-ray sources is only relevant near the brightest sources. In a second step, I correlated our catalogue with available optical, infrared and radio catalogues, as well as with previous X-ray catalogues. Here, we can find distinct counterparts in the X-ray and radio band. In the optical and NIR, the selection of true counterparts is challenging, due to the high stellar density in the SMC field. Searching the literature, it was possible to identify 49 HMXB, 4 SSSs in the SMC together with 34 foreground stars and 72 AGN behind the SMC. Based on these sources, I developed a source classification scheme with the main purpose to discriminate between sources in front of, within, and behind the SMC. This allowed to classify candidates for foreground stars (128), SMC HMXBs (45), faint SSSs (8) as well as AGN (2105) and galaxy clusters

(13) behind the SMC. Finally, statistical properties of the individual source samples are discussed.

As part of the statistical investigation of the point-source catalogue, I analysed luminosity functions for the individual source classes. For BeXRBs, this is the most precise measurement of their luminosity function from a homogeneous sample so far. The broken power-law parametrisation of the luminosity function confirms the turn over at $\sim 9 \times 10^{35}$ erg s^{-1} in the (2.0−12.0) keV band reported by Shtykovskiy & Gilfanov (2005). The bright-end slope of the luminosity function of BeXRBs is found to be significantly steeper than expected from the universal HMXB luminosity function. This is likely caused by a different luminosity function of BeXRBs and SgXRBs. The relative contributions of BeXRBs and SgXRBs depend on the star formation history of their host galaxy in the past ∼40 Myr and influences the luminosity function of the HMXB population of this galaxy and its hard X-ray emission.

The majority of X-ray sources in our catalogue are background sources behind the SMC. The spectral properties and luminosity functions of unclassified sources and AGN candidates is consistent with expectations from deep-field studies. The X-ray detected AGN in the SMC field will provide a valuable sample of background sources. After further investigation of these sources (determination of unique counter parts and optical spectroscopy), they will provide an astrometric reference frame for investigations of proper motions of stars in the SMC and allow to study absorption effects by the ISM of the SMC.

During the XMM-*Newton* survey, we discovered four new hard X-ray transients in bright outburst. These sources could be clearly identified as BeXRBs, in contrast to the faint HMXB candidates found in the point-source catalogue. One example has been presented in Sec. 5.3, where the X-ray source was identified as a BeXRB pulsar in the SMC. Although the survey focused on the SMC wing and outer area of the bar, three of these new systems are located in the bar of the SMC where the bulk of the BeXRB population is located. This suggests that undiscovered systems still exist there. The four new systems, as well as new candidates in the catalogue, further increase the sample of known HMXBs in the SMC. An further enlargement of this homogeneous sample is highly desired for statistical investigations, e. g. to characterise accretion processes and supernova explosions.

The analysis of the catalogue revealed the first candidate for a Be/WD system in the SMC with SSS emission. This illustrated that XMMU J052016.0-692505 (Kahabka et al. 2006) in the LMC is not a unique case. Recently, Li et al. (2012) reported the discovery of another Be/WD system in the wing of the SMC. The system MAXI J0158-744 was found as bright SSS source and is associated with both a nova explosion and an early-type Be star counterpart. Also an X-ray outburst of CI Cam is suggested to originate from a nova explosion in a B[e]/WD system (Filippova et al. 2011). With more and more evidence, a new class of SSS might be recognised that is made up of binary systems of WDs accreting from early-type emission-line stars.

New X-ray data of SMC 3 show that two scenarios can qualitatively explain the spectral evolution and the shape of the light curve. The evolution of the X-ray spectra is incompatible with varying photoelectric absorption by neutral gas, but is consistent with energy-independent intensity variations and/or with temperature variations. As suggested before by Kahabka (2004), Compton scattering in a predominantly ionised stellar wind could lead to the observed intensity variations if the stellar wind density (mass loss rate) and the ionisation rate are high enough. Additional temperature changes in the burning layer of the WD, which are caused by variable accretion, can reduce the required wind densities. The understanding of absorption in SSS is important to see if their population can account for the rate of type Ia SN (Hachisu et al. 2010).

The EPIC mosaic image reveals diffuse emission in the north-western rim of the northern part of the bar. The comparison with other wavelengths shows that these regions have high Hα emission from ionised gas but low H I emission from neutral gas, which would absorb X-rays. Here outflows

might occur, but this needs further investigations. No diffuse emission was found in most parts of the wing and in the south-western part of the SMC bar. In the latter region, the detection of the diffuse SMC component is probably prevented by absorption. To separate the diffuse SMC emission from background components, a spectral analysis was performed. The spectrum of the SMC emission can be described with an optically-thin collisionally-ionized plasma model. The spectral analysis allows to derive the luminosity distribution of the emitting plasma and also yields indications for strong absorption of the diffuse X-ray emission. I obtain an absorbed and unabsorbed luminosity of the SMC plasma in the (0.2−2.0) keV band with statistical uncertainties of $7.08^{+0.06}_{-0.06} \times 10^{36}$ erg s^{-1} and $3.95^{+0.05}_{-0.07} \times 10^{37}$ erg s^{-1} , respectively. The total luminosity can only be estimated with high uncertainties due to absorption effects that cannot be constrained well with the existing data. In contrast to previous ROSAT studies, I find a relatively homogeneously temperature around $kT = 0.2$ keV. The spatial distribution of the diffuse emission cannot be explained by unresolved point sources like CVs and active binaries. The regions of high luminosity clearly correlate with star-formation indicators and I show that this star-formation occurred ∼40 Myr ago. For the inner bar, an unabsorbed $L_{0.2-2.0\mathrm{keV}}/\mathrm{SFR}_{40\mathrm{Myr}}$ ratio of $2.5^{+0.85}_{-0.7} \times 10^{38}$ erg s^{-1} per $M_\odot$ yr^{-1} is derived.

The results of the thesis yield deeper insights into the statistical and individual properties of X-ray emitting sources in the SMC and help to improve the understanding of the X-ray point-source population of the SMC and its interstellar medium. The source catalogue, the mosaic image, and the parametrisation of the diffuse emission will be publicly available and will provide complementary information to future studies.

8. Outlook

8.1. Further investigation of the XMM-Newton data

During the PhD thesis, the XMM-*Newton* data of the SMC have been used to investigate new transient sources, the X-ray source population as a whole and the diffuse emission. Similar studies will be done for the currently ongoing LMC survey, an XMM-*Newton very-large programme*. Due to the more recent star formation in the LMC about 12 Myr ago (Harris & Zaritsky 2009), a comparison with the SMC will yield a better understanding of the evolution of the HMXB population and the hot ISM dependent on star formation history.

The SMC survey data can be used for more detailed studies of the individual source classes: E. g. the XMM-*Newton* SMC catalogue lists 211 detections of 49 HMXBs. For 142 detections, the statistics allows a spectral analysis. Additional systems have been observed in later observations. A homogeneous analysis of spectral and temporal behaviour of the SMC HMXB population can yield further insights to the HMXB population of the SMC. This study will be complementary to the large sample investigated with RXTE that is biased to bright outbursts and high pulsed fractions. Additional 45 HMXB candidates need further investigation. With optical follow-up observations of these systems one can search for Hα emission. In X-rays, *Swift* monitoring might help to find outbursts of BeXRBs and trigger follow-up XMM-*Newton* observations. Due to its large effective area, XMM-*Newton* is ideally suited to build up a large sample of observed BeXRBs. Because of the transient nature of these systems, this can only by done step by step.

The XMM-*Newton* SMC point-source catalogue revealed new candidates for faint SSSs. Only one has been investigated in detail so far (Sec. 5.2). The same holds for Be/WDs candidates.

The XMM-*Newton* survey of the SMC provides a complete census of the SNR population down to an X-ray surface brightness of some 10^{-14} erg cm^{-2} s^{-1} arcmin^{-2}. This comprises 23 SNRs and candidates (Haberl et al. 2012a). The EPIC mosaic image revealed three new candidates for large and old SNRs, that will need deeper X-ray observations for further investigation. A homogeneous analysis of the XMM-*Newton* data will allow to describe the population of the SMC. A first investigation has been done as part of an internship by Joseph DeRose under my supervision.

AGN behind the SMC are interesting objects for proper motion studies, boresight corrections and investigation of the ISM of the SMC. The XMM-*Newton* catalogue contains 2105 candidates for AGN that ideally need to be confirmed by optical spectroscopy. For up to 167 AGN candidates, an X-ray spectral analysis is possible. Also the comparison with the recently published *Spitzer* SMC survey will further affirm the background origin of these sources. From a comparison of deep merged radio-continuum images (Wong et al. 2011, 2012) with the XMM-*Newton* point-source catalogue, Danica Drašković found 96 associations. Most of these are background objects (Sturm et al., in preparation).

Also an extension of the survey in the eastern part of the wing towards the supergiant shell SMC-SGS 1 can lead to the discovery of additional BeXRBs, as e. g. SXP1062 (Hénault-Brunet et al. 2012; Haberl et al. 2012b), and will allow the study of the diffuse emission in this region.

After some time, an update of the XMM-*Newton* point-source catalogue will be worth to consider. This update can contain the following improvements: (i) A deeper source detection using combined information of overlapping regions. At the time of the catalogue creation, SAS version 10 did not

allow to handle a large number of images simultaneously. This is possible with the 64-bit SAS version 11. (ii) Further improved astrometry by using additional identified sources for boresight correction that will be available after investigation of good candidates in the current catalogue. (iii) A two-dimensional PSF model is available in SAS 11 and will further improve the coordinate precision and reduce the contribution of spurious detections. (iv) New observations, performed after the SMC survey, can be included into a catalogue update.

8.2. The SMC in the forthcoming eROSITA all-sky survey

The extended ROentgen Survey with an Imaging Telescope Array (eROSITA, Predehl et al. 2010; Merloni et al. 2012) is currently developed at MPE and will be the prime instrument on board the Russian Spectrum-Roentgen-Gamma (SRG) satellite, planned for launch in 2014. During the first 4 years, the satellite will perform an all-sky survey. This will yield 8 complete coverages of the SMC, separated by 6 months. The following consideration was part of a poster that I presented at the *First eROSITA International Conference* (Garmisch-Partenkirchen, Germany, 2011 October 17–20).

Assuming a Sun-pointing scanning axis, the total exposure of the SMC will be around 3450 s in the bar and 3800 s in the wing. Simulated eROSITA spectra for one scanning period (438 s exposure) of the SSS SMC 3 and the BeXRB SXP 6.85 in bright state are presented in Figure 8.1. The spectral parameters were determined from XMM-*Newton* observations on 2009 October 3 and 2006 October 3. The simulated spectra allow to derive the SSS temperature and power-law photon index with a statistical accuracy of 14% and 64%, respectively.

If we demand 15 counts for a detection with eROSITA, this simulation yields a flux threshold for source detection of 5.0×10^{-14} erg cm $^{-2}$ s^{-1} and 5.2×10^{-13} erg cm $^{-2}$ s^{-1} for a SSS and a HMXB, respectively. Compared to the XMM-*Newton* survey, this is higher by a factor of ∼20, but allows to detect systems already in moderate outbursts with luminosities of $\gtrsim 10^{35}$ erg s^{-1}. The repeated coverage of the SMC during the eROSITA survey every six months enables to monitor the BeXRB population and will lead to the discovery of new BeXRBs and probably new SSS that were in off-state during the ROSAT all-sky survey. Their classification will be possible from spectral properties and source variability. This will be especially interesting to probe the BeXRB population in the outer fields of the SMC, which have not been monitored extensively so far and to study long-term light curves over 4 years. Discoveries of bright outburst can be used to trigger follow-up X-ray observations. The feasibility of triggering an XMM-*Newton* observation by the outburst of a BeXRB was e. g. demonstrated by an XMM-*Newton* ToO observation of IGR J05414-6858 (Sturm et al. 2012c).

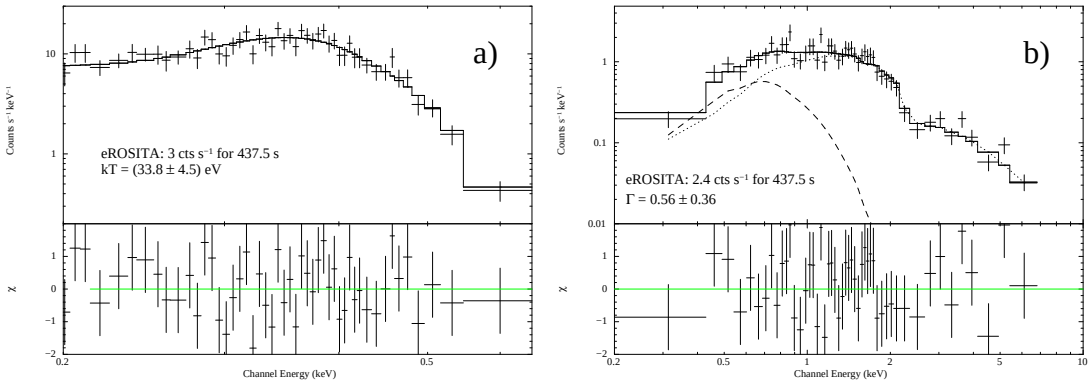

Figure 8.1. Simulated eROSITA spectra with an exposure of 438 s: (a) SMC 3 simulated with black-body emission. (b) SXP 6.85 simulated with black-body and power-law emission.

Acknowledgements

The last lines of this thesis are dedicated to the people who supported me during this time. First, I want to thank Jochen Greiner for giving me the possibility of writing my PhD thesis at the technische Universität München and for his comments that helped to improve the thesis.

I am most grateful to my supervisor Frank Haberl for the great opportunity of analysing the XMM-*Newton large-programme* survey data, for his guidance over the past years, and for being accessible for help and discussions at any time. Thank you very much.

Furthermore, I am also very grateful to Wolfgang Pietsch. His extensive experience contributed substantially to the success of this thesis.

I would like to thank Jai Won Kim for all her commitment of creating the web interface and for her help with database-related problems.

Here, I also have to mention the high-energy group members Hermann Brunner, Vadim Burwitz, Konrad Dennerl, Michael Freyberg, Martin Henze, as well as the members of the SMC large-programme collaboration Jean Ballet, Dominik Bomans, David A.H. Buckley, Malcolm J. Coe, Robin Corbet, Matthias Ehle, Miroslav D. Filipović, Marat Gilfanov, Despina Hatzidimitriou, Sandro Mereghetti Steve Snowden, and Andrea Tiengo for their support and helpful discussions that substantially helped to improve the thesis.

I would like to thank Harald Baumgartner for system administration and Birgit Boller for administrative support.

All other colleagues and my fellow students at MPE, IMPRS, and TUM, I thank for the pleasant environment and some great time.

Last, but by no means least, I thank my family and my friends. This dissertation would not have been possible without them.

This thesis is based on observations with XMM-Newton, an ESA Science Mission with instruments and contributions directly funded by ESA Member States and the USA (NASA). The XMM-Newton project is supported by the Bundesministerium für Wirtschaft und Technologie/Deutsches Zentrum für Luft- und Raumfahrt (BMWI/DLR, FKZ 50 OX 0001) and the Max-Planck Society.

I acknowledge support by the Bundesministerium für Wirtschaft und Technologie/Deutsches Zentrum für Luft- und Raumfahrt (BMWI/DLR grant FKZ 50 OR 0907).

Bibliography

Abbe, C. 1867, MNRAS, 27, 257

Abbey, T., Carpenter, J., Read, A., et al. 2006, in ESA Special Publication, Vol. 604, The X-ray Universe 2005, ed. A. Wilson, 943

Abdo, A. A., Ackermann, M., Ajello, M., et al. 2010a, A&A, 512, A7

Abdo, A. A., Ackermann, M., Ajello, M., et al. 2010b, A&A, 523, A46

Antoniou, V., Zezas, A., Hatzidimitriou, D., & Kalogera, V. 2010, ApJ, 716, L140

Antoniou, V., Zezas, A., Hatzidimitriou, D., & McDowell, J. C. 2009, ApJ, 697, 1695

Apparao, K. M. V. 1991, A&A, 248, 139

Arnaud, K. A. 1996, in Astronomical Society of the Pacific Conference Series, Vol. 101, Astronomical Data Analysis Software and Systems V, ed. G. H. Jacoby & J. Barnes, 17

Aschenbach, B. 2002, in Society of Photo-Optical Instrumentation Engineers (SPIE) Conference Series, Vol. 4496, Society of Photo-Optical Instrumentation Engineers (SPIE) Conference Series, ed. P. Gorenstein & R. B. Hoover, 8–22

Aschenbach, B. 2007, in Society of Photo-Optical Instrumentation Engineers (SPIE) Conference Series, Vol. 6688, Society of Photo-Optical Instrumentation Engineers (SPIE) Conference Series

Azzopardi, M., Vigneau, J., & Macquet, M. 1975, A&AS, 22, 285

Badenes, C., Maoz, D., & Draine, B. T. 2010, MNRAS, 407, 1301

Bauer, M. 2004, Dissertation, Technische Universität München

Bekki, K. & Stanimirović, S. 2009, MNRAS, 395, 342

Berghoefer, T. W., Schmitt, J. H. M. M., Danner, R., & Cassinelli, J. P. 1997, A&A, 322, 167

Bertelli, G., Nasi, E., Girardi, L., & Marigo, P. 2009, A&A, 508, 355

Bica, E., Bonatto, C., Dutra, C. M., & Santos, J. F. C. 2008, MNRAS, 389, 678

Bildsten, L., Chakrabarty, D., Chiu, J., et al. 1997, ApJS, 113, 367

Blackburn, J. K. 1995, in Astronomical Society of the Pacific Conference Series, Vol. 77, Astronomical Data Analysis Software and Systems IV, ed. R. A. Shaw, H. E. Payne, & J. J. E. Hayes, 367

Bock, D. C.-J., Large, M. I., & Sadler, E. M. 1999, AJ, 117, 1578

Böhringer, H., Briel, U. G., Schwarz, R. A., et al. 1994, Natur, 368, 828

Bolatto, A. D., Simon, J. D., Stanimirović, S., et al. 2007, ApJ, 655, 212

Bonatto, C. & Bica, E. 2010, MNRAS, 403, 996

Bonfini, P., Hatzidimitriou, D., Pietsch, W., & Reig, P. 2009, A&A, 507, 705

Bonnet, R. M. 1988, in ESA Special Publication, Vol. 281, ESA Special Publication, 85–94

Borkowski, K. J., Lyerly, W. J., & Reynolds, S. P. 2001, ApJ, 548, 820

Briel, U. G., Burwitz, V., Dennerl, K., et al. 2005, in Society of Photo-Optical Instrumentation Engineers (SPIE) Conference Series, Vol. 5898, Society of Photo-Optical Instrumentation Engineers (SPIE) Conference Series, ed. O. H. W. Siegmund, 194–200

Brightman, M. & Nandra, K. 2012, MNRAS, 422, 1166

Brüns, C., Kerp, J., Staveley-Smith, L., et al. 2005, A&A, 432, 45

Cappelluti, N., Brusa, M., Hasinger, G., et al. 2009, A&A, 497, 635

Carter, J. A. & Read, A. M. 2007, A&A, 464, 1155

Cash, W. 1979, ApJ, 228, 939

Cavaliere, A. & Fusco-Femiano, R. 1976, A&A, 49, 137

Cioni, M.-R., Loup, C., Habing, H. J., et al. 2000, A&AS, 144, 235

Coe, M., Corbets, R. H. D., McGowan, K. E., & McBride, V. A. 2010a, in Astronomical Society of the Pacific Conference Series, Vol. 422, High Energy Phenomena in Massive Stars, ed. J. Martí, P. L. Luque-Escamilla, & J. A. Combi, 224

Coe, M. J. 2005, MNRAS, 358, 1379
Coe, M. J., Edge, W. R. T., Galache, J. L., & McBride , V. A. 2005, MNRAS, 356, 502
Coe, M. J., Haberl, F., Sturm, R., et al. 2012, MNRAS, 424, 282
Coe, M. J., Haberl, F., Sturm, R., et al. 2011, MNRAS, 414, 3281
Coe, M. J., McBride, V. A., & Corbet, R. H. D. 2010b, MNRAS, 401, 252
Corbet, R. H. D. 1984, A&A, 141, 91
Corbet, R. H. D., Coe, M. J., McGowan, K. E., et al. 2009, in IAU Symposium, Vol. 256, IAU Symposium, ed. J. T. van Loon & J. M. Oliveira, 361–366
de Avillez, M. A. & Breitschwerdt, D. 2005, A&A, 436, 585
de Chambure, D., Lainé, R., van Katwijk, K., & Kletzkine, P. 1999a, ESA Bulletin, 100, 30
de Chambure, D., Laine, R., van Katwijk, K., et al. 1999b, in Society of Photo-Optical Instrumentation Engineers (SPIE) Conference Series, Vol. 3737, Society of Photo-Optical Instrumentation Engineers (SPIE) Conference Series, ed. F. Merkle, 396–408
De Luca, A. & Molendi, S. 2004, A&A, 419, 837
den Herder, J. W., Brinkman, A. C., Kahn, S. M., et al. 2001, A&A, 365, L7
DENIS Consortium. 2005, VizieR Online Data Catalog, 2263, 0
Dennerl, K. 2010, Space Sci. Rev., 157, 57
Diago, P. D., Gutiérrez-Soto, J., Fabregat, J., & Martayan, C. 2008, A&A, 480, 179
Dias, B., Coelho, P., Barbuy, B., Kerber, L., & Idiart, T. 2010, A&A, 520, A85
Dickel, J. R., Gruendl, R. A., McIntyre, V. J., & Amy, S. W. 2010, AJ, 140, 1511
Dickey, J. M. & Lockman, F. J. 1990, ARA&A, 28, 215
Dobrzycki, A., Macri, L. M., Stanek, K. Z., & Groot, P. J. 2003a, AJ, 125, 1330
Dobrzycki, A., Stanek, K. Z., Macri, L. M., & Groot, P. J. 2003b, AJ, 126, 734
Dray, L. M. 2006, MNRAS, 370, 2079
Eger, P. 2008, Master's thesis, Technische Universität München
Eger, P. & Haberl, F. 2008, A&A, 491, 841
Englhauser, J. 1996, Dissertation, Technische Universität München
Evans, C. J., Howarth, I. D., Irwin, M. J., Burnley, A. W., & Harries, T. J. 2004, MNRAS, 353, 601
Evans, I. N., Primini, F. A., Glotfelty, K. J., et al. 2010, ApJS, 189, 37
Eyer, L. 2002, Acta Astron., 52, 241
Fabian, A. C., Zoghbi, A., Ross, R. R., et al. 2009, Natur, 459, 540
Favata, F. 2002, in Astronomical Society of the Pacific Conference Series, Vol. 277, Stellar Coronae in the Chandra and XMM-NEWTON Era, ed. F. Favata & J. J. Drake, 115
Filipović, M. D., Bohlsen, T., Reid, W., et al. 2002, MNRAS, 335, 1085
Filipović, M. D., Cohen, M., Reid, W. A., et al. 2009, MNRAS, 399, 769
Filipović, M. D., Haberl, F., Winkler, P. F., et al. 2008, A&A, 485, 63
Filipović, M. D., Haynes, R. F., White, G. L., & Jones, P. A. 1998, A&AS, 130, 421
Filippova, E., Revnivtsev, M., & Lutovinov, A. 2011, in Astronomical Society of the Pacific Conference Series, Vol. 447, Evolution of Compact Binaries, ed. L. Schmidtobreick, M. R. Schreiber, & C. Tappert, 227
Fitzgerald, M. P. 1970, A&A, 4, 234
Freyberg, M. J., Briel, U. G., Dennerl, K., et al. 2004, in Society of Photo-Optical Instrumentation Engineers (SPIE) Conference Series, Vol. 5165, Society of Photo-Optical Instrumentation Engineers (SPIE) Conference Series, ed. K. A. Flanagan & O. H. W. Siegmund, 112–122
Friedman, H., Lichtman, S. W., & Byram, E. T. 1951, Physical Review, 83, 1025
Fujimoto, M. Y. 1982, ApJ, 257, 752
Galache, J. L., Corbet, R. H. D., Coe, M. J., et al. 2008, ApJS, 177, 189
Ghosh, P. & Lamb, F. K. 1979, ApJ, 234, 296
Giacconi, R., Gursky, H., Paolini, F. R., & Rossi, B. B. 1962, Physical Review Letters, 9, 439
Gies, D. R. 2000, in Astronomical Society of the Pacific Conference Series, Vol. 214, IAU Colloq. 175: The Be Phenomenon in Early-Type Stars, ed. M. A. Smith, H. F. Henrichs, & J. Fabregat, 668
Gilfanov, M. & Bogdán, Á. 2010, Natur, 463, 924

Gordon, K. D., Meixner, M., Meade, M. R., et al. 2011, AJ, 142, 102
Gordon, K. D., Witt, A. N., Carruthers, G. R., Christensen, S. A., & Dohne, B. C. 1994, ApJ, 432, 641
Grandi, P., Tagliaferri, G., Giommi, P., Barr, P., & Palumbo, G. G. C. 1992, ApJS, 82, 93
Gregory, P. C. & Loredo, T. J. 1996, ApJ, 473, 1059
Greiner, J., ed. 1996, Lecture Notes in Physics, Berlin Springer Verlag, Vol. 472, Supersoft X-Ray Sources
Greiner, J., Bickert, K., Luthardt, R., et al. 1996, in Lecture Notes in Physics, Berlin Springer Verlag, Vol. 472, Supersoft X-Ray Sources, ed. J. Greiner, 267
Greiner, J., Hasinger, G., & Kahabka, P. 1991, A&A, 246, L17
Grimm, H.-J., Gilfanov, M., & Sunyaev, R. 2003, MNRAS, 339, 793
Güdel, M., Audard, M., Reale, F., Skinner, S. L., & Linsky, J. L. 2004, A&A, 416, 713
Güdel, M. & Nazé, Y. 2009, A&A Rev., 17, 309
Guerrero, M. A. & Chu, Y.-H. 2008, ApJS, 177, 216
Haberl, F. 1995, A&A, 296, 685
Haberl, F., Dennerl, K., Filipović, M. D., et al. 2001, A&A, 365, L208
Haberl, F., Eger, P., & Pietsch, W. 2008, A&A, 489, 327
Haberl, F., Filipović, M. D., Pietsch, W., & Kahabka, P. 2000, A&AS, 142, 41
Haberl, F. & Motch, C. 1995, A&A, 297, L37
Haberl, F. & Pietsch, W. 2004, A&A, 414, 667
Haberl, F. & Pietsch, W. 2008, A&A, 484, 451
Haberl, F. & Sasaki, M. 2000, A&A, 359, 573
Haberl, F., Sturm, R., Ballet, J., et al. 2012a, A&A, 545, A128
Haberl, F., Sturm, R., Filipović, M. D., Pietsch, W., & Crawford, E. J. 2012b, A&A, 537, L1
Hachisu, I., Kato, M., & Nomoto, K. 2010, ApJ, 724, L212
Harris, J. & Zaritsky, D. 2004, AJ, 127, 1531
Harris, J. & Zaritsky, D. 2006, AJ, 131, 2514
Harris, J. & Zaritsky, D. 2009, AJ, 138, 1243
Hasinger, G., Altieri, B., Arnaud, M., et al. 2001, A&A, 365, L45
Hasinger, G., Cappelluti, N., Brunner, H., et al. 2007, ApJS, 172, 29
Hénault-Brunet, V., Oskinova, L. M., Guerrero, M. A., et al. 2012, MNRAS, 420, L13
Henze, M., Pietsch, W., Haberl, F., et al. 2011, A&A, 533, A52
Hickox, R. C., Narayan, R., & Kallman, T. R. 2004, ApJ, 614, 881
Hilditch, R. W., Howarth, I. D., & Harries, T. J. 2005, MNRAS, 357, 304
Hirata, K., Kajita, T., Koshiba, M., Nakahata, M., & Oyama, Y. 1987, Physical Review Letters, 58, 1490
Høg, E., Fabricius, C., Makarov, V. V., et al. 2000, A&A, 355, L27
Hopkins, P. F., Hernquist, L., Cox, T. J., & Kereš, D. 2008, ApJS, 175, 356
Howarth, I. D. & Phillips, A. P. 1986, MNRAS, 222, 809
Ikhsanov, N. R. 2007, MNRAS, 375, 698
Jansen, F., Lumb, D., Altieri, B., et al. 2001, A&A, 365, L1
Jones, D. H., Read, M. A., Saunders, W., et al. 2009, MNRAS, 399, 683
Jordan, S., Schmutz, W., Wolff, B., Werner, K., & Muerset, U. 1996, A&A, 312, 897
Joye, W. A. 2006, in Astronomical Society of the Pacific Conference Series, Vol. 351, Astronomical Data Analysis Software and Systems XV, ed. C. Gabriel, C. Arviset, D. Ponz, & S. Enrique, 574
Kahabka, P. 2004, A&A, 416, 57
Kahabka, P. 2006, Advances in Space Research, 38, 2836
Kahabka, P. & Haberl, F. 2006, A&A, 452, 431
Kahabka, P., Haberl, F., Pakull, M., et al. 2008, A&A, 482, 237
Kahabka, P., Haberl, F., Payne, J. L., & Filipović, M. D. 2006, A&A, 458, 285
Kahabka, P. & Pietsch, W. 1993, in Lecture Notes in Physics, Berlin Springer Verlag, Vol. 416, New Aspects of Magellanic Cloud Research, ed. B. Baschek, G. Klare, & J. Lequeux, 71–73

Kahabka, P. & Pietsch, W. 1996, A&A, 312, 919
Kahabka, P., Pietsch, W., Filipović , M. D., & Haberl, F. 1999, A&AS, 136, 81
Kahabka, P. & van den Heuvel, E. P. J. 1997, ARA&A, 35, 69
Kallivayalil, N., van der Marel, R. P., & Alcock, C. 2006, ApJ, 652, 1213
Kapakos, E., Hatzidimitriou, D., & Soszyński, I. 2011, MNRAS, 415, 1366
Kato, D., Nagashima, C., Nagayama, T., et al. 2007, PASJ, 59, 615
Keller, S. C. & Wood, P. R. 2006, ApJ, 642, 834
Keller, S. C., Wood, P. R., & Bessell, M. S. 1999, A&AS, 134, 489
Kelly, B. C., Bechtold, J., & Siemiginowska, A. 2009, ApJ, 698, 895
Klein, U. 2012, The ISM of Dwarf Galaxies, ed. P. Papaderos, S. Recchi, & G. Hensler, 23
Knigge, C., Coe, M. J., & Podsiadlowski, P. 2011, Natur, 479, 372
Koyama, K., Kinugasa, K., Matsuzaki, K., et al. 1997, PASJ, 49, L7
Kozłowski, S. & Kochanek, C. S. 2009, ApJ, 701, 508
Kozłowski, S., Kochanek, C. S., & Udalski, A. 2011, ApJS, 194, 22
Kuntz, K. D. & Snowden, S. L. 2000, ApJ, 543, 195
Kuntz, K. D. & Snowden, S. L. 2008, A&A, 478, 575
Kurucz, R. L. 1979, ApJS, 40, 1
La Palombara, N., Sidoli, L., Esposito, P., Tiengo, A., & Mereghetti, S. 2009, A&A, 505, 947
Lasker, B. M., Lattanzi, M. G., McLean, B. J., et al. 2008, AJ, 136, 735
Laycock, S., Corbet, R. H. D., Coe, M. J., et al. 2005, ApJS, 161, 96
Laycock, S., Zezas, A., Hong, J., Drake, J. J., & Antoniou, V. 2010, ApJ, 716, 1217
Leavitt, H. S. & Pickering, E. C. 1912, Harvard College Observatory Circular, 173, 1
Leong, C., Kellogg, E., Gursky, H., Tananbaum, H., & Giacconi, R. 1971, ApJ, 170, L67
Leroy, A., Bolatto, A., Stanimirović, S., et al. 2007, ApJ, 658, 1027
Li, F., Jernigan, G., & Clark, G. 1977, IAU Circ., 3125, 1
Li, K. L., Kong, A. K. H., Charles, P. A., et al. 2012, ApJ, 761, 99
Liedahl, D. A. 1999, in Lecture Notes in Physics, Berlin Springer Verlag, Vol. 520, X-Ray Spectroscopy in Astrophysics, ed. J. van Paradijs & J. A. M. Bleeker, 189
Lindsay, E. M. 1961, AJ, 66, 169
Lomb, N. R. 1976, AP&SS, 39, 447
Longair, M. S. 1999, in Lecture Notes in Physics, Berlin Springer Verlag, Vol. 520, X-Ray Spectroscopy in Astrophysics, ed. J. van Paradijs & J. A. M. Bleeker, 1
Lopes de Oliveira, R., Motch, C., Haberl, F., Negueruela, I., & Janot-Pacheco, E. 2006, A&A, 454, 265
Lumb, D. H., Warwick, R. S., Page, M., & De Luca, A. 2002, A&A, 389, 93
Mac Low, M.-M. & Ferrara, A. 1999, ApJ, 513, 142
Maccacaro, T., Gioia, I. M., Wolter, A., Zamorani, G., & Stocke, J. T. 1988, ApJ, 326, 680
Martayan, C., Baade, D., & Fabregat, J. 2010, A&A, 509, A11
Mas-Hesse, J. M., Otí-Floranes, H., & Cerviño, M. 2008, A&A, 483, 71
Mason, K. O., Breeveld, A., Much, R., et al. 2001, A&A, 365, L36
Massey, P. 2002, ApJS, 141, 81
Massey, P., Olsen, K. A. G., & Parker, J. W. 2003, PASP, 115, 1265
Matz, S. M., Share, G. H., Leising, M. D., Chupp, E. L., & Vestrand, W. T. 1988, Natur, 331, 416
Mauch, T., Murphy, T., Buttery, H. J., et al. 2003, MNRAS, 342, 1117
McBride, V. A., Coe, M. J., Negueruela, I., Schurch , M. P. E., & McGowan, K. E. 2008, MNRAS, 388, 1198
McCray, R. 2007, in American Institute of Physics Conference Series, Vol. 937, Supernova 1987A: 20 Years After: Supernovae and Gamma-Ray Bursters, ed. S. Immler, K. Weiler, & R. McCray, 3–14
McGowan, K. E., Coe, M. J., Schurch, M. P. E., et al. 2008, MNRAS, 383, 330
Mennickent, R. E., Pietrzyński, G., Gieren, W., & Szewczyk, O. 2002, A&A, 393, 887
Mereghetti, S., Krachmalnicoff, N., La Palombara, N., et al. 2010, A&A, 519, A42

Merloni, A., Predehl, P., Becker, W., et al. 2012, ArXiv e-prints
Meszaros, P. 1992, High-energy radiation from magnetized neutron stars
Mewe, R. 1999, in Lecture Notes in Physics, Berlin Springer Verlag, Vol. 520, X-Ray Spectroscopy in Astrophysics, ed. J. van Paradijs & J. A. M. Bleeker, 109
Meyssonnier, N. & Azzopardi, M. 1993, A&AS, 102, 451
Mills, B. Y., Little, A. G., Durdin, J. M., & Kesteven, M. J. 1982, MNRAS, 200, 1007
Mineo, S., Gilfanov, M., & Sunyaev, R. 2012a, MNRAS, 419, 2095
Mineo, S., Gilfanov, M., & Sunyaev, R. 2012b, MNRAS, 426, 1870
Misanovic, Z., Pietsch, W., Haberl, F., et al. 2006, A&A, 448, 1247
Mitsuda, K., Inoue, H., Koyama, K., et al. 1984, PASJ, 36, 741
Miyaji, T., Ishisaki, Y., Ogasaka, Y., et al. 1998, A&A, 334, L13
Monet, D. G., Levine, S. E., Canzian, B., et al. 2003, AJ, 125, 984
Morgan, D. H. 1992, MNRAS, 258, 639
Muller, E., Staveley-Smith, L., Zealey, W., & Stanimirović, S. 2003, MNRAS, 339, 105
Murphy, M. T. & Bessell, M. S. 2000, MNRAS, 311, 741
Nazé, Y., Hartwell, J. M., Stevens, I. R., et al. 2002, ApJ, 580, 225
Nazé, Y., Hartwell, J. M., Stevens, I. R., et al. 2003, ApJ, 586, 983
Nazé, Y., Manfroid, J., Stevens, I. R., Corcoran, M. F., & Flores, A. 2004, ApJ, 608, 208
Negueruela, I., Smith, D. M., Reig, P., Chaty, S., & Torrejón, J. M. 2006, in ESA Special Publication, Vol. 604, The X-ray Universe 2005, ed. A. Wilson, 165
Nomoto, K., Saio, H., Kato, M., & Hachisu, I. 2007, ApJ, 663, 1269
Nomoto, K., Thielemann, F.-K., & Yokoi, K. 1984, ApJ, 286, 644
Novara, G., La Palombara, N., Mereghetti, S., et al. 2011, A&A, 532, A153
Okazaki, A. T. 2001, PASJ, 53, 119
Okazaki, A. T. & Negueruela, I. 2001, A&A, 377, 161
Orio, M., Zezas, A., Munari, U., Siviero, A., & Tepedelenlioglu, E. 2007, ApJ, 661, 1105
Owen, R. A., Filipović, M. D., Ballet, J., et al. 2011, A&A, 530, A132
Owen, R. A. & Warwick, R. S. 2009, MNRAS, 394, 1741
Paczynski, B. & Rudak, B. 1980, A&A, 82, 349
Paresce, F. 1984, AJ, 89, 1022
Pawsey, J. L. 1959, in IAU Symposium, Vol. 9, URSI Symp. 1: Paris Symposium on Radio Astronomy, ed. R. N. Bracewell, 405
Payne, J. L., Filipović, M. D., Reid, W., et al. 2004, MNRAS, 355, 44
Piatek, S., Pryor, C., & Olszewski, E. W. 2008, AJ, 135, 1024
Pietsch, W., Freyberg, M., & Haberl, F. 2005, A&A, 434, 483
Pietsch, W., Misanovic, Z., Haberl, F., et al. 2004, A&A, 426, 11
Pols, O. R., Cote, J., Waters, L. B. F. M., & Heise, J. 1991, A&A, 241, 419
Pradhan, A. C., Murthy, J., & Pathak, A. 2011, ApJ, 743, 80
Predehl, P., Andritschke, R., Böhringer, H., et al. 2010, in Society of Photo-Optical Instrumentation Engineers (SPIE) Conference Series, Vol. 7732, Society of Photo-Optical Instrumentation Engineers (SPIE) Conference Series
Price, R. E., Groves, D. J., Rodrigues, R. M., et al. 1971, ApJ, 168, L7
Primini, F. A., Forman, W., & Jones, C. 1993, ApJ, 410, 615
Protassov, R., van Dyk, D. A., Connors, A., Kashyap, V. L., & Siemiginowska, A. 2002, ApJ, 571, 545
Raguzova, N. V. 2001, A&A, 367, 848
Rauch, T. & Deetjen, J. L. 2003, in Astronomical Society of the Pacific Conference Series, Vol. 288, Stellar Atmosphere Modeling, ed. I. Hubeny, D. Mihalas, & K. Werner, 103
Rauch, T. & Werner, K. 2010, Astronomische Nachrichten, 331, 146
Read, A. M., Sembay, S. F., Abbey, T. F., & Turner, M. J. L. 2006, in ESA Special Publication, Vol. 604, The X-ray Universe 2005, ed. A. Wilson, 925
Reig, P. 2011, AP&SS, 332, 1

Reig, P., Fabregat, J., & Coe, M. J. 1997, A&A, 322, 193
Revnivtsev, M., Sazonov, S., Churazov, E., et al. 2009, Natur, 458, 1142
Revnivtsev, M., Sazonov, S., Gilfanov, M., Churazov, E., & Sunyaev, R. 2006, A&A, 452, 169
Rohrbach, J. G., Ness, J.-U., & Starrfield, S. 2009, AJ, 137, 4627
Rosati, P., Borgani, S., & Norman, C. 2002, ARA&A, 40, 539
Russell, S. C. & Dopita, M. A. 1992, ApJ, 384, 508
Sasaki, M., Haberl, F., & Pietsch, W. 2000, A&AS, 147, 75
Sasaki, M., Haberl, F., & Pietsch, W. 2002, A&A, 392, 103
Scargle, J. D. 1982, ApJ, 263, 835
Schwering, P. B. W. & Israel, F. P. 1991, A&A, 246, 231
Seward, F. D. & Mitchell, M. 1981, ApJ, 243, 736
Shapiro, P. R. & Field, G. B. 1976, ApJ, 205, 762
Shtykovskiy, P. & Gilfanov, M. 2005, MNRAS, 362, 879
Skrutskie, M. F., Cutri, R. M., Stiening, R., et al. 2006, AJ, 131, 1163
Smith, C., Leiton, R., & Pizarro, S. 2000, in Astronomical Society of the Pacific Conference Series, Vol. 221, Stars, Gas and Dust in Galaxies: Exploring the Links, ed. D. Alloin, K. Olsen, & G. Galaz, 83
Smith, R. K., Brickhouse, N. S., Liedahl, D. A., & Raymond, J. C. 2001, ApJ, 556, L91
Snowden, S. L., Collier, M. R., & Kuntz, K. D. 2004, ApJ, 610, 1182
Snowden, S. L., Egger, R., Freyberg, M. J., et al. 1997, ApJ, 485, 125
Stanimirović, S., Staveley-Smith, L., Dickey, J. M., Sault, R. J., & Snowden, S. L. 1999, MNRAS, 302, 417
Stanimirović, S., Staveley-Smith, L., & Jones, P. A. 2004, ApJ, 604, 176
Staveley-Smith, L., Sault, R. J., Hatzidimitriou, D., Kesteven, M. J., & McConnell, D. 1997, MNRAS, 289, 225
Stiele, H., Pietsch, W., Haberl, F., & Freyberg, M. 2008, A&A, 480, 599
Stiele, H., Pietsch, W., Haberl, F., et al. 2011, A&A, 534, A55
Strüder, L., Briel, U., Dennerl, K., et al. 2001, A&A, 365, L18
Strüder, L., Meidinger, N., Pfeffermann, E., et al. 2000, in Society of Photo-Optical Instrumentation Engineers (SPIE) Conference Series, Vol. 4012, Society of Photo-Optical Instrumentation Engineers (SPIE) Conference Series, ed. J. E. Truemper & B. Aschenbach, 342–352
Sturm, R., Haberl, F., Coe, M. J., et al. 2011a, A&A, 527, A131
Sturm, R., Haberl, F., Greiner, J., et al. 2011b, A&A, 529, A152
Sturm, R., Haberl, F., Hasinger, G., Kenzaki, K., & Itoh, M. 2009, PASJ, 61, 895
Sturm, R., Haberl, F., Pietsch, W., et al. 2012a, A&A, submitted
Sturm, R., Haberl, F., Pietsch, W., et al. 2012b, A&A, 537, A76
Sturm, R., Haberl, F., Pietsch, W., & Immler, S. 2011c, The Astronomer's Telegram, 3537, 1
Sturm, R., Haberl, F., Rau, A., et al. 2012c, A&A, 542, A109
Subramanian, S. & Subramaniam, A. 2012, ApJ, 744, 128
Sunyaev, R. A., Kaniovskii, A. S., Efremov, V. V., et al. 1990, Soviet Astronomy Letters, 16, 171
Svoboda, R., McNaught, R. H., Jones, A., et al. 1987, IAU Circ., 4340, 1
Tajer, M., Trinchieri, G., Wolter, A., et al. 2005, A&A, 435, 799
Taylor, G. 1950, Royal Society of London Proceedings Series A, 201, 159
Taylor, M. 2011, Astrophysics Source Code Library, 5001
Tiengo, A., Esposito, P., & Mereghetti, S. 2008, ApJ, 680, L133
Tinney, C. G., Da Costa, G. S., & Zinnecker, H. 1997, MNRAS, 285, 111
Townsend, L. J., Coe, M. J., Corbet, R. H. D., et al. 2011, MNRAS, 410, 1813
Townsend, L. J., Coe, M. J., McBride, V. A., et al. 2010, MNRAS, 403, 1239
Turner, M. J. L., Abbey, A., Arnaud, M., et al. 2001, A&A, 365, L27
Udalski, A., Kubiak, M., & Szymanski, M. 1997, Acta Astron., 47, 319
Udalski, A., Szymanski, M., Kubiak, M., et al. 1998, Acta Astron., 48, 147
Udalski, A., Szymanski, M. K., Soszynski, I., & Poleski, R. 2008, Acta Astron., 58, 69

Urry, C. M. & Padovani, P. 1995, PASP, 107, 803
van der Heyden, K. J., Bleeker, J. A. M., & Kaastra, J. S. 2004, A&A, 421, 1031
Véron-Cetty, M.-P. & Véron, P. 2006, A&A, 455, 773
Vink, J. 2012, A&A Rev., 20, 49
Vogel, M. & Morgan, D. H. 1994, A&A, 288, 842
Voit, G. M. 2005, Reviews of Modern Physics, 77, 207
Walter, R., Zurita Heras, J., Bassani, L., et al. 2006, A&A, 453, 133
Wang, Q. & Wu, X. 1992, ApJS, 78, 391
Wargelin, B. J., Markevitch, M., Juda, M., et al. 2004, ApJ, 607, 596
Waters, L. B. F. M., Pols, O. R., Hogeveen, S. J., Cote, J., & van den Heuvel, E. P. J. 1989, A&A, 220, L1
Watson, M. G., Schröder, A. C., Fyfe, D., et al. 2009, A&A, 493, 339
Wayte, S. R. 1990, ApJ, 355, 473
Weaver, R., McCray, R., Castor, J., Shapiro, P., & Moore, R. 1977, ApJ, 218, 377
Wegner, W. 1994, MNRAS, 270, 229
Weisskopf, M. C., Tananbaum, H. D., Van Speybroeck, L. P., & O'Dell, S. L. 2000, in Society of Photo-Optical Instrumentation Engineers (SPIE) Conference Series, Vol. 4012, Society of Photo-Optical Instrumentation Engineers (SPIE) Conference Series, ed. J. E. Truemper & B. Aschenbach, 2–16
Welsh, B. Y. & Shelton, R. L. 2009, AP&SS, 323, 1
Westerlund, B. E. 1990, A&A Rev., 2, 29
Westerlund, B. E. 1997, The Magellanic Clouds
Wilkes, B. J., Wright, A. E., Jauncey, D. L., & Peterson, B. A. 1983, Proceedings of the Astronomical Society of Australia, 5, 2
Wilms, J., Allen, A., & McCray, R. 2000, ApJ, 542, 914
Wilson, C. A., Finger, M. H., Coe, M. J., & Negueruela, I. 2003, ApJ, 584, 996
Winkler, P. F., Young, A. L., Braziunas, D., et al. 2005, in Bulletin of the American Astronomical Society, Vol. 37, American Astronomical Society Meeting Abstracts, 132.03
Winston, E., Megeath, S. T., Wolk, S. J., et al. 2007, ApJ, 669, 493
Wisniewski, J. P., Draper, Z. H., Bjorkman, K. S., et al. 2010, ApJ, 709, 1306
Witt, A. N. & Gordon, K. D. 2000, ApJ, 528, 799
Wolter, H. 1952, Annalen der Physik, 445, 94
Wong, G. F., Crawford, E. J., Filipović, M. D., et al. 2012, Serbian Astronomical Journal, 184, 93
Wong, G. F., Filipović, M. D., Crawford, E. J., et al. 2011, Serbian Astronomical Journal, 183, 103
Woosley, S. E., Heger, A., & Weaver, T. A. 2002, Reviews of Modern Physics, 74, 1015
Worsley, M. A., Fabian, A. C., Bauer, F. E., et al. 2005, MNRAS, 357, 1281
Wright, C. O., Egan, M. P., Kraemer, K. E., & Price, S. D. 2003, AJ, 125, 359
Wright, N. J., Drake, J. J., & Civano, F. 2010, ApJ, 725, 480
Yokogawa, J., Imanishi, K., Tsujimoto, M., Koyama, K., & Nishiuchi, M. 2003, PASJ, 55, 161
Zaritsky, D. & Harris, J. 2004, ApJ, 604, 167
Zaritsky, D., Harris, J., Thompson, I. B., Grebel, E. K., & Massey, P. 2002, AJ, 123, 855
Zel'Dovich, Y. B. & Raizer, Y. P. 1966, Physics of Shock Waves and High-Temperature Hydrodynamic Phenomena, ed. W. D. Hayes & R. F. Probstein, Vol. 1
Zezas, A. & Orio, M. 2008, The Astronomer's Telegram, 1379, 1
Ziolkowski, J. 2002, Mem. Soc. Astron. Italiana, 73, 1038

A. Acronyms

AGN	Active Galactic Nucleus
ARF	ancillary response file
AOCS	Attitude & Orbit Control Subsystem
BH	black hole
CCD	charge-coupled device
CCF	current calibration file
CIF	CCF index file
CIE	collisional ionisation equilibrium
ClG	cluster of galaxies
CTI	charge transfer inefficiency
CV	cataclysmic variable
CXB	cosmic X-ray background
ECF	energy conversion factor
EPIC	European Photon Imaging Camera (on XMM-Newton)
ERM	EPIC Radiation Monitor
ESA	European Space Agency
FFT	fast Fourier transform
FoV	field of view
FTS	Faulkes Telescope South
FWC	filter wheel closed
GTI	good time interval
HMXB	high-mass X-ray binary
IRSF	InfraRed Survey Facility
ICM	intracluster medium
IR	Infrared
ISM	interstellar medium
LHB	local hot bubble
LMC	Large Magellanic Cloud
MCPS	Magellanic Cloud Photometric Survey
MIP	minimum ionising particle
NIR	near infrared
NLTE	non-local thermal equilibrium
NS	neutron star
ODF	observation data file
OGLE	optical gravitational lensing experiment
OOT	out of time
PSF	point spread function
QPB	quiescent particle background
RMF	redistribution matrix file
RXTE	Rossi X-ray Timing Explorer
SAS	Science Analysis Software
SFR	star formation rate
SgXRB	supergiant X-ray binary
SFXT	supergiant fast X-ray transient
SNR	supernova remnant
SMC	Small Magellanic Cloud
SPF	soft proton flare
SSS	super-soft X-ray source
SWCX	solar-wind charge exchange
ToO	target of opportunity
UV	ultraviolet
WD	white dwarf

B. Tables

Table B.1. Results for the spectral fits of the diffuse emission.

(1) ID	(2) RA	(3) Dec	(4) χ^2_ν	(5) dof	(6) kT	(7) EM	(8) L	(9) F	(10) N_H^{smc*}	(11) N_H^{gal}	(12) N_H^{smc}
1-3	10.0	-73.40	1.33	170	–	$0.00^{+0.06}_{-0.00}$	–	–	–	3.41	3.31
1-4	10.0	-73.25	1.11	128	$0.99^{+0.66}_{-0.51}$	$0.09^{+0.06}_{-0.06}$	$0.02^{+0.01}_{-0.01}$	$0.94^{+0.67}_{-0.58}$	$4.09^{+0.00}_{-1.86}$	3.33	4.09
1-5	10.0	-73.10	1.01	183	$1.26^{+0.45}_{-0.24}$	$0.33^{+0.11}_{-0.10}$	$0.07^{+0.02}_{-0.02}$	$4.25^{+0.91}_{-0.98}$	$0.94^{+1.11}_{-0.73}$	3.44	3.85
1-6	10.0	-72.95	1.22	145	$1.08^{+0.23}_{-0.23}$	$0.17^{+0.08}_{-0.07}$	$0.04^{+0.02}_{-0.02}$	$1.85^{+0.94}_{-0.77}$	$2.88^{+0.62}_{-2.38}$	3.53	3.50
1-7	10.0	-72.80	1.57	84	$2.00^{+0.00}_{-1.95}$	$0.07^{+0.05}_{-0.06}$	$0.02^{+0.01}_{-0.01}$	$0.65^{+0.45}_{-0.46}$	$2.18^{+0.00}_{-1.04}$	3.59	2.18
1-8	10.0	-72.65	1.53	45	–	$0.05^{+0.05}_{-0.05}$	–	–	–	3.54	1.04
2-1	10.5	-73.70	1.13	66	–	$0.02^{+0.08}_{-0.02}$	–	–	–	3.25	3.29
2-2	10.5	-73.55	1.49	138	$1.36^{+0.52}_{-0.30}$	$0.11^{+0.04}_{-0.04}$	$0.02^{+0.01}_{-0.01}$	$0.63^{+0.27}_{-0.21}$	$5.26^{+0.00}_{-1.06}$	3.27	5.26
2-3	10.5	-73.40	1.63	251	–	$0.00^{+0.04}_{-0.00}$	–	–	–	3.37	5.28
2-4	10.5	-73.25	1.44	250	$1.04^{+0.33}_{-0.28}$	$0.05^{+0.03}_{-0.03}$	$0.01^{+0.01}_{-0.01}$	$0.38^{+0.32}_{-0.25}$	$5.71^{+0.00}_{-2.25}$	3.48	5.71
2-5	10.5	-73.10	1.39	277	$2.00^{+0.00}_{-1.95}$	$0.45^{+0.05}_{-0.05}$	$0.09^{+0.01}_{-0.01}$	$2.67^{+0.40}_{-0.29}$	$4.38^{+0.00}_{-0.88}$	3.52	4.38
2-6	10.5	-72.95	1.20	200	$2.00^{+0.00}_{-0.00}$	$0.46^{+0.05}_{-0.03}$	$0.10^{+0.01}_{-0.01}$	$3.04^{+0.36}_{-0.36}$	$3.83^{+0.00}_{-0.55}$	3.47	3.83
2-7	10.5	-72.80	1.34	285	–	$0.01^{+0.03}_{-0.01}$	–	–	–	3.44	2.40
2-8	10.5	-72.65	1.27	149	$0.86^{+0.00}_{-0.32}$	$0.05^{+0.03}_{-0.03}$	$0.01^{+0.01}_{-0.01}$	$0.84^{+0.53}_{-0.52}$	$1.50^{+0.00}_{-1.01}$	3.35	1.50
3-1	11.0	-73.70	0.90	59	–	$0.00^{+0.09}_{-0.00}$	–	–	–	3.36	4.56
3-2	11.0	-73.55	1.30	243	$1.34^{+0.00}_{-0.37}$	$0.13^{+0.05}_{-0.04}$	$0.03^{+0.01}_{-0.01}$	$0.64^{+0.27}_{-0.22}$	$6.06^{+0.00}_{-1.60}$	3.35	6.06
3-3	11.0	-73.40	1.14	424	$0.88^{+0.19}_{-0.14}$	$0.14^{+0.03}_{-0.04}$	$0.03^{+0.01}_{-0.01}$	$1.09^{+0.26}_{-0.27}$	$7.34^{+0.08}_{-2.83}$	3.40	7.42
3-4	11.0	-73.25	1.11	439	$0.99^{+0.14}_{-0.11}$	$0.29^{+0.04}_{-0.07}$	$0.07^{+0.01}_{-0.02}$	$1.66^{+0.34}_{-0.35}$	$8.60^{+0.00}_{-2.89}$	3.25	8.60
3-5	11.0	-73.10	1.22	272	$0.81^{+0.21}_{-0.13}$	$0.22^{+0.04}_{-0.05}$	$0.05^{+0.01}_{-0.01}$	$1.94^{+0.40}_{-0.45}$	$6.53^{+0.00}_{-1.22}$	3.33	6.53
3-6	11.0	-72.95	1.25	245	$0.22^{+0.06}_{-0.03}$	$0.49^{+0.26}_{-0.26}$	$0.06^{+0.02}_{-0.03}$	$1.92^{+0.57}_{-0.66}$	$4.29^{+0.00}_{-1.52}$	3.50	4.29
3-7	11.0	-72.80	1.30	210	$0.92^{+0.90}_{-0.42}$	$0.03^{+0.03}_{-0.03}$	$0.01^{+0.01}_{-0.01}$	$0.40^{+0.36}_{-0.35}$	$2.84^{+0.00}_{-1.42}$	3.45	2.84
3-8	11.0	-72.65	1.29	109	$0.71^{+0.49}_{-0.28}$	$0.07^{+0.04}_{-0.03}$	$0.02^{+0.01}_{-0.01}$	$1.12^{+0.53}_{-0.52}$	$2.44^{+0.00}_{-1.23}$	3.53	2.44
4-1	11.5	-73.70	1.28	132	$0.56^{+0.28}_{-0.22}$	$0.16^{+0.12}_{-0.07}$	$0.03^{+0.01}_{-0.01}$	$1.54^{+0.49}_{-0.50}$	$4.85^{+0.00}_{-2.29}$	3.31	4.85
4-2	11.5	-73.55	1.41	290	$0.32^{+0.09}_{-0.05}$	$0.50^{+0.21}_{-0.17}$	$0.07^{+0.02}_{-0.02}$	$2.34^{+0.44}_{-0.43}$	$6.17^{+0.00}_{-0.85}$	3.38	6.17
4-3	11.5	-73.40	1.41	228	$0.88^{+0.12}_{-0.08}$	$0.24^{+0.03}_{-0.04}$	$0.06^{+0.01}_{-0.01}$	$1.66^{+0.26}_{-0.29}$	$8.08^{+0.00}_{-1.57}$	3.22	8.08
4-4	11.5	-73.25	1.27	392	$0.84^{+0.07}_{-0.07}$	$0.53^{+0.11}_{-0.08}$	$0.12^{+0.03}_{-0.02}$	$5.47^{+0.46}_{-0.47}$	$5.24^{+1.73}_{-1.39}$	3.25	9.44
4-5	11.5	-73.10	0.99	123	$0.82^{+0.21}_{-0.16}$	$0.49^{+0.18}_{-0.19}$	$0.11^{+0.04}_{-0.05}$	$3.14^{+0.76}_{-0.72}$	$8.95^{+1.07}_{-4.97}$	3.25	10.03
4-6	11.5	-72.95	1.14	192	$0.89^{+0.14}_{-0.12}$	$0.31^{+0.11}_{-0.09}$	$0.07^{+0.03}_{-0.02}$	$3.38^{+0.68}_{-0.65}$	$4.75^{+2.07}_{-3.29}$	3.29	6.82
4-7	11.5	-72.80	1.17	269	$0.23^{+0.02}_{-0.02}$	$0.82^{+0.41}_{-0.17}$	$0.11^{+0.04}_{-0.02}$	$7.54^{+0.71}_{-0.72}$	$1.03^{+0.74}_{-0.52}$	3.34	4.80
4-8	11.5	-72.65	1.35	418	$0.22^{+0.01}_{-0.02}$	$0.74^{+0.24}_{-0.11}$	$0.09^{+0.02}_{-0.01}$	$7.42^{+0.57}_{-0.57}$	$0.56^{+0.49}_{-0.29}$	3.50	3.13
4-9	11.5	-72.50	1.22	298	$0.13^{+0.02}_{-0.00}$	$0.92^{+0.29}_{-0.14}$	$0.08^{+0.02}_{-0.01}$	$3.47^{+0.65}_{-0.52}$	$0.01^{+0.43}_{-0.01}$	3.44	2.78
4-10	11.5	-72.35	1.29	95	$0.17^{+0.38}_{-0.02}$	$2.28^{+0.60}_{-1.15}$	$0.24^{+0.06}_{-0.11}$	$7.14^{+2.23}_{-1.96}$	$2.94^{+0.00}_{-0.94}$	3.42	2.94
4-11	11.5	-72.20	0.91	88	$0.10^{+0.01}_{-0.01}$	$2.36^{+0.95}_{-0.65}$	$0.12^{+0.04}_{-0.03}$	$2.60^{+0.83}_{-0.71}$	$0.00^{+0.58}_{-0.00}$	3.15	2.09
4-12	11.5	-72.05	1.13	48	$2.00^{+0.00}_{-1.95}$	$0.46^{+0.14}_{-0.13}$	$0.10^{+0.02}_{-0.03}$	$6.65^{+1.33}_{-1.59}$	$0.00^{+1.05}_{-0.00}$	3.19	1.05
4-13	11.5	-71.90	1.15	36	$0.70^{+0.00}_{-0.42}$	$0.22^{+0.15}_{-0.13}$	$0.05^{+0.04}_{-0.03}$	$5.29^{+3.00}_{-3.07}$	$0.28^{+0.67}_{-0.28}$	3.00	0.95

Table B.1. Continued.

ID	RA	Dec	χ^2_ν	dof	kT	EM	L	F	N_H^{smc*}	N_H^{gal}	N_H^{smc}
5-1	12.0	-73.70	1.05	119	$0.32^{+0.10}_{-0.06}$	$0.29^{+0.11}_{-0.09}$	$0.04^{+0.01}_{-0.01}$	$1.90^{+0.48}_{-0.48}$	$4.04^{+0.00}_{-1.09}$	3.24	4.04
5-2	12.0	-73.55	1.45	282	$0.30^{+0.02}_{-0.02}$	$0.38^{+0.04}_{-0.04}$	$0.05^{+0.00}_{-0.00}$	$5.33^{+0.46}_{-0.43}$	$0.00^{+0.10}_{-0.00}$	3.43	5.45
5-3	12.0	-73.40	1.25	320	$0.68^{+0.05}_{-0.08}$	$0.46^{+0.17}_{-0.10}$	$0.10^{+0.03}_{-0.02}$	$3.92^{+0.41}_{-0.43}$	$6.54^{+2.16}_{-1.88}$	3.30	8.70
5-4	12.0	-73.25	1.16	337	$0.79^{+0.06}_{-0.07}$	$0.46^{+0.10}_{-0.07}$	$0.10^{+0.02}_{-0.02}$	$5.64^{+0.52}_{-0.58}$	$3.94^{+1.78}_{-1.27}$	3.39	10.23
5-5	12.0	-73.10	2.00	45	$2.00^{+0.00}_{-0.00}$	$0.55^{+0.15}_{-0.14}$	$0.11^{+0.03}_{-0.03}$	$3.35^{+1.01}_{-1.07}$	$4.29^{+2.56}_{-1.69}$	3.32	12.20
5-6	12.0	-72.95	1.00	132	$1.09^{+0.22}_{-0.09}$	$0.30^{+0.08}_{-0.12}$	$0.07^{+0.02}_{-0.02}$	$1.41^{+0.39}_{-0.31}$	$9.03^{+0.67}_{-3.56}$	3.27	9.70
5-7	12.0	-72.80	1.42	259	$0.26^{+0.04}_{-0.02}$	$0.48^{+0.05}_{-0.07}$	$0.07^{+0.01}_{-0.01}$	$6.36^{+0.59}_{-0.60}$	$0.00^{+0.10}_{-0.00}$	3.28	7.34
5-8	12.0	-72.65	1.06	318	$0.25^{+0.01}_{-0.01}$	$0.71^{+0.09}_{-0.02}$	$0.10^{+0.01}_{-0.01}$	$8.89^{+0.54}_{-0.51}$	$0.00^{+0.22}_{-0.00}$	3.61	3.87
5-9	12.0	-72.50	1.15	431	$0.21^{+0.02}_{-0.01}$	$0.63^{+0.20}_{-0.14}$	$0.08^{+0.02}_{-0.01}$	$6.09^{+0.61}_{-0.61}$	$0.34^{+0.53}_{-0.34}$	3.51	4.26
5-10	12.0	-72.35	1.18	453	$0.16^{+0.02}_{-0.01}$	$1.74^{+0.27}_{-0.52}$	$0.18^{+0.03}_{-0.05}$	$3.03^{+0.51}_{-0.55}$	$4.81^{+0.00}_{-0.72}$	3.40	4.81
5-11	12.0	-72.20	1.12	352	$0.19^{+0.03}_{-0.02}$	$0.66^{+0.13}_{-0.26}$	$0.08^{+0.01}_{-0.03}$	$3.40^{+0.56}_{-0.68}$	$2.16^{+0.00}_{-0.93}$	3.21	2.16
5-12	12.0	-72.05	1.21	273	$0.22^{+0.06}_{-0.03}$	$0.30^{+0.11}_{-0.13}$	$0.04^{+0.01}_{-0.02}$	$2.58^{+0.74}_{-0.84}$	$1.32^{+0.00}_{-0.84}$	3.26	1.32
5-13	12.0	-71.90	1.41	98	–	$0.00^{+0.02}_{-0.00}$	–	–	–	3.24	0.87
6-1	12.5	-73.70	1.67	145	$0.71^{+0.17}_{-0.11}$	$0.19^{+0.04}_{-0.06}$	$0.04^{+0.01}_{-0.01}$	$2.05^{+0.45}_{-0.44}$	$4.68^{+0.00}_{-2.76}$	3.22	4.68
6-2	12.5	-73.55	1.17	367	$0.93^{+0.07}_{-0.11}$	$0.30^{+0.05}_{-0.04}$	$0.07^{+0.01}_{-0.01}$	$4.41^{+0.45}_{-0.47}$	$2.10^{+1.09}_{-0.74}$	3.32	6.46
6-3	12.5	-73.40	1.28	250	$0.25^{+0.03}_{-0.02}$	$3.03^{+0.60}_{-0.77}$	$0.39^{+0.06}_{-0.08}$	$8.02^{+0.60}_{-0.60}$	$7.71^{+0.00}_{-0.59}$	3.22	7.71
6-4	12.5	-73.25	1.10	216	$0.47^{+0.18}_{-0.11}$	$1.00^{+0.38}_{-0.48}$	$0.19^{+0.03}_{-0.07}$	$4.83^{+0.42}_{-0.47}$	$8.68^{+0.00}_{-3.31}$	3.24	8.68
6-5	12.5	-73.10	1.06	308	$0.29^{+0.05}_{-0.06}$	$1.50^{+1.60}_{-0.53}$	$0.21^{+0.18}_{-0.07}$	$4.18^{+0.48}_{-0.51}$	$8.86^{+1.80}_{-1.87}$	3.36	10.66
6-6	12.5	-72.95	1.27	289	$0.74^{+0.07}_{-0.11}$	$0.50^{+0.21}_{-0.10}$	$0.12^{+0.04}_{-0.02}$	$4.78^{+0.48}_{-0.54}$	$5.95^{+2.82}_{-1.84}$	3.29	10.54
6-7	12.5	-72.80	1.49	275	$0.18^{+0.02}_{-0.02}$	$7.65^{+0.80}_{-3.41}$	$0.83^{+0.09}_{-0.35}$	$5.97^{+0.66}_{-0.66}$	$9.46^{+0.00}_{-1.47}$	3.26	9.46
6-8	12.5	-72.65	1.26	387	$0.22^{+0.01}_{-0.01}$	$1.77^{+0.37}_{-0.16}$	$0.23^{+0.03}_{-0.02}$	$17.08^{+0.74}_{-0.76}$	$0.65^{+0.24}_{-0.21}$	3.67	3.93
6-9	12.5	-72.50	1.10	497	$0.25^{+0.01}_{-0.01}$	$1.71^{+0.20}_{-0.16}$	$0.23^{+0.02}_{-0.02}$	$17.86^{+0.70}_{-0.84}$	$0.78^{+0.27}_{-0.12}$	3.58	3.51
6-10	12.5	-72.35	1.23	491	$0.20^{+0.00}_{-0.01}$	$2.58^{+0.19}_{-0.50}$	$0.31^{+0.02}_{-0.03}$	$11.28^{+0.50}_{-0.55}$	$3.21^{+0.00}_{-0.41}$	3.33	3.21
6-11	12.5	-72.20	1.25	417	$0.19^{+0.01}_{-0.01}$	$1.61^{+0.16}_{-0.22}$	$0.19^{+0.02}_{-0.02}$	$7.64^{+0.46}_{-0.49}$	$2.64^{+0.00}_{-0.28}$	3.40	2.64
6-12	12.5	-72.05	1.14	362	$0.22^{+0.03}_{-0.02}$	$0.57^{+0.12}_{-0.24}$	$0.07^{+0.01}_{-0.03}$	$4.31^{+0.64}_{-0.63}$	$1.70^{+0.00}_{-1.42}$	3.22	1.70
6-13	12.5	-71.90	1.27	132	$0.22^{+0.06}_{-0.03}$	$0.25^{+0.09}_{-0.11}$	$0.03^{+0.01}_{-0.01}$	$2.03^{+0.63}_{-0.67}$	$1.48^{+0.00}_{-0.78}$	3.23	1.48
6-14	12.5	-71.75	1.31	40	$0.69^{+0.21}_{-0.20}$	$0.19^{+0.06}_{-0.06}$	$0.05^{+0.01}_{-0.02}$	$4.09^{+1.34}_{-1.38}$	$0.90^{+0.00}_{-0.54}$	3.31	0.90
7-1	13.0	-73.70	1.35	277	$1.01^{+0.13}_{-0.10}$	$0.28^{+0.04}_{-0.04}$	$0.06^{+0.01}_{-0.01}$	$1.97^{+0.38}_{-0.38}$	$6.37^{+0.00}_{-0.48}$	3.24	6.37
7-2	13.0	-73.55	1.23	397	$0.73^{+0.08}_{-0.10}$	$0.30^{+0.03}_{-0.07}$	$0.07^{+0.01}_{-0.01}$	$2.37^{+0.29}_{-0.25}$	$7.08^{+0.00}_{-2.02}$	3.29	7.08
7-3	13.0	-73.40	1.08	385	$0.32^{+0.06}_{-0.02}$	$1.60^{+0.24}_{-0.51}$	$0.23^{+0.03}_{-0.05}$	$5.40^{+0.38}_{-0.50}$	$8.33^{+0.00}_{-0.47}$	3.26	8.33
7-4	13.0	-73.25	1.40	316	$0.80^{+0.07}_{-0.06}$	$0.49^{+0.06}_{-0.12}$	$0.11^{+0.01}_{-0.03}$	$3.76^{+0.37}_{-0.33}$	$7.56^{+1.37}_{-2.35}$	3.17	8.93
7-5	13.0	-73.10	1.24	262	$0.29^{+0.02}_{-0.03}$	$2.34^{+0.44}_{-0.60}$	$0.33^{+0.02}_{-0.08}$	$8.01^{+0.55}_{-0.54}$	$7.46^{+0.00}_{-1.20}$	3.26	7.46
7-6	13.0	-72.95	1.26	469	$0.19^{+0.01}_{-0.01}$	$8.90^{+0.91}_{-0.97}$	$1.01^{+0.08}_{-0.09}$	$12.50^{+0.43}_{-0.44}$	$7.90^{+0.00}_{-0.14}$	3.32	7.90
7-7	13.0	-72.80	1.50	228	$0.21^{+0.02}_{-0.01}$	$9.48^{+1.02}_{-1.10}$	$1.14^{+0.09}_{-0.18}$	$17.82^{+0.62}_{-0.68}$	$7.36^{+0.00}_{-0.08}$	3.39	7.36
7-8	13.0	-72.65	1.45	231	$0.20^{+0.01}_{-0.01}$	$5.51^{+0.99}_{-0.95}$	$0.66^{+0.09}_{-0.10}$	$13.46^{+0.82}_{-0.77}$	$5.92^{+0.00}_{-0.40}$	3.51	5.92
7-9	13.0	-72.50	1.42	162	$0.24^{+0.02}_{-0.01}$	$1.35^{+1.11}_{-0.34}$	$0.18^{+0.07}_{-0.04}$	$10.19^{+0.80}_{-0.83}$	$1.98^{+0.90}_{-0.76}$	3.48	3.69
7-10	13.0	-72.35	1.32	354	$0.23^{+0.01}_{-0.01}$	$1.57^{+0.36}_{-0.24}$	$0.21^{+0.04}_{-0.03}$	$13.02^{+0.65}_{-0.71}$	$1.55^{+0.53}_{-0.43}$	3.40	3.63
7-11	13.0	-72.20	1.11	254	$0.19^{+0.01}_{-0.03}$	$2.47^{+0.67}_{-0.96}$	$0.29^{+0.08}_{-0.10}$	$8.29^{+0.81}_{-0.88}$	$3.64^{+0.87}_{-1.24}$	3.36	4.60
7-12	13.0	-72.05	1.31	219	$0.17^{+0.01}_{-0.02}$	$1.85^{+0.17}_{-0.30}$	$0.20^{+0.02}_{-0.03}$	$6.88^{+0.65}_{-0.70}$	$2.28^{+0.00}_{-0.46}$	3.45	2.28
7-13	13.0	-71.90	1.19	315	$0.20^{+0.03}_{-0.03}$	$0.42^{+0.16}_{-0.18}$	$0.05^{+0.02}_{-0.02}$	$2.50^{+0.57}_{-0.57}$	$2.03^{+0.00}_{-1.03}$	3.19	2.03
7-14	13.0	-71.75	1.26	227	$0.86^{+0.55}_{-0.46}$	$0.02^{+0.03}_{-0.02}$	$0.01^{+0.01}_{-0.01}$	$0.49^{+0.50}_{-0.46}$	$1.26^{+0.00}_{-1.26}$	3.21	1.26
7-15	13.0	-71.60	1.17	251	$1.09^{+0.00}_{-0.92}$	$0.03^{+0.04}_{-0.03}$	$0.01^{+0.01}_{-0.01}$	$0.54^{+0.61}_{-0.46}$	$0.94^{+0.00}_{-0.94}$	3.00	0.94
8-1	13.5	-73.70	1.52	213	$2.00^{+0.00}_{-1.95}$	$0.14^{+0.04}_{-0.04}$	$0.03^{+0.01}_{-0.01}$	$0.78^{+0.23}_{-0.23}$	$4.56^{+0.00}_{-0.58}$	3.22	4.56

Table B.1. Continued.

ID	RA	Dec	χ^2_ν	dof	kT	EM	L	F	N_H^{smc*}	N_H^{gal}	N_H^{smc}
8-2	13.5	-73.55	1.60	323	$0.77^{+0.21}_{-0.13}$	$0.15^{+0.03}_{-0.03}$	$0.03^{+0.01}_{-0.01}$	$1.31^{+0.23}_{-0.25}$	$6.40^{+0.00}_{-0.98}$	3.28	6.40
8-3	13.5	-73.40	1.20	482	$0.28^{+0.04}_{-0.03}$	$1.21^{+0.40}_{-0.30}$	$0.17^{+0.04}_{-0.04}$	$3.33^{+0.41}_{-0.46}$	$8.59^{+0.00}_{-0.81}$	3.15	8.59
8-4	13.5	-73.25	1.38	505	$0.27^{+0.04}_{-0.03}$	$1.69^{+0.67}_{-0.54}$	$0.23^{+0.07}_{-0.07}$	$3.77^{+0.45}_{-0.46}$	$9.37^{+0.00}_{-1.47}$	3.07	9.37
8-5	13.5	-73.10	1.16	499	$0.19^{+0.01}_{-0.01}$	$5.37^{+0.44}_{-1.65}$	$0.59^{+0.05}_{-0.16}$	$7.38^{+0.51}_{-0.55}$	$7.42^{+0.00}_{-0.84}$	3.21	7.42
8-6	13.5	-72.95	1.24	546	$0.24^{+0.01}_{-0.01}$	$3.85^{+0.36}_{-0.41}$	$0.50^{+0.04}_{-0.05}$	$10.88^{+0.48}_{-0.52}$	$6.91^{+0.00}_{-0.26}$	3.34	6.91
8-7	13.5	-72.80	1.48	296	$0.22^{+0.01}_{-0.01}$	$4.29^{+0.59}_{-0.82}$	$0.54^{+0.05}_{-0.09}$	$8.65^{+0.49}_{-0.56}$	$7.96^{+0.00}_{-0.41}$	3.36	7.96
8-8	13.5	-72.65	1.46	165	$0.22^{+0.01}_{-0.02}$	$4.33^{+1.37}_{-0.99}$	$0.55^{+0.13}_{-0.06}$	$10.88^{+1.08}_{-1.01}$	$6.73^{+0.00}_{-0.77}$	3.41	6.73
8-9	13.5	-72.50	1.30	267	$0.24^{+0.01}_{-0.01}$	$2.58^{+0.28}_{-0.41}$	$0.34^{+0.03}_{-0.05}$	$10.43^{+0.64}_{-0.63}$	$5.02^{+0.00}_{-0.49}$	3.53	5.02
8-10	13.5	-72.35	1.39	351	$0.25^{+0.01}_{-0.01}$	$2.26^{+0.24}_{-0.19}$	$0.31^{+0.03}_{-0.02}$	$21.74^{+0.61}_{-0.59}$	$1.25^{+0.26}_{-0.21}$	3.31	3.42
8-11	13.5	-72.20	1.24	426	$0.23^{+0.02}_{-0.02}$	$1.81^{+0.42}_{-0.51}$	$0.24^{+0.04}_{-0.06}$	$10.53^{+0.60}_{-0.61}$	$3.03^{+0.25}_{-0.99}$	3.32	3.28
8-12	13.5	-72.05	1.16	333	$0.19^{+0.01}_{-0.01}$	$1.16^{+0.12}_{-0.27}$	$0.14^{+0.01}_{-0.03}$	$6.30^{+0.46}_{-0.49}$	$1.98^{+0.00}_{-0.55}$	3.25	1.98
8-13	13.5	-71.90	1.24	486	$0.23^{+0.02}_{-0.02}$	$0.47^{+0.06}_{-0.07}$	$0.06^{+0.01}_{-0.01}$	$4.00^{+0.41}_{-0.48}$	$1.48^{+0.00}_{-0.17}$	3.29	1.48
8-14	13.5	-71.75	1.28	335	$0.27^{+0.03}_{-0.04}$	$0.20^{+0.06}_{-0.04}$	$0.03^{+0.01}_{-0.01}$	$2.10^{+0.39}_{-0.41}$	$1.54^{+0.00}_{-0.29}$	3.06	1.54
8-15	13.5	-71.60	1.29	276	$0.86^{+0.19}_{-0.26}$	$0.04^{+0.02}_{-0.02}$	$0.01^{+0.01}_{-0.00}$	$0.79^{+0.49}_{-0.38}$	$0.97^{+0.00}_{-0.62}$	2.96	0.97
8-16	13.5	-71.45	1.27	96	$0.27^{+0.09}_{-0.06}$	$0.33^{+0.15}_{-0.16}$	$0.05^{+0.02}_{-0.02}$	$3.91^{+1.25}_{-1.29}$	$1.06^{+0.00}_{-1.06}$	2.97	1.06
9-1	14.0	-73.70	1.05	51	$2.00^{+0.00}_{-0.00}$	$0.35^{+0.10}_{-0.13}$	$0.07^{+0.02}_{-0.03}$	$2.34^{+0.78}_{-0.83}$	$3.56^{+0.00}_{-2.18}$	3.17	3.56
9-2	14.0	-73.55	1.15	297	$0.27^{+0.10}_{-0.03}$	$0.37^{+0.14}_{-0.15}$	$0.05^{+0.02}_{-0.02}$	$2.15^{+0.65}_{-0.68}$	$4.04^{+0.00}_{-0.98}$	3.12	4.04
9-3	14.0	-73.40	1.23	329	$0.69^{+0.10}_{-0.11}$	$0.21^{+0.06}_{-0.05}$	$0.05^{+0.01}_{-0.01}$	$2.92^{+0.46}_{-0.48}$	$3.36^{+0.94}_{-1.46}$	3.12	4.30
9-4	14.0	-73.25	1.32	347	$0.24^{+0.03}_{-0.02}$	$1.26^{+0.30}_{-0.29}$	$0.16^{+0.03}_{-0.03}$	$4.68^{+0.52}_{-0.47}$	$5.33^{+0.00}_{-0.64}$	3.19	5.33
9-5	14.0	-73.10	1.34	461	$0.27^{+0.02}_{-0.03}$	$0.75^{+0.21}_{-0.11}$	$0.10^{+0.02}_{-0.01}$	$2.99^{+0.34}_{-0.36}$	$6.14^{+0.00}_{-0.43}$	3.18	6.14
9-6	14.0	-72.95	1.14	339	$0.26^{+0.02}_{-0.02}$	$1.86^{+0.48}_{-0.34}$	$0.25^{+0.05}_{-0.04}$	$6.03^{+0.53}_{-0.45}$	$6.88^{+0.00}_{-0.51}$	3.29	6.88
9-7	14.0	-72.80	1.18	361	$0.96^{+0.07}_{-0.08}$	$0.37^{+0.05}_{-0.05}$	$0.09^{+0.01}_{-0.01}$	$5.16^{+0.52}_{-0.60}$	$2.37^{+1.03}_{-0.75}$	3.35	8.48
9-8	14.0	-72.65	1.15	135	$0.20^{+0.03}_{-0.01}$	$8.76^{+2.36}_{-3.53}$	$1.05^{+0.23}_{-0.38}$	$15.76^{+1.57}_{-1.57}$	$7.32^{+0.00}_{-0.66}$	3.48	7.32
9-9	14.0	-72.50	1.31	310	$0.23^{+0.02}_{-0.01}$	$3.56^{+0.49}_{-0.58}$	$0.47^{+0.05}_{-0.07}$	$8.77^{+0.55}_{-0.62}$	$7.47^{+0.00}_{-0.38}$	3.42	7.47
9-10	14.0	-72.35	1.30	274	$0.21^{+0.01}_{-0.01}$	$5.01^{+0.60}_{-1.26}$	$0.63^{+0.06}_{-0.06}$	$13.20^{+0.53}_{-0.51}$	$6.13^{+0.00}_{-0.24}$	3.30	6.13
9-11	14.0	-72.20	1.10	335	$0.24^{+0.02}_{-0.02}$	$1.52^{+0.77}_{-0.32}$	$0.21^{+0.09}_{-0.04}$	$12.21^{+0.70}_{-0.68}$	$1.93^{+1.22}_{-0.65}$	3.33	4.30
9-12	14.0	-72.05	1.13	260	$0.23^{+0.01}_{-0.01}$	$0.68^{+0.14}_{-0.11}$	$0.09^{+0.02}_{-0.01}$	$7.68^{+0.52}_{-0.52}$	$0.32^{+0.42}_{-0.32}$	3.44	3.03
9-13	14.0	-71.90	1.38	460	$0.22^{+0.01}_{-0.02}$	$1.21^{+0.65}_{-0.16}$	$0.16^{+0.07}_{-0.02}$	$11.02^{+0.55}_{-0.52}$	$1.13^{+0.99}_{-0.34}$	3.03	2.93
9-14	14.0	-71.75	1.14	441	$0.25^{+0.01}_{-0.01}$	$0.91^{+0.15}_{-0.12}$	$0.13^{+0.02}_{-0.01}$	$9.95^{+0.58}_{-0.59}$	$0.86^{+0.67}_{-0.43}$	3.08	2.32
9-15	14.0	-71.60	1.12	236	$0.21^{+0.02}_{-0.02}$	$1.01^{+0.24}_{-0.41}$	$0.13^{+0.02}_{-0.05}$	$6.79^{+0.96}_{-0.99}$	$2.07^{+0.00}_{-1.35}$	3.03	2.07
9-16	14.0	-71.45	1.58	77	$0.09^{+0.00}_{-0.00}$	$2.33^{+1.43}_{-1.77}$	$0.12^{+0.07}_{-0.12}$	$1.35^{+0.83}_{-0.87}$	$1.67^{+0.00}_{-1.67}$	2.81	1.67
10-2	14.5	-73.55	1.16	72	$2.00^{+0.00}_{-1.95}$	$0.28^{+0.09}_{-0.09}$	$0.06^{+0.02}_{-0.01}$	$1.93^{+0.66}_{-0.70}$	$3.42^{+0.00}_{-1.42}$	3.16	3.42
10-3	14.5	-73.40	1.30	243	$1.42^{+0.00}_{-0.22}$	$0.17^{+0.05}_{-0.04}$	$0.04^{+0.01}_{-0.01}$	$1.23^{+0.32}_{-0.28}$	$3.68^{+0.00}_{-1.16}$	2.97	3.68
10-4	14.5	-73.25	1.34	356	$0.75^{+0.09}_{-0.12}$	$0.25^{+0.04}_{-0.04}$	$0.06^{+0.01}_{-0.01}$	$3.10^{+0.53}_{-0.43}$	$4.08^{+0.00}_{-1.15}$	3.16	4.08
10-5	14.5	-73.10	1.14	389	$0.31^{+0.05}_{-0.03}$	$0.80^{+0.14}_{-0.16}$	$0.12^{+0.02}_{-0.02}$	$4.44^{+0.43}_{-0.44}$	$5.23^{+0.00}_{-0.42}$	3.16	5.23
10-6	14.5	-72.95	1.26	446	$0.27^{+0.02}_{-0.03}$	$1.15^{+0.27}_{-0.19}$	$0.16^{+0.03}_{-0.02}$	$4.15^{+0.38}_{-0.40}$	$6.74^{+0.00}_{-0.54}$	3.20	6.74
10-7	14.5	-72.80	1.34	289	$0.28^{+0.04}_{-0.03}$	$1.45^{+0.33}_{-0.32}$	$0.21^{+0.04}_{-0.04}$	$4.25^{+0.40}_{-0.44}$	$8.31^{+0.00}_{-0.61}$	3.14	8.31
10-8	14.5	-72.65	1.25	302	$0.24^{+0.02}_{-0.01}$	$5.05^{+0.83}_{-1.17}$	$0.66^{+0.09}_{-0.14}$	$11.19^{+0.81}_{-0.92}$	$8.11^{+0.00}_{-0.75}$	3.32	8.11
10-9	14.5	-72.50	1.20	347	$0.19^{+0.01}_{-0.01}$	$9.31^{+0.79}_{-2.53}$	$1.06^{+0.09}_{-0.25}$	$10.35^{+0.68}_{-0.82}$	$8.63^{+0.00}_{-0.56}$	3.33	8.63
10-10	14.5	-72.35	1.32	280	$0.20^{+0.01}_{-0.01}$	$9.37^{+1.34}_{-1.25}$	$1.13^{+0.13}_{-0.12}$	$15.96^{+0.71}_{-0.72}$	$7.61^{+0.00}_{-0.16}$	3.28	7.61
10-11	14.5	-72.20	1.26	403	$0.19^{+0.00}_{-0.01}$	$4.75^{+0.49}_{-1.29}$	$0.55^{+0.06}_{-0.14}$	$13.52^{+0.48}_{-0.46}$	$4.33^{+0.38}_{-0.68}$	3.23	5.29
10-12	14.5	-72.05	1.23	419	$0.24^{+0.01}_{-0.01}$	$1.09^{+0.24}_{-0.17}$	$0.15^{+0.03}_{-0.02}$	$10.48^{+0.52}_{-0.58}$	$1.15^{+0.57}_{-0.00}$	3.25	4.31
10-13	14.5	-71.90	1.33	337	$0.26^{+0.03}_{-0.02}$	$0.70^{+0.21}_{-0.16}$	$0.10^{+0.03}_{-0.02}$	$8.09^{+0.53}_{-0.59}$	$0.91^{+0.74}_{-0.61}$	3.13	3.57

Table B.1. Continued.

ID	RA	Dec	χ^2_ν	dof	kT	EM	L	F	N_H^{smc*}	N_H^{gal}	N_H^{smc}
10-14	14.5	-71.75	1.21	294	$0.27^{+0.02}_{-0.01}$	$0.33^{+0.04}_{-0.04}$	$0.05^{+0.01}_{-0.00}$	$4.88^{+0.51}_{-0.49}$	$0.00^{+0.00}_{-0.00}$	3.05	2.95
10-15	14.5	-71.60	1.21	274	$0.27^{+0.02}_{-0.02}$	$0.30^{+0.05}_{-0.04}$	$0.04^{+0.01}_{-0.01}$	$4.50^{+0.59}_{-0.62}$	$0.00^{+0.20}_{-0.00}$	2.86	2.19
10-16	14.5	-71.45	1.05	90	–	$0.04^{+0.06}_{-0.04}$	–	–	–	2.78	2.28
10-17	14.5	-71.30	1.88	38	$0.69^{+0.37}_{-0.27}$	$0.12^{+0.07}_{-0.07}$	$0.03^{+0.02}_{-0.02}$	$2.33^{+1.26}_{-1.32}$	$1.85^{+0.00}_{-1.29}$	2.66	1.85
11-3	15.0	-73.40	0.92	106	$2.00^{+0.00}_{-1.95}$	$0.32^{+0.13}_{-0.15}$	$0.07^{+0.03}_{-0.03}$	$4.30^{+1.83}_{-1.98}$	$0.00^{+0.48}_{-0.00}$	2.97	3.16
11-4	15.0	-73.25	0.89	148	$1.02^{+0.00}_{-0.32}$	$0.18^{+0.12}_{-0.07}$	$0.04^{+0.02}_{-0.02}$	$3.23^{+1.12}_{-1.15}$	$0.28^{+1.57}_{-0.28}$	3.12	4.30
11-5	15.0	-73.10	1.09	160	$0.20^{+0.02}_{-0.01}$	$2.74^{+0.55}_{-0.68}$	$0.32^{+0.05}_{-0.07}$	$8.62^{+0.86}_{-0.85}$	$4.59^{+0.00}_{-0.56}$	3.18	4.59
11-6	15.0	-72.95	1.42	238	$0.19^{+0.01}_{-0.01}$	$4.15^{+0.35}_{-1.77}$	$0.46^{+0.04}_{-0.18}$	$8.07^{+0.69}_{-0.75}$	$5.80^{+0.00}_{-1.47}$	3.18	5.80
11-7	15.0	-72.80	1.44	205	$0.26^{+0.03}_{-0.02}$	$1.94^{+0.25}_{-0.49}$	$0.26^{+0.03}_{-0.03}$	$7.69^{+0.62}_{-0.63}$	$5.74^{+0.00}_{-0.82}$	3.07	5.74
11-8	15.0	-72.65	1.15	436	$0.24^{+0.02}_{-0.01}$	$3.31^{+0.49}_{-0.69}$	$0.43^{+0.05}_{-0.08}$	$8.73^{+0.65}_{-0.65}$	$7.24^{+0.00}_{-0.62}$	3.16	7.24
11-9	15.0	-72.50	1.08	288	$0.22^{+0.03}_{-0.02}$	$4.77^{+1.41}_{-2.29}$	$0.61^{+0.14}_{-0.27}$	$12.60^{+0.83}_{-0.90}$	$6.41^{+0.12}_{-2.11}$	3.47	6.54
11-10	15.0	-72.35	1.34	418	$0.19^{+0.00}_{-0.00}$	$9.47^{+0.48}_{-0.78}$	$1.09^{+0.05}_{-0.07}$	$19.86^{+0.64}_{-0.75}$	$5.71^{+0.00}_{-0.10}$	3.18	5.71
11-11	15.0	-72.20	1.40	327	$0.23^{+0.00}_{-0.00}$	$2.05^{+0.23}_{-0.16}$	$0.27^{+0.03}_{-0.02}$	$19.38^{+0.52}_{-0.50}$	$1.13^{+0.28}_{-0.20}$	3.01	4.28
11-12	15.0	-72.05	1.39	413	$0.24^{+0.01}_{-0.00}$	$2.56^{+0.13}_{-0.23}$	$0.35^{+0.02}_{-0.03}$	$26.65^{+0.54}_{-0.75}$	$0.81^{+0.12}_{-0.21}$	3.12	3.51
11-13	15.0	-71.90	1.47	437	$0.23^{+0.01}_{-0.00}$	$2.53^{+0.36}_{-0.41}$	$0.34^{+0.04}_{-0.05}$	$20.16^{+0.56}_{-0.63}$	$1.88^{+0.37}_{-0.48}$	3.06	3.93
11-14	15.0	-71.75	1.25	338	$0.22^{+0.02}_{-0.02}$	$0.76^{+0.28}_{-0.16}$	$0.10^{+0.03}_{-0.02}$	$7.07^{+0.59}_{-0.55}$	$1.05^{+0.70}_{-0.55}$	3.11	4.16
11-15	15.0	-71.60	1.34	337	$0.24^{+0.02}_{-0.01}$	$0.92^{+0.51}_{-0.22}$	$0.13^{+0.07}_{-0.03}$	$9.27^{+0.71}_{-0.75}$	$1.10^{+1.31}_{-0.65}$	2.90	3.71
11-16	15.0	-71.45	1.02	261	$0.21^{+0.02}_{-0.01}$	$1.61^{+0.33}_{-0.52}$	$0.21^{+0.03}_{-0.06}$	$7.42^{+0.83}_{-0.90}$	$3.56^{+0.00}_{-0.94}$	2.66	3.56
11-17	15.0	-71.30	1.08	29	$0.08^{+0.08}_{-0.00}$	$3.83^{+1.62}_{-1.64}$	$0.13^{+0.06}_{-0.06}$	$1.45^{+0.94}_{-0.61}$	$0.00^{+0.00}_{-0.00}$	2.67	2.87
12-4	15.5	-73.25	1.53	152	$0.88^{+0.12}_{-0.07}$	$0.26^{+0.08}_{-0.06}$	$0.06^{+0.02}_{-0.01}$	$3.80^{+0.75}_{-0.76}$	$2.66^{+1.56}_{-1.35}$	3.33	4.22
12-5	15.5	-73.10	0.95	210	$0.80^{+0.14}_{-0.10}$	$0.25^{+0.07}_{-0.05}$	$0.06^{+0.02}_{-0.01}$	$3.44^{+0.63}_{-0.62}$	$3.21^{+1.43}_{-1.42}$	2.90	4.64
12-6	15.5	-72.95	1.22	257	$0.76^{+0.09}_{-0.09}$	$0.36^{+0.12}_{-0.07}$	$0.08^{+0.03}_{-0.02}$	$4.81^{+0.71}_{-0.73}$	$3.69^{+1.89}_{-1.47}$	2.94	5.57
12-7	15.5	-72.80	1.24	221	$0.22^{+0.02}_{-0.02}$	$2.43^{+0.65}_{-0.54}$	$0.31^{+0.20}_{-0.06}$	$9.33^{+0.85}_{-0.96}$	$4.80^{+0.00}_{-0.68}$	2.89	4.80
12-8	15.5	-72.65	1.28	273	$0.23^{+0.01}_{-0.01}$	$2.57^{+0.33}_{-0.36}$	$0.33^{+0.04}_{-0.04}$	$8.35^{+0.57}_{-0.65}$	$5.81^{+0.00}_{-0.25}$	2.86	5.81
12-9	15.5	-72.50	1.18	433	$0.24^{+0.01}_{-0.01}$	$2.39^{+0.23}_{-0.32}$	$0.32^{+0.03}_{-0.04}$	$9.46^{+0.52}_{-0.62}$	$5.38^{+0.00}_{-0.28}$	3.27	5.38
12-10	15.5	-72.35	1.21	334	$0.24^{+0.01}_{-0.01}$	$3.83^{+0.34}_{-0.48}$	$0.51^{+0.04}_{-0.06}$	$15.95^{+0.84}_{-0.93}$	$4.97^{+0.00}_{-0.36}$	3.19	4.97
12-11	15.5	-72.20	1.37	763	$0.23^{+0.00}_{-0.00}$	$2.09^{+0.14}_{-0.13}$	$0.28^{+0.02}_{-0.01}$	$21.66^{+0.50}_{-0.54}$	$0.68^{+0.16}_{-0.13}$	2.95	4.72
12-12	15.5	-72.05	1.59	1173	$0.23^{+0.00}_{-0.00}$	$2.85^{+0.09}_{-0.19}$	$0.38^{+0.01}_{-0.02}$	$27.37^{+0.39}_{-0.52}$	$1.01^{+0.08}_{-0.17}$	3.00	4.76
12-13	15.5	-71.90	1.66	629	$0.18^{+0.00}_{-0.00}$	$14.69^{+0.32}_{-0.43}$	$1.68^{+0.04}_{-0.05}$	$29.49^{+0.64}_{-0.66}$	$5.44^{+0.00}_{-0.09}$	3.19	5.44
12-14	15.5	-71.75	1.40	470	$0.19^{+0.01}_{-0.01}$	$2.71^{+0.37}_{-0.53}$	$0.33^{+0.04}_{-0.06}$	$7.53^{+0.49}_{-0.52}$	$5.04^{+0.00}_{-0.33}$	3.16	5.04
12-15	15.5	-71.60	1.13	339	$0.20^{+0.00}_{-0.01}$	$1.13^{+0.21}_{-0.48}$	$0.14^{+0.02}_{-0.05}$	$4.52^{+0.44}_{-0.46}$	$3.74^{+0.00}_{-0.68}$	2.85	3.74
12-16	15.5	-71.45	1.18	330	$0.23^{+0.05}_{-0.02}$	$0.95^{+0.17}_{-0.51}$	$0.13^{+0.02}_{-0.06}$	$5.91^{+0.73}_{-0.78}$	$3.15^{+0.00}_{-2.16}$	2.74	3.15
13-4	16.0	-73.25	1.26	109	$1.04^{+0.58}_{-0.45}$	$0.15^{+0.12}_{-0.10}$	$0.03^{+0.03}_{-0.02}$	$1.58^{+1.26}_{-1.02}$	$3.42^{+0.92}_{-3.38}$	3.19	4.34
13-5	16.0	-73.10	1.20	220	$0.55^{+0.09}_{-0.11}$	$0.41^{+0.11}_{-0.08}$	$0.08^{+0.01}_{-0.02}$	$4.10^{+0.65}_{-0.70}$	$4.83^{+0.00}_{-1.02}$	2.87	4.83
13-6	16.0	-72.95	1.05	259	$0.28^{+0.05}_{-0.04}$	$0.91^{+0.36}_{-0.25}$	$0.13^{+0.04}_{-0.03}$	$4.28^{+0.70}_{-0.72}$	$5.63^{+0.00}_{-0.84}$	2.83	5.63
13-7	16.0	-72.80	1.17	182	$1.23^{+0.11}_{-0.13}$	$0.51^{+0.09}_{-0.07}$	$0.11^{+0.02}_{-0.02}$	$8.32^{+1.08}_{-0.97}$	$0.01^{+0.27}_{-0.01}$	2.81	5.14
13-8	16.0	-72.65	1.09	244	$0.38^{+0.12}_{-0.05}$	$0.66^{+0.16}_{-0.22}$	$0.11^{+0.02}_{-0.03}$	$4.22^{+0.49}_{-0.59}$	$5.77^{+0.00}_{-0.92}$	2.91	5.77
13-9	16.0	-72.50	1.13	381	$0.22^{+0.01}_{-0.01}$	$3.61^{+0.38}_{-0.40}$	$0.46^{+0.02}_{-0.04}$	$12.88^{+0.51}_{-0.60}$	$5.07^{+0.00}_{-0.15}$	3.07	5.07
13-10	16.0	-72.35	1.56	218	$0.22^{+0.01}_{-0.02}$	$3.47^{+0.72}_{-0.36}$	$0.45^{+0.07}_{-0.04}$	$13.54^{+0.80}_{-0.86}$	$4.67^{+0.00}_{-0.25}$	3.04	4.67
13-11	16.0	-72.20	1.87	718	$0.19^{+0.00}_{-0.00}$	$11.37^{+0.33}_{-0.55}$	$1.32^{+0.04}_{-0.05}$	$24.28^{+0.56}_{-0.58}$	$5.67^{+0.00}_{-0.05}$	2.78	5.67
13-12	16.0	-72.05	3.03	95	$0.20^{+0.01}_{-0.01}$	$16.28^{+1.61}_{-1.91}$	$2.02^{+0.16}_{-0.11}$	$44.12^{+1.51}_{-1.45}$	$5.69^{+0.00}_{-1.14}$	3.04	5.69
13-13	16.0	-71.90	1.93	807	$0.16^{+0.00}_{-0.00}$	$18.55^{+0.37}_{-0.47}$	$1.92^{+0.04}_{-0.05}$	$22.15^{+0.45}_{-0.44}$	$6.13^{+0.00}_{-0.08}$	3.07	6.13
13-14	16.0	-71.75	1.41	413	$0.17^{+0.01}_{-0.01}$	$3.61^{+0.29}_{-0.55}$	$0.40^{+0.03}_{-0.09}$	$6.31^{+0.50}_{-0.54}$	$5.46^{+0.00}_{-0.57}$	3.10	5.46

Table B.1. Continued.

ID	RA	Dec	χ^2_ν	dof	kT	EM	L	F	N_H^{smc*}	N_H^{gal}	N_H^{smc}
13-15	16.0	-71.60	1.16	324	$0.22^{+0.02}_{-0.01}$	$0.54^{+0.09}_{-0.13}$	$0.07^{+0.01}_{-0.02}$	$3.27^{+0.41}_{-0.42}$	$2.84^{+0.00}_{-0.67}$	2.86	2.84
13-16	16.0	-71.45	0.98	336	$0.26^{+0.04}_{-0.04}$	$0.20^{+0.03}_{-0.05}$	$0.03^{+0.01}_{-0.01}$	$2.89^{+0.63}_{-0.66}$	$0.00^{+0.51}_{-0.00}$	2.71	2.70
14-4	16.5	-73.25	1.35	186	–	$0.00^{+0.04}_{-0.00}$	–	–	–	2.96	4.19
14-5	16.5	-73.10	1.56	389	$0.83^{+0.07}_{-0.11}$	$0.20^{+0.03}_{-0.04}$	$0.05^{+0.01}_{-0.01}$	$2.05^{+0.34}_{-0.33}$	$5.34^{+0.00}_{-1.56}$	2.72	5.34
14-6	16.5	-72.95	1.09	345	$0.22^{+0.04}_{-0.03}$	$0.87^{+0.41}_{-0.32}$	$0.11^{+0.04}_{-0.03}$	$2.99^{+0.60}_{-0.68}$	$5.11^{+0.00}_{-0.71}$	2.79	5.11
14-7	16.5	-72.80	1.22	236	$0.18^{+0.03}_{-0.02}$	$1.68^{+0.36}_{-0.88}$	$0.18^{+0.04}_{-0.09}$	$3.38^{+0.81}_{-0.88}$	$5.32^{+0.00}_{-1.58}$	2.90	5.32
14-8	16.5	-72.65	1.21	197	$0.95^{+0.09}_{-0.13}$	$0.37^{+0.08}_{-0.07}$	$0.09^{+0.02}_{-0.02}$	$4.78^{+0.66}_{-0.74}$	$3.24^{+1.31}_{-1.27}$	2.88	6.02
14-9	16.5	-72.50	1.22	270	$0.20^{+0.02}_{-0.01}$	$2.21^{+0.36}_{-0.60}$	$0.27^{+0.03}_{-0.08}$	$7.29^{+0.53}_{-0.54}$	$4.71^{+0.00}_{-0.50}$	3.01	4.71
14-10	16.5	-72.35	1.24	231	$0.20^{+0.04}_{-0.01}$	$3.72^{+0.46}_{-0.78}$	$0.45^{+0.04}_{-0.15}$	$13.52^{+0.82}_{-0.84}$	$4.12^{+0.00}_{-2.27}$	2.94	4.12
14-11	16.5	-72.20	2.41	489	$0.19^{+0.01}_{-0.00}$	$5.62^{+0.33}_{-0.58}$	$0.65^{+0.04}_{-0.06}$	$13.30^{+0.65}_{-0.69}$	$5.22^{+0.00}_{-0.16}$	2.89	5.22
14-12	16.5	-72.05	1.79	768	$0.19^{+0.00}_{-0.00}$	$14.31^{+0.56}_{-0.59}$	$1.67^{+0.06}_{-0.06}$	$26.98^{+0.56}_{-0.52}$	$6.31^{+0.00}_{-0.04}$	2.93	6.31
14-13	16.5	-71.90	1.79	690	$0.23^{+0.01}_{-0.01}$	$1.07^{+0.14}_{-0.10}$	$0.14^{+0.02}_{-0.01}$	$11.34^{+0.46}_{-0.45}$	$0.61^{+0.31}_{-0.21}$	3.02	6.56
14-14	16.5	-71.75	1.05	42	$0.27^{+0.05}_{-0.07}$	$1.28^{+3.14}_{-0.44}$	$0.19^{+0.37}_{-0.06}$	$15.58^{+2.89}_{-2.71}$	$0.82^{+3.50}_{-0.82}$	3.07	6.00
14-15	16.5	-71.60	1.54	83	$0.25^{+0.03}_{-0.03}$	$0.60^{+0.12}_{-0.10}$	$0.09^{+0.02}_{-0.01}$	$8.45^{+1.27}_{-1.26}$	$0.00^{+0.26}_{-0.00}$	2.87	3.25
15-4	17.0	-73.25	1.34	110	–	$0.00^{+0.02}_{-0.00}$	–	–	–	2.78	3.92
15-5	17.0	-73.10	1.11	258	$0.54^{+0.00}_{-0.25}$	$0.11^{+0.13}_{-0.04}$	$0.02^{+0.04}_{-0.01}$	$1.08^{+0.36}_{-0.34}$	$4.99^{+0.00}_{-1.76}$	2.71	4.99
15-6	17.0	-72.95	1.31	290	$0.81^{+0.10}_{-0.11}$	$0.23^{+0.06}_{-0.06}$	$0.05^{+0.01}_{-0.01}$	$2.83^{+0.45}_{-0.47}$	$4.33^{+1.09}_{-1.83}$	2.87	5.42
15-7	17.0	-72.80	1.35	252	$0.81^{+0.13}_{-0.19}$	$0.14^{+0.04}_{-0.05}$	$0.03^{+0.01}_{-0.01}$	$1.52^{+0.40}_{-0.34}$	$5.22^{+0.44}_{-2.46}$	2.83	5.66
15-8	17.0	-72.65	1.25	214	$0.27^{+0.06}_{-0.04}$	$0.82^{+0.35}_{-0.30}$	$0.11^{+0.04}_{-0.04}$	$3.48^{+0.57}_{-0.62}$	$5.96^{+0.00}_{-1.37}$	2.80	5.96
15-9	17.0	-72.50	1.25	109	$0.19^{+0.01}_{-0.01}$	$2.18^{+0.31}_{-0.39}$	$0.25^{+0.03}_{-0.04}$	$7.43^{+0.64}_{-0.64}$	$3.79^{+0.00}_{-0.35}$	3.05	3.79
15-10	17.0	-72.35	1.25	308	$0.28^{+0.03}_{-0.03}$	$0.55^{+0.50}_{-0.13}$	$0.08^{+0.06}_{-0.02}$	$5.93^{+0.51}_{-0.54}$	$1.48^{+1.98}_{-0.76}$	2.88	4.22
15-11	17.0	-72.20	1.47	253	$0.27^{+0.03}_{-0.04}$	$0.38^{+0.15}_{-0.08}$	$0.05^{+0.02}_{-0.01}$	$2.27^{+0.41}_{-0.40}$	$4.14^{+0.00}_{-0.72}$	2.93	4.14
15-12	17.0	-72.05	1.36	222	$1.08^{+0.13}_{-0.11}$	$0.12^{+0.04}_{-0.03}$	$0.03^{+0.01}_{-0.01}$	$1.54^{+0.38}_{-0.40}$	$2.37^{+2.78}_{-1.35}$	3.03	5.50
15-13	17.0	-71.90	1.23	98	$0.19^{+0.41}_{-0.07}$	$2.93^{+0.97}_{-1.71}$	$0.34^{+0.11}_{-0.20}$	$5.46^{+1.85}_{-2.01}$	$6.28^{+0.00}_{-2.59}$	3.03	6.28
16-3	17.5	-73.40	1.06	139	$1.06^{+0.30}_{-0.70}$	$0.09^{+0.05}_{-0.06}$	$0.02^{+0.01}_{-0.01}$	$0.92^{+0.69}_{-0.54}$	$3.33^{+0.07}_{-3.33}$	2.93	3.40
16-4	17.5	-73.25	1.35	357	$1.22^{+0.40}_{-0.23}$	$0.20^{+0.05}_{-0.04}$	$0.04^{+0.01}_{-0.01}$	$1.43^{+0.30}_{-0.32}$	$4.85^{+0.00}_{-1.17}$	2.80	4.85
16-5	17.5	-73.10	1.20	245	$0.79^{+0.26}_{-0.22}$	$0.29^{+0.12}_{-0.11}$	$0.07^{+0.01}_{-0.02}$	$2.70^{+0.71}_{-0.66}$	$6.08^{+0.00}_{-3.10}$	2.64	6.08
16-6	17.5	-72.95	1.23	286	$1.03^{+0.10}_{-0.12}$	$0.31^{+0.08}_{-0.06}$	$0.07^{+0.02}_{-0.01}$	$3.45^{+0.70}_{-0.73}$	$3.24^{+1.53}_{-1.40}$	2.79	5.82
16-7	17.5	-72.80	1.22	408	$0.79^{+0.10}_{-0.09}$	$0.20^{+0.02}_{-0.04}$	$0.05^{+0.01}_{-0.01}$	$2.17^{+0.29}_{-0.32}$	$5.06^{+0.00}_{-1.24}$	2.80	5.06
16-8	17.5	-72.65	1.25	350	$0.20^{+0.02}_{-0.01}$	$2.06^{+0.38}_{-0.38}$	$0.25^{+0.04}_{-0.04}$	$6.01^{+0.52}_{-0.50}$	$5.21^{+0.00}_{-0.42}$	2.80	5.21
16-9	17.5	-72.50	1.20	221	$0.28^{+0.03}_{-0.02}$	$1.06^{+0.20}_{-0.26}$	$0.15^{+0.02}_{-0.03}$	$6.74^{+0.70}_{-0.72}$	$3.96^{+0.00}_{-0.86}$	2.87	3.96
16-10	17.5	-72.35	1.27	232	$0.23^{+0.02}_{-0.02}$	$1.38^{+0.28}_{-0.42}$	$0.18^{+0.03}_{-0.05}$	$6.95^{+0.87}_{-0.77}$	$3.84^{+0.00}_{-0.96}$	2.96	3.84
16-11	17.5	-72.20	1.42	254	–	$0.00^{+0.05}_{-0.00}$	–	–	–	2.84	4.07
16-12	17.5	-72.05	1.34	248	$1.98^{+0.00}_{-1.82}$	$0.05^{+0.04}_{-0.04}$	$0.01^{+0.01}_{-0.01}$	$0.32^{+0.31}_{-0.29}$	$4.28^{+0.00}_{-3.25}$	3.07	4.28
16-13	17.5	-71.90	1.32	87	$0.07^{+0.00}_{-0.00}$	$23.44^{+20.84}_{-22.31}$	$0.63^{+0.00}_{-0.63}$	$1.07^{+0.94}_{-1.02}$	$4.28^{+0.00}_{-3.57}$	2.98	4.28
17-2	18.0	-73.55	0.87	80	$1.08^{+0.41}_{-0.24}$	$0.14^{+0.08}_{-0.06}$	$0.03^{+0.02}_{-0.01}$	$1.34^{+0.73}_{-0.61}$	$3.44^{+0.00}_{-1.20}$	3.08	3.44
17-3	18.0	-73.40	1.46	255	$0.82^{+0.13}_{-0.15}$	$0.11^{+0.03}_{-0.03}$	$0.03^{+0.01}_{-0.01}$	$1.42^{+0.34}_{-0.35}$	$3.81^{+0.00}_{-0.95}$	2.95	3.81
17-4	18.0	-73.25	1.45	264	$1.09^{+0.00}_{-0.54}$	$0.04^{+0.03}_{-0.03}$	$0.01^{+0.01}_{-0.01}$	$0.28^{+0.26}_{-0.22}$	$5.53^{+0.00}_{-2.69}$	2.84	5.53
17-5	18.0	-73.10	1.13	432	$1.83^{+0.00}_{-0.48}$	$0.19^{+0.05}_{-0.05}$	$0.04^{+0.01}_{-0.01}$	$0.92^{+0.28}_{-0.23}$	$5.97^{+0.00}_{-1.56}$	2.76	5.97
17-6	18.0	-72.95	1.02	284	$0.83^{+0.14}_{-0.17}$	$0.16^{+0.06}_{-0.06}$	$0.04^{+0.01}_{-0.01}$	$2.28^{+0.77}_{-0.68}$	$3.31^{+1.03}_{-2.48}$	2.56	4.34
17-7	18.0	-72.80	1.26	201	$0.92^{+0.17}_{-0.19}$	$0.18^{+0.04}_{-0.04}$	$0.04^{+0.01}_{-0.01}$	$1.85^{+0.47}_{-0.47}$	$4.81^{+0.00}_{-1.52}$	2.76	4.81
17-8	18.0	-72.65	1.09	234	$0.28^{+0.05}_{-0.03}$	$0.57^{+0.16}_{-0.16}$	$0.08^{+0.02}_{-0.02}$	$3.39^{+0.53}_{-0.53}$	$4.41^{+0.00}_{-0.91}$	2.92	4.41
17-9	18.0	-72.50	1.38	334	$0.24^{+0.03}_{-0.02}$	$0.88^{+0.18}_{-0.20}$	$0.12^{+0.02}_{-0.02}$	$4.63^{+0.54}_{-0.59}$	$3.88^{+0.00}_{-0.47}$	2.89	3.88

Table B.1. Continued.

ID	RA	Dec	χ^2_ν	dof	kT	EM	L	F	N_H^{smc*}	N_H^{gal}	N_H^{smc}
17-10	18.0	-72.35	1.26	149	$0.29^{+0.12}_{-0.05}$	$0.24^{+0.10}_{-0.11}$	$0.04^{+0.01}_{-0.01}$	$1.70^{+0.54}_{-0.55}$	$3.73^{+0.00}_{-1.04}$	2.79	3.73
17-11	18.0	-72.20	1.34	196	$0.24^{+0.08}_{-0.05}$	$0.41^{+0.35}_{-0.25}$	$0.05^{+0.04}_{-0.03}$	$1.99^{+0.90}_{-0.83}$	$4.25^{+0.00}_{-2.12}$	3.15	4.25
18-2	18.5	-73.55	0.80	46	$0.22^{+0.05}_{-0.02}$	$1.41^{+0.39}_{-0.74}$	$0.17^{+0.04}_{-0.08}$	$6.46^{+1.12}_{-1.12}$	$3.60^{+0.00}_{-1.93}$	2.88	3.60
18-3	18.5	-73.40	1.28	272	$0.80^{+0.12}_{-0.17}$	$0.14^{+0.05}_{-0.04}$	$0.03^{+0.01}_{-0.01}$	$1.72^{+0.34}_{-0.40}$	$3.90^{+1.08}_{-2.12}$	2.91	4.98
18-4	18.5	-73.25	1.41	314	$2.00^{+0.00}_{-0.00}$	$0.13^{+0.04}_{-0.04}$	$0.03^{+0.01}_{-0.01}$	$0.56^{+0.19}_{-0.19}$	$6.71^{+0.00}_{-1.13}$	2.53	6.71
18-5	18.5	-73.10	1.18	478	$0.99^{+0.15}_{-0.16}$	$0.15^{+0.06}_{-0.04}$	$0.03^{+0.01}_{-0.01}$	$1.52^{+0.47}_{-0.45}$	$4.06^{+1.58}_{-2.15}$	2.77	5.64
18-6	18.5	-72.95	1.05	380	$0.22^{+0.89}_{-0.06}$	$0.19^{+0.17}_{-0.18}$	$0.02^{+0.02}_{-0.02}$	$0.82^{+0.53}_{-0.69}$	$3.98^{+0.00}_{-3.98}$	2.68	3.98
18-7	18.5	-72.80	1.03	226	$0.27^{+0.10}_{-0.07}$	$0.40^{+0.47}_{-0.26}$	$0.05^{+0.34}_{-0.03}$	$2.24^{+1.08}_{-0.97}$	$4.26^{+0.38}_{-3.07}$	2.84	4.63
18-8	18.5	-72.65	1.17	233	$1.07^{+0.25}_{-0.14}$	$0.22^{+0.06}_{-0.05}$	$0.05^{+0.01}_{-0.01}$	$2.15^{+0.53}_{-0.47}$	$4.02^{+0.00}_{-1.41}$	2.92	4.02
18-9	18.5	-72.50	1.08	182	$0.55^{+0.22}_{-0.12}$	$0.12^{+0.04}_{-0.05}$	$0.03^{+0.01}_{-0.01}$	$1.48^{+0.48}_{-0.50}$	$3.83^{+0.00}_{-1.08}$	2.86	3.83
18-10	18.5	-72.35	1.66	147	–	$0.00^{+0.04}_{-0.00}$	–	–	–	2.83	3.43
18-11	18.5	-72.20	1.05	143	$1.54^{+0.00}_{-0.39}$	$0.34^{+0.09}_{-0.08}$	$0.08^{+0.02}_{-0.02}$	$2.96^{+0.70}_{-0.72}$	$2.85^{+1.13}_{-1.32}$	2.80	3.98
19-1	19.0	-73.70	0.98	33	$0.21^{+0.03}_{-0.05}$	$0.48^{+0.74}_{-0.16}$	$0.06^{+0.07}_{-0.02}$	$4.67^{+1.42}_{-1.39}$	$0.13^{+2.25}_{-0.13}$	3.18	3.76
19-2	19.0	-73.55	1.13	78	$0.21^{+0.02}_{-0.01}$	$2.57^{+0.52}_{-0.89}$	$0.30^{+0.05}_{-0.09}$	$8.87^{+0.76}_{-0.77}$	$4.30^{+0.00}_{-0.96}$	2.93	4.30
19-3	19.0	-73.40	1.36	88	$0.16^{+0.01}_{-0.01}$	$7.07^{+0.58}_{-0.79}$	$0.69^{+0.06}_{-0.28}$	$10.74^{+0.90}_{-0.94}$	$5.22^{+0.00}_{-0.35}$	2.72	5.22
19-4	19.0	-73.25	1.56	247	$0.19^{+0.01}_{-0.02}$	$3.40^{+0.52}_{-1.18}$	$0.37^{+0.06}_{-0.12}$	$6.45^{+0.67}_{-0.82}$	$5.94^{+0.20}_{-1.29}$	2.67	6.14
19-5	19.0	-73.10	1.16	354	$0.68^{+0.41}_{-0.51}$	$0.03^{+0.15}_{-0.03}$	$0.01^{+0.02}_{-0.01}$	$0.28^{+0.30}_{-0.26}$	$5.99^{+0.28}_{-2.91}$	2.88	6.27
19-6	19.0	-72.95	1.23	433	$0.91^{+0.21}_{-0.12}$	$0.12^{+0.03}_{-0.04}$	$0.03^{+0.01}_{-0.01}$	$1.15^{+0.35}_{-0.38}$	$5.40^{+0.00}_{-1.02}$	2.76	5.40
20-1	19.5	-73.70	1.55	22	$0.15^{+0.05}_{-0.03}$	$5.49^{+1.33}_{-2.59}$	$0.48^{+0.11}_{-0.26}$	$9.78^{+2.45}_{-2.52}$	$3.40^{+0.00}_{-0.86}$	3.11	3.40
20-2	19.5	-73.55	1.19	71	$0.92^{+0.08}_{-0.09}$	$0.28^{+0.04}_{-0.03}$	$0.06^{+0.01}_{-0.01}$	$5.88^{+0.62}_{-0.63}$	$0.00^{+0.37}_{-0.00}$	2.99	3.54
20-3	19.5	-73.40	1.21	158	$0.75^{+0.06}_{-0.11}$	$0.48^{+0.08}_{-0.06}$	$0.11^{+0.02}_{-0.01}$	$7.57^{+0.74}_{-0.74}$	$2.37^{+1.24}_{-0.85}$	2.80	4.12
20-4	19.5	-73.25	1.20	327	$1.01^{+0.11}_{-0.15}$	$0.14^{+0.04}_{-0.03}$	$0.03^{+0.01}_{-0.01}$	$1.94^{+0.43}_{-0.43}$	$1.97^{+2.06}_{-1.16}$	2.83	4.65
20-5	19.5	-73.10	1.41	317	$1.08^{+0.11}_{-0.09}$	$0.12^{+0.03}_{-0.03}$	$0.03^{+0.01}_{-0.01}$	$0.96^{+0.22}_{-0.21}$	$5.23^{+0.00}_{-0.94}$	2.75	5.23
20-6	19.5	-72.95	1.38	238	$1.07^{+0.09}_{-0.14}$	$0.20^{+0.04}_{-0.04}$	$0.05^{+0.01}_{-0.01}$	$1.41^{+0.36}_{-0.29}$	$6.19^{+0.00}_{-0.69}$	2.78	6.19
21-2	20.0	-73.55	1.43	61	$0.23^{+0.04}_{-0.05}$	$0.67^{+0.69}_{-0.16}$	$0.08^{+0.07}_{-0.02}$	$7.46^{+1.76}_{-1.52}$	$0.12^{+1.40}_{-0.12}$	3.05	3.51
21-3	20.0	-73.40	1.22	189	$0.97^{+0.21}_{-0.15}$	$0.20^{+0.04}_{-0.05}$	$0.05^{+0.02}_{-0.01}$	$2.01^{+0.47}_{-0.52}$	$4.38^{+0.00}_{-1.51}$	2.90	4.38
21-4	20.0	-73.25	1.52	170	–	$0.00^{+0.02}_{-0.00}$	–	–	–	2.86	4.07
21-5	20.0	-73.10	1.32	193	$1.09^{+0.25}_{-0.07}$	$0.22^{+0.08}_{-0.05}$	$0.05^{+0.02}_{-0.01}$	$1.93^{+0.51}_{-0.41}$	$4.45^{+0.00}_{-0.53}$	2.83	4.45
22-3	20.5	-73.40	1.19	149	$2.00^{+0.00}_{-0.00}$	$0.10^{+0.06}_{-0.07}$	$0.02^{+0.01}_{-0.01}$	$0.76^{+0.45}_{-0.49}$	$3.25^{+0.00}_{-1.04}$	2.85	3.25
22-4	20.5	-73.25	1.54	169	–	$0.00^{+0.01}_{-0.00}$	–	–	–	2.85	3.88
22-5	20.5	-73.10	1.29	113	$2.00^{+0.00}_{-0.00}$	$0.11^{+0.06}_{-0.03}$	$0.02^{+0.01}_{-0.01}$	$0.70^{+0.38}_{-0.36}$	$4.21^{+0.00}_{-1.03}$	2.80	4.21
23-3	21.0	-73.40	0.82	29	$0.31^{+0.29}_{-0.14}$	$0.38^{+1.10}_{-0.27}$	$0.05^{+0.12}_{-0.04}$	$5.60^{+3.77}_{-3.87}$	$0.00^{+3.12}_{-0.00}$	2.92	3.12
23-4	21.0	-73.25	2.02	41	$2.00^{+0.00}_{-0.00}$	$0.17^{+0.09}_{-0.10}$	$0.04^{+0.02}_{-0.02}$	$1.09^{+0.62}_{-0.61}$	$4.10^{+0.00}_{-1.57}$	2.92	4.10

Notes. (1) Region identification (cf. Figure 6.8). (2-3) J2000 coordinates of the box centre. (4) Reduced χ^2 for the best fit. (5) Degrees of freedom for all spectra of this box. (6) Best-fit temperature in keV. (7) Best-fit emission measure per area in 10^{53} cm^{-3} arcsec^{-2}. (8) Unabsorbed luminosity of the SMC plasma in the (0.2–2.0) keV band in 10^{36} erg s^{-1}. (9) Absorbed flux from the SMC plasma component for the complete box in the (0.5–1.0) keV band in 10^{-14} erg cm^{-2} s^{-1}. (10) Best-fit absorbing column density for the SMC plasma in 10^{21} cm^{-2} (11) Line-of-sight column density of Galactic foreground N_H in 10^{20} cm^{-2}. (12) Total line-of-sight column density of SMC N_H in 10^{21} cm^{-2}.

Table B.2. XMM-*Newton* observations of the SMC.

(1) ID	(2) ObsID	(3) Target	(4) Date	(5) RA (J2000)	(6) Dec (J2000)	(7) ΔRA (″)	(8) ΔDec (″)	(9) ExpID	(10) Time (UT)	(11) Filter	(12) Mode	(13) Exp (s)	(14) Net Exp (s)
S1	0601210101	SMC survey 1	2009 May 14	$00^h58^m16^s.4$	-71°28′45″	1.42	0.85	M1S001	09:14:24	medium	ff	29419	4280
								M2S002	09:14:26	medium	ff	29425	4284
								PNS003	09:36:46	thin	ff	27512	3551
S2	0601210201	SMC survey 2	2009 Sep. 25	$00^h53^m58^s.9$	-71°43′48″	-0.91	0.1	M1S001	00:15:42	medium	ff	37420	37362
								M2S002	00:15:42	medium	ff	37425	37368
								PNS003	00:38:05	thin	ff	35834	35782
S3	0601210301	SMC survey 3	2009 May 18	$00^h49^m01^s.8$	-71°56′42″	0.53	-0.25	M1U002	10:29:15	medium	ff	31614	27589
								M2U002	10:29:34	medium	ff	31603	27580
								PNU002	10:47:01	thin	ff	30304	26332
S4	0601210401	SMC survey 4	2009 Sep. 25	$01^h02^m59^s.3$	-71°36′41″	-1.27	1.63	M1S001	11:22:24	medium	ff	37521	37464
								M2S002	11:22:23	medium	ff	37526	37469
								PNS003	11:44:46	thin	ff	35934	35882
S5	0601210501	SMC survey 5	2009 Sep. 25	$00^h58^m54^s.9$	-71°49′48″	0.47	-0.37	M1S001	22:30:43	medium	ff	50321	41464
								M2S002	22:30:43	medium	ff	50326	41469
								PNS003	22:53:05	thin	ff	48734	39923
S6	0601210601	SMC survey 6	2009 Sep. 27	$00^h55^m20^s.2$	-72°01′42″	-0.0	0.92	M1S001	00:10:53	medium	ff	38520	34617
								M2S002	00:10:53	medium	ff	38525	34622
								PNS003	00:33:16	thin	ff	36933	34278
S7	0601210701	SMC survey 7	2009 Sep. 27	$00^h49^m28^s.7$	-72°17′14″	0.78	0.82	M1S001	11:35:54	medium	ff	38621	38616
								M2S002	11:35:53	medium	ff	38626	38621
								PNS003	11:58:16	thin	ff	37034	37034
S8	0601210801	SMC survey 8	2009 Oct. 9	$00^h56^m15^s.5$	-72°21′55″	1.16	-0.34	M1S001	18:33:30	medium	ff	24620	24615
								M2S002	18:33:31	medium	ff	24625	24620
								PNS003	18:55:52	thin	ff	23034	23034
S9	0601210901	SMC survey 9	2009 Sep. 27	$00^h48^m08^s.9$	-72°37′39″	1.12	1.0	M1S001	23:02:34	medium	ff	41138	34083
								M2S002	23:02:33	medium	ff	41148	34091
								PNS003	23:24:56	thin	ff	39685	32742
S10	0601211001	SMC survey 10	2009 Nov. 9	$00^h43^m56^s.7$	-72°44′38″	-1.2	-2.56	M1S001	21:16:08	medium	ff	36520	26268
								M2S002	21:16:06	medium	ff	36525	26289
								PNS003	21:38:29	thin	ff	34934	24688
S11	0601211101	SMC survey 11	2009 Oct. 18	$00^h42^m29^s.5$	-73°02′27″	-0.1	-2.35	M1S001	22:47:09	medium	ff	31619	27114
								M2S002	22:47:09	medium	ff	31624	27119
								PNS003	23:09:31	thin	ff	30034	25534
S12	0601211201	SMC survey 12	2009 Oct. 20	$00^h42^m25^s.2$	-73°20′11″	1.82	0.06	M1S001	22:51:09	medium	ff	33119	29514

Table B.2. Continued.

ID	ObsID	Target	Date	RA	Dec	ΔRA	ΔDec	ExpID	Time	Filter	Mode	Exp	Net Exp
								M2S002	22:51:08	medium	ff	33124	29519
								PNS003	23:13:31	thin	ff	31534	27931
S13	0601211301	SMC survey 13	2009 Oct. 3	$00^h46^m28^s.7$	-73°24′25″	-0.36	-0.72	M1S001	05:08:47	medium	ff	32420	32363
								M2S002	05:08:46	medium	ff	32425	32368
								PNS003	05:31:10	thin	ff	30833	30779
S14	0601211401	SMC survey 14	2009 Nov. 4	$00^h52^m19^s.2$	-73°09′03″	0.89	0.67	M1S001	21:38:31	medium	ff	46520	32718
								M2S002	21:38:30	medium	ff	46525	32717
								PNS003	22:00:51	thin	ff	44290	31370
S15	0601211501	SMC survey 15	2009 Oct. 13	$00^h56^m25^s.5$	-73°02′58″	2.43	0.63	M1S001	00:02:01	medium	ff	37620	36863
								M2S002	00:02:00	medium	ff	37625	36868
								PNS003	00:24:22	thin	ff	36034	35280
S16	0601211601	SMC survey 16	2009 Oct. 11	$00^h58^m21^s.5$	-72°48′27″	0.71	-2.54	M1S001	22:43:47	medium	ff	43350	30443
								M2S002	22:43:46	medium	ff	43358	30443
								PNS003	23:06:08	thin	ff	41769	29100
S17	0601211701	SMC survey 17	2009 Oct. 16	$01^h02^m23^s.1$	-72°35′23″	1.37	1.36	M1S001	01:05:21	medium	ff	36738	20744
								M2S002	01:05:17	medium	ff	36785	20744
								PNS003	01:57:40	thin	ff	33664	17626
S18	0601211801	SMC survey 18	2009 Nov. 13	$01^h04^m04^s.7$	-72°22′52″	1.82	1.89	M1S001	20:59:56	medium	ff	2535	0
								M1U002	22:23:04	medium	ff	31531	22358
								M2S002	20:59:56	medium	ff	2540	0
								M2U002	22:23:11	medium	ff	31531	22377
								PNS003	21:22:19	thin	ff	34934	21659
S19	0601211901	SMC survey 19	2009 Nov. 30	$01^h08^m33^s.2$	-72°09′54″	0.19	0.86	M1S001	14:46:19	medium	ff	31619	31585
								M2S002	14:46:19	medium	ff	31624	31598
								PNS003	15:08:40	thin	ff	30034	30001
S20	0601212001	SMC survey 20	2009 Nov. 27	$01^h12^m56^s.4$	-72°22′38″	3.56	3.12	M1U002	22:39:06	medium	ff	28231	28126
								M2U002	22:39:09	medium	ff	28234	28113
								PNU002	23:04:04	thin	ff	26490	26368
S21	0601212101	SMC survey 21	2009 Nov. 16	$01^h11^m32^s.3$	-72°43′31″	1.02	-0.54	M1S001	05:48:08	medium	ff	34019	34014
								M2S002	05:48:06	medium	ff	34024	34019
								PNS003	06:10:27	thin	ff	32434	32434
S22	0601212201	SMC survey 22	2009 Nov. 19	$01^h13^m35^s.3$	-73°01′05″	1.35	1.0	M1S001	20:45:30	medium	ff	34521	22841
								M2S002	20:45:31	medium	ff	34523	22835
								PNS003	21:07:51	thin	ff	32934	22028
S23	0601212301	SMC survey 23	2009 Sep. 9	$01^h17^m03^s.4$	-73°04′05″	2.14	-0.44	M1S001	09:13:53	medium	ff	33421	33330
								M2S002	09:13:53	medium	ff	33426	33335

Table B.2. Continued.

ID	ObsID	Target	Date	RA	Dec	ΔRA	ΔDec	ExpID	Time	Filter	Mode	Exp	Net Exp
								PNS003	09:36:15	thin	ff	31834	31743
S24	0601212401	SMC survey 24	2009 Jun 29	$01^h20^m47^s.6$	-73°15′35″	2.13	2.05	M1S001	14:46:19	medium	ff	36619	26962
								M2S002	14:46:18	medium	ff	36624	26967
								PNS003	15:08:41	thin	ff	35034	25372
S25	0601212501	SMC survey 25	2009 Sep. 9	$01^h12^m31^s.5$	-73°18′24″	1.58	-0.12	M1S001	19:13:54	medium	ff	33421	33416
								M2S002	19:13:53	medium	ff	33426	33421
								PNS003	19:36:15	thin	ff	31834	31831
S26	0601212601	SMC survey 26	2009 Jun 29	$01^h08^m33^s.1$	-72°54′46″	2.64	-0.38	M1S001	06:04:39	medium	ff	28720	17760
								M2S002	06:04:38	medium	ff	28725	17770
								PNS003	06:27:01	thin	ff	27134	16803
S27	0601212701	SMC survey 27	2009 Dec. 26	$01^h07^m54^s.8$	-73°09′25″	2.4	0.17	M1S001	07:25:22	medium	ff	36622	36616
								M2S002	07:25:20	medium	ff	36624	36619
								PNS003	07:47:42	thin	ff	35034	35034
S28	0601212801	SMC survey 28	2009 Dec. 7	$01^h01^m54^s.0$	-73°07′05″	-0.14	1.26	M1U002	23:35:54	medium	ff	21352	17646
								M2U002	23:36:22	medium	ff	21325	17620
								PNU002	00:01:35	thin	ff	19563	15863
S29	0601212901	SMC survey 29	2009 Sep. 13	$00^h57^m04^s.8$	-73°20′23″	-0.06	1.02	M1S001	13:29:26	medium	ff	36120	34514
								M2S002	13:29:24	medium	ff	36125	34520
								PNS003	13:51:46	thin	ff	34534	32934
S30	0601213001	SMC survey 30	2009 Sep. 13	$00^h53^m18^s.3$	-73°32′45″	1.17	-1.84	M1S001	01:11:03	medium	ff	41720	40402
								M2S002	01:11:03	medium	ff	41725	40407
								PNS003	01:33:26	thin	ff	40134	38816
S31	0601213201	SMC survey 17	2010 Mar. 12	$01^h02^m23^s.1$	-72°35′23″	-0.42	0.7	M1S001	00:56:15	medium	ff	13619	10862
								M2S002	00:56:15	medium	ff	13624	10867
								PNS003	01:18:37	thin	ff	12034	9334
S32	0601213301	SMC survey 28	2010 Mar. 12	$01^h01^m54^s.0$	-73°07′05″	-0.02	4.25	M1S001	05:26:15	medium	ff	12621	8518
								M2S002	05:26:15	medium	ff	12626	8523
								PNS003	05:48:37	thin	ff	11034	8234
S33	0601213401	SMC survey 1	2010 Mar. 16	$00^h58^m16^s.4$	-71°28′45″	-0.19	1.31	M1S001	10:05:12	medium	ff	21521	15198
								M2S002	10:05:14	medium	ff	21526	15198
								PNU002	11:27:06	thin	ff	16224	12000
C1	0123110201	1ES0102-72	2000 Apr. 16	$01^h03^m50^s.0$	-72°01′55″	0.22	-1.41	M1S003	20:09:25	thin	lw	18800	17915
								M2S005	20:09:26	thin	lw	18799	17914
								PNS001	19:56:32	thin	ff	19301	18418
C2	0123110301	1ES0102-72	2000 Apr. 17	$01^h03^m50^s.0$	-72°01′55″	0.44	-0.83	M1S004	04:43:37	medium	lw	17800	11725
								M2S006	04:43:36	medium	lw	17799	11725

Table B.2. Continued.

ID	ObsID	Target	Date	RA	Dec	ΔRA	ΔDec	ExpID	Time	Filter	Mode	Exp	Net Exp
								PNS002	04:30:44	medium	ff	18300	12229
C3	0135720601	1ES0102-72	2001 Apr. 14	$01^h03^m50\overset{s}{.}0$	-72°01′55″	0.47	-0.68	M1S003	20:47:25	thin	lw	32900	13352
								M2S005	20:47:25	thin	lw	32900	13352
								PNS001	01:20:28	thin	ff	16200	9393
								PNS009	21:03:15	thin	sw	12600	0
C4	0135720801	1ES0102-72	2001 Dec. 25	$01^h04^m00\overset{s}{.}0$	-72°00′16″	2.35	-0.07	M1S003	18:44:37	thin	lw	32133	27568
								M2S005	18:44:37	thin	lw	32133	27565
								PNS001	19:00:33	thin	sw	31317	26759
C5	0135720901	1ES0102-72	2002 Apr. 20	$01^h04^m01\overset{s}{.}7$	-72°01′51″	1.39	0.54	M1S003	22:28:33	thin	ti	13026	10077
								M2S005	22:28:22	thin	lw	13043	10085
								PNS001	23:01:44	thin	ff	13774	9134
C6	0135721001	1ES0102-72	2002 May 18	$01^h04^m01\overset{s}{.}7$	-72°01′51″	0.02	1.61	M1S003	11:09:57	thin	ti	13089	9393
								M1S018	15:01:36	thin	lw	16691	7459
								M2S005	10:39:47	thin	lw	14890	9385
								M2S019	14:57:17	thin	ti	16687	7467
								PNS001	11:43:08	thin	ff	12216	10516
								PNS017	15:55:51	thin	lw	13000	4256
C7	0135721101	1ES0102-72	2002 Oct. 13	$01^h03^m43\overset{s}{.}5$	-72°01′31″	0.17	2.07	M1S003	03:19:38	thin	lw	23676	23064
								M2S005	03:19:38	thin	lw	23677	23066
								PNS001	03:24:22	thin	sw	10240	0
								PNS017	06:53:28	thin	lw	10237	9837
C8	0135721301	1ES0102-72	2002 Dec. 14	$01^h03^m56\overset{s}{.}4$	-72°00′28″	0.64	0.73	M1S003	03:53:55	thin	lw	28678	28372
								M2S005	03:53:55	thin	lw	28677	28367
								PNS001	03:58:40	thin	sw	10940	0
								PNS017	07:39:23	thin	lw	14538	14222
C9	0135721401	1ES0102-72	2003 Apr. 20	$01^h04^m18\overset{s}{.}1$	-72°02′32″	1.43	0.81	M1S003	12:04:59	calc	ff	9176	0
								M1U002	15:03:09	thin	lw	34532	30351
								M2S005	12:04:58	calc	ff	9181	0
								M2U002	15:03:14	thin	lw	34533	30365
								PNS001	12:27:08	calc	ff	7278	0
								PNS017	19:21:26	medium	lw	18741	18725
								PNU002	14:56:20	medium	sw	13604	0
C10	0135721501	1ES0102-72	2003 Oct. 27	$01^h03^m45\overset{s}{.}6$	-72°01′07″	0.09	1.22	M1S003	07:55:06	thin	lw	30177	24241
								M2S005	07:55:06	thin	lw	30181	24249
								PNS001	08:17:30	thick	ff	28535	22597
C11	0135721701	1ES0102-72	2003 Nov. 16	$01^h03^m45\overset{s}{.}6$	-72°01′07″	0.31	1.64	M1S003	06:12:02	thin	lw	27322	25158

Table B.2. Continued.

ID	ObsID	Target	Date	RA	Dec	ΔRA	ΔDec	ExpID	Time	Filter	Mode	Exp	Net Exp
								M2S005	06:12:03	thin	lw	27322	25170
								PNS001	06:34:29	thick	ff	31218	24492
C12	0135721901	1ES0102-72	2004 Apr. 28	$01^h04^m17\overset{s}{.}3$	-72°02′38″	0.0	1.13	M1S003	07:09:57	thin	lw	33280	32977
								M2S005	07:09:57	thin	lw	33285	32971
								PNS001	07:29:42	thick	lw	31800	31484
C13	0135722401	1ES0102-72	2004 Oct. 14	$01^h03^m45\overset{s}{.}6$	-72°01′07″	0.1	-0.46	M1S003	09:04:02	thick	lw	30878	30419
								M2S005	09:04:02	thick	lw	30883	30406
								PNS001	09:09:28	thick	sw	30672	30191
C14	0135722001	1ES0102-72	2004 Oct. 26	$01^h04^m03\overset{s}{.}6$	-72°01′44″	0.63	0.56	M1S003	06:56:39	thin	lw	31679	31599
								M2S005	06:56:39	thin	lw	31683	31601
								PNS001	07:25:23	thick	lw	29659	29578
C15	0135722101	1ES0102-72	2004 Nov. 7	$01^h03^m59\overset{s}{.}6$	-72°01′44″	0.37	1.89	M1S003	03:38:05	thin	lw	31577	24008
								M1S019	22:38:09	calc	ff	17441	0
								M2S005	03:38:04	thin	lw	31583	23998
								M2S020	22:38:08	calc	ff	17444	0
								PNS001	04:00:29	thin	ff	29937	22638
								PNS021	23:00:29	calc	ff	15122	0
C16	0135722201	1ES0102-72	2004 Nov. 7	$01^h04^m03\overset{s}{.}6$	-72°01′57″	0.64	1.01	M1U002	13:09:50	thin	lw	22643	0
								M1U003	21:15:30	thin	lw	2294	0
								M2S005	13:06:24	thin	lw	22858	0
								M2U002	21:18:05	thin	lw	2144	0
								PNS001	13:28:49	thin2	ff	10565	0
								PNU014	16:36:13	thin	ff	5383	0
								PNU027	18:15:48	thin2	ff	12781	0
C17	0135722301	1ES0102-72	2004 Nov. 7	$01^h03^m59\overset{s}{.}6$	-72°01′57″	-0.31	1.74	M1S003	22:35:47	thin	lw	31636	14035
								M2U002	22:44:58	thin	lw	31094	14038
								PNS001	22:58:12	thin	ff	30000	13768
C18	0135722501	1ES0102-72	2005 Apr. 17	$01^h04^m17\overset{s}{.}3$	-72°02′38″	0.25	1.64	M1S003	22:15:58	thin	lw	36878	23753
								M2S005	22:15:58	thin	lw	36882	23769
								PNS001	22:44:29	thin	lw	34872	21804
C19	0135722601	1ES0102-72	2005 Nov. 5	$01^h03^m47\overset{s}{.}1$	-72°00′57″	0.14	1.07	M1S003	06:45:03	thin	lw	30207	28998
								M2S005	06:45:04	thin	lw	30211	29009
								PNS001	06:50:29	medium	sw	30001	28796
C20	0135722701	1ES0102-72	2006 Apr. 20	$01^h04^m01\overset{s}{.}7$	-72°01′51″	0.02	2.32	M1S003	02:25:04	thin	lw	30207	30203
								M2S005	02:25:03	thin	lw	30212	30208
								PNS001	02:30:30	thin	sw	30001	30000

Table B.2. Continued.

ID	ObsID	Target	Date	RA	Dec	ΔRA	ΔDec	ExpID	Time	Filter	Mode	Exp	Net Exp
C21	0412980101	1ES0102-72	2006 Nov. 5	$01^h03^m47\overset{s}{.}1$	-72°00′57″	1.34	2.64	M1S002	00:55:20	thin	lw	32127	30986
								M2S003	00:55:20	thin	lw	32131	31000
								PNS001	01:00:46	medium	sw	31971	30889
C22	0412980201	1ES0102-72	2007 Apr. 25	$01^h04^m01\overset{s}{.}7$	-72°01′51″	0.04	2.21	M1S002	12:36:26	thin	lw	36128	19571
								M2S003	12:36:26	thin	lw	36133	19586
								PNS001	12:41:52	thin	sw	35972	19435
C23	0412980301	1ES0102-72	2007 Oct. 26	$01^h03^m47\overset{s}{.}1$	-72°00′57″	1.29	1.49	M1S002	09:49:09	thin	lw	36828	34966
								M2S003	09:49:09	thin	lw	36833	34972
								PNS001	09:54:35	medium	sw	36671	34811
C24	0412980501	1ES0102-72	2008 Apr. 19	$01^h04^m01\overset{s}{.}7$	-72°01′51″	-0.61	1.78	M1S002	09:22:50	thin	lw	29627	21997
								M2S003	09:22:50	thin	lw	29633	22005
								PNS001	09:28:17	thin	sw	29471	21738
C25	0412980701	1ES0102-72	2008 Nov. 14	$01^h04^m01\overset{s}{.}7$	-72°01′51″	1.97	2.54	M1S002	19:49:11	thin	lw	28628	28604
								M2S003	19:49:11	thin	lw	28633	28607
								PNS001	19:54:36	medium	sw	28471	28438
C26	0412980801	1ES0102-72	2009 Apr. 13	$01^h04^m01\overset{s}{.}7$	-72°01′51″	1.09	1.31	M1S002	00:04:42	thin	lw	28628	6522
								M2S003	00:04:42	thin	lw	28633	6527
								PNS001	00:10:08	thin	sw	28471	6369
C27	0412980901	1ES0102-72	2009 Oct. 21	$01^h04^m01\overset{s}{.}7$	-72°01′51″	1.63	2.05	M1S002	09:03:03	thin	lw	28628	28624
								M2S003	09:03:03	thin	lw	28633	28629
								PNS001	09:08:28	medium	sw	28471	28471
C28	0412981001	1ES0102-72	2010 Apr. 21	$01^h04^m01\overset{s}{.}7$	-72°01′51″	-0.15	0.93	M1S002	01:36:37	thin	lw	30228	27254
								M2S003	01:36:37	thin	lw	30233	27260
								PNS001	01:42:03	thin	sw	30072	27101
C29	0412981301	1ES0102-72	2010 Oct. 18	$01^h04^m01\overset{s}{.}7$	-72°01′51″	–	–	M1S002	21:41:20	thin	lw	7223	0
								M1U002	00:21:44	thin	lw	22103	20230
								M2S003	21:41:20	thin	lw	7231	0
								M2U002	00:21:51	thin	lw	22102	20237
								PNS001	21:46:45	thin	sw	31573	0
C30	0412981401	1ES0102-72	2011 Apr. 20	$01^h04^m05\overset{s}{.}2$	-72°01′06″	–	–	M1S002	23:41:18	thin	lw	34828	28770
								M2S003	23:41:18	thin	lw	34833	28776
								PNS001	23:46:44	thin	sw	34671	28617
C31	0412981501	1ES0102-72	2011 Nov. 4	$01^h04^m05\overset{s}{.}2$	-72°01′06″	–	–	M1S002	09:18:39	thin	lw	29927	29924
								M2S003	09:18:39	thin	lw	29933	29929
								PNS001	09:37:48	thin	ti	28936	0
C32	0412981601	1ES0102-72	2011 Nov. 4	$01^h01^m45\overset{s}{.}0$	-71°55′45″	–	–	M1U002	18:40:27	calc	ff	28717	28712

Table B.2. Continued.

ID	ObsID	Target	Date	RA	Dec	ΔRA	ΔDec	ExpID	Time	Filter	Mode	Exp	Net Exp
								M2U002	18:40:30	medium	ff	28720	28715
								PNU002	19:00:13	thin	ti	28936	0
A1	0112780201	RX J0059.2-7138	2000 Sep. 19	$00^h59^m13^s.0$	-71°38′50″	-0.36	-4.78	M1S002	02:05:37	medium	ti	4116	2425
								M2S003	02:05:34	thin	ti	4163	2428
								PNS001	01:24:24	medium	sw	8598	4900
A2	0110000101	IKT 5	2000 Oct. 15	$00^h49^m07^s.0$	-73°14′06″	-0.64	-1.21	M1S003	15:18:28	medium	ff	26897	25388
								M2S004	15:18:22	medium	ff	26897	25388
								PNS005	16:24:25	medium	eff	23000	21599
A3	0110000201	IKT 18	2000 Oct. 17	$00^h59^m26^s.0$	-72°10′11″	-0.07	1.87	M1S003	15:10:44	medium	ff	19747	16656
								M2S004	15:10:35	medium	ff	19747	16656
								PNS005	16:16:36	medium	eff	15850	13418
A4	0110000301	IKT 23	2000 Oct. 17	$01^h04^m52^s.0$	-72°23′10″	1.74	1.49	M1S003	21:45:54	medium	ff	32630	11854
								M2S004	21:45:53	medium	ff	32659	11854
								PNS005	22:51:56	medium	eff	30950	8148
A5	0112780601	RX J0059.2-7138	2001 Apr. 29	$00^h59^m13^s.0$	-71°38′50″	0.0	0.0	M1S002	21:07:59	medium	ti	4966	52
								M2S003	20:58:31	thin	sw	5795	52
								PNS001	21:14:07	medium	sw	5000	0
A6	0011450101	SMC X-1	2001 May 31	$01^h17^m05^s.1$	-73°26′35″	0.77	-0.23	M1S001	02:20:10	thin	ff	59018	43157
								M2S002	02:20:10	thin	ff	59018	43157
								PNS003	02:59:37	thin	ff	56390	40790
A7	0084200801	SMC Pointing 8	2001 Oct. 17	$00^h54^m31^s.7$	-73°40′56″	-0.14	-0.13	M1S001	10:07:40	medium	ff	21115	11491
								M2S002	10:07:40	medium	ff	21115	11491
								PNS003	10:46:50	thin	ff	18500	8866
A8	0011450201	SMC X-1	2001 Nov. 16	$01^h17^m05^s.1$	-73°26′35″	-0.41	0.21	M1S001	03:23:32	thin	ti	40761	40035
								M2S002	03:23:32	thin	ti	40761	40027
								PNS003	03:39:16	thin	sw	40218	0
A9	0018540101	HD 5980	2001 Nov. 20	$00^h59^m26^s.8$	-72°09′55″	0.67	0.84	M1S001	23:42:37	medium	ff	27025	1469
								M2S003	23:42:37	medium	ff	27025	1471
								PNS002	00:21:48	medium	ff	24410	1347
A10	0084200101	SMC Pointing 1	2002 Mar. 30	$00^h56^m41^s.7$	-72°20′24″	0.62	0.18	M1S001	13:48:28	medium	ff	21279	9197
								M2S002	13:48:29	medium	ff	21279	9197
								PNS003	14:21:45	thin	ff	18999	7927
A11	0142660801	RXJ0059.4-7118	2003 Nov. 17	$00^h59^m26^s.4$	-71°18′48″	0.04	-0.78	M1S001	03:55:54	thin	ff	12397	7338
								M2S002	03:55:56	thin	ff	12345	7337
								PNS003	04:18:12	thin	ff	11785	5996
A12	0157960201	XTE J0055-727	2003 Dec. 18	$00^h55^m22^s.0$	-72°42′00″	2.37	0.79	M1S004	14:32:45	medium	lw	3198	0

Table B.2. Continued.

ID	ObsID	Target	Date	RA	Dec	ΔRA	ΔDec	ExpID	Time	Filter	Mode	Exp	Net Exp
								M1U002	15:45:40	medium	ff	14760	14346
								M2S005	14:32:54	medium	ff	18673	14309
								PNS003	14:52:23	medium	lw	17198	14017
A13	0164560401	XTE J0051-727	2004 Apr. 28	$00^h51^m15^s.0$	-72°44′24″	0.0	0.0	M1S001	22:07:38	medium	ff	739	0
								M2S002	22:07:38	medium	ff	791	0
								PNS003	22:27:43	medium	lw	777	0
A14	0212282601	HD 5980	2005 Mar. 27	$00^h59^m26^s.8$	-72°09′54″	0.94	0.8	M1S001	16:20:35	medium	ff	26406	4495
								M2S002	16:20:35	medium	ff	26398	4501
								PNS003	16:42:56	closed	ff	34402	0
A15	0304250401	HD 5980	2005 Nov. 27	$00^h59^m26^s.8$	-72°09′54″	0.65	1.36	M1S009	06:22:46	medium	ff	17571	17503
								M2S010	06:22:48	medium	ff	17574	17511
								PNS011	06:45:04	medium	ff	15937	15866
A16	0304250501	HD 5980	2005 Nov. 29	$00^h59^m26^s.8$	-72°09′54″	2.29	-0.08	M1S001	05:11:36	medium	ff	16570	16565
								M2S002	05:11:33	medium	ff	16575	16570
								PNS003	05:33:52	medium	ff	14937	14933
A17	0304250601	HD 5980	2005 Dec. 11	$00^h59^m26^s.8$	-72°09′54″	0.8	-0.03	M1S001	12:48:45	medium	ff	16669	16664
								M2S002	12:48:42	medium	ff	16674	16669
								PNU002	14:25:31	medium	ff	10566	10566
A18	0311590601	Nova SMC 2005	2006 Mar. 13	$01^h14^m59^s.9$	-73°25′36″	2.41	1.98	M1S002	15:17:13	thin	ff	11370	6765
								M2S003	15:17:13	thin	ff	11375	6770
								PNS001	15:39:31	thin	ff	9737	5126
A19	0301170501	SMC Field-5	2006 Mar. 19	$00^h48^m23^s.4$	-73°41′00″	0.0	0.0	M1S001	14:23:19	medium	ff	13198	621
								M1U002	19:38:30	medium	ff	2155	0
								M2S002	14:23:17	medium	ff	13198	621
								M2U002	19:38:36	medium	ff	2153	0
								PNS003	14:45:35	medium	ff	19437	0
A20	0301170101	SMC Field-1	2006 Mar. 22	$01^h08^m06^s.4$	-72°52′23″	-0.24	1.81	M1S001	21:39:54	medium	ff	23172	17960
								M2S002	21:39:54	medium	ff	23174	17961
								PNS003	22:02:14	medium	ff	21537	17107
A21	0301170201	SMC Field-2	2006 Mar. 23	$00^h52^m12^s.1$	-72°01′42″	0.49	3.01	M1S001	04:48:17	medium	ff	23569	18364
								M2S002	04:48:18	medium	ff	23574	18369
								PNS003	05:10:34	medium	ff	21937	16737
A22	0301170601	SMC Field-6	2006 Mar. 27	$00^h40^m23^s.8$	-72°46′50″	-0.95	0.29	M1S001	12:21:01	thin	ff	24872	14035
								M2S002	12:20:59	thin	ff	24875	14038
								PNS003	12:43:17	thin	ff	23238	12677
A23	0301170301	SMC Field-3	2006 Apr. 6	$00^h42^m46^s.6$	-73°35′38″	-0.51	-0.51	M1S001	04:32:35	medium	ff	21570	17065

Table B.2. Continued.

ID	ObsID	Target	Date	RA	Dec	ΔRA	ΔDec	ExpID	Time	Filter	Mode	Exp	Net Exp
								M2S002	04:32:32	medium	ff	21575	17070
								PNS003	04:54:50	medium	ff	19937	15437
A24	0402000101	RXJ0103.8-7254	2006 Oct. 3	$01^h03^m52^s.2$	-72°54′28″	1.35	-2.35	M1S001	00:09:09	thin	ff	21619	20288
								M2S002	00:09:11	thin	ff	21625	20291
								PNS003	00:31:26	thin	ff	20037	18705
A25	0404680101	SMC Pointing 5_1	2006 Oct. 5	$00^h47^m36^s.0$	-73°08′24″	0.21	-2.78	M1S001	00:22:33	medium	ff	23099	9294
								M2S002	00:22:36	medium	ff	23101	9296
								PNS003	00:44:52	thin	ff	21514	7714
A26	0404680201	SMC Pointing 5_2	2006 Nov. 1	$00^h52^m26^s.4$	-72°52′12″	1.61	0.26	M1S001	00:56:29	medium	ff	32318	32282
								M2S002	00:56:29	medium	ff	32324	32290
								PNS003	01:18:46	thin	ff	30737	30703
A27	0403970301	SMC01: N19	2007 Mar. 12	$00^h47^m39^s.4$	-72°59′31″	-0.02	1.56	M1S001	20:02:20	thin	ff	38826	24662
								M2S002	20:02:18	thin	ff	38834	24674
								PNS003	21:02:54	thin	eff	34949	20927
A28	0404680301	SMC Pointing 5_3	2007 Apr. 11	$00^h51^m00^s.7$	-73°24′17″	0.38	-1.15	M1S001	19:38:25	medium	ff	23606	17618
								M2S002	19:38:25	medium	ff	23613	17626
								PNS003	20:00:45	thin	ff	22024	16039
A29	0404680501	SMC Pointing 5_5	2007 Apr. 12	$01^h07^m42^s.3$	-72°30′11″	0.29	1.37	M1S001	03:07:23	medium	ff	23621	23216
								M2S002	03:07:22	medium	ff	23626	23221
								PNS003	03:29:42	thin	ff	22037	21637
A30	0501470101	RX J0059.6-7138	2007 Jun 4	$00^h59^m41^s.8$	-71°38′15″	1.76	1.41	M1S001	08:59:50	thin	ff	33405	10560
								M2S002	08:59:50	thin	ff	33410	10565
								PNS003	09:22:09	thin	ff	31822	10318
A31	0500980201	SMC Pointing 6_2	2007 Jun 6	$01^h00^m00^s.0$	-72°27′00″	2.72	1.57	M1S001	08:52:16	medium	ff	28621	12905
								M2S002	08:52:11	medium	ff	28626	12913
								PNS003	09:14:30	thin	ff	27038	11421
A32	0500980101	SMC Pointing 6_1	2007 Jun 23	$00^h53^m02^s.4$	-72°26′17″	4.25	0.9	M1S001	05:51:39	medium	ff	25673	24164
								M2S002	05:51:39	medium	ff	25678	24169
								PNS003	06:13:58	thin	ff	24088	22688
A33	0503000201	SMC Field-5	2007 Oct. 28	$00^h48^m23^s.4$	-73°41′00″	1.55	-0.29	M1S001	05:49:58	medium	ff	21531	20301
								M2S002	05:49:58	medium	ff	21536	20301
								PNS003	06:11:55	medium	ff	19969	19164
A34	0503000301	SMC Field-6	2008 Mar. 16	$00^h40^m23^s.8$	-72°46′50″	-2.35	0.98	M1S001	15:25:16	thin	ff	9129	5353
								M1U002	18:39:00	thin	ff	14711	0
								M2S002	15:25:15	thin	ff	9147	5353
								M2U002	18:39:04	thin	ff	14703	0

Table B.2. Continued.

ID	ObsID	Target	Date	RA	Dec	ΔRA	ΔDec	ExpID	Time	Filter	Mode	Exp	Net Exp
								PNS003	15:47:13	thin	ff	28865	0
A35	0656780101	RX J0049.0-725	2010 Mar. 24	$00^h49^m05^s.9$	-72°50′55″	1.22	0.33	M1S001	01:24:49	medium	lw	6959	6955
								M2S002	01:24:47	medium	lw	6963	6960
								PNS003	01:53:20	medium	lw	5000	5000
A36	0656780201	RX J0049.0-725	2010 Mar. 27	$00^h49^m05^s.9$	-72°50′55″	0.37	0.44	M1S001	12:20:41	medium	lw	12528	8719
								M2S002	12:20:42	medium	lw	12533	8724
								PNS003	12:49:15	medium	lw	10569	6969
A37	0656780301	RX J0049.0-725	2010 Mar. 30	$00^h49^m05^s.9$	-72°50′55″	0.48	2.15	M1S001	08:49:55	medium	lw	6959	6955
								M2S002	08:49:55	medium	lw	6964	6961
								PNS003	09:18:28	medium	lw	5000	5000
A38	0677980301	SXP175	2011 Apr. 8	$01^h01^m55^s.7$	-72°24′26″	–	–	M1S002	09:22:42	medium	ff	18120	5372
								M2S006	09:22:42	medium	ff	18125	5377
								PNS001	09:45:05	medium	ff	16533	5134
O1	0112880901	CF Tuc	2000 Nov. 30	$00^h53^m04^s.8$	-74°39′07″	1.5	1.73	M1S001	12:12:57	medium	ff	40548	39542
								M2S002	12:12:54	medium	ff	40547	39542
								PNS003	12:54:23	medium	ff	38150	37150
O2	0142661001	RXJ0050.5-7455	2003 Nov. 16	$00^h50^m35^s.1$	-74°55′44″	-1.57	-2.42	M1U002	16:55:51	thin	ff	15119	12106
								M2U002	16:55:54	thin	ff	15122	12109
								PNU002	17:19:00	thin	ff	13437	10429
O3	0142660401	RXJ0059.1-7505	2003 Nov. 16	$00^h59^m10^s.7$	-75°05′23″	0.45	-0.9	M1S001	21:50:00	thin	ff	18671	16445
								M2S002	21:50:02	thin	ff	18676	16471
								PNS003	22:12:21	thin	ff	17036	14806
O4	0301150101	F00521-7054	2006 Mar. 22	$00^h53^m56^s.1$	-70°38′04″	-1.26	2.1	M1U002	17:50:55	thin	ff	10460	8270
								M2U002	18:05:32	thin	ff	9589	8228
								PNU002	18:08:59	thin	ff	9081	7778
O5	0301151601	F00521-7054	2006 Apr. 22	$00^h53^m56^s.1$	-70°38′04″	1.11	1.48	M1S001	00:55:16	thin	ff	13970	12165
								M2S002	00:55:14	thin	ff	13975	12170
								PNS003	01:17:32	thin	ff	12338	10538
O6	0602520401	NGC 602	2010 Mar. 25	$01^h29^m23^s.5$	-73°30′20″	–	–	M1S001	12:23:09	medium	ff	66220	63494
								M2S002	12:23:09	medium	ff	66225	63494
								PNS003	12:45:30	medium	ff	64635	62164
O7	0602520201	NGC 602	2010 Mar. 31	$01^h29^m23^s.5$	-73°30′20″	–	–	M1S001	12:04:11	medium	ff	110967	85028
								M1U002	20:17:30	medium	ff	4129	0
								M2S002	12:04:11	medium	ff	110982	85041
								M2U002	20:17:25	medium	ff	4139	0
								PNS003	12:26:33	medium	ff	116883	85083

Table B.2. Continued.

ID	ObsID	Target	Date	RA	Dec	ΔRA	ΔDec	ExpID	Time	Filter	Mode	Exp	Net Exp
O8	0602520301	NGC 602	2010 Apr. 2	$01^h29^m23\overset{s}{.}5$	-73°30′20″	–	–	M1S001	19:58:02	medium	ff	82902	52094
								M2S002	19:58:05	medium	ff	82933	52099
								PNS003	20:20:25	medium	ff	91076	50820
O9	0602520501	NGC 602	2010 Apr. 12	$01^h29^m23\overset{s}{.}5$	-73°30′20″	–	–	M1S001	10:58:23	medium	ff	9560	0
								M1U002	14:34:32	medium	ff	43652	39701
								M2S002	10:58:23	medium	ff	9620	0
								M2U002	14:40:43	medium	ff	43290	39678
								PNS003	11:20:46	medium	ff	55034	40363
O10	0164570701	GRB 050326	2005 Mar. 26	$00^h27^m34\overset{s}{.}1$	-71°22′34″	–	–	M1U002	18:43:46	medium	ff	44432	11172
								M2U002	18:43:58	thin	ff	44424	11160
								PNU002	19:34:25	thin	ff	41100	10206

Notes. (1) ID of the observation, where S,A,C, and O denote observations from the large-programme SMC survey, archival data, calibration observations and outer fields. (2) XMM-*Newton* observation Id. (3) Name of the observation target. (4) Date of the beginning of the observation. (5-6) Pointing direction. (7-8) Boresight correction. Only available for observations that were used for the point-source catalogue. (9) Exposure Id. (10) Start time of the exposure. (11) Instrument filter. (12) Instrument mode (see Table 2.2). (13) Total exposure time. (14) Exposure time after standard GTI screening, not considering the instrumental death time.

C. EPIC images

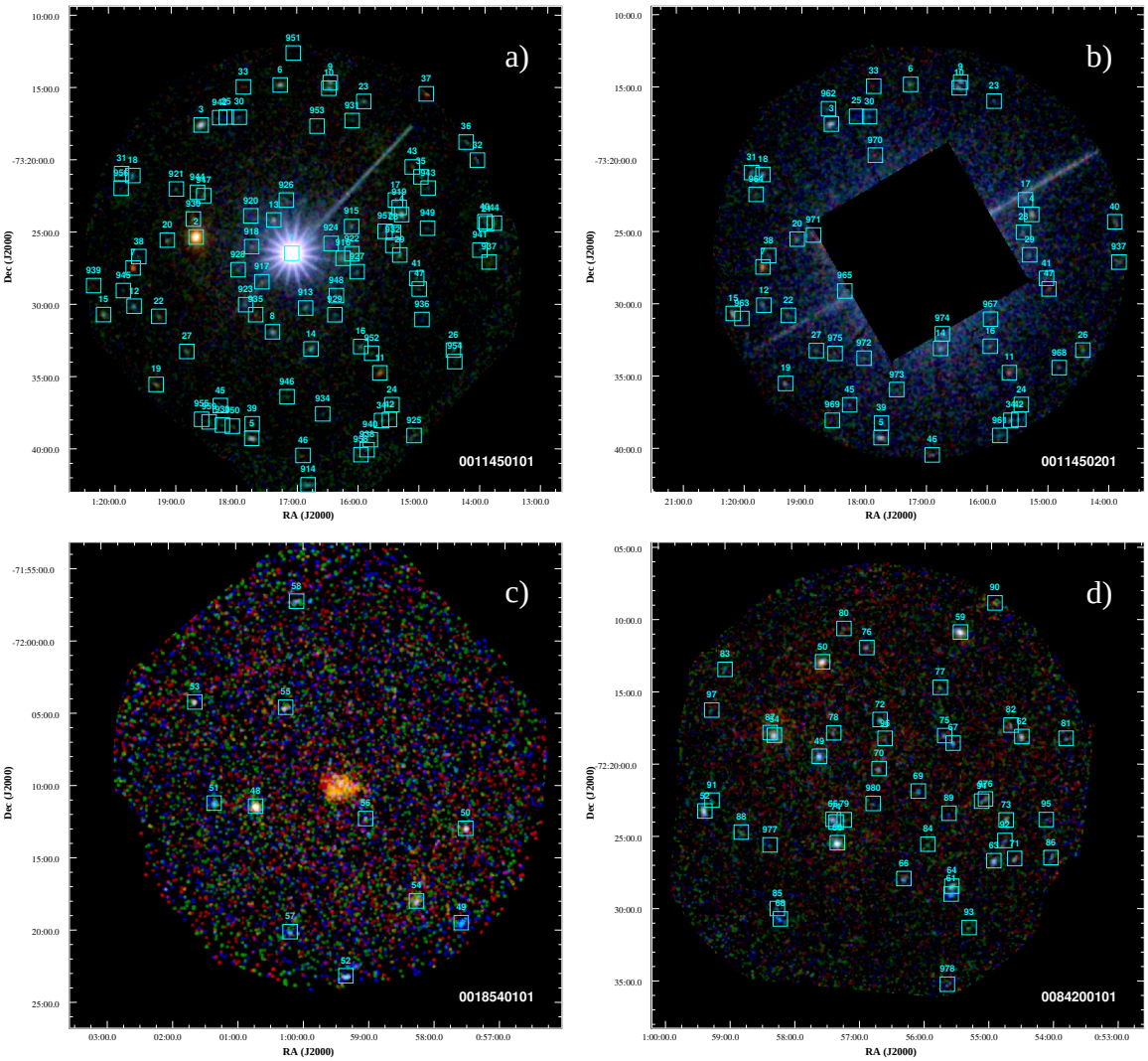

Figure C.1. Combined EPIC images of the individual observations. Colours (red/green/blue) represent logarithmically scaled intensities in the (0.2–1.0)/(1.0–2.0)/(2.0–4.5) keV bands. Detections, which were used for the point-source catalogue, are marked with $1' \times 1'$ boxes and labelled with the source-catalogue number. Continued on next page.

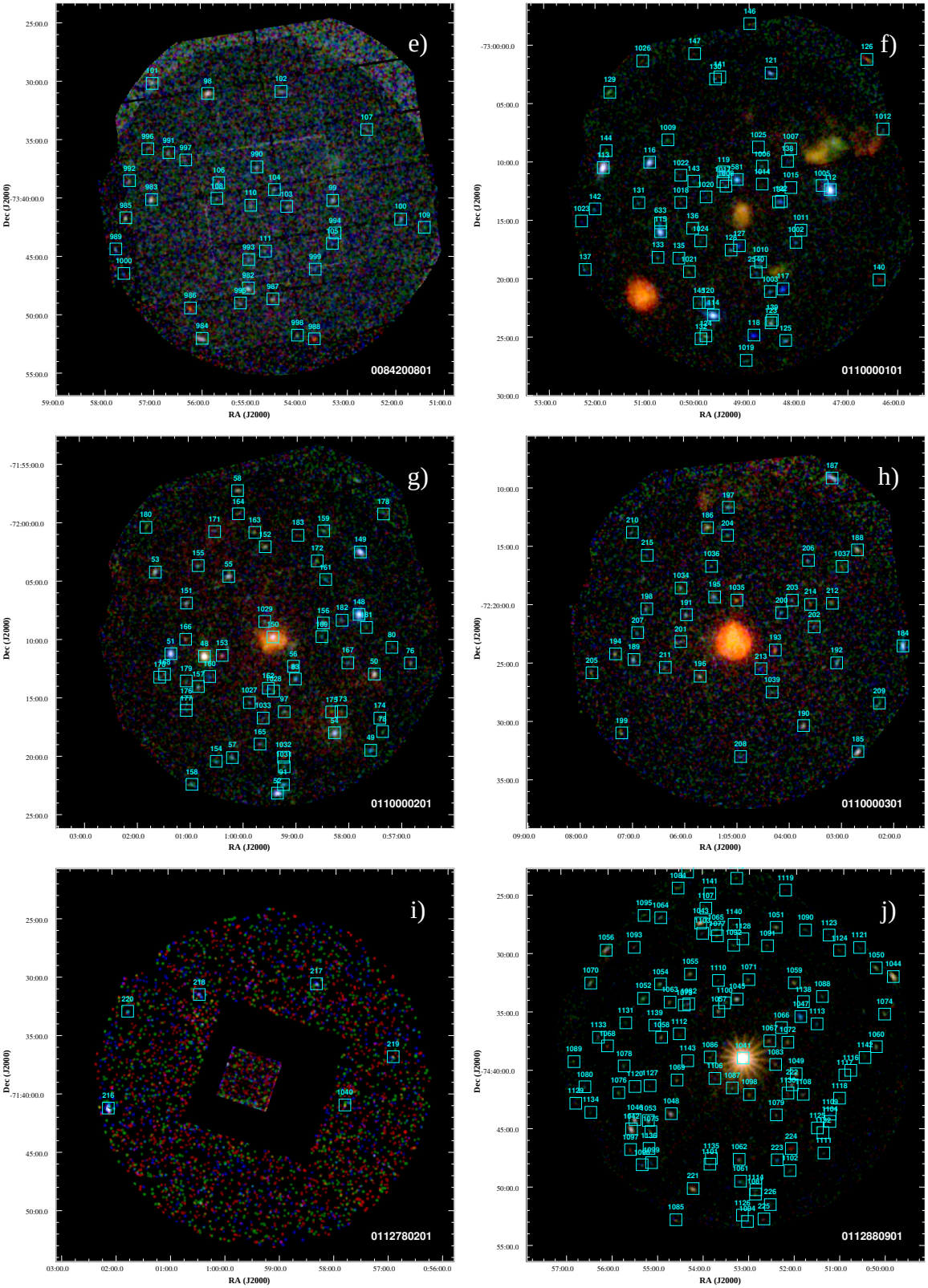

Figure C.1. Continued from previous page.

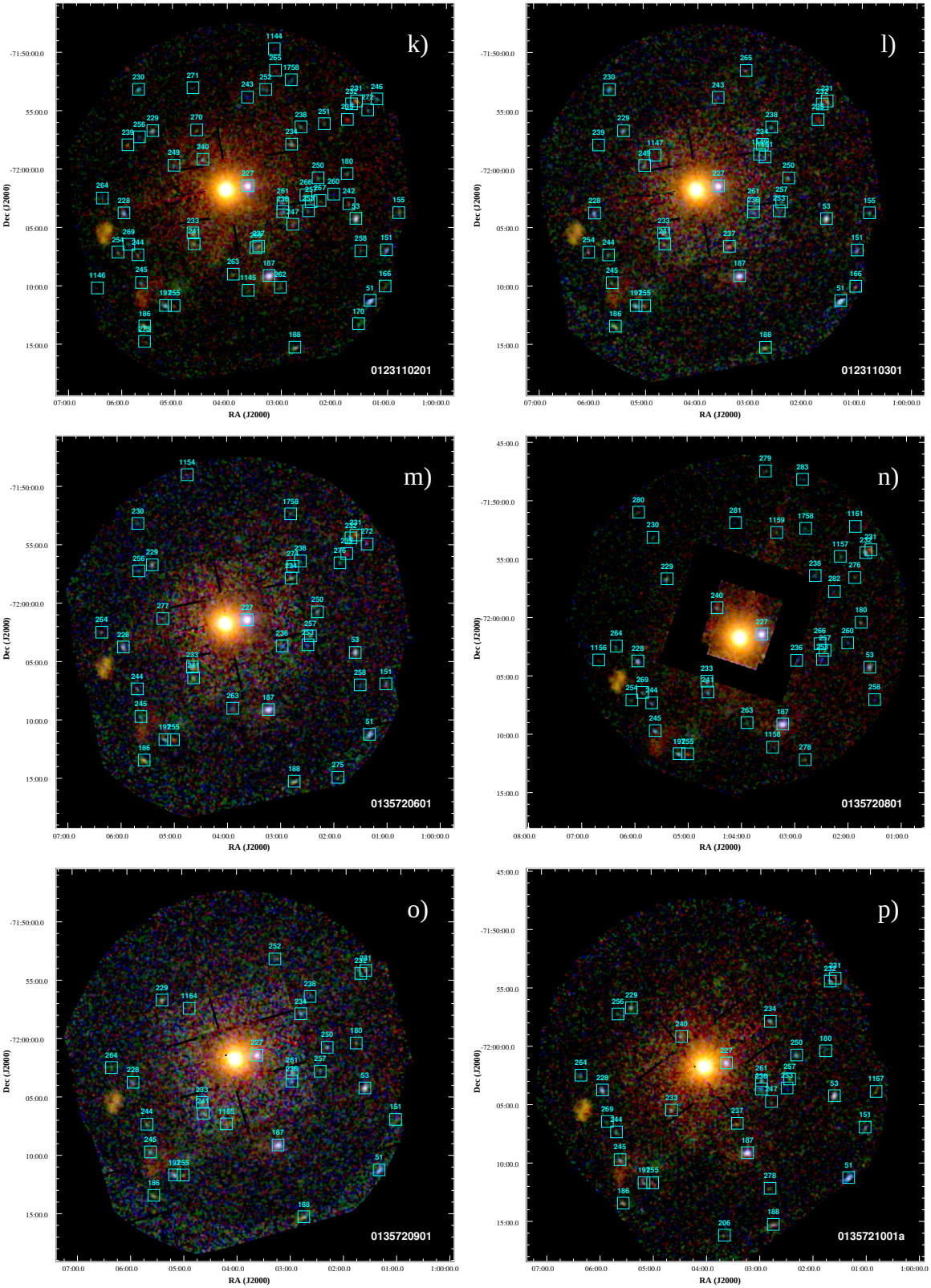

Figure C.1. Continued from previous page.

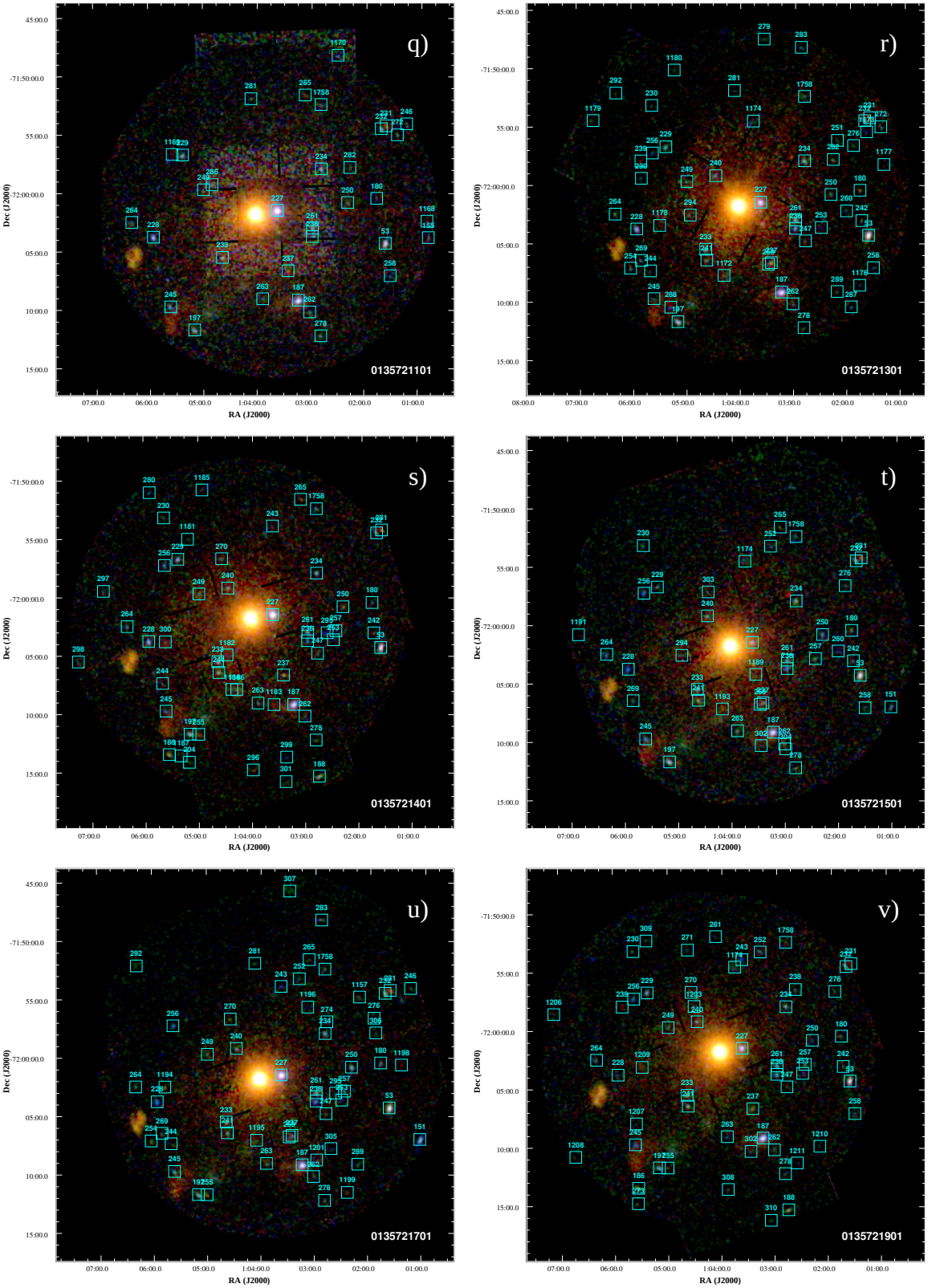

Figure C.1. Continued from previous page.

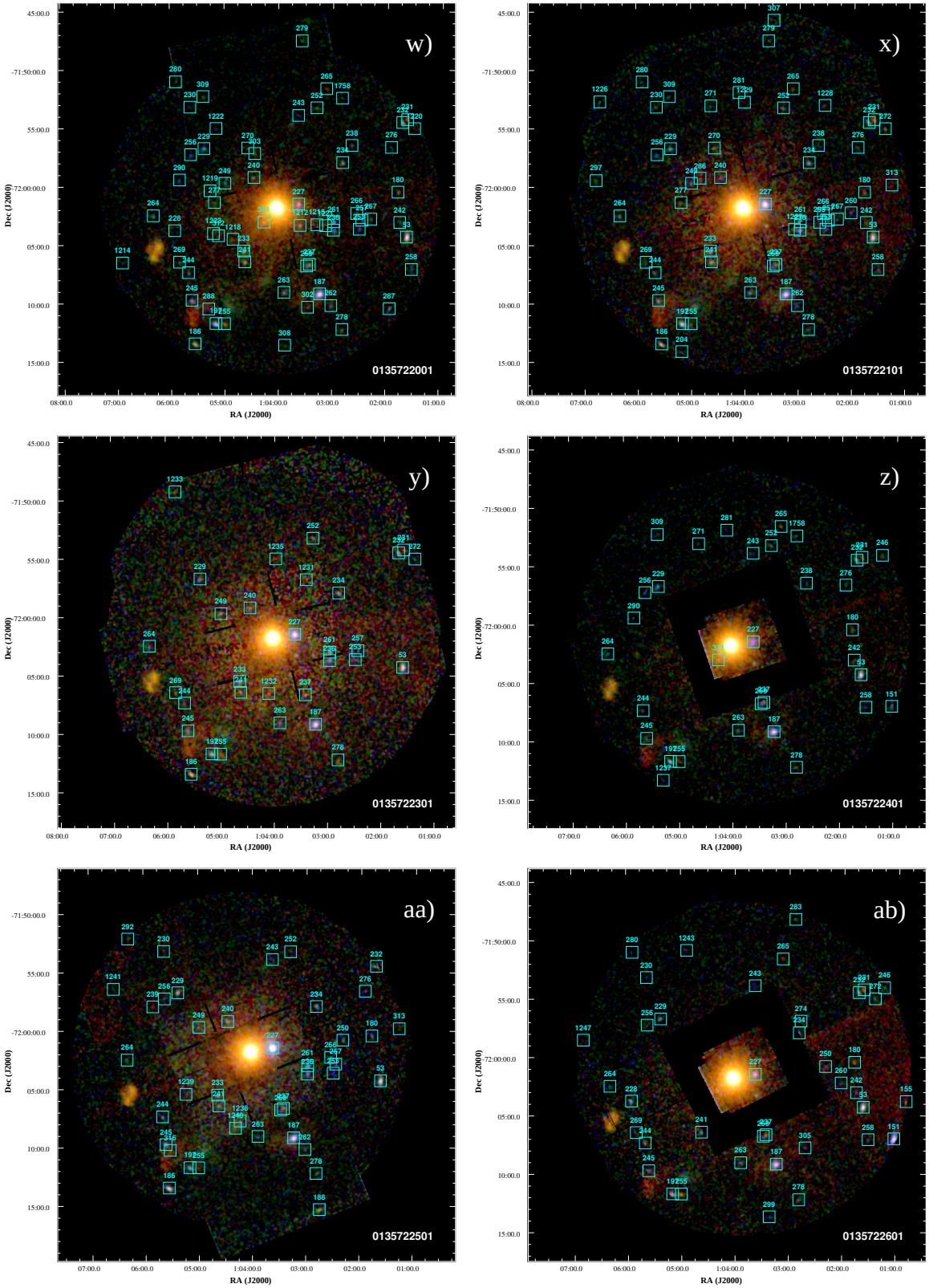

Figure C.1. Continued from previous page.

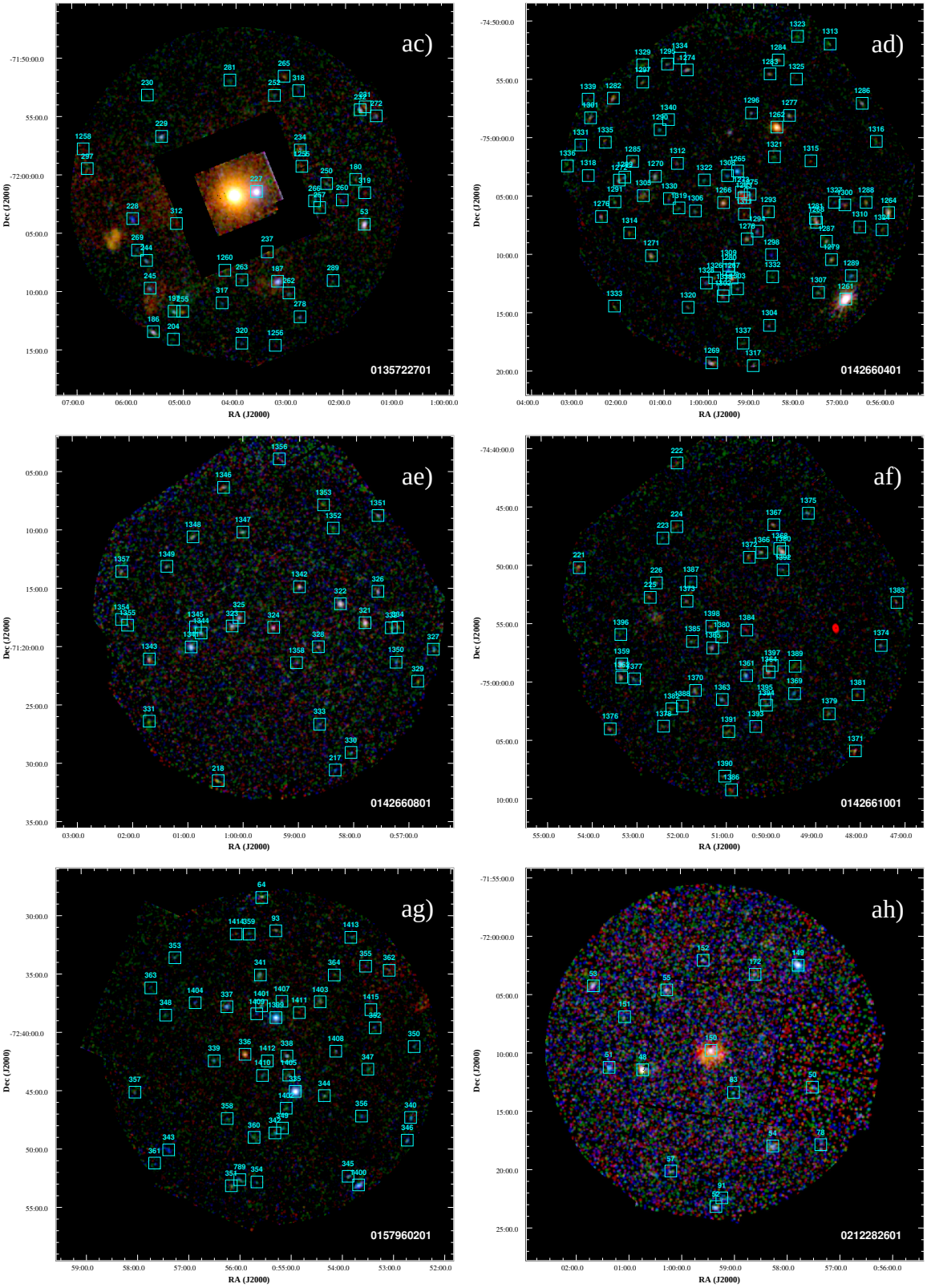

Figure C.1. Continued from previous page.

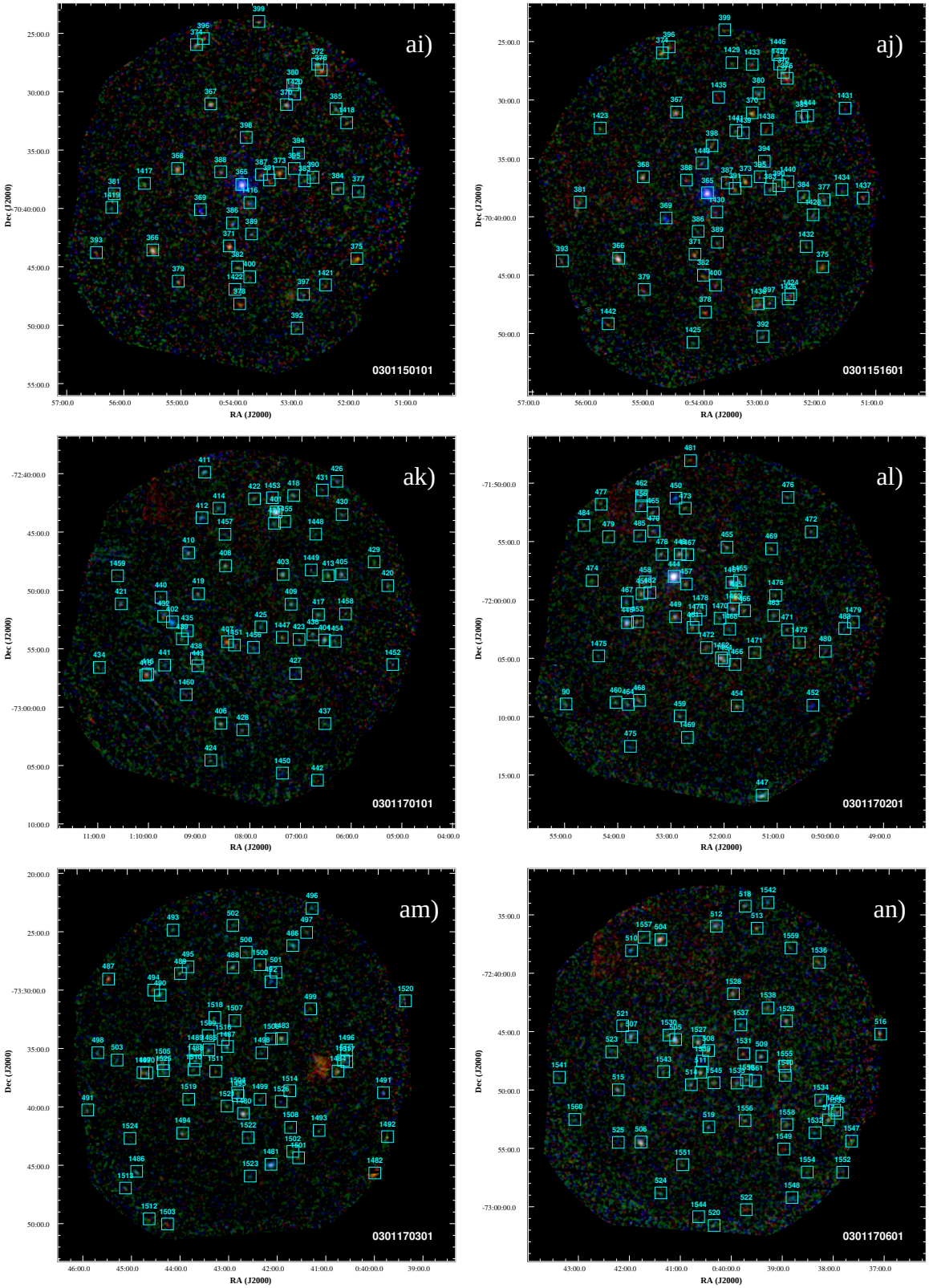

Figure C.1. Continued from previous page.

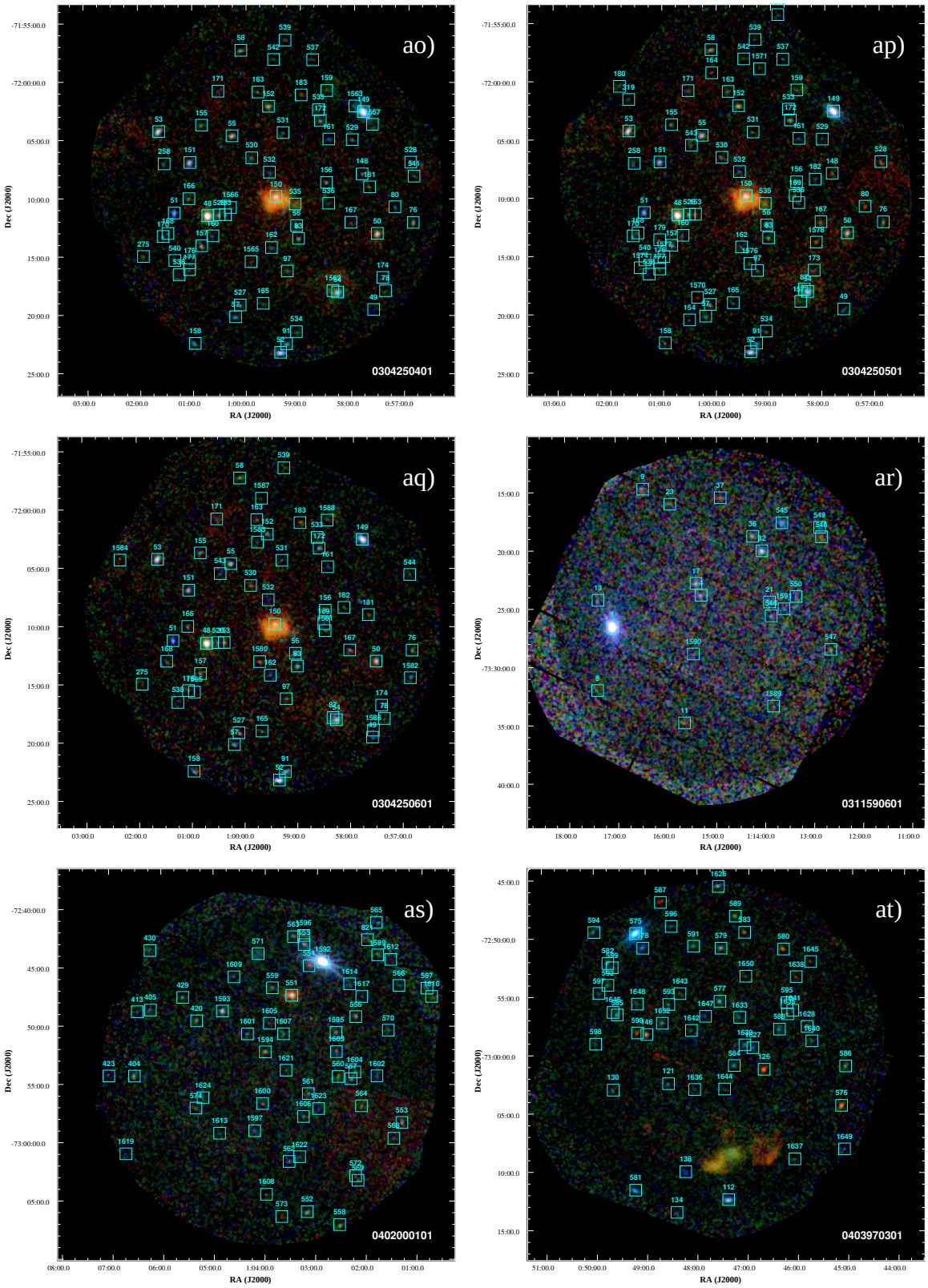

Figure C.1. Continued from previous page.

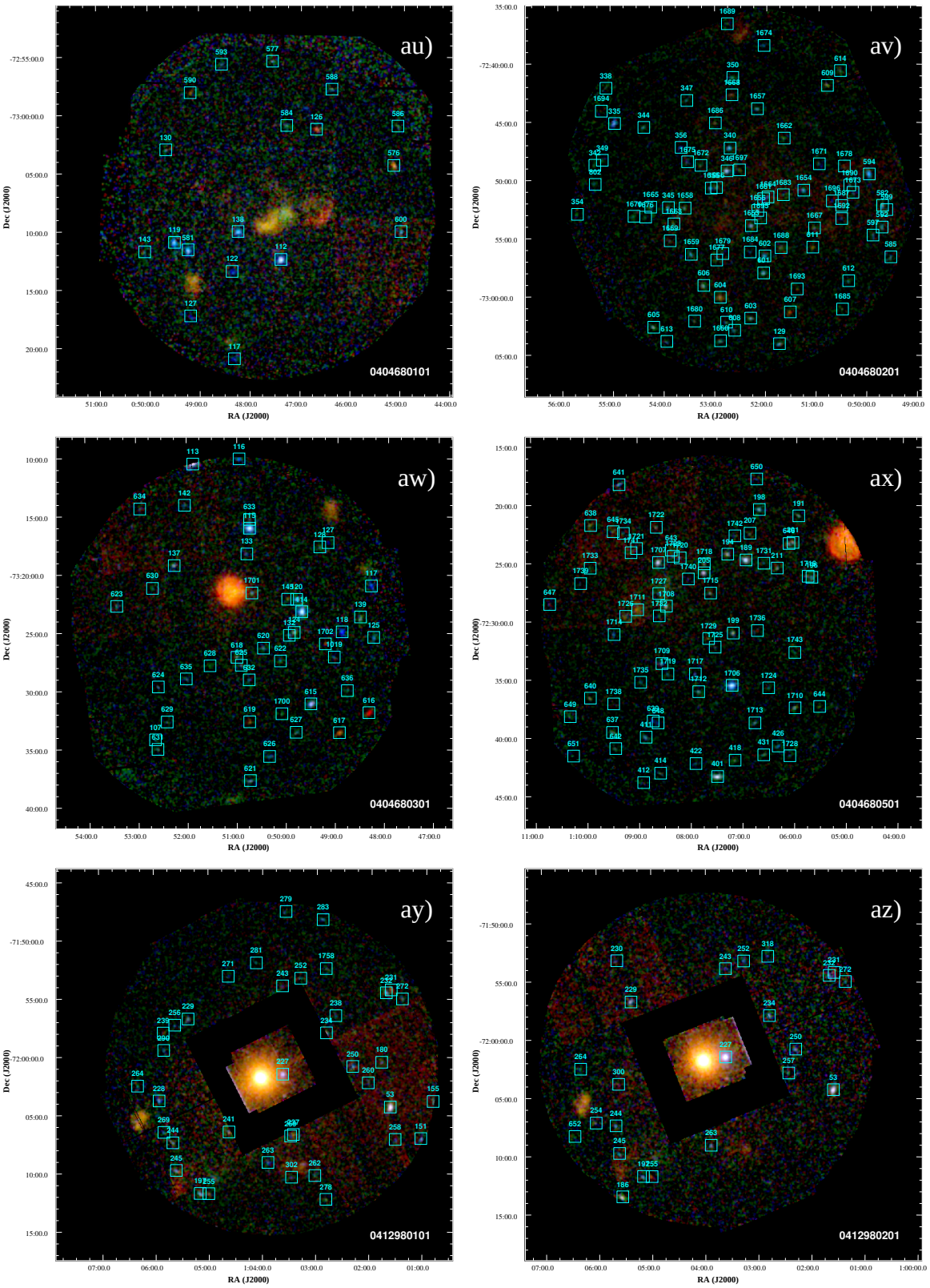

Figure C.1. Continued from previous page.

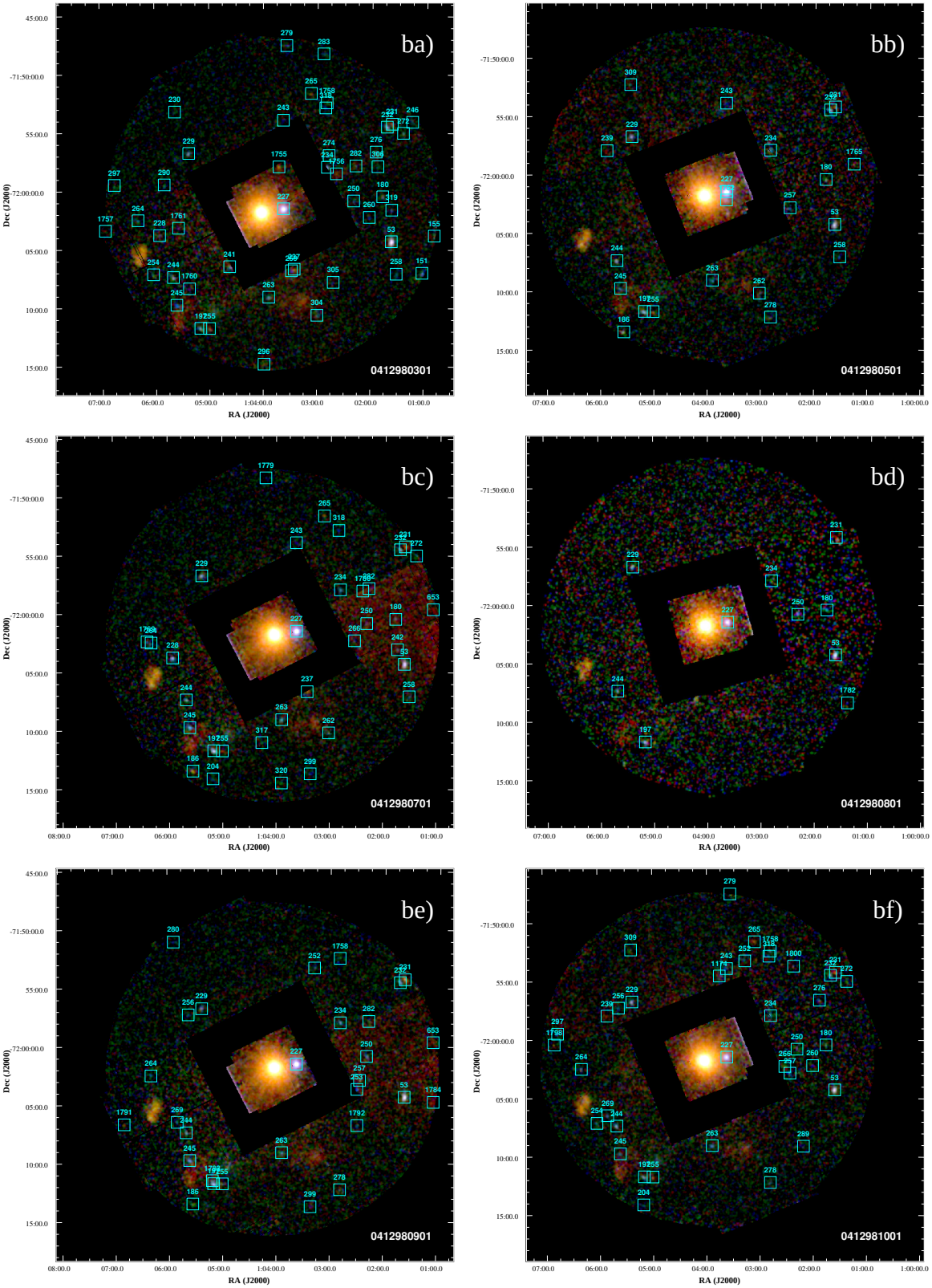

Figure C.1. Continued from previous page.

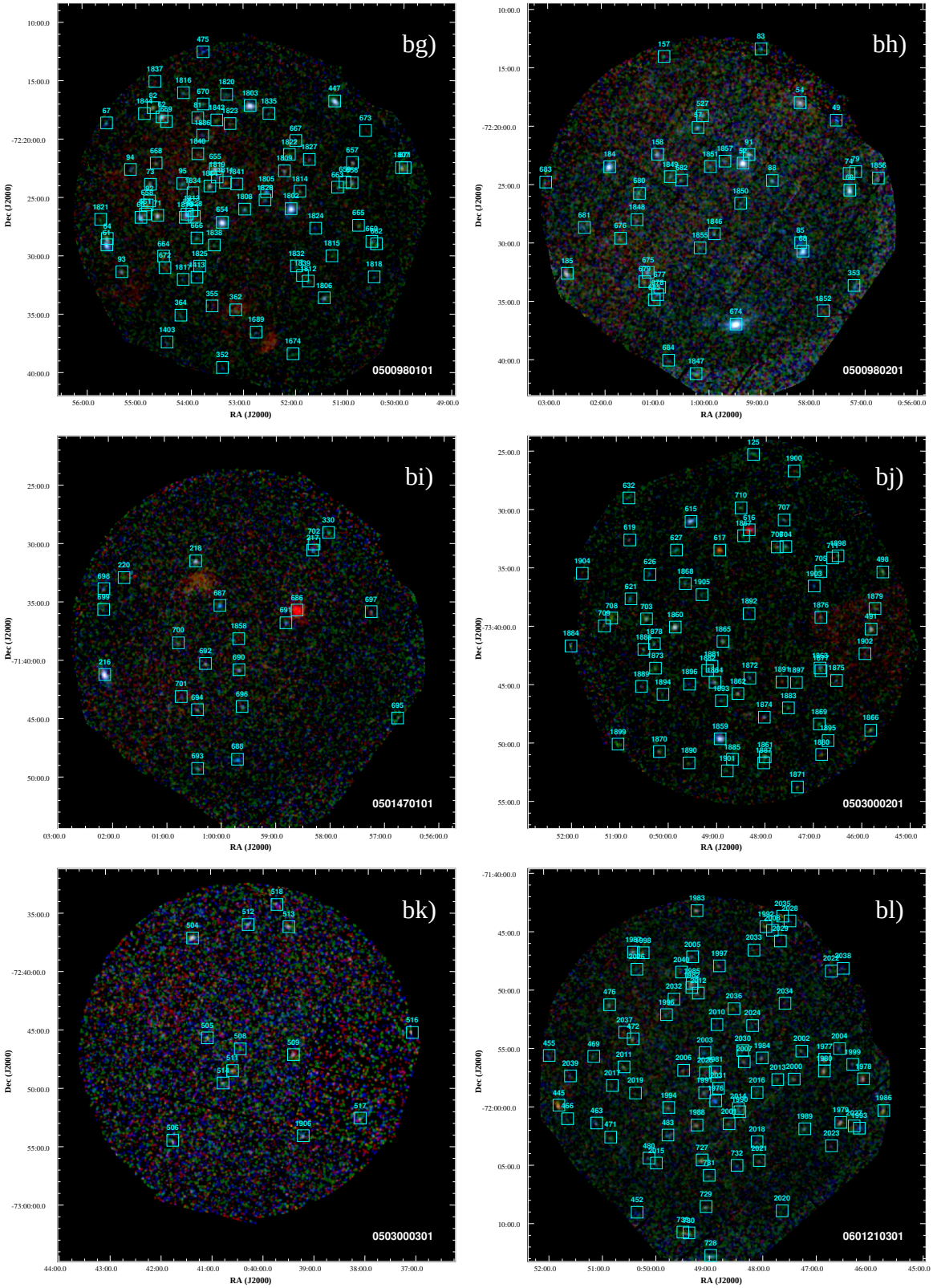

Figure C.1. Continued from previous page.

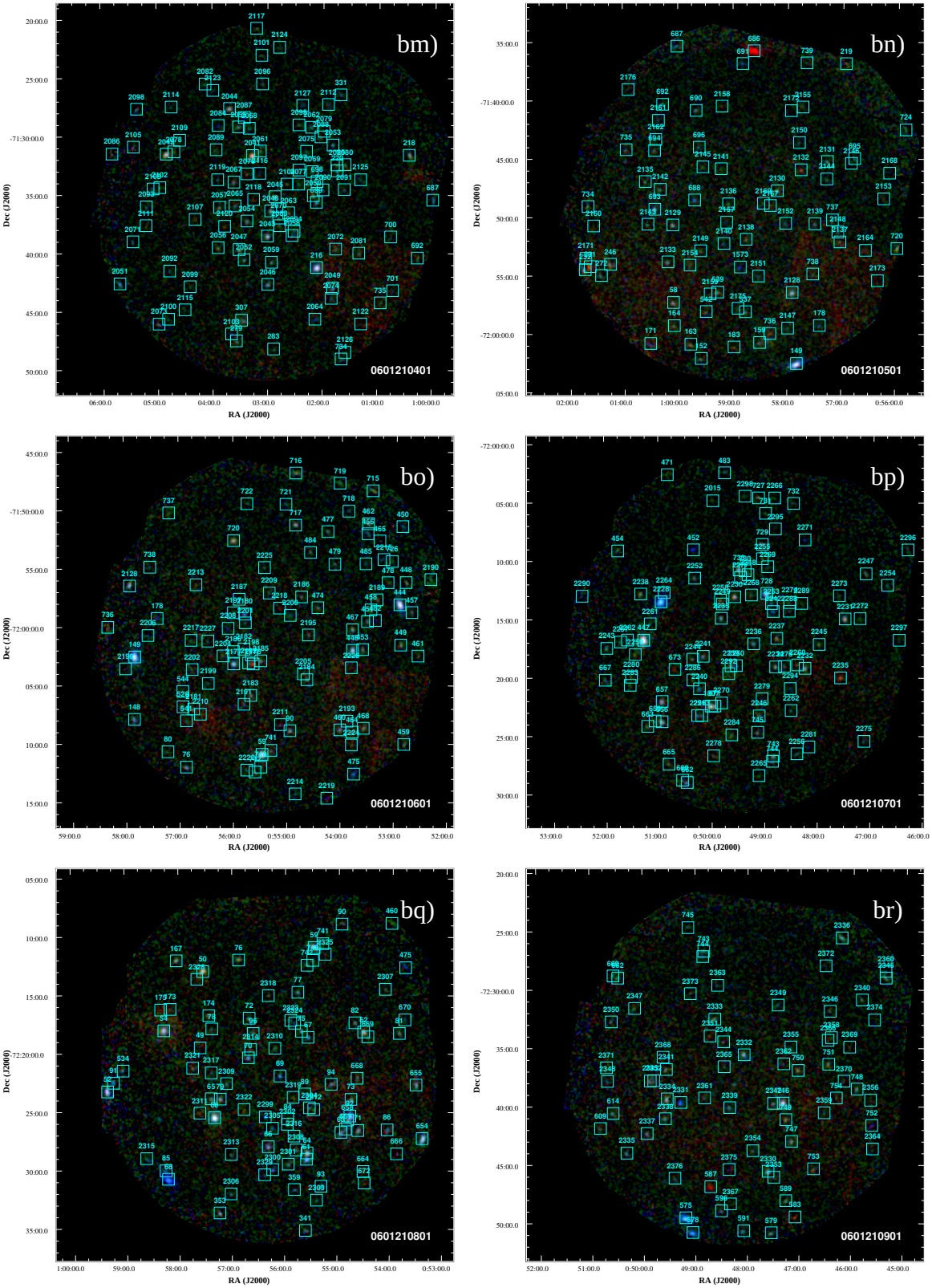

Figure C.1. Continued from previous page.

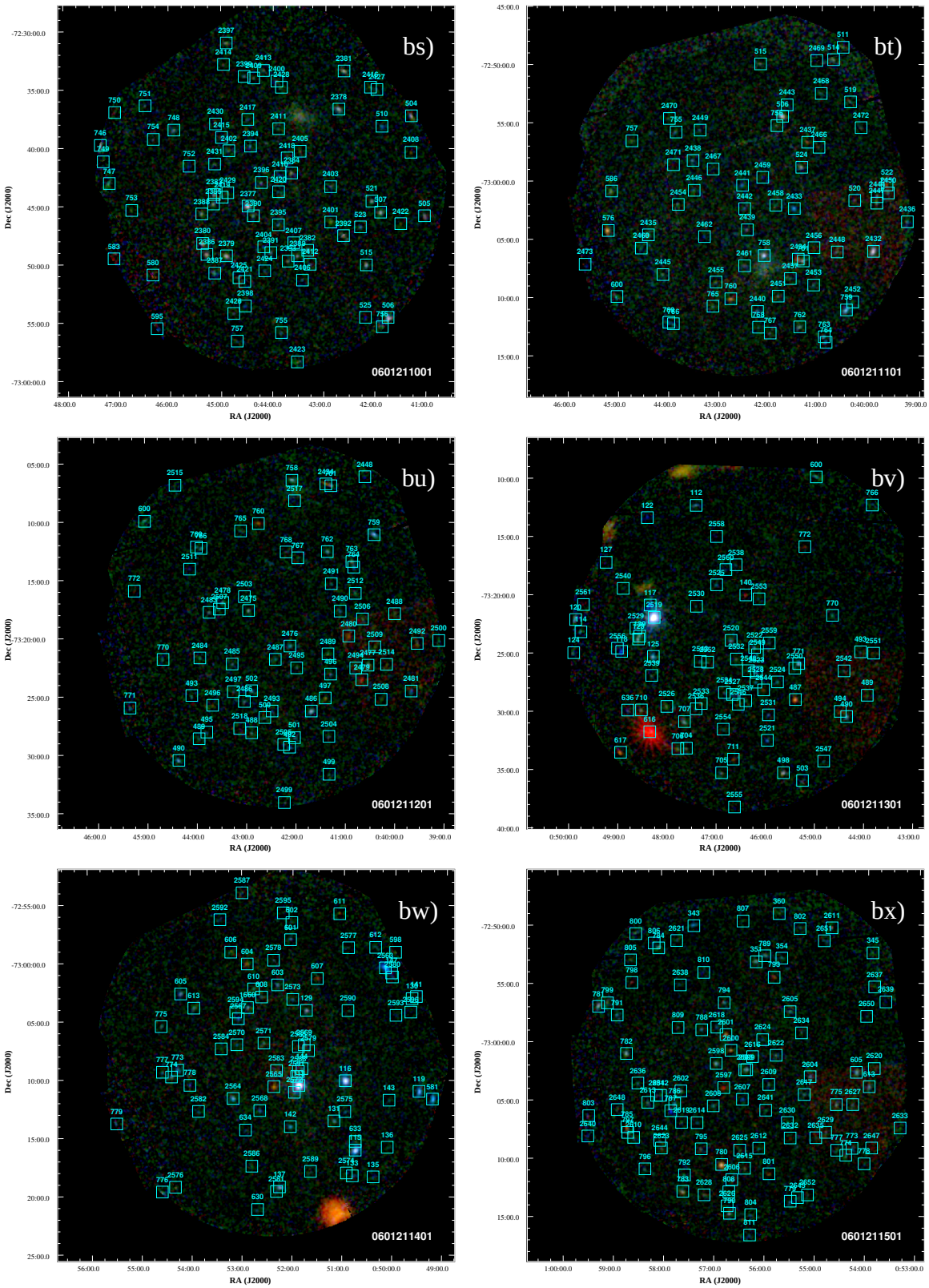

Figure C.1. Continued from previous page.

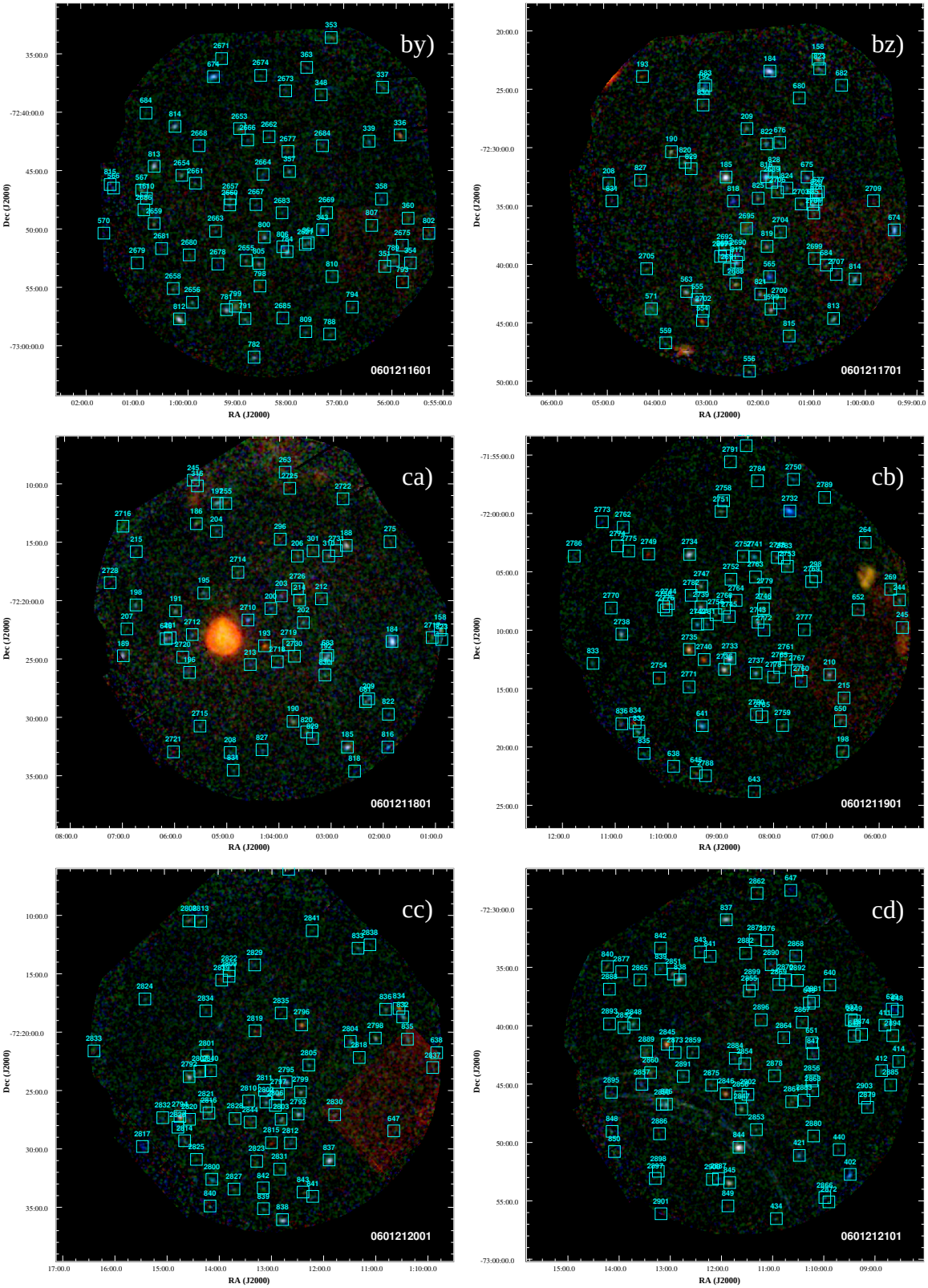

Figure C.1. Continued from previous page.

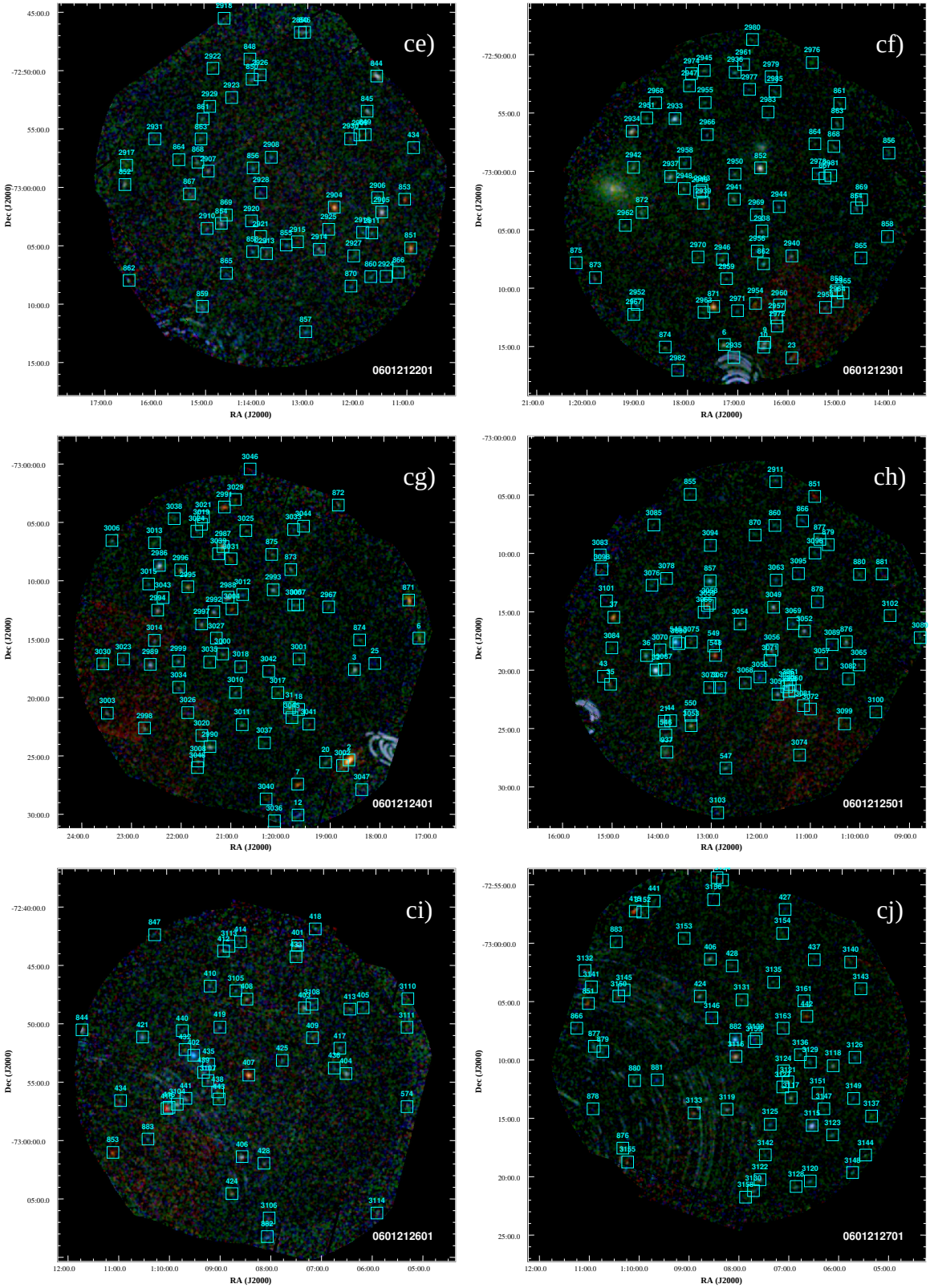

Figure C.1. Continued from previous page.

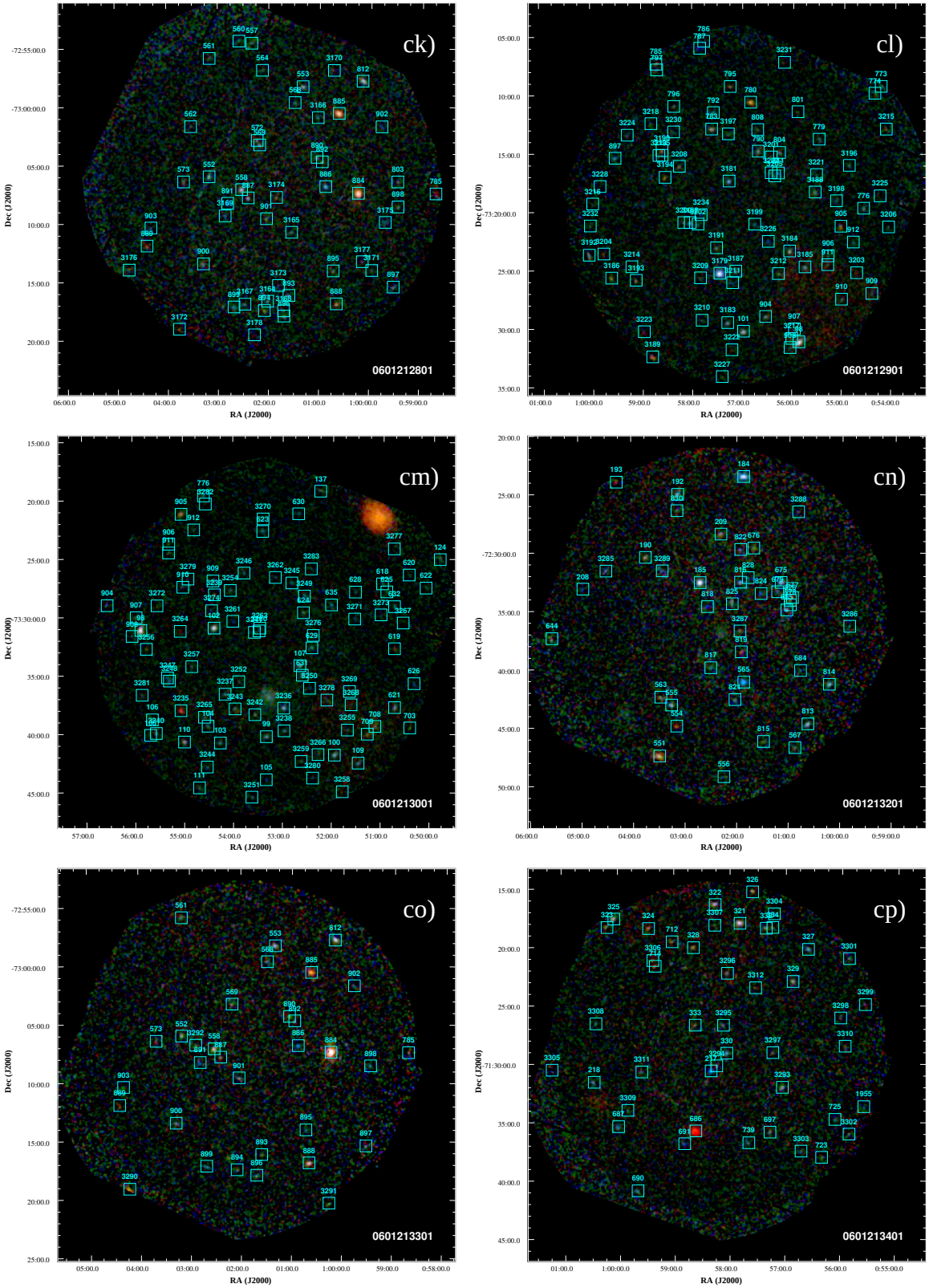

Figure C.1. Continued from previous page.

Figure C.2. Combined EPIC mosaic image of the *main field*. Red, green, and blue represent logarithmically scaled intensities in the (0.2−1.0), (1.0−2.0), and (2.0−4.5) keV bands. Super-soft X-ray sources appear in red, Galactic stars in red or orange, AGN in green, blue or white, high-mass X-ray binaries in blue or white. Extended red or orange sources are identified as SNRs. ClGs appear as extended green sources. Large-scale red structures originate from diffuse X-ray emission. Detector background is subtracted and intervals with high background were carefully removed. EPIC-MOS CCDs in *anomalous state* were removed. Artefacts, like single reflections of photons from SMC X-1, have been excluded. The image is corrected for exposure and vignetting and was smoothed adaptively. For more details, see Section 3.3.14.